10 W-Average-Power Single-Frequency Ti:sapphire Laser with Tuning Agility

–

A Breakthrough in High-Resolution 3D Water-Vapor Measurement

DISSERTATION

zur Erlangung des

Doktorgrades der Naturwissenschaften (Dr. rer. nat.)

Fakultät Naturwissenschaften
Universität Hohenheim

Institut für Physik und Meteorologie

vorgelegt von

Simon Metzendorf
aus Heppenheim (Bergstr.)

2018

Dekan: Prof. Dr. Uwe Beifuß
Fakultät Naturwissenschaften
Universität Hohenheim

1. berichtende Person: Prof. Dr. Volker Wulfmeyer
Institut für Physik und Meteorologie
Universität Hohenheim

2. berichtende Person: Prof. Dr. Paolo Di Girolamo
Scuola di Ingegneria
Università degli Studi della Basilicata

Eingereicht am: 17.08.2018

Mündliche Prüfung am: 21.11.2018

Die vorliegende Arbeit wurde am 15.11.2018 von der Fakultät Naturwissenschaften der Universität Hohenheim als „Dissertation zur Erlangung des Doktorgrades der Naturwissenschaften (Dr. rer. nat.)“ angenommen.

Kurzfassung

Die Kenntnis über die Wasserdampfverteilung in der Atmosphäre ist von großer Bedeutung für den Menschen und seine Umwelt. Als meteorologische Variable hat Wasserdampf einen erheblichen Einfluss auf die Entwicklung von Wetter und Klima und ist dementsprechend auch ein wichtiger Indikator für deren Änderung. Simulationen und Vorhersagen hängen dabei von der Verfügbarkeit und der Qualität der Beobachtungsdaten ab, welche zur Initialisierung und Validierung der numerischen Modelle dienen. Zur korrekten Beschreibung ist es entscheidend, die Transport- und Austauschprozesse im System Land–Atmosphäre vollständig zu erfassen. Zudem weist die Wasserdampfverteilung in der atmosphärischen Grenzschicht eine hohe Variabilität auf. Daher sind Messungen des Wasserdampffeldes mit hoher räumlicher und zeitlicher Auflösung sowie Genauigkeit von essenzieller Notwendigkeit.

Lidar-Messgeräte, wie sie am *Institut für Physik und Meteorologie* der *Universität Hohenheim* entwickelt und betrieben werden, eignen sich hervorragend, um solche Messungen durchzuführen. Für die Bestimmung des Wasserdampfs empfiehlt sich die Technik des Differentiellen Absorptions-Lidars (DIAL). Das Hohenheim-DIAL ist ein mobiles, bodengestütztes System mit beweglicher Sende- und Empfangseinheit. Das DIAL-Prinzip und die Bedingung, das Feuchtigkeitsfeld der unteren Troposphäre flächenmäßig zu detektieren, stellen hohe Anforderungen an den Lasertransmitter; insbesondere hinsichtlich der spektralen Eigenschaften (Frequenzstabilität $\delta\nu < 210\,\mathrm{MHz}$, Spektrale Reinheit $SP > 99.5\,\%$, u.a.) und der Ausgangsleistung ($P = 10\,\mathrm{W}$). Im Rahmen dieser Arbeit wurde ein neuer Lasertransmitter realisiert und eingesetzt, der die Anforderungen erfüllt und sogar übertrifft. Hierbei handelt es sich um ein gepulstes, aktiv frequenzstabilisiertes Titan-Saphir-Lasersystem, welches mittels eines Nd:YAG Master-Oscillator-Power-Amplifiers (MOPA) gepumpt und durch zwei Diodenlaser abwechselnd geseedet wird.

Als Pumpquelle kamen nacheinander zwei kommerzielle Spezialanfertigungen von diodengepumpten, gütegeschalteten und frequenzverdoppelten Nd:YAG-Lasern in MOPA-Architektur zum Einsatz. Die zum Pumpen des Ti:Saphir-Lasers relevanten Eigenschaften wurden untersucht; darüber hinaus auch das Frequenzverhalten für andere potentielle Anwendungen. Der zweite Nd:YAG-MOPA ist durch seine hohe mittlere Ausgangsleistung (von bis zu $P_{532} = 63\,\mathrm{W}$ bei $\lambda = 532\,\mathrm{nm}$ bzw. eine Pulsenergie von bis zu $E_{532} = 210\,\mathrm{mJ}$ bei einer Repetitionsrate von $f_{rep} = 300\,\mathrm{Hz}$) und seinem äußerst homogenen Top-Hat-Strahlprofil ideal dafür geeignet, den Ti:Saphir-Kristall effizient und beschädigungsfrei durch seine beiden Endflächen zu pumpen.

Die Komponenten zum Injection-Seeding des Titan-Saphir-Lasers, um einen schmalbandigen Betrieb abwechselnd zwischen zwei Frequenzen (Online und Offline) zu erreichen, wurden umfassend überarbeitet. Es werden nun moderne, kommerzielle External-Cavity-Diode-Laser (ECDL) verwendet. Ein analoges Regelsignal eines Wellenlängen-Messgeräts kann die Frequenz eines ECDLs präzise auf einen definierten Wert stabilisieren (Standardabweichung $\delta\nu < 1\,\mathrm{MHz}$). Die Frequenz lässt sich aber auch gemäß diverser Funktionen durchstimmen. Die Online-Offline-Schaltung erfolgt mit einem Faser-Schalter. Das Übersprechen (*crosstalk*) der Kanäle ist außerordentlich gering ($< -61\,\mathrm{dB}$), die Schaltzeit ausreichend kurz und die räumliche Übereinstimmung der Signale aufgrund der Wellenleitung nahezu ideal. Der Aufbau wurde hinsichtlich minimaler Leistungsverluste und Austauschbarkeit von Komponenten optimiert. Die Leistung der Seeder vor dem Laser-Resonator ist mit 17–20 mW mehr als ausreichend.

Der Titan-Saphir-Laser besteht aus einem Ring-Resonator mit vier Spiegeln in Bow-Tie-Anordnung. Mittels geeigneter Komponenten wird die Betriebswellenlänge bei $\lambda = 818\,\mathrm{nm}$ vorselektiert und unidirektionale Propagation gewährleistet. Der Laser-Kristall ist in einer eigenentwickelten Kühlerhalterung montiert, wovon zwei Design-Varianten eingesetzt und verglichen wurden. Der gewinngeschaltete Ti:Saphir-Laser ist darauf ausgelegt im dynamisch-stabilen Zustand der thermischen Linse betrieben zu werden, welche sich im Kristall bei hohen Leistungen ausbildet. Hierzu wurde der Resonator durch theoretische Analyse vorab und dem Vermessen der thermischen Linsen-Brennweite entsprechend konzipiert. Die Implementierung einer Zylinderlinse kompensiert die stärkere Modenkontraktion in der tangentialen Ebene. Dies ermöglicht den stabilen Betrieb mit einer mittleren Ausgangsleistung von $P = 10\,\mathrm{W}$ (entsprechend $E = 33{,}\overline{3}$ mJ bei $f_{rep} = 300\,\mathrm{Hz}$; Pulsdauer $\Delta t \approx 30\,\mathrm{ns}$). Mit einer modifizierten Zylinderlinsen-Konfiguration wurde eine maximale Leistung von $P_{max} = 11{,}8\,\mathrm{W}$ ($E_{max} = 39{,}\overline{3}$ mJ) erreicht. Dies sind die höchsten Werte, die für einen derartigen Laser bzw. einen Transmitter, dessen Leistung aus einer einzigen Strahlungsquelle entspringt (keine weitere Verstärkung oder Konversion), bisher erzielt wurden. Der Laser-Resonator wird aktiv auf die Frequenz des Seeders stabilisiert, gemäß einer Pound-Drever-Hall-Technik. Hierdurch wird ein permanenter Single-Frequency-Betrieb bei sehr hoher Frequenzstabilität (Standardabweichung $\delta\nu < 2\,\mathrm{MHz}$) und schmaler Linienbreite ($\Delta\nu < 63\,\mathrm{MHz}$) umgesetzt. Die ermittelten Werte entsprechen der Auflösungsgrenze des charakterisierenden Wellenlängen-Messgeräts. Die Laseremission erfolgt in der transversalen Gauß-Mode TEM_{00}. Die Strahlqualität beträgt $M^2 \leq 1{,}06$.

Das Lasersystem bewährte sich im Hohenheim-DIAL während mehrerer Messkampagnen. Die Robustheit zeigte sich bspw. bei einem ununterbrochenen Betrieb von über 30 Std., sowie einem Überseetransport in die USA, die das System unversehrt meisterte. Es werden exemplarisch eine in Vertikalposition durchgeführte und zwei scannende Wasserdampf-DIAL-Messungen gezeigt, welche eine hohe Auflösung und Genauigkeit demonstrieren. Die Vertikalmessung wurde erstmals bei einer Laser-Betriebsleistung von 10 W durchgeführt. Ferner werden zwei spezielle DIAL-Messungen behandelt: Mit Messungen auf ein stark zurückreflektierendes Objekt konnte für den Lasertransmitter eine hohe spektrale Reinheit von $\geq 99{,}97\,\%$ nachgewiesen werden, wodurch sich dieser sogar für den Weltraumeinsatz qualifiziert. Schließlich wird durch eine Atmosphärenmessung bei kontinuierlich durchgestimmter Online-Wellenlänge die Frequenz-Agilität des Lasers veranschaulicht und die Wasserdampf-Absorptionslinie experimentell bestimmt. Der Vergleich mit dem Spektrum aus einer Datenbank zeigt eine sehr gute Übereinstimmung ($\approx$ 5–10 % Abweichung im Absolutwert des Absorptionslinien-Wirkungsquerschnitts).

Abstract

The knowledge concerning the water-vapor distribution in the atmosphere is of great importance for humans and their environment. As a meteorological variable, water vapor has a substantial influence on the development of weather and climate. Accordingly, it is a key indicator for weather and climate change. Corresponding simulations and forecasts depend on the availability and quality of observational data for initializing and validating numerical models. For a correct approach, it is crucial to capture the transport and exchange processes of the land–atmosphere system comprehensively. Furthermore, the water-vapor distribution exhibits a high variability in the atmospheric boundary layer. Therefore, measurements of the humidity field with high spatial and temporal resolution as well as accuracy are essential.

Lidar instruments, as developed and operated at the *Institute of Physics and Meteorology* of the *University of Hohenheim*, are very well suited to carry out such measurements. Most appropriate for the determination of water vapor is the differential absorption lidar (DIAL) technique. The Hohenheim-DIAL is a mobile, ground-based, scanning system. The DIAL methodology and the ability for spatial scans of the lower troposphere impose stringent requirements on the laser transmitter, in particular on its spectral (e.g., frequency stability $\delta\nu < 210\,\mathrm{MHz}$, spectral purity $SP > 99.5\,\%$) and power performance ($P = 10\,\mathrm{W}$). In this thesis, a new laser transmitter was realized and applied in the Hohenheim-DIAL, fulfilling and even exceeding the requirements. It is a pulsed, actively frequency-stabilized titanium–sapphire laser system, pumped with a Nd:YAG master-oscillator power-amplifier (MOPA) and alternately seeded by two diode lasers.

As pump source, two commercially custom-made, diode-pumped, Q-switched, and frequency-doubled Nd:YAG lasers in MOPA architecture were employed. The relevant properties for pumping the Ti:sapphire laser were studied, as well as the frequency behavior for other potential applications of the Nd:YAG laser. The second Nd:YAG MOPA provides a considerably higher average output power (up to $P_{532} = 63\,\mathrm{W}$ at $\lambda = 532\,\mathrm{nm}$, or a pulse energy of up to $E_{532} = 210\,\mathrm{mJ}$ at a repetition rate of $f_{rep} = 300\,\mathrm{Hz}$) and an almost ideal top-hat beam profile. Thus, efficient end-pumping of the Ti:sapphire crystal was enabled without any optical damage.

The components for injection seeding of the titanium–sapphire laser, making narrowband operation at two alternating frequencies (online and offline) possible, were substantially improved. Now, advanced commercial external-cavity diode lasers (ECDL) are applied. With an

analog regulation signal of a wavelength meter, the frequency of an ECDL can be stabilized precisely to a defined value (standard deviation $\delta\nu < 1\,\mathrm{MHz}$). Optionally, the frequency can be tuned according to various mathematical functions. The online–offline-switching is accomplished with a fiber switch. The crosstalk is extraordinarily low ($< -61\,\mathrm{dB}$), the switching time sufficiently short ($\approx 1.5\,\mathrm{ms}$), and the spatial overlap of the signals, due to the waveguide, almost perfect. The setup was optimized with regard to minimal power losses, while respecting interchangeability of the components. The power of the seeders in front of the resonator is more than sufficient, 17–20 mW.

The Ti:sapphire laser consists of a ring resonator with four mirrors in a bow-tie layout. With adequate components, the operation wavelength at $\lambda = 818\,\mathrm{nm}$ is pre-selected and unidirectional propagation is ensured. The laser crystal is installed in an in-house-manufactured cooling mount, of which two designs were utilized and compared. The gain-switched Ti:sapphire laser was developed to operate in a dynamically stable state of the thermal lens, which arises in the crystal at high powers. To this end, the resonator was theoretically analyzed beforehand and the focal length of the thermal lens measured. The implementation of a cylindrical lens compensates the stronger contraction of the eigenmode in the tangential plane. By these means, a stable operation with an average output power of $P = 10\,\mathrm{W}$ (corresponding to $E = 33{,}\overline{3}\,\mathrm{mJ}$ at $f_{rep} = 300\,\mathrm{Hz}$; pulse duration $\Delta t \approx 30\,\mathrm{ns}$) was realized. With a modified configuration of the cylindrical lens a maximum output power of $P_{max} = 11.8\,\mathrm{W}$ ($E_{max} = 39{,}\overline{3}\,\mathrm{mJ}$) was achieved. These values are the highest which were obtained so far for a laser of this kind, i.e., a laser transmitter whose power originates from a single radiation source (without further amplification or conversion). The laser cavity is actively stabilized to the frequency of the seeder, following a Pound–Drever–Hall technique. This yields permanent single-frequency operation with very high frequency stability (standard deviation $\delta\nu < 2\,\mathrm{MHz}$) and a narrow linewidth ($\Delta\nu < 63\,\mathrm{MHz}$). These results correspond to the resolution limit of the characterizing wavelength meter. Laser emission occurs in the fundamental transverse mode, TEM_{00}. The beam quality is $M^2 \leq 1.06$.

The laser system of the Hohenheim-DIAL has been successfully operated on several field campaigns. Its robustness has been demonstrated, for instance, during an uninterrupted operation for over 30 hours and an overseas transport to the USA which the system endured without damage. This work presents a vertical pointing and two scanning water-vapor DIAL measurements, confirming a high resolution and accuracy. The vertical measurement was executed for the first time at $10\,\mathrm{W}$ laser operation. Furthermore, two special DIAL measurements are discussed: The measurements on a strongly backscattering target demonstrate a high spectral purity $\geq 99.97\,\%$ of the laser transmitter. Hence, it even qualifies for a space-borne platform. Finally, an atmospheric measurement with a tuning online wavelength shows the frequency-agility of the laser and allows to determine the water-vapor absorption line experimentally. The comparison with the spectrum of a database shows a very good agreement ($\approx$ 5–10 % deviation in the absorption cross section's absolute value).

Contents

CHAPTER 1

Introduction

Water is a fundamental substance for the existence of life. On Earth it appears by nature in all classic states of matter: solid, liquid, and gaseous. As gaseous substance—water vapor—it is present in the atmosphere and plays a key role for the development of weather and climate. There are several processes which are strongly influenced by water vapor, first and foremost the radiative energy budget of the Earth. For a clear sky, water vapor contributes by approximately $60\,\%$ to the global atmospheric greenhouse effect, making it the most important greenhouse gas. The effect brings about a global mean temperature of $15\,^{\circ}\mathrm{C}$ at the surface and enables life as we know it [1]. With the formation of clouds and the resulting precipitation, further impact of atmospheric water vapor is given, e.g., on the hydrological cycle. It is also of great importance in the interaction between the atmosphere and the land surface.

Due to the strong involvement in these processes, water vapor counts as an indicator for climate change. According to the fifth assessment report of the *Intergovernmental Panel on Climate Change (IPCC)*, the observed increase of water vapor in the troposphere at near-global spatial scales is consistent with its increase of temperature [2, 3]. What is more, the feedback of water vapor to the climate change is such that it even amplifies global warming. At the latest, the consequences of heat waves and extreme precipitation events urge for a better understanding of the triggering mechanisms. It has been stated that he occurrence of extreme events will increase, along with an intensification or prolongation hereof.

The humidity field in the atmosphere exhibits a high variability. This is particularly true for the lower part of the troposphere which is in direct contact to the Earth's surface. The denominated boundary layer is subject to meteorological phenomena with space scales $\lesssim 3\,\mathrm{km}$ and time scales $\lesssim 1\,\mathrm{h}$ [4]. Surface forcings (e.g., evaporation, transpiration/respiration, or combustion) are the source of water vapor. Consequently, the major part of atmospheric water vapor is distributed in the boundary layer, and the remaining part in the free atmosphere above has at least passed through this layer. The result is an extraordinary activity and heterogeneity that is challenging to capture by measurements, or to simulate with models. The latter require to be compared and corrected with measured variables to run a reliable forecast [5]. The accuracy of these predictions depends sensitively on the quality of the measurements. In brief, the higher the spatial and the temporal resolution, as well as the accuracy of the measurements, the better the insights into the transport processes of the atmosphere and the forecasts.

Many instruments for measuring atmospheric water vapor are available. They are based on different techniques and are operated from various platforms and locations. A review of observation systems focusing on the lower troposphere was provided by WULFMEYER *et al.* [6]. Special emphasis to airborne devices is given, e.g., in [7]. In these works, lidar (light detection and ranging) systems were assessed to have strong advantages over other techniques for the analysis of atmospheric variables, in general. A characteristic feature of lidar is the capability of a range-resolved detection, occurring virtually at the same time. Moreover, this profiling is accomplished with high resolution and accuracy. Different types of lidar come along with diverse atmospheric properties of interest (e.g., temperature, wind speed, concentration of a trace gas, like water vapor). Temperature, by way of example, is best determined by rotational Raman lidar [8]. With Raman lidar it is also possible to measure water vapor. However, differential absorption lidar (DIAL) is the methodology which currently delivers the most accurate results for the measurement of humidity fields while independent of experimental calibration parameters [9–16].

The *Institute of Physics and Meteorology* of the *University of Hohenheim* specializes in investigating the processes in the atmospheric boundary layer. To meet the needs of measurements, remote sensing instruments are operated which are ground-based, mobile, and able to spatially scan the lower troposphere. Among these are a Raman lidar and a DIAL system, being developed to render and advance the highest performance level. The DIAL technique and the intended application impose stringent requirements to the laser transmitter. Reduced to the bare essentials, the demands are a powerful output and exceptional spectral properties of the laser [11, 17–21]. Particularly, the combination of these criteria is hard to find in other applications. Already the particular regime of the power category (including the parameters for the energy, repetition rate and the duration of the laser pulse) is not widespread. The selection of the wavelength as well as the imperative narrowband and spectrally pure operation are further complicating factors. Hence, laser complying with the requirements for a water-vapor DIAL are not commercially available. The development in this domain is conducted only by research institutes involved in remote sensing [17, 22–29]. Over the past years, considerable progress has been made. A laser transmitter that generates an average output power of 10 W from a single radiation source, though, was not yet realized. This power category meets the demands of a reference system for scanning water-vapor DIAL measurements from the ground level up to the lower troposphere [18, 19]. An improved performance, also regarding the spectral characteristics, yet enhances the resolution and accuracy of the humidity measurement.

The goal of this work was to develop a laser transmitter which achieves a new performance class and comes closest to the mentioned reference system. For this purpose, the power level was to be increased, whilst keeping the mandatory spectral properties. Further improvements of the specifications were desirable as well. It was possible to resort to the previous works by SCHILLER and WAGNER [25, 26, 30, 31]. Although the original concept of an injection-seeded Ti:sapphire laser system was maintained, the system was rebuilt from the ground up. Almost all components were replaced, a changed resonator design and laser crystal cooling mount applied, as well as advanced stabilization controls implemented. As transmitter of the Hohenheim-DIAL, this laser system enabled three-dimensional measurements of the water-vapor field in the atmospheric boundary layer with high resolution and accuracy. The system participated in several field campaigns, proving its robustness and endurance. Owing to the laser operation and the resulting humidity observations, important contributions to many atmospheric analyses were made.

There has always been a close connection of laser and lidar development. The situation of the laser transmitter for water-vapor DIAL illustrates that lasers are especially developed for one application. Conversely, this work also aims to contribute to the general development of lasers, thereby offering a tool for other applications. Notably, the field of spectroscopy is in search of a powerful, universal laser source. Nobel laureate Theodor W. HÄNSCH expressed it the following way, when once asked in an interview [32] which invention he was still missing:

> *„Ich würde sofort einen Laser kaufen, der in eine Schuhschachtel passt und sich vom UV bei 200 nm bis zu 10 µm im Infrarot abstimmen lässt, das wäre gut. Am besten kontinuierlich und als Femtosekunden-Laser, ich würde beides kaufen.“*
>
> “I would immediately buy a laser, which fits into a shoebox and is tunable from the UV at 200 nm up to 10 µm in the infrared, that would be great. A continuous-wave or a femtosecond laser would be best, I would buy both.”

Even if some effort may still be necessary to produce such a device, a pulsed Ti:sapphire laser system as presented in this thesis provides excellent characteristics. The injection-seeding technique allows for versatile frequency switching and tuning capabilities. As a demonstration, tuning frequency measurements of the atmosphere were carried out in the scope of this work. The principle for an extension of the spectral coverage of a Ti:sapphire laser to the range from 190 nm to 6000 nm with the help of non-linear conversion and widely tunable seed-sources had already been reported [33, 34].

The thesis is structured as follows. Chapter 2 explains the fundamentals of lidar and DIAL. Then, the requirements of a laser transmitter for ground-based, scanning water-vapor DIAL measurements are determined and current comparable systems discussed. To complete the chapter, an overview of the *University of Hohenheim*'s DIAL system is given.

In the next three chapters, each of the major components of the new laser transmitter are extensively presented and characterized. Chapter 3 deals with the pump source. Two custom-built pump lasers based on Nd:YAG master-oscillator power-amplifier came into operation. Both of them are described, their performance analyzed, and the adaption of the laser beam addressed.

The injection seeding devices are the topic of Chapter 4. All essential parts such as the diode lasers, the frequency control concept, and the frequency switch, are discussed. The whole injection seeding path is evaluated with respect to the power decay. The mode matching of the seed laser beam is also dealt with.

The main component of the system, the Ti:sapphire laser, is explored in detail in Chapter 5. With a theoretical formulation of the laser eigenmode, taking particular account of the thermal lens variation, it is aimed for dynamically stable operation. The resonator design is complemented by consideration of further aspects, e.g., the geometrical layout of the cavity. Then, the experimental setup of the Ti:sapphire laser which was realized is discussed. The investigation and implementation of different crystal cooling mount concepts, the accomplishment of unidirectional laser propagation in the resonator, as well as the wavelength selection, its precise control, and the active stabilization to achieve single-frequency emission are treated in individual subsections. The performance of the laser is demonstrated with several measurements.

Chapter 6 features atmospheric measurements carried out with the Hohenheim-DIAL, employing the Ti:sapphire laser system as transmitter. First, the completed field campaigns and other activities are reviewed. Subsequently, examples of water-vapor DIAL illustrate the aptitude of the system for the high-resolution-and-accuracy measurements of atmospheric humidity. In addition, special atmospheric measurements are presented. A characterization with a hard target specifies the spectral purity of the transmitter. The measurement with a tuning online frequency also shows the frequency-agility of the laser system and its potential for spectroscopic investigations of the atmosphere.

Finally, Chapter 7 summarizes this work and gives an outlook on the future development of the system. Supplementary measurement results and photos of the Hohenheim-DIAL and its transmitter, as well as basic equations for reference are provided in the appendices.

CHAPTER **2**

Theoretical Foundations and System Overview

Nowadays, there are lidar systems for profiling the atmosphere that greatly vary in size and elaborateness. The dimensions of the whole device range from compact boxes with less than $1\,\mathrm{m}^3$ up to intermodal transport containers with $6\,\mathrm{m}$ or even $12\,\mathrm{m}$ length. Likewise, the degree of complexity covers simple, but easily maintained setups with the possibility of being remotely controlled, as well as highly developed arrangements operated by a team of scientists [35].

The specific type of the lidar system depends of course on its final application, i.e., which atmospheric property will be investigated. Atmospheric properties are thermodynamic quantities, such as temperature, pressure, and the number density of elementary entities (particles, molecules), as well as their size and shape, or their speed and direction of propagation. Furthermore there are many different lidar techniques at disposal: elastic-backscatter lidar, Raman lidar, differential absorption lidar, resonance fluorescence lidar, Doppler lidar, and others [36]. More than one technique might be suitable for the determination of some meteorological variables; other variables will favor one certain technique only. The height at which the atmosphere is examined and the platform from which the observation takes place, also plays a considerable role. Beyond the majority of the systems that are ground-based, lidars can be operated on ships, airborne, and from space [7, 35, 37–41]. Finally, the performance required from the lidar system (e.g., range, resolution, and sensitivity), has an influence on its categorization.

In the large spectrum of lidar instruments, the water-vapor DIAL of the *University of Hohenheim* ranks in the category of systems providing leading-edge performance. It is conceived as the reference system for measuring three-dimensional distributions of water vapor from ground level up to the (lower) troposphere with high resolution and accuracy [19]. This poses great demands on both the transmitter and the receiver of the system. Especially the transmitter has to vanquish stringent requirements. On the one hand, this is due to the DIAL technique which claims an outstanding frequency-stable and narrowband operation of the laser. On the other hand, the comprehensive measurement conditions ask for, *inter alia*, a high laser output power. Altogether, this leads to a sophisticated transmitter consisting of multiple combined lasers. Hence, the laser transmitter constitutes a big part of the DIAL system in terms of size ratio, financial expenses, development and operating efforts.

In the following, an introduction to lidar and DIAL theory is given. Then, the particular requirements for the laser transmitter of a water-vapor DIAL are explored, and currently available transmitter assessed. Next, the Hohenheim-DIAL is described, delineating historical development of the system as well as the present setup. In further subsections, the laser transmitter is outlined, and information on the scanner, the receiver, the data acquisition, as well as the infrastructure is provided.

2.1 Fundamentals of Lidar and DIAL

2.1.1 Lidar

Lidar (light detection and ranging) belongs to the remote sensing techniques that can actively analyze properties in their surroundings. The term of remote sensing refers to a contact-free measurement at a certain distance, in contrast to sensors that are applied on site (*in situ*) and often need direct contact. There are passive and active remote sensing methods. Passive methods make use of already existent radiation in the environment and its interaction with matter, whereas active methods send a defined electromagnetic wave to the object of interest and evaluate its reaction with it. Among the numerous applications for lidar, the measurement of meteorological variables in the atmosphere represents a prime discipline.

The fundamental principle of lidar is to send out a laser pulse and detect the fraction of light that is scattered back by the object of interest as a function of time. The time t can be assigned to the distance R of the object via $2R = ct$, where c is the propagation speed of light in the corresponding medium. Hence, having multiple objects along the signal path, a range-resolved measurement is possible. The spatial resolution ΔR depends on the pulse length Δt of the laser and is determined accordingly by

$$\Delta R = c\,\Delta t/2\,. \tag{2.1}$$

This quantity can also be understood as the (effective) range cell responsible for the backscattering. The energy of the laser pulse has an influence on the maximum range of the measurement and is related to the pulse length and the peak power $\hat{P}$ of the laser by

$$E = \hat{P}\,\Delta t\,. \tag{2.2}$$

Profiling the atmosphere leads to an interaction of the laser light with molecules and particles in the air. Scattering and absorption processes occur. Both are dependent on the wavelength λ of the laser radiation and carry the information about the meteorological variables. The fraction of the initial laser power that is scattered back and detected by the system, is expressed by the basic lidar equation [6, 36],

$$\hat{P}(R,\lambda) = \underbrace{\hat{P}_0\,\eta\,\frac{c\,\Delta t}{2}\,\frac{A}{R^2}\,O(R)}_{\text{system setup}}\;\underbrace{\beta(R,\lambda)\;T^2(R,\lambda)}_{\text{atmospheric information}}\;+\;\hat{P}_{bg}(\lambda)\,. \tag{2.3}$$

It consists of system factors, the backscatter coefficient $\beta(R,\lambda)$, the transmission term $T^2(R,\lambda)$ involving the absorption processes, and a background contribution $\hat{P}_{bg}(\lambda)$ arising from radiation in the environment and detector noise. The term considering the system setup includes the initial peak power $\hat{P}_0$, the overall efficiency η of the transmitter and receiver optics, the range cell, as well as the telescope area A over R^2 and an overlap function $O(R)$. The latter describe the geometric relation of transmitter beam and field-of-view of the receiver telescope, assuming an isotropic scattering with spherical surface [42].

The term that contains the atmospheric information (i.e., backscatter coefficient and transmission) is different according to the individual lidar technique. In general, it is expressed as follows. The transmission term obeys the universal Beer–Lambert–Bouguer law for the attenuation of light in matter. It accounts for the propagation of the laser pulse from the transmitter's origin to the scattering volume at range R and back,

$$T^2(R,\lambda) = \exp\left[-2\int_0^R \alpha(r,\lambda)\,\mathrm{d}r\right] . \tag{2.4}$$

The extinction[1] coefficient $\alpha(r,\lambda)$ is a degree for the "weakening" of the laser beam in the atmosphere. For the simple case of single, elastic scattering with absorption by a specific trace gas, the extinction coefficient can be represented by the sum of the corresponding extinction coefficients for the particles, the molecules and the trace gas of interest,

$$\alpha(r,\lambda) = \alpha_{par}(r,\lambda) + \alpha_{mol}(r,\lambda) + \alpha_{gas}(r,\lambda) . \tag{2.5}$$

Likewise, the backscatter coefficient can be separated in respective coefficients for particles and molecules,

$$\beta(R,\lambda) = \beta_{par}(R,\lambda) + \beta_{mol}(R,\lambda) . \tag{2.6}$$

More advanced lidar techniques require special attention to the variable that carries the physical property and an adaption of these terms. For instance, the rotational Raman lidar technique includes inelastic scattering processes of the molecules, and differential absorption lidar looks at the spectral radiative transfer with high resolution. In conclusion, by rearranging the lidar equation the relevant meteorological variable can be accessed.

2.1.2 DIAL

DIAL is the acronym for differential absorption lidar. The underlying idea [9,10] of this methodology is to put in relation (typically two) different elastic backscatter lidar signals that solely differ by their emission wavelength. In the simplest case, this leads only to a distinct absorption of the trace gas of interest, while the other parameters, in particular the system factors, remain the same for both signals. By an adept analytical combination of the signals, the dependence on identical parameters is eliminated. The relevant quantity can be calculated without having to determine these constants; an external calibration for them as for other lidar techniques is not necessary.

Setting the different emission wavelengths to strong and weak absorption of the trace gas results in a high signal-to-noise ratio, thus, in an exceptional accuracy. However, the wavelengths still have to be chosen close enough to each other, so that signal changes due to the atmosphere,

---

[1] usually also referred to as attenuation coefficient

apart from the gas under investigation, are negligible. In fact, the difference of the wavelengths is on such a small scale that in DIAL methodology the use of frequencies is more appropriate. The laser frequencies that are tuned to a line position of strong and weak absorption, are commonly denominated as online (ν_{on}) and offline (ν_{off}) frequency, respectively.

In the following, the methodology [6, 11, 43] for a DIAL, profiling water vapor with two frequencies, is elaborated. Proceeding from the basic lidar equation (2.3), the backscatter and transmission term is examined more closely. Now, the signal's spectral distribution and how it develops in the course of the backscattering and absorption processes has to be taken into consideration. This is represented by an integration over all frequencies of the spectral functions of the laser transmitter, the absorption lines, the scattering, and the receiver's interference filter,

$$\begin{aligned} \beta(R,\nu_0)\ T^2(R,\nu_0) = \\ &\beta_{par}(R,\nu_0)\, T^2_{air}(R,\nu_0) \int_{-\infty}^{\infty} S_l(\nu-\nu_0)\, T^2_{wv}(R,\nu)\, F_r(R,\nu)\,\mathrm{d}\nu \\ &+ \beta_{mol}(R,\nu_0)\, T^2_{air}(R,\nu_0) \int_{-\infty}^{\infty} \big\{ [\, S_l(\nu-\nu_0)\, T_{wv}(R,\nu)\,] \\ &\qquad \times DB(R,\nu) \big\}\ T_{wv}(R,\nu)\, F_r(\nu)\,\mathrm{d}\nu\ , \end{aligned} \tag{2.7}$$

where $S_l(\nu-\nu_0)$ is the originally emitted, normalized laser spectrum with center frequency ν_0, and $F_r(\nu)$ the receiver's spectral transmission function of the narrowband interference filter. The change of spectral distribution due to Rayleigh scattering is mainly given by Doppler broadening $DB(R,\nu)$. The latter term is detailed in, e.g., [11,44,45]. Analogous to the observations made in the previous section, the backscattering comprises coefficients from particles and molecules. The transmission of the atmosphere has a contribution due to the extinction of water vapor as well as the residual particles and molecules in the air,

$$\begin{aligned} T_{air}(R,\nu) &= \exp\left[-\int_0^R [\,\alpha_{par}(r,\nu)+\alpha_{mol}(r,\nu)\,]\,\mathrm{d}r\right], \\ T_{wv}(R,\nu) &= \exp\left[-\int_0^R \alpha_{wv}(r,\nu)\,\mathrm{d}r\right]. \end{aligned} \tag{2.8}$$

In the formulation (2.7) it is assumed that for the particles and molecules the frequency dependence of the backscatter and extinction coefficients is insignificant. Hence, these parameters can be detached from the integrals of the spectral distribution.

The extinction coefficient of water vapor (or other trace gases) $\alpha_{wv}(r,\nu)$ is defined as the product of its number density $N_{wv}(r)$ and its cross section $\sigma_{wv}(r,\nu)$, which describes the probability for the attenuation process,

$$\alpha_{wv}(r,\nu) = N_{wv}(r)\ \sigma_{wv}(r,\nu)\ . \tag{2.9}$$

The DIAL methodology aims at determining the number density. Inserting the equations (2.7), (2.8), and (2.9) into the lidar equation (2.3) results in a comprehensive equation of the atmosphere's return signal for the case of elastic single scattering with emphasis on the frequency behavior. Its composition of several integrals makes the analytical inversion difficult [11]. The direct inversion yields too large uncertainties due to critical assumptions and the strong variability of the atmosphere. However, under certain conditions the equation can be simplified, allowing a unique solution for the number density. In the approach that is called *narrowband DIAL*, the laser spectrum is represented by a Dirac delta function, the receiver filter transmission spectrum is considered as constant, and the Doppler broadening can be treated by applying a correction term in the end [6]. These conditions, in particular the use of a delta function for the spectral distribution of the laser transmitter, are the reason for very high frequency stability and bandwidth limitation requirements of the laser (these are detailed in the next section).

The procedure for solving for the number density consists, first, in taking the ratio of the return signals at the online frequency and at the offline frequency (with prior subtraction of the background signal, respectively). This way, system constants and identical parameters cancel out. Further assumptions are that the system efficiency and the overlap function are the same for the online and the offline signal, and also that the latter is constant in range. Second, the logarithm is applied to address the exponent in the transmission term. Then, differentiating with respect to the range R leads to the extinction coefficient, where range-independent parameters are eliminated. Finally, the DIAL equation reads [6, 18]

$$N_{wv}(R) = \frac{1}{2\left[\sigma_{wv}(R,\nu_{on}) - \sigma_{wv}(R,\nu_{off})\right]} \left\{ \frac{\mathrm{d}}{\mathrm{d}R} \ln \left[\frac{\hat{P}(R,\nu_{off}) - \hat{P}_{bg}(\nu_{off})}{\hat{P}(R,\nu_{on}) - \hat{P}_{bg}(\nu_{on})} \right] + K \right\}. \tag{2.10}$$

In this equation, the absorption cross sections remain, and thus have to be known for the calculation of the water-vapor number density. The cross section of water vapor can be computed with spectroscopy databases (e.g., HITRAN [46]), requiring some input parameters. For example, the water-vapor cross section depends on the air pressure and the temperature, although for a suitable choice of wavelength/absorption line, the variation due to these attributes is small in the atmosphere [11, 47]. As the cross section depends on the number density as well, an iterative calculation of the equation (2.10) might be necessary. The data processing is explained in more detail, e.g., in reference [48].

The quantity K in the DIAL equation is a correction term that accounts for the Doppler-broadened Rayleigh backscattering. The term is given by

$$K = \frac{\mathrm{d}}{\mathrm{d}R} \ln \left[\frac{\beta_{par} + \beta_{mol}\, T_{wv}^{-1}(R,\nu_{on}) \int_{-\infty}^{\infty} T_{wv}(R,\nu)\, DB(R,\nu-\nu_{on})\, \mathrm{d}\nu}{\beta_{par} + \beta_{mol}} \right] \tag{2.11}$$

and becomes relevant when steep gradients of particle backscattering exist in the atmosphere [45, 49]. This holds, provided that the online frequency of the laser is tuned to the maximum of the water-vapor absorption line. If the online frequency is not at the peak, but located on the slope of the absorption line, according to a sensitivity analysis [44, 50], the correction term has a minor impact. In Chapter 6.2.2, a corresponding measurement as function of the frequency is provided. This measurement was enabled by the frequency-agility of the transmitter. For cases, where no Rayleigh–Doppler correction is necessary, the Schotland approximation (Equation 2.10 with $K = 0$) is valid [9, 10].

Another advantage of the DIAL methodology (in comparison to passive remote sensing techniques) is that both, the systematic errors and the noise errors, are well understood, e.g., [11, 18, 19, 21]. An estimation for the relative systematic error of the water-vapor number density is described by the relation [6]

$$\frac{\Delta N_{wv}}{N_{wv}} \approx \frac{\Delta \sigma_{wv}}{\sigma_{wv}} , \tag{2.12}$$

which is obtained from propagation of error, demonstrating a direct proportionality to the relative error of the water-vapor absorption cross section. In this equation, σ_{wv} stands for the differential cross section of the online and offline frequency. The uncertainty in the cross section can be assigned to (insufficient) frequency performance of the laser transmitter, as well as to spectroscopic errors [11, 47]. Frequency performance comprises the stability, bandwidth and spectral purity of the laser radiation. This emphasizes again the high demands that are placed on the transmitter. Spectroscopic deviations also relate to the dependence of the cross section on pressure and temperature. Combining all these error sources may partially compensate, as shown by end-to-end performance models [6, 51, 52]. Therefore, the overall relative bias of a water-vapor DIAL measurement can even be lower than the relative error of a single error source.

2.2 Water-Vapor DIAL Systems

2.2.1 Transmitter Requirements

The realization of a DIAL system is characterized by high requirements. These apply primarily to the transmitter. Of course, there are also important conditions to be fulfilled by the other constituents. For instance, the detector of a ground-based DIAL has to handle a large dynamic range of the backscattered signal [18,19,43]. Here, only the requirements of the laser transmitter are dealt with. They refer to the system category of a water-vapor DIAL, that is ground-based, enables scanning measurements, and delivers the performance of a reference system. The requirements may also be applicable to other system classes, e.g., air- and space-borne platforms. As for every specific application, a few details might then have to be adapted. In particular, as dealing within the scope of a reference system, the mentioned values should not all be understood as absolute minimum qualification for water-vapor DIAL measurements. By way of example, it is also possible to perform such measurements with compact systems of low transmitter output power, while accepting restrictions with respect to power performance.

In the following compilation of transmitter requirements, information was retrieved from various system classes. Table 2.1 lists spectral characteristics, properties that relate to the power–energy–time domain, as well as stability and quality criteria. The order of listing and of the discussion is provided with regard to the first concern during development of a laser transmitter. It should be noted that most of the properties are interdependent.

Primary parameter is the wavelength of operation. Several factors contribute to the choice of wavelength [18, 43, 54]. In summary, there are atmospheric conditions, considerations about technical availability, and human concerns. Atmospheric conditions are the following. The wavelength has to be located at absorption lines with a strong backscattering at the online frequency and a close-by region of low absorption for the offline frequency. In this regard, the range of interest in the atmosphere (more precisely, the height above ground level) also plays a role. Additionally, the absorption lines have to show a low dependence on parameters that

Parameter	**Symbol**	**Requirement**	
Wavelength region	λ	720–$730\,\mathrm{nm}$ 815–$825\,\mathrm{nm}$ 925–$945\,\mathrm{nm}$ 1400–$1500\,\mathrm{nm}$	
Average output power	P	$10\,\mathrm{W}$	
Repetition rate	f_{rep}	100–$1000\,\mathrm{Hz}$	
Pulse energy	E	100–$10\,\mathrm{mJ}$	
Pulse duration (FWHM)	Δt	$\lesssim 200\,\mathrm{ns}$	
Bandwidth (FWHM)	$\Delta\nu$	$< 390\,\mathrm{MHz}$	$(< 160\,\mathrm{MHz})$
Frequency stability (1σ)	$\delta\nu$	$< 210\,\mathrm{MHz}$	$(< 60\,\mathrm{MHz})$
Spectral purity	SP	$> 99.5\,\%$	$(> 99.9\,\%)$
Tunability, coarse		≈ 1–$3\,\mathrm{nm}$	
Tunability, fine (mode-hop free)		$\gtrsim 20\,\mathrm{GHz}$	
Energy stability (pulse to pulse)	ΔE	$\gtrsim 96\,\%$	
Conversion efficiency (opt.–opt.)	η_{total}	$\gtrsim 20\,\%$	
Linear polarization ratio		$\gtrsim 99\,\%$	
Beam quality	M^2	$\lesssim 2$	
Beam divergence	θ	$\lesssim 1\,\mathrm{mrad}$	
Pointing stability	$\Delta\theta$	$\lesssim 10\,\mu\mathrm{rad}$	
References: [11,17–21,25,31,53,54]			

Table 2.1: Requirements for a transmitter of a water-vapor DIAL. The intended application is a high-performance system for ground-based, scanning measurements in the troposphere. The most critical parameters to be met are bandwidth, frequency stability, and spectral purity (requirements for a space-borne platform in parenthesis). The parameters of the power–energy–time domain are significant to obtain high spatial and temporal resolution, especially in scanning mode. The specifications in the lower part of the table are given for orientational purposes.

influence the absorption cross section, e.g., temperature and pressure. Moreover, at the chosen wavelength the intervention by other gases and the background radiation should be as low as possible. Technical considerations for the wavelength selection are the availability of laser materials enabling reasonable high output powers as well as of detectors with sufficient sensitivity. Human concerns are eye-safety. Unfortunately, development of laser [55] and detector techniques at eye-safe wavelength regions are not advanced enough. New materials which allow laser operation at such regions are currently being investigated [56]. The most suitable wavelengths for water-vapor DIAL are listed in Table 2.1 accordingly.

Merely a small fraction of the original sent out intensity is returned from the atmosphere (due to scattering into all directions and attenuation). Thus, a high laser output with respect to pulse energy, but also to power on average over time, is required. Pulse energy E and average output power P are linked by the pulse repetition rate f_{rep} (i.e., the frequency of the perpetual pulse series) via

$$P = E\, f_{rep}\ . \tag{2.13}$$

In reality, not all parameters can be kept high at will or simultaneously, because damage thresholds of the involved laser optics put a limit to them. Therefore, a compromise has to be found. Pulse energy and average output power have influence on the maximum measurement range and the range resolution. As lidar signals are often averaged over a certain time, one might look first at the average output power of the transmitter. For a reference system able to carry out scanning water-vapor DIAL measurements from ground-level up to the top of the troposphere an average output power of $P = 10\,\mathrm{W}$ was established [18, 19].

Sufficient temporal resolution to perceive the evolution of the atmosphere at fixed pointing measurements, can already be obtained at rather low repetition rates of a few tens of Hz. When performing scanning measurements, the repetition rate in combination with the scanning speed basically determine the (lateral) spatial resolution. To be able to quasi-instantaneously captivate one entire plane of the atmosphere, and furthermore several of such measurements in quick succession (to obtain high temporal resolution), scanning speed and repetition rate must be maximized [19]. On the other hand, an upper limit of the repetition rate is given by the need of avoiding range ambiguity for two consecutive lidar signals. In addition, the devices of the DIAL system (e.g., the online–offline switch, the active frequency stabilization technique, monitoring instruments of the transmitter, as well as the receiver's data acquisition, naturally) must be ready to handle the high pulse repetition frequency. All in all, this leads to suitable repetition rates from $100\,\mathrm{Hz}$ to $1000\,\mathrm{Hz}$. These values refer to a system switching alternately between online and offline frequency. Hence, pulses of the same frequency appear at the half value of the repetition rate.

According to Equation (2.13) specifying P and f_{rep} automatically sets E. Obviously, a higher repetition rate requires less energy per pulse to maintain the same average output power. This yields pulse energies from $E = 100\,\mathrm{mJ}$ at $f_{rep} = 100\,\mathrm{Hz}$ to $E = 10\,\mathrm{mJ}$ at $f_{rep} = 1000\,\mathrm{Hz}$.

The duration of the laser pulse (also, pulse length or pulse width) is usually defined as the full width at half maximum (FWHM) of the power progression over time. For the lidar signal it represents the extent of the range cell and therewith the spatial resolution of the measurement along the line of sight. By averaging the lidar signals this raw resolution gets coarser. Pulses with a clean shape and duration in the order of ns are necessary to sufficiently resolve atmospheric phenomena [11, 57]. With a suggested [17, 31] pulse length $\Delta t < 200\,\mathrm{ns}$, according to Equation (2.1), the raw range resolution is $\Delta R < 30\,\mathrm{m}$. Using Equation (2.2) shows that for the given values, peak powers $\hat{P}$ in the order of MW are easily reached. In combination with small beam widths this yields very high power and energy densities, indicating the proximity to the damage threshold at which such a system operates.

The spectral properties belong to the most important parameters of a water-vapor DIAL transmitter. As explained in the previous section, this is due to the assumption of a delta function for the spectral distribution of the laser radiation that is emitted into the atmosphere, in the narrowband DIAL methodology. The term narrowband, thus, puts in relation the spectral distribution of the laser and the water-vapor absorption line in the atmosphere. By knowing the absorption cross section of water vapor, it is possible to deduce the required laser bandwidth, frequency stability, and spectral purity. The absorption cross section is composed of the strength S

and the shape function Λ of the absorption line,

$$\sigma = S\,\Lambda. \tag{2.14}$$

Both functions depend on further thermodynamic quantities and can be determined or approximated. A calculation of the required laser bandwidth and the frequency stability was performed in [11]. A derivation of the spectral purity can be found, e.g., in reference [21]. Table 2.1 lists the mandatory values for the three parameters in order to achieve a relative error $< 3\,\%$ in the water-vapor DIAL measurement within the troposphere. The values were calculated for an operation wavelength in the $720\,\mathrm{nm}$ region. However, they can also be applied to the other wavelength regions. Additionally, the stricter requirements for humidity measurements from space with DIAL are listed [20, 53].

It should be noted that the spectral bandwidth and the duration of a laser pulse are related to each other by its Fourier transform. From this follows that for a given pulse length a certain limitation for the bandwidth exists and *vice versa*. The limitation depends on the pulse shape, the definition of the widths in the temporal and the frequency domain, as well as a potential chirp. For a pulse shape of a Gaussian function and a pulse length at FWHM results the time–bandwidth product [58],

$$\Delta t \cdot \Delta\nu \geq \frac{2\ln 2}{\pi} \approx 0.441\ . \tag{2.15}$$

In the limit that equality holds, a pulse is called (Fourier) transform-limited. This relation has to be considered, because the pulse length is also associated with the (raw) range resolution of the lidar signal, as stated before (Equation 2.1). On that account, the range resolution cannot be increased indefinitely, as the shortening of the pulse length leads to a broader bandwidth. For instance, to avoid a bandwidth higher than $\Delta\nu = 160\,\mathrm{MHz}$, the pulse length must be larger than $\Delta t \approx 3\,\mathrm{ns}$, and consequently the value for the raw range resolution has to be greater than $\Delta R \approx 0.4\,\mathrm{m}$.

The tunability of the laser is useful to reach different absorption lines at the operating wavelength region. This enables reacting to variable atmospheric conditions or measurement types. Several lines with high and low absorption are to be found within a range of $1\,\mathrm{nm}$ to $3\,\mathrm{nm}$. The slope of a single absorption line extends to $\approx 20\,\mathrm{GHz}$. The laser should be continuously (i.e., without mode hops) tunable at least over this range, to be able to quickly address different absorption strengths. This also allows to take spectroscopic analyses on the atmosphere (see Chapter 6.2.2). Bigger changes of the wavelength (in the range of nm) should be possible with moderate adjustment effort.

The stability and quality criteria respective the power–energy–time domain are subordinate. Although, the lidar signals are averaged, the fluctuation of the energy from pulse to pulse ought to be low [17, 25]. Otherwise this could decrease the precision in the DIAL measurement, when the transmitter is alternating between the on- and offline frequency [18]. The efficiency of the optical conversion from the radiation of the pump source to the generated output by the transmitter, might be of interest for the electrical power budget of the DIAL system [31]. Likewise, a depolarization of the transmitter's laser radiation could impair the system efficiency [25]. As the DIAL measurement is triggered to the transmitter laser pulse (see Chapter 5.8), the stability of the repetition rate is not considered relevant.

The spatial properties of the laser beam are not of utmost concern, but nevertheless should be mentioned. Beam profile and divergence (i.e., the transverse intensity distribution and the expansion of the beam during propagation, respectively) stay the same for the online and the offline signal. Therefore, it is unlikely that they will affect the DIAL evaluation. These parameters can, though, influence the system efficiency or the overlap function between transmitter and receiver [25, 31]. Furthermore, intensity spikes in the profile might overstrain optical elements in the transmitter path. That is why, a laser beam with fairly good beam quality and low divergence is appreciated. The latter still can be and is often adjusted with a beam expander or the sending telescope, whereas the beam profile should inherently feature a uniform intensity distribution and approximate circular symmetry. Finally, the pointing stability of the laser beam could impact, again, on the system efficiency. This happens by a change of the transmitter and receiver's field of view if the laser beam is sent out directly via a bending mirror, or through coupling-losses if the laser beam is transmitted through a fiber. For a space-borne DIAL application the strictest requirement in this regard is the spatial alignment of the probed volumes, which is specified with $< \pm 10\,\mu\mathrm{rad}$ [20].

The specifications of the parameters have to be fulfilled over time periods that correspond to the durations of DIAL measurements. At field campaigns, measurements are typically made throughout the entire day, consecutively for several weeks. Interruptions and limitations of the measurements are influenced by weather conditions, but also by the human factor. Exceptionally, studies are needed that comprehend daytime measurements with a transition of night. The time period of uninterrupted operation of the laser transmitter, thus, extends approximately from $3\,\mathrm{hours}$ to $12\,\mathrm{hours}$, seldom up to $\approx 30\,\mathrm{hours}$.

The operation of a laser implies a certain infrastructure. The laser transmitter requires space, has a definite weight and an electrical power consumption. In addition, the ambient conditions ideally provide a constant room temperature, low humidity, as well as the absence of disturbances by vibrations or acoustical noise. These factors always play a considerable role in the development of a lidar system, as for some of them clear limitations hold. For example, the overall efficiency from electrical input to laser radiation output, often referred to as wall-plug efficiency, can decide whether a realization of a lidar system is possible or not. This is especially true for space-borne systems like satellites that have limited power supply. As expected, a reference system has high demands also in this point of view. The Hohenheim-DIAL tries not to put any restrictions on space, weight, or power consumption to the laser transmitter. Nevertheless, being a mobile system that is operated "in the field", the situation is different to optics laboratories. The laser mainly has to prove for robustness against vibrations, notable temperature variations and higher air humidity (see Section 2.3.5).

In conclusion, of the mentioned requirements the most important are the spectral characteristics. Concerning this matter, no compromises can be made, whereas a lower output power would restrict the range properties of the DIAL but not preclude the measurement. From the stated parameters, further requirements are derived for the sub-components of the laser transmitter. A laser system consisting of a pump laser and an injection seeder, will depend strongly on the pump laser if high output powers shall be achieved, and likewise, its frequency characteristics will be (co-)determined by the seeder. As the requirements of the pump source are imperative, they are treated in an own section in Chapter 3. Other deduced requirements are mentioned when the topic is discussed.

2.2.2 Available Transmitter

Over the course of time, DIAL systems for water-vapor profiling have been developed with continuous improvement of their performance. These systems feature more and more laser transmitter that deliver average output powers exceeding $1\,\mathrm{W}$. In Table 2.2, the principal transmitter specifications of present water-vapor DIAL systems with output powers in the Watt regime are listed. Among them is also the previous laser transmitter of the Hohenheim-DIAL. Although, some systems are close to fulfill the demands elaborated in the previous section, all of the requirements had not yet been met. Specifically, the achievement of an average output power of $P = 10\,\mathrm{W}$ with one single radiation source was an unrealized long-term goal.

The table shows that there are different approaches regarding the transmitter concept, i.e., how the necessary laser radiation for water-vapor measurements is generated. Consequently, the resulting parameters vary. As transmitter type, laser systems based on Ti:sapphire, Alexandrite, and Nd:YGG, as well as optical parametric oscillators (OPO) with and without additional amplification-stage are used. The choice of the wavelength of operation comes along with the method of radiation generation but is attributed also to the application area of the DIAL. Besides the laser transmitter of the Hohenheim-DIAL, that was designed according to the criteria mentioned before, the transmitter devices of *DLR* are most likely to be suitable for this system class. Other systems are ruled out for the purpose of scanning measurements because of their low pulse repetition rate. All transmitter types have in common that they make use of a powerful neodymium-based solid-state laser as pump or primary laser source. Many systems also apply the principle of injection seeding for spectral control of the laser radiation.

Water-vapor DIAL systems with substantial less output power (i.e., in the mW regime) were not registered in the table as these clearly fall into another category. Such systems are aimed to be compact, have a low electrical power consumption, and meant to be operated remotely as well as permanently on long-term time scales. The transmitter of these systems are based on (amplified) diode lasers [59–63] or fiber lasers [64]. In spite of their low optical power they are very interesting to establish networks with multiple, similar DIAL instruments covering a large geographical region and providing water-vapor data with more spatial density than before. This is significant in meteorology as data assimilation improves models for weather forecast [5, 6].

Institution, Location/System Name **Transmitter Type**	**Main Wavelength**	**Energetic Properties**	**Spectral Properties**	**References**
DLR, Oberpfaffenhofen Nd:YGG-MOPA (diode-pumped, injection-seeded)	$\lambda = 935\,\text{nm}$	$P = 3.05\,\text{W}$ $f_{rep} = 100\,\text{Hz}$ $E = 30.5\,\text{mJ}$	$\Delta\nu \approx 14\,\text{MHz}$ $\delta\nu = 2.9\,\text{MHz}^{r}$ $SP > 99.996\,\%$	[29,65]
DLR, WALES OPO (Nd:YAG-MOPA-pumped, injection-seeded)	$\lambda = 935\,\text{nm}$	$P = 4.5\,\text{W}$ (6 W) $f_{rep} = 100\,\text{Hz}$ $E = 45\,\text{mJ}$ (60 mJ)	$\Delta\nu = 150\,\text{MHz}^{f}$ $\delta\nu \leq 30\,\text{MHz}$ $SP \geq 99.9\,\%$ (99 %)	[28,66]
IPM, Hohenheim (until 2010) Ti:sapphire laser (Nd:YAG-MOPA-pumped, injection-seeded)	$\lambda = 820\,\text{nm}$	$P = 4$–$5\,\text{W}$ (6.75 W) $f_{rep} = 250\,\text{Hz}$ $E = 16$–$20\,\text{mJ}$ (27 mJ)	$\Delta\nu = 157\,\text{MHz}^{f}$ $\delta\nu = 10\,\text{MHz}^{s}$ $SP \geq 99.9\,\%$ (99.6 %)	[25,26,31]
KIT IMK-IFU, Zugspitze Two OPOs with Ti:sapphire amplifier (Nd:YAG-pumped, injection-seeded)	$\lambda = 817\,\text{nm}$	$P = 5\,\text{W}^{a}$ $f_{rep} = 20\,\text{Hz}$ $E = 250\,\text{mJ}^{a}$	$\Delta\nu \leq 220\,\text{MHz}^{f}$ $\delta\nu = 35\,\text{MHz}$ $SP > 99.9\,\%$	[24,67,68]
LATMOS, LEANDRE II Alexandrite laser (flashlamp-pumped, Lyot filter, two etalons)	$\lambda = 730\,\text{nm}$	$P = 1\,\text{W}$ $f_{rep} = 2 \times 10\,\text{Hz}$ $E = 50\,\text{mJ}$	$\Delta\nu = 731\,\text{MHz}$ $\delta\nu < 141\,\text{MHz}$ $SP > 99.99\,\%$	[22,69]
MPI for Meteorology, Hamburg Ti:sapphire laser (Nd:YAG-pumped, injection-seeded)	$\lambda = 820\,\text{nm}$	$P = 0.75\,\text{W}$ (0.93 W) $f_{rep} = 50\,\text{Hz}$ $E = 15\,\text{mJ}$ (18.6 mJ)	$\Delta\nu = 22.5\,\text{MHz}^{f}$ $\delta\nu < 57\,\text{MHz}^{i}$ $SP = 99.97\,\%$	[23,70]
NASA LaRC, LASE Ti:sapphire laser (Nd:YAG-pumped, injection-seeded)	$\lambda = 815\,\text{nm}$	$P = 0.9\,\text{W}$ (1.5 W) $f_{rep} = 2 \times 5\,\text{Hz}$ $E = 90\,\text{mJ}$ (150 mJ)	$\Delta\nu < 158\,\text{MHz}$ $\delta\nu < 113\,\text{MHz}$ $SP > 99\,\%$	[27,40]
Annotations: a: around 800 nm, f: FWHM, i: value of injection seeder only, r: RMS, s : 1σ				

Table 2.2: Water-vapor DIAL transmitter with an average output power in the Watt regime, listed in alphabetical order. The most essential performance parameters of one single radiation source are specified; symbols as in Table 2.1. The values in parenthesis were achieved temporarily or with restrictions to the other parameters. See the references and Section 2.3.1 for the full name of the institutions.

2.3 The Water-Vapor DIAL of the *University of Hohenheim*

2.3.1 History

The water-vapor DIAL of the *University of Hohenheim* was realized within the cadre of the package project “Lidar Reference System Based on a High-Power Laser” funded by the German Research Foundation (*DFG*[2]). The planning and development started in 2004 and consisted of three projects with the participation of several research groups. The first project pursued the creation of a pulsed high-power laser, based on a rod geometry with diodes, intended as pump source of the lidar transmitter. It was carried out by the *University of Potsdam* and the company *IBL*[3] [71]. The second project was a joint effort of the *Institute of Physics and Meteorology (IPM)* at the *University of Hohenheim* and the *Institute of Atmospheric Physics* of the German Aerospace Center (*DLR*[4]) in Oberpfaffenhofen. The subject was the development of the main Ti:sapphire laser system as frequency converter for the DIAL transmitter, as well as the injection-seeder module for the spectral control, respectively [72]. The third project provided the mobile, scanning platform, including the receiver, and the data acquisition of the lidar system [73]. It was conducted by the *Leibniz Institute for Tropospheric Research* in Leipzig and incorporated own and external manufacturing, where the detector was also developed by *DLR*. The complete laser transmitter, being the combination of the first two projects, was finally integrated in this platform.

The Hohenheim-DIAL premiered operation during the “Convective and Orographically-induced Precipitation Study” (COPS) in 2007 [74–76]. In this field campaign the system contributed, among numerous other instruments, to intercomparison research of water-vapor retrieval [14] and convection initiation processes in the atmosphere [77]. Scanning DIAL measurements of water vapor were demonstrated for the first time with this system at the FLUXPAT campaign 2009 [78] within the “Transregional Collaborative Research Centre 32” (TR32) [79, 80].

The development of a lidar system is a continuous procedure, especially when it pioneers at a certain domain of activity. Learning through campaigning, the Hohenheim-DIAL offered room for improvement. This work proceeds with the previous transmitter development by SCHILLER and WAGNER [25, 26, 30, 31]. It describes a transmitter based on the same idea of an injection-seeded Ti:sapphire laser system but with all-new components, advanced approaches, considering and eliminating the issues that were formerly encountered. Meanwhile, further improvement was undertaken on the infrastructure of the Hohenheim-DIAL (see Section 2.3.5).

2.3.2 Setup of the System

The setup of the Hohenheim-DIAL is depicted in Figure 2.1. Principal components are the laser transmitter, the scanner unit enabling the three-dimensional emission and collection of the lidar signal, further optical elements, and the detector with subsequent data acquisition. The whole setup is assembled in a (semi-)trailer[5] of $12.5\,\mathrm{m}$ length, $2.6\,\mathrm{m}$ width, and $4\,\mathrm{m}$ height. It is custom-built and composed of three modules. The first is decoupled from the others and

---

[2] *Deutsche Forschungsgemeinschaft*

[3] see footnote 1 on page 25

[4] *Deutsches Zentrum für Luft- und Raumfahrt*

[5] *Schmitz Cargobull*, Sattelanhänger

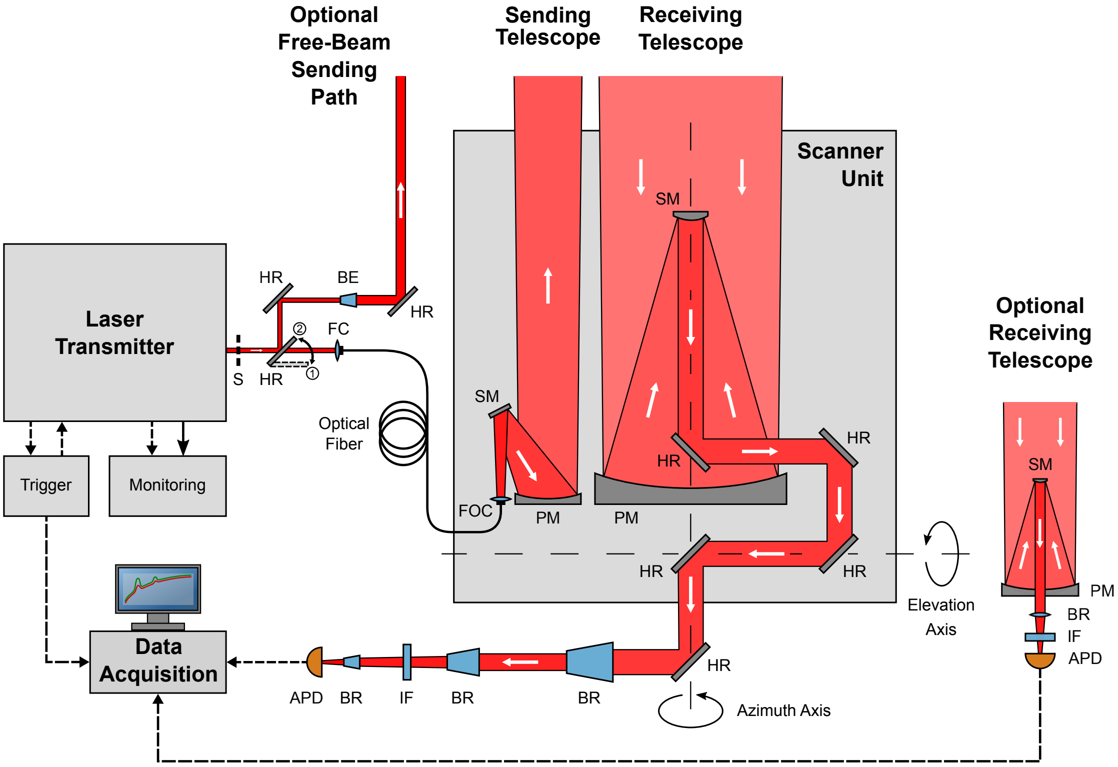

Figure 2.1: Schematic representation of the water-vapor DIAL of the *University of Hohenheim*. In essence, the setup consists of the laser transmitter, trigger devices, the scanner unit (including sending and receiving telescope), optical elements for the sending and receiving path, as well as the detector with data acquisition. In vertical pointing mode, it is possible to use a free-beam path for the emission of the laser light into the atmosphere. Optionally, a small receiving telescope with a second detector can be used in addition. Several monitoring instruments for the transmitter ensure proper laser operation. APD – avalanche photodiode (detector), BE / BR – beam expander/reducer, FC / FOC – fiber (output) coupler, HR – highly reflective mirror, IF – interference filter, PM / SM – primary/secondary mirror of the telescope, S – shutter.

incorporates machines causing strong vibrations (chillers, compressors, etc). The laboratory module, the main part, is air-conditioned and provides optical tables and racks for the lidar system arrangement. In the third module the scanner unit is housed, which moves out through a sliding roof. Photos with an exterior and interior view of the system can be found in Appendix D. The following sections provide more details about the components.

2.3.3 Laser Transmitter

The transmitter of the Hohenheim-DIAL is a Ti:sapphire laser system. Thus, it is a system of various lasers functioning together, the central component being the titanium–sapphire laser (see Figure 2.2) operating at wavelengths near 818 nm. As pump source a pulsed Nd:YAG

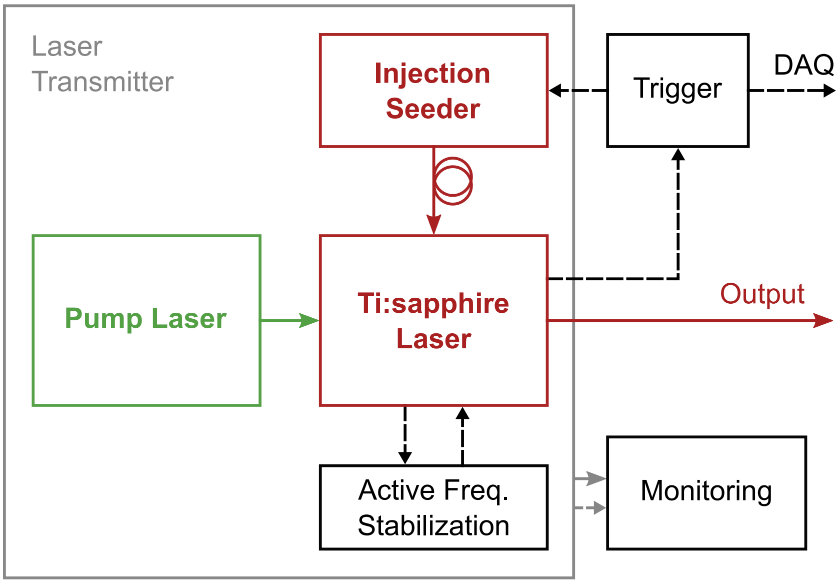

Figure 2.2: Block diagram of the laser transmitter with involved trigger and monitoring devices. The lasers include their power supply and control drivers as well as their water cooling and/or temperature control. Solid arrow lines symbolize laser beams (in free space or fibers). Dashed lines are electrical connections.

laser is applied. It is configured in a master-oscillator power-amplifier (MOPA) architecture, providing high pulse energies. For pumping the Ti:sapphire crystal, the fundamental radiation at $1064\,\mathrm{nm}$ of the Nd:YAG MOPA is eventually frequency-doubled to $532\,\mathrm{nm}$. The control and enhancement of the Ti:sapphire laser's spectral properties is achieved with the injection seeding technique. The seeder unit implements two diode lasers operating at the online and offline frequency, and a switch to alternately select between both of them. The diode lasers in turn are frequency stabilized with a wavelength meter and a helium–neon laser as reference. Then, single-frequency operation of the Ti:sapphire laser is attained by additional components that actively stabilize the resonator cavity to the seed laser. Furthermore, there are devices that generate or delay the trigger signals to initiate the data acquisition at the right time, as well as the switching of online–offline operation. Finally, several monitoring instruments exist to survey and characterize the performance of the laser system.

The choice of a Ti:sapphire laser system as transmitter for the water-vapor DIAL results from a comprehensive consideration of the stated requirements and the properties offered by the transmitter type. The arguments put forward relate mainly to the crystal material and to the resonator concept. The laser active medium titanium–sapphire (see Chapter 5.1) has a broad spectral emission band allowing tunable laser operation in the wavelength range of approximately $670\,\mathrm{nm}$ to $1070\,\mathrm{nm}$. Hence, it covers three of the suitable wavelength regions for measuring water vapor with DIAL (see Table 2.1). This enables the flexibility to (re)construct the laser system in a straightforward manner for each wavelength region. The availability of crystals with a high figure of merit enables a laser operation with high efficiency. Best efficiency is obtained for the wavelength region of $815–825\,\mathrm{nm}$, as it is closest to the maximum of the emission spectrum. Moreover, with sapphire being the host material of the laser crystal, a high hardness and thermal conductivity is given. To pump the absorption band of Ti:sapphire, powerful neodymium-based solid-state lasers exist.

The approach of using a laser resonator to produce the coherent radiation needed for the DIAL measurement, has the advantage of being able to predetermine some of the attributes inherent to the radiation. In particular, the spatial characteristics (e.g., the transverse mode) are defined by the resonator design. In contrast to the laser resonator, other transmitter concepts that rely on frequency-conversion with an OPO, or a successive amplification of the radiation, lack the possibility of controlling these parameters independently from the incident radiation. At least one of the parameters is usually deteriorated by the conversion or the amplification process, respectively. The Ti:sapphire laser resonator has in common with the other concepts, that it can be readily injection seeded. This is essential to obtain narrowband and spectrally pure laser operation. The complexity of the different transmitter types is also comparable. In summary, the Ti:sapphire laser system represents a well-suited water-vapor DIAL transmitter with high technical maturity.

2.3.4 Scanner, Receiver and Data Acquisition

The scanner unit of the Hohenheim-DIAL resides in an own compartment of the trailer, which is accessed through the laboratory module and is exposed to ambient conditions during measurements. On the scanner unit a small and a large telescope are mounted, assuming the task of sending the laser pulses into the atmosphere and collecting the backscattered light, respectively. During the scanning process, sending and receiving telescope are moved together, pointing in the same direction all the time. Different scan patterns are possible with the control software: varying elevation angle (range–height indicator, RHI), varying azimuth angle (conical scans as the plan position indicator, PPI), and manifold of these covering a defined volume of the hemisphere above the DIAL system. The scanner unit is actuated with speeds of $0.1\,^\circ/\mathrm{s}$ to $6\,^\circ/\mathrm{s}$, resulting, by way of example, in a full PPI (360°) per minute at fastest.

The laser radiation is guided from the transmitter to the sending telescope with an optical multimode fiber[6]. The amount of laser power that can be transmitted through the fiber depends on a few factors. On the one hand, there are the fiber coupling efficiency and the losses by the fiber length. For the multimode fiber, coupling efficiencies of $\approx 80\,\%$ or more are reached and an attenuation of $\approx 2\,\mathrm{dB/km}$ is specified. The fiber coupler consists of a suitable focusing lens[7] in an in-house constructed adjustable mount. On the other hand, the fiber has a maximum power limit which is given by damage thresholds (fiber connectors, fiber core), as well as the effect of stimulated Brillouin scattering (SBS) [81]. The sending telescope has an off-axis design with a primary mirror diameter of $210\,\mathrm{mm}$. The reflectivity of its installed mirrors is $R \approx 87.5\,\%$ at $820\,\mathrm{nm}$ [82]. Alternatively, the laser radiation can be directed into the atmosphere on a free-beam path including a beam expander[8] and a highly reflective bending mirror[9] (see Figure 2.1).

---

[6] *LEONI*, FiberTech AS1000/1100IRST-20m

[7] *CVI / Melles Griot*, PLCX-25.4-128.8-UV-700-900 ($f_{nom} = +250\,\mathrm{mm}$)

[8] optionally *CVI*, HEBX-10-5X-820 (5x expander), or *Thorlabs*, BE10M-B (10x expander)

[9] *Laser Components*, HR820/45 PW2025UV 206088-1

In this arrangement, only vertical pointing DIAL measurements are possible, but the full output power of the laser can be used.

The larger receiving telescope is built in a Nasmyth–Cassegrain reflector design with a primary mirror diameter of $800\,\mathrm{mm}$. It is an afocal system that yields a collimated beam. This is necessary as the beam of the collected light has to cover a certain distance back to the laboratory module, before it is scaled down through three beam reducing stages and finally focused onto the detector. The bending mirrors that form the path which directs the beam to the detector are arranged in *coudé* configuration. This concept considers the two rotational axes of the scanner unit and leads to an almost perfectly fixed focus point on the detector surface. The mirrors of the receiving telescope and the *coudé* path have at $820\,\mathrm{nm}$ a total reflectivity of $R \approx 77.2\,\%$ [82].

Before the signal light from the atmosphere is focused onto the detector it passes an interference filter[10]. This filter blocks the background radiation around a $1.5\,\mathrm{nm}$-wide band of the emitted wavelength with $\approx 92\,\%$ peak transmission [78]. In the case of changing the emission wavelength beyond the transmission region of the bandpass filter, models with different center wavelength are at disposal ($817.8\,\mathrm{nm}$, $818.8\,\mathrm{nm}$, and $820.3\,\mathrm{nm}$). As detectors, modules based on an avalanche photodiode[11] (APD) are used. The APD material for the multiplication process is silicon and has an active area diameter of $3\,\mathrm{mm}$ (effectively usable $2\,\mathrm{mm}$). Further specifications are $30\,\mathrm{A/W}$ for the responsivity, $0.5\,\mathrm{pA}/\sqrt{\mathrm{Hz}}$ for the noise current, and $100\,\mathrm{nA}$ for the dark current (at $T = 22\,°\mathrm{C}$). According to the data sheet, the APD model has an implemented thermoelectric cooler. The custom-made module also includes in its mount a preamplifier with low noise and is subsequently driven by another external amplifier.

The data acquisition system (DAQ) consists of a high-performance computer with a transient recorder card. The board[12] features a 14-bit analog-to-digital converter with simultaneous sampling (up to $50\,\mathrm{MS/s}$) on four channels. The DAQ records the amplified lidar signal of the APD, obtaining two triggers which are related to the laser pulse emission (initiation of the time-of-flight measurement), and to the frequency switch (definition of the online or offline frequency state). The temporal organization of the trigger signals and the instrumentation was revised within this work and is described in Chapter 5.8. Generally, the sampling rate of the DAQ is set to $10\,\mathrm{MHz}$, which results in raw data with a range resolution of $\Delta R = 15\,\mathrm{m}$. From hardware side, the DAQ is capable to handle the backscattered signal of every laser pulse up to a repetition rate of $1000\,\mathrm{Hz}$. Yet the software of the DAQ must also be able to process the data quick enough and store it to the disk drive. The software which was originally developed was written in *C++* and allowed to record the measurement on a single-shot basis. Recently a new DAQ software has been programmed in *LabVIEW*. This enables an easier adaption of the software to specific demands. The collected data is also directly (pre-)averaged on a small time scale (usually $\Delta t = 0.1\,\mathrm{s}$), facilitating the handling due to the reduced data amount. The resolution is still high enough for the atmospheric studies. Later in the data processing, the signals are averaged typically over $\Delta t = 1\,\mathrm{s}$ to $1\,\mathrm{min}$ in time. A single-shot analysis becomes relevant only for very fast scans, or for laser characterization purposes. Within the DIAL processing, averaging over the range bins is carried out as well, resulting in a water-vapor field with typical

---

[10] *Barr Associates*, 2006-10852

[11] *PerkinElmer*, C30956E-TC

[12] *Spectrum Systementwicklung Microelectronic*, MI.4032

range resolutions of $\Delta R = 37.5\,\mathrm{m}$ to $300\,\mathrm{m}$.

There are some additional components. A safety radar[13] that is mounted on the scanner unit alongside the telescopes, keeps the volume around the pointing direction under surveillance of incoming objects. If necessary, a shutter[14] is activated, so that no laser light is sent out of the laboratory module. Ground-based DIAL measurements give rise to lidar signals with a huge dynamical range. Thus, the distribution of the signal on two detector modules, each dedicated to a different range section, might be helpful. For vertical measurements, moreover, a supplementary receiving telescope[15] with particular adjustment of the field-of-view for low heights can be applied. In this case, the second detector is mounted, together with focusing and filtering optics, directly on the Schmidt–Cassegrain telescope. Further information about the scanner, receiver and the data processing can be found in [47, 48, 82].

2.3.5 Infrastructure

As an extraordinary performance is expected from the devices of the *University of Hohenheim*-DIAL, the housing platform of the system seeks to provide laboratory conditions as best as possible. Here, the challenge lies in that the platform is mobile and exposed at all time to the elements, where the interior directly adjoins the outside area. For the climatization of the laboratory compartment, the trailer is equipped with an air conditioner, based on typical carrier transport refrigeration and heating units, but modified for room-temperature operation. On the one hand, these are strong machines, capable of running all year round at any European weather. On the other hand, the trailer air-conditioning cannot regulate the temperature to a constant value as precise as known from usual optics laboratories, i.e., at sub-Kelvin precision. Furthermore, the motors of the fans responsible for the air circulation inside, cause a high noise level and exhibit minor residual vibrations.

Temperature and relative humidity are continuously logged and monitored with several instruments[16,17,18] at different places inside of the laboratory and scanner module, as well as outside of the trailer. The temperature inside in the front and in the rear area of the trailer is depicted in Figure 2.3 for ten consecutive days during the month May 2016. The graph shows typically occurring temperature variations. In the first four and last five days no major devices were running. Thus, the trailer was in state of rest and the air-conditioning was reacting only to the diurnal temperature cycle outside. Inside, a temperature deviation of up to $\Delta T \approx \pm 1.5\,\mathrm{K}$ close to the set point ($T = 21\,^{\circ}\mathrm{C}$) remained. The temperature in the front area is generally higher than in the rear area of the trailer. This is presumably due to the exhaust heat of the uninterruptible power supply (see below) which is located in the front. One day before the laser system was turned on (grayed background in the figure), the air-conditioning reached a state of equilibrium with a constant temperature. The temperature variation of the non-operative system depends on the external weather conditions and human interference (opening/closing of the laboratory com-

---

[13] *Furuno*, NAVnet 1732 C-Map NT, modified marine model

[14] *U.S. Laser Corp.*, water-cooled beam deflection shutter assembly N1031-1-B with controller N8022

[15] *Meade Instruments*, 8 inch LX200R

[16] *Voltcraft*, DL-121TH

[17] *TFA Dostmann*, KlimaLogg Pro

[18] *Better networks*, MessPC Ethernetbox 2

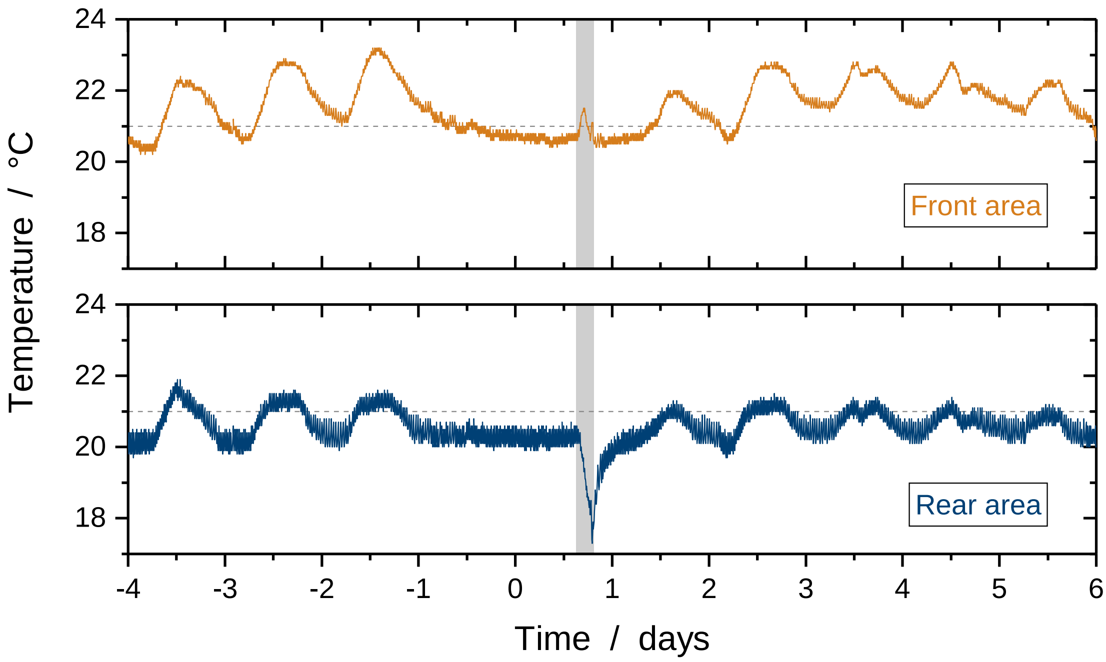

Figure 2.3: Typical temperature behavior in the front (**top**) and rear area (**bottom**) of the Hohenheim-DIAL. The case depicts the days before and after the operation of the complete laser system (grayed background). During operation, the temperature deviates more from the set point (dashed lined) in the rear area. The temperature variation without operation is attributed here to the diurnal cycle of the external temperature.

partment door). With the complete laser system running, the presence of several heat sources clearly impacted on the temperature behavior. The air-conditioning kept the cooling phases for longer time periods, whereby the temperature is thrown stronger off balance, especially in the rear part of the trailer. There, the deviation from the temperature set point was $\Delta T \approx 3\,\mathrm{K}$. The pump laser was identified as primary heat source responsible for the temperature build up.

In some cases, at power outages or during transportation of the trailer, when the air-conditioning is not given, the temperature can rise (or rarely fall) by $\Delta T \approx 10\,\mathrm{K}$ from room-temperature. To be advised in time, a GSM module[19] was installed in the trailer which is programmed to warn via short message when the temperature is outside of a certain range. The side panels of the trailer possess a good insulation, revealing a low heat exchange of interior and exterior section. The relative humidity in the trailer is generally kept at a low level of $(35 \pm 10)\,\%$. Meanwhile, the fan motors of the air-conditioner were replaced by new ones, so that the loudness could be reduced from previously $\approx 89\,\mathrm{dB}$ to now $\approx 71\,\mathrm{dB}$.

A power disruption or outage that happens while devices are running or even during full operation of the DIAL system, can have catastrophic consequences. Such a situation is seldom but unfortunately inevitable, especially during field campaigns, where power supply is not always

---

[19] *Conrad Electronic*, GX106

as stable as expected. The lasers that depend on an active (after-)cooling are the most critical components. For this reason, the trailer was upgraded with an uninterruptible power supply[20] (UPS). The UPS is determined to bridge the electrical load of all devices short-term with exception of the air-conditioning. With a specified electrical power of $40\,\mathrm{kVA}$ it has a runtime of approximately $6\,\mathrm{min}$ at peak load, or approximately $15\,\mathrm{min}$ to $30\,\mathrm{min}$ if the main devices of the DIAL (laser transmitter, scanner, computers) are running. Within this time the laser and scanner can be shut down quickly but still properly. Additionally, the UPS corrects the power source from issues such as voltage spikes and noise.

Three identical breadboards[21] serve as table for all optical components. They are mounted lengthwise together and reside on a common steel girder base plate, on which the scanner unit is also built. The base plate prevents a deformation of the floor and a dislocation of the free propagating beam from the receiving telescope to the detector. During the transport of the trailer the breadboards are lifted up with bellows cylinders to absorb vibrations. The three breadboards provide in total a space of $4.5\,\mathrm{m} \times 1.0\,\mathrm{m}$ with a height above of $0.7\,\mathrm{m}$ for the optical components. Above the middle breadboard on which the Ti:sapphire laser is situated a laminar flow module[22] is installed to clean the air.

For water cooling, the Hohenheim-DIAL has its own water circulation. This primary cooling circuit is supplied by an air–water heat exchanger[23], located in the trailer's energy compartment. The heat exchanger has a cooling capacity of $6.2\,\mathrm{kW}$ with a pump performance of $17\,\mathrm{l}/\,\mathrm{min}$ at $3.5\,\mathrm{bar}$. The temperature of the primary water is set to $20\,^{\circ}\mathrm{C}$. In the energy module there are also nitrogen gas bottles at disposal, for flushing special optical sub-components, where necessary.

---

[20] *Newave*, DPA UPScale

[21] *Qioptiq / Linos*, G437824312 (*TMC* Series 78 CleanTopII Breadboards)

[22] *BDK Luft- und Reinraumtechnik*, FFM 06.12

[23] *Termotek*, P607

CHAPTER 3

Pump Source

In order to supply the Ti:sapphire laser with energy a pump source is required. There are several possibilities of optically pumping a solid-state laser. However, for Ti:sapphire lasers, flashlamp pumping becomes difficult due to a short fluorescence lifetime of the laser material (properties of the material are given in Chapter 5.1). Laser diodes would be a desired pump source, because of their high efficiency and longtime durability. Unfortunately, this technology is still in an early stage, being restricted basically by the lack of laser diodes with high power output in the green region of the visible spectrum. [83, 84]. This is where the absorption band of Ti:sapphire is located. Thus, the common pumping method to date is to use another solid-state laser. The latter is based on a neodymium-doped gain medium whose inherent emission radiation is frequency-doubled [85].

The specific domain of average output power, pulse energy, duration and repetition rate, which is demanded by water-vapor DIAL measurements (see Chapter 2.2.1), induces the pulses of the Ti:sapphire laser to be gain-switched by the pump pulses. This again determines the needed magnitude of these parameters for the pump laser itself and confines the countless number of available neodymium-based lasers. Yet, beam quality, stability of all parameters and further properties have to be considered. Altogether, a pump laser with the required performance is not commercially produced in series. Therefore, custom-built models have to be obtained.

For the laser system described in this work, two Nd:YAG lasers in master-oscillator power-amplifier (MOPA) architecture have been used as pump source. The first laser is a revised version of the pump laser that was applied in the transmitter developed by SCHILLER [25, 26] for the Hohenheim-DIAL. After completion of the improved Nd:YAG-MOPA in 2011 by *IBL*[1] the laser has been operated for four years. Since 2015 a second pump laser is used. It has been custom-made by *Proton Laser Applications*[2] to meet the increased demands of the *Institute of Physics and Meteorology*. The replacement of the first pump laser was necessary as the achievement of higher output powers of the Ti:sapphire laser came to a point where the limiting factor was solely the pump power. In addition, benefit was gained from further technological progress that these laser models experienced during the last years.

In the first section of this chapter, the requirements of the pump source will be quantified.

---

[1] *IBL Innovative Berlin Laser*, Germany

[2] *Proton Laser Applications*, Spain

Then, the two pump lasers are described—each in a particular section. The sections begin with the presentation of the setup of the laser. In the following subsection, the performance regarding power and energy is characterized. The properties related to the beam profile are shown in the third subsection. The description of the arrangement for the optimal adaption of the pump laser beam to the Ti:sapphire laser mode is given in another subsection. The sections for every pump laser close with the spectral characteristics of the laser, which are briefly described.

3.1 Pump Laser Requirements

The requirements of the pump source can be deduced in a straightforward manner from the requirements given to the DIAL transmitter, i.e., the Ti:sapphire laser system (Section 2.2.1). The circumstance that the pulsed operation of the Ti:sapphire laser is achieved by gain of the pump pulses, directly transfers some of the required parameters to the pump laser. In the first place, this is the pulse repetition rate. The repetition rate required for the pump laser automatically is the same as the repetition rate required for the DIAL transmitter ($f_{rep} = 100\,\mathrm{Hz}$ to $1000\,\mathrm{Hz}$).

Similarly, the pulse duration of the pump laser is closely related to the requirement of the DIAL transmitter. In gain switching, the resulting pulse length of the laser is in the same order as the pulse length of the pump source. Therefore, the need of a pulse duration $\Delta t < 200\,\mathrm{ns}$ for the Ti:sapphire laser leads back to a pulse duration of the pump laser within the nanosecond regime, too. Usually, such pulse widths are delivered by Q-switched solid-state lasers [85].

The claimed output power of the DIAL transmitter can be calculated back to the output power which is requested from the pump laser. Detailed theoretical analysis takes several laser resonator and crystal parameters into consideration. Thus, it can give precise results for different configurations [30, 31]. In the following, a simplified calculation will provide an estimation for the magnitude order of the pump power that is needed. Still, some of the results gained by the theoretical design or the precedent laser model [25] are utilized.

From the output power of the Ti:sapphire laser, the pump power which is needed in the green spectral region can be approached by $P_{pump} = 1/\eta_{total}\, P_{laser}$. The total efficiency of the laser is a product of several efficiency factors, $\eta_{total} = \eta_s\, \eta_f\, \ldots$ [30, 86]. Among these factors are the Stokes efficiency[3] η_s, and the fluorescence storage efficiency η_f,

$$\eta_s = \frac{\nu_l}{\nu_p} = \frac{\lambda_p}{\lambda_l}\,, \tag{3.1}$$

$$\eta_f = \frac{1 - \exp(-\Delta t_p/\tau_f)}{\Delta t_p/\tau_f}\,, \tag{3.2}$$

where ν_l, ν_p are the lasing and pumping frequencies, λ_l, λ_p the corresponding wavelengths, Δt_p is the pump pulse length, and τ_f the fluorescence lifetime of Ti:sapphire. The Stokes efficiency can be regarded as the theoretical upper limit for the total efficiency of the laser regarding energy conservation. In reality, the total efficiency of the Ti:sapphire laser will only be lower than this quantity. The fluorescence storage efficiency is given as example, on how other parameters of the pump source—here the pulse length Δt_p—influence the determination of the

---

[3] also referred to as quantum defect or color efficiency

required pump power (since it influences η_{total}), and why for a precise determination an iterative analysis is necessary. Other efficiency factors account for the accomplishment of the adjustment and the crystal performance, which both further reduce the total laser efficiency. In the previous works, theoretical and experimental values of $\eta_{total} \approx 29\,\%$ and $25\,\%$, respectively, have been found, for the case of operating the Ti:sapphire laser at $\lambda_l = 820\,\mathrm{nm}$ and pumping the crystal with $\lambda_p = 532\,\mathrm{nm}$.

Neodymium-based lasers usually provide this radiation by the second harmonic generation (SHG) of its fundamental emission wavelength, which is situated in the infrared spectrum. The SHG naturally is beset with losses, too. Consequently, the required fundamental power is of further interest. Again, this power can be calculated from the conversion efficiency η_{SHG} of the non-linear crystal, with $P_{infrared} = 1/\eta_{SHG}\ P_{green}$. Depending on the non-linear crystal selected and other conditions for the SHG, typically, values of $40\,\%$ to $70\,\%$ for η_{SHG} are reached [85].

Then, the numerical values for the powers read as follows. From an average output power of $P_{laser} = 10\,\mathrm{W}$ and a total efficiency of $\eta_{total} = 25\,\%$ of the Ti:sapphire laser results a needed pump power of $P_{pump} = P_{green} = 40\,\mathrm{W}$. Assuming an SHG conversion efficiency of $\eta_{SHG} = 50\,\%$, this leads to an average output power of $P_{infrared} = 80\,\mathrm{W}$ at the fundamental wavelength. As already stated, this is a rough estimate for the numerical values, rather than an accurate investigation. Moreover, in the course of time, it can be expected, that the output power of a laser decreases due to degeneration of the optics and flashlamp or pump diodes drop off. Therefore, it is suggested to allocate a certain overhead power, and to come up with, e.g., $P_{green} = 50\,\mathrm{W}$ and $P_{infrared} = 100\,\mathrm{W}$ [87].

An important property, that does not evidently follow from the DIAL transmitter requirements, is the beam quality of the pump laser. The shape of the beam profile, how it develops during propagation of the beam, and especially how it impacts on the Ti:sapphire crystal plays a crucial role when the laser crystal is end-pumped [85]. In the end-pumping geometry, the pump radiation is transferred longitudinally into to the laser crystal [88]. This provides high pumping efficiency, and laser operation in the fundamental transverse mode TEM_{00}, given that the pump beam is matched to the laser mode. When dealing with high average powers, heating effects in the laser material have to be considered (see below and Chapter 5.2). End-pumping from both sides provides a more axially uniform heat deposition in the crystal and thereby less thermal stress [89]. That is why the Ti:sapphire crystal has always been end-pumped from both sides in this work.

Regarding the pump laser's beam profile on the end-surfaces and inside the crystal along the beam propagation, the spatial overlap of pump beam and Ti:sapphire laser beam ideally has to be maximized. Assuming a Gaussian beam (TEM_{00} mode) for the Ti:sapphire laser, thus, demands a coinciding Gaussian pump beam, i.e., with identical beam waist or divergence. This simplified approach is correct with respect to optimizing the efficiency of the pump radiation transfer. Additionally, with Gaussian beams, the matching of the beam mode of the pump laser to the Ti:sapphire laser mode can readily be calculated [90]. The experimental realization then usually corresponds well with the theoretical model. However, in order to keep thermal induced processes such as thermal lensing low, a more even transverse distribution of the pump beam, as well as a slightly increased beam width are convenient. A flat beam profile, often referred to as top-hat beam, causes less aberrations of the thermal lens [91]. Hence, a top-hat beam is the favored beam profile to pump with. Building lasers which deliver high pump powers while simultaneously providing a smooth beam profile, can be very challenging. In fact, the beam quality differs from the ideal case. To quantify this, the M^2 factor can be used, but limited to non-top-hat beam profiles only. For a perfect top-hat beam the M^2 factor becomes infinite [92, 93]. This can lead to a false conclusion, since high M^2 values are often related to beam profiles with a poor quality. From an experimental standpoint it may be more reasonable to stress that the beam profile has a homogenous distribution. Most notably, so-called hot spots (i.e., small intensity peaks with the risk of exceeding the damage threshold of the optics) have to be completely avoided. Rotational symmetry with respect to the beam propagation axis is significant for the profile, as well.

For all the so far mentioned points, the stability of the particular parameter is important, too. For instance, a change of the pump power immediately affects the output power of the Ti:sapphire laser. As stated in Section 2.2.1, the pulse-to-pulse stability is relevant (deviation $\lesssim 4\,\%$), as well as a reasonable retention of the power level on a long-term basis. Likewise, the ratio of linear polarization directly alters the pump efficiency if the laser asks for a specific orientation. Then, the pump radiation should be linearly polarized as best as possible. For the repetition rate of the pump source the same applies as for the DIAL transmitter.

Considering the beam profile of the pump laser, the required stability cannot be readily quantified. A constancy of the beam quality is needed so that the mode matching with the Ti:sapphire laser is not affected, as well as avoiding a change of the Ti:sapphire resonator mode itself by influence of the thermal lens. Most notable in this regard is the pointing stability of the pump beam. A change of the pump beam position on the laser crystal alters the overlap with the laser beam and, hence, reduces the total efficiency of the laser. Furthermore, a consequence would be the transverse dislocation of the thermal lens, which in turn would result in a deterioration of the laser resonance adjustment. That is why the pointing has to be kept as stable as possible. A sensitivity analysis [94] showed that displacement misalignments of $\approx 20\,\%$ of the beam radius can cause an output power decrease of $\approx 5\,\%$. By way of example, for a pump beam radius of $w_{pump} \approx 0.8\,\mathrm{mm}$ this corresponds to a displacement of $0.16\,\mathrm{mm}$. The stability of the pump source is also influential during the development of the (pumped) laser.

Spectral characteristics, like frequency stability, bandwidth, or single-frequency operation, are not key features for pumping. As long as the pump laser radiation resides within the absorption spectrum of the laser material, and preferably close to the maximum of it, further frequency properties are not relevant. If the radiation (or a part of it) is to be utilized for other lidar techniques, as rotational Raman lidar for temperature profiling in the atmosphere, then frequency stability and laser bandwidth is significant [95, 96]. In this case, means have to be found to achieve the specific spectral requirements. Injection seeding of the oscillator could be an option. When designing the pump laser setup, the potential implementation of injection seeding components should be anticipated.

Last but not least, object properties and electrical power consumption of the laser should be considered, although in a reference lidar such as the Hohenheim-DIAL these factors were not found to be overly limiting. For the pump laser, an optical table with a space of $1.5 \times 1.0 \times 0.7\,\mathrm{m}^3$ is available for the laser head; a 19-inch rack[4] of $2\,\mathrm{m}$ height and $0.9\,\mathrm{m}$ depth is intended for electronics and water chillers. As the pump laser most likely has the highest electrical power con-

---

[4] *Knürr*, Miracel NS25 41HE B600 T900 1.136.016.1

sumption of the entire laser system, it is desirable to reach a wall-plug efficiency of $\eta_{wp} = 10\,\%$ or higher [87].

3.2 *IBL* Pump Laser

In the first part of this work, a pulsed solid-state laser was applied, as pump source that had originally been developed from 2005 on within a collaboration of *University of Potsdam*, the company *IBL* and *University of Hohenheim*. This laser is a fully diode-pumped Nd:YAG-MOPA with frequency-doubled output [87]. It served as pump source for the preceding laser transmitter of the DIAL system [25, 26]. In 2011, at the beginning of this work, the Nd:YAG-MOPA underwent a complete redesign at *IBL* to improve its overall performance, particularly with regard to its stability and beam quality. The improved pump laser was then used without further changes for four years, including field campaigns of the Hohenheim-DIAL with long-term operation (see Section 6.1.1).

3.2.1 Setup

This section describes the setup of the *IBL* pump laser. The focus is set on the changes that were performed in comparison to the original model. Further details are, thus, to be found in [25, 26, 87]. Besides, information is restricted for some components of the laser, since it is intellectual property of *IBL*.

The optical setup (see Figure 3.1) primarily consists of the laser oscillator, two amplifying stages (preamplifier and main amplifier), and the second harmonic generation. The first and probably most impactful change was performed on the oscillator. Instead of the prior linear resonator, a triangular ring layout was chosen [97, 98]. The advantages of a ring resonator are explained in Chapter 5.2.2. This was accompanied by the decision to retrofit an injection seeder for the oscillator at a later stage. A different design of the resonator naturally involves reviewing the available space on the ground plate, where the parts are mounted on. Consequently, all components had to be disassembled and rearranged. Additionally, a second pump chamber was implemented in the oscillator. Now two identical pump chambers are responsible for the generation of the laser light at $1064\,\mathrm{nm}$. Every chamber comprises a Nd:YAG rod of $3\,\mathrm{mm}$ diameter and $50\,\mathrm{mm}$ length, which is side-pumped by six laser diodes. Other components of the oscillator are: a Pockels cell, acting as Q-switch for the creation of energetic pulses; a Faraday isolator, a half-wave plate, and a quartz polarization rotator, which are responsible for unidirectional propagation of the laser beam within the ring resonator; two lenses and an iris to inhibit higher laser modes; and a shutter. All parts are situated in the optical path, which is defined by three mirrors forming a triangle. The mirrors are highly reflective, except the output coupler, which has a reflectivity of $R = 60\,\%$.

The setting of the amplifying stages is made up of two pump chambers, a quartz rotator in between, and beam adapting lenses before and after the amplification. The pump chambers of the pre-amplifying stage are identical, with a Nd:YAG rod of $3\,\mathrm{mm}$ diameter and $80\,\mathrm{mm}$ length being side-pumped by 12 laser diodes. For the main-amplifier pump chambers even bigger rods of $8\,\mathrm{mm}$ diameter and $90\,\mathrm{mm}$ length are used. They are side-pumped in the first pump chamber by 32 and in the second one by 24 laser diodes. During the revision of the pump laser the

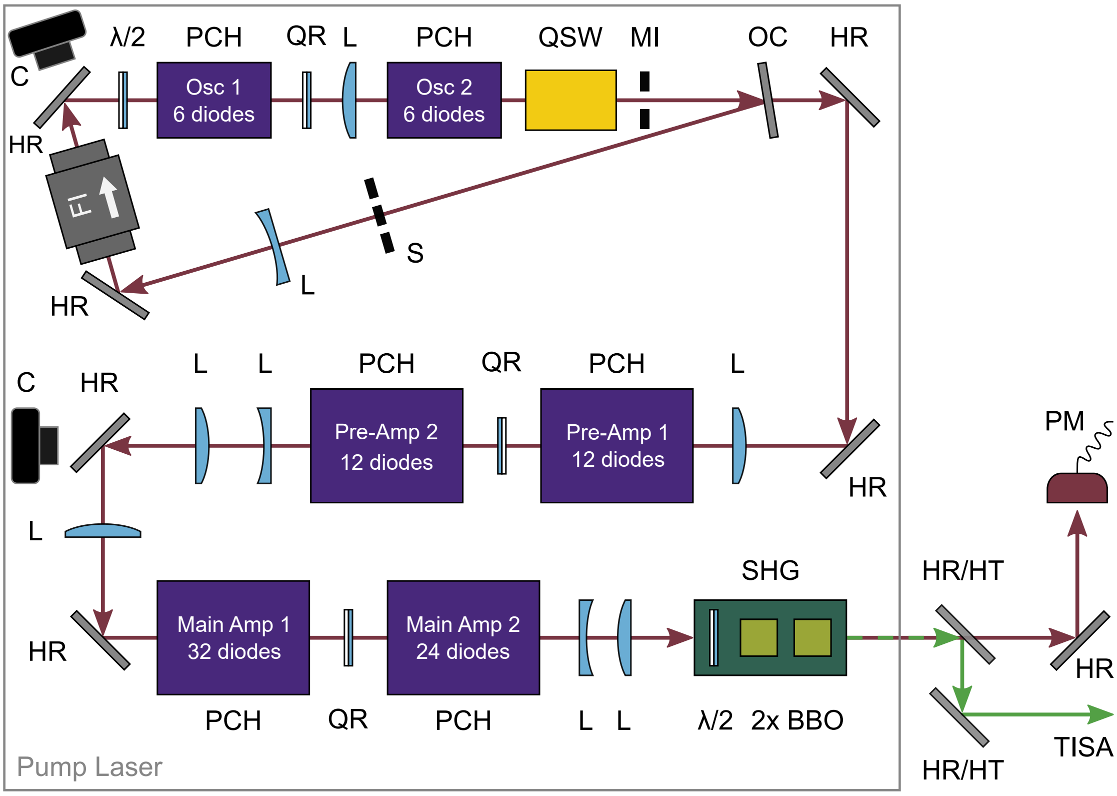

Figure 3.1: Setup of the *IBL* pump laser. The Nd:YAG MOPA architecture consists of a triangular laser resonator as master oscillator (Osc) and two linear stages as power amplifier (Amp). The HR/HT mirrors are highly reflective at $532\,\mathrm{nm}$ and anti-reflective at $1064\,\mathrm{nm}$. They were installed outside of the laser case to simultaneously serve as bending mirrors and direct the pump beam to the Ti:sapphire laser setup (TISA). This also enables to easily access the residual infrared power for monitoring purposes. BBO – Beta-Barium-Borate crystal, C – camera, FI – Faraday isolator, HR – highly reflective mirror at $1064\,\mathrm{nm}$, $\lambda/2$ – half-wave plate, L – lens, MI – mode iris, OC – output coupler, PCH – pump chamber (with number of laser diodes pumping the Nd:YAG rod), PD – photodiode, PM – power meter, QR – quartz rotator, QSW – Q-switch, S – shutter, SHG – second harmonic generation.

laser diodes in every pump chamber were verified and partially exchanged by new ones. The correct functionality and the arrangement of the laser diodes around the Nd:YAG crystal rod are important as both influence the spatial intensity distribution of the laser beam. Achieving a homogenous illumination and a rotationally symmetric beam profile can be demanding and represents one of the manufacturer's secrets. Two cameras[5] were implemented in the setup of the laser to monitor the beam profile at the oscillator and behind the preamplifiers. A monitoring camera for the final beam profile (after main amplification and SHG) was included in the setup of the Ti:sapphire laser.

---

[5] *Thorlabs*, DCC1545M (CMOS Camera, Monochrome Sensor)

As a final step, the radiation is converted from its fundamental wavelength, $\lambda = 1064\,\mathrm{nm}$, to its second harmonic, $\lambda = 532\,\mathrm{nm}$, and both radiations are then separated. The nonlinear frequency conversion is performed with two Beta-Barium-Borate (BBO) crystals in series. The crystals are housed in heat insulating mounts and thermoelectrically stabilized to a temperature of $40\,^{\circ}\mathrm{C}$. With a motorized half-wave plate in front of the crystals, the amount of the frequency-doubled $532\,\mathrm{nm}$-radiation can be controlled and maximized. The harmonic separation is realized with two dichroic mirrors[6] (coated for maximum reflectivity at $532\,\mathrm{nm}$ and maximum transmissivity at $1064\,\mathrm{nm}$), which were placed outside of the laser to simultaneously serve as bending mirrors to direct the beam to the Ti:sapphire laser setup.

The case of the laser head has a dimension of $1.2 \times 0.6 \times 0.3\,\mathrm{m}^3$ and a weight of approximately $150\,\mathrm{kg}$. The central control unit, the high voltage power supply for the pump chambers, and further electronics drivers reside in a 19-inch rack. Together with the water chillers it takes up the entire space of the rack. The chillers are two water–water coolers which are connected to the water circulation of the DIAL system. One cooler[7] is in charge of heat removal of the oscillator's pump chambers, with a temperature set to $25\,^{\circ}\mathrm{C}$. The other cooler[8] is responsible for the pump chambers of the amplifiers and set to a temperature of $21\,^{\circ}\mathrm{C}$. The electrical power consumption of the laser operating at full power is at maximum $10\,\mathrm{kW}$, according to the manufacturer.

3.2.2 Power Characteristics

The laser can be characterized in many aspects regarding its power performance. According to Equation (2.13), for a given pulse repetition rate it is equivalent to look at the average output power or the pulse energy. In this thesis, all mentioned values of the pulse energy were calculated from the measured average output power and the repetition rate of the pump laser. The *IBL* pump laser operates at a repetition rate of $f_{rep} = 250\,\mathrm{Hz}$.

The output power of the pump laser depends on the temporal condition of the light pulses emitted by the laser diodes in the different pump chambers. The pulses can be manipulated in their duration and in their time delay to one another. In simple terms, the output power increases if the pulse duration of the laser diodes becomes longer, or if the delay time of the laser diodes relative to each other becomes shorter. This can only be done to a certain point, otherwise the output power decreases or components get damaged. The mentioned parameters can be changed for the Q-switch in the oscillator, as well as for the pump chambers in the oscillator, the preamplifier, and the main amplifier. The delay always refers to the pulse time of the pump chambers in the oscillator. To control the output power, the manufacturer recommends setting the pulse durations to fixed values ($\Delta t_{Qsw} = 202\,\mu\mathrm{s}$, $\Delta t_{osc} = 160\,\mu\mathrm{s}$, $\Delta t_{pre} = 250\,\mu\mathrm{s}$, $\Delta t_{main} = 260\,\mu\mathrm{s}$), representing the maximum possible values. Then, the laser is powered up by successively decreasing the delay time of the Q-switch, the preamplifier, and the main amplifier until the minimal values are reached ($t_{Qsw} = 75\,\mu\mathrm{s}$, $t_{pre} = t_{main} = 67\,\mu\mathrm{s}$). Figure 3.2 shows how the output power augments when the delay times are decreased in this manner. It should be noted that the power is given at $532\,\mathrm{nm}$, and that the SHG conversion of the infrared into

---

[6] *CVI / Melles Griot*, BSR-51-LW-3-1037-UV

[7] *Termotek*, P305

[8] *Termotek*, P204

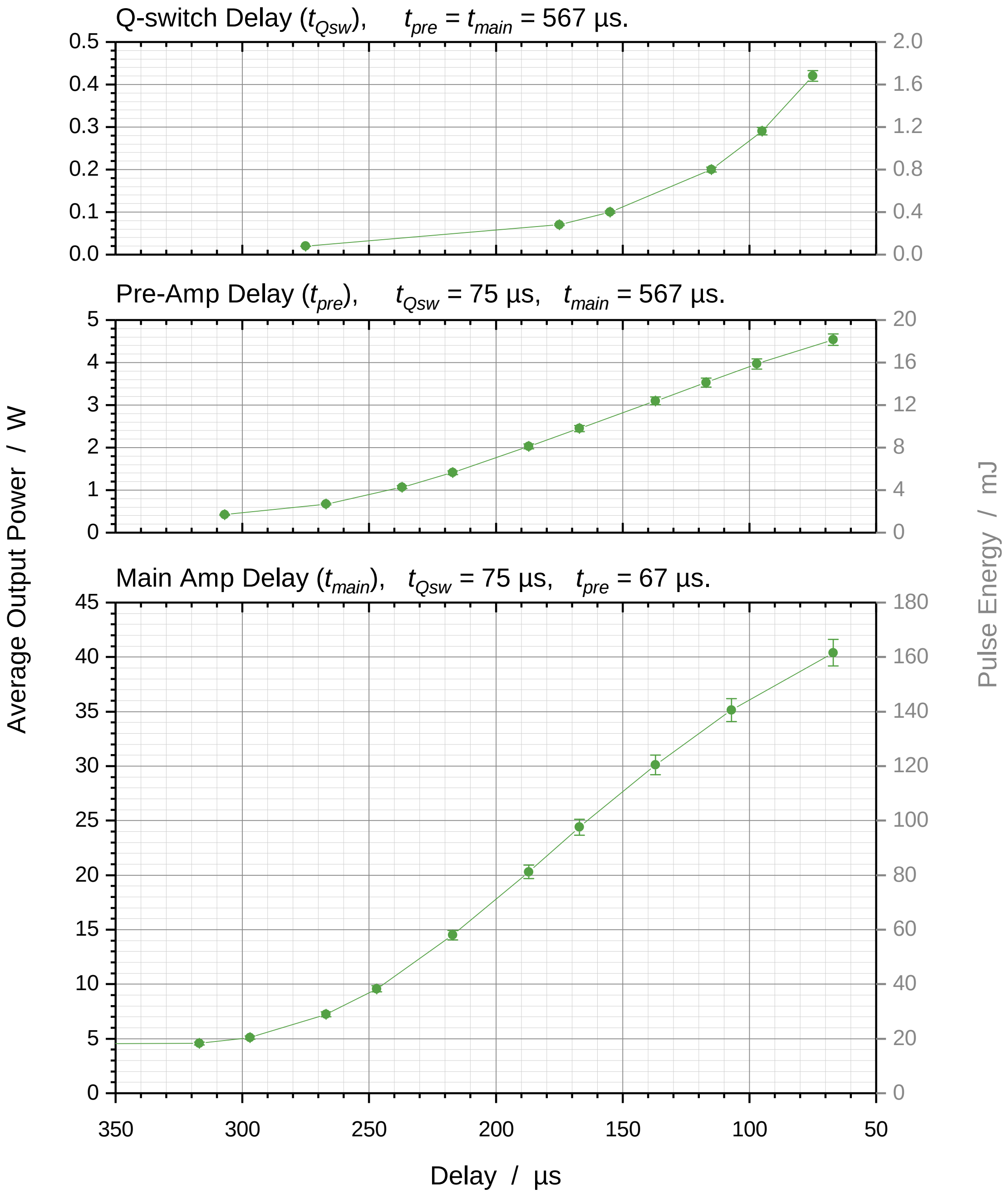

Figure 3.2: Average output power at 532 nm of the *IBL* pump laser, measured as a function of the time delays between the trigger/pump chamber pulses of the Q-switch, the preamplifier, and the main amplifier respective to the oscillator. The power-up procedure consists in consecutively reducing these delays. The delay values (x-axis) decrease from left to right. The pulse energies on the right y-axis were calculated with the repetition rate of 250 Hz. The solid line is only a guide to the eye.

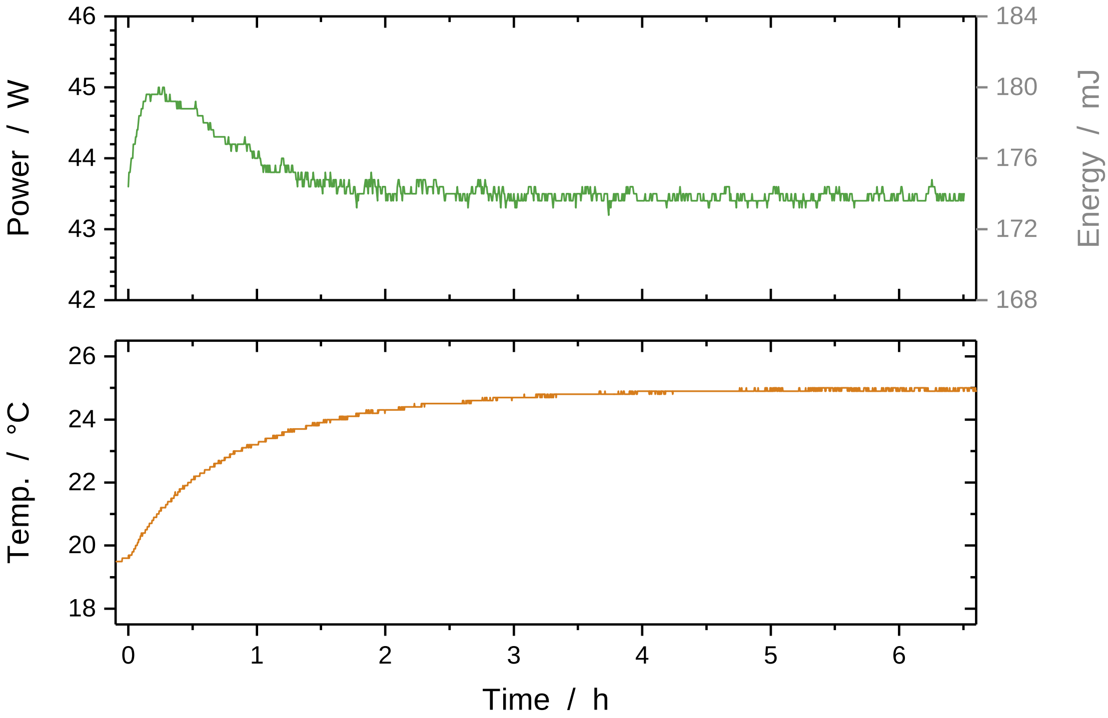

Figure 3.3: Long-term measurement of the output power at $532\,\mathrm{nm}$ and the temperature inside of the *IBL* laser. After a warm-up period, constant values are reached.

the green laser radiation is more efficient, the higher the fundamental infrared power $P_{\mathit{1064,tot}}$. The conversion efficiency changes according to $\eta_{\mathit{SHG}} \propto P_{\mathit{1064,tot}}$ [85]. For the *IBL* pump laser the efficiency is $\eta_{\mathit{SHG}} \approx 50\,\%$ at full output power and goes down to efficiencies such as, e.g., $\eta_{\mathit{SHG}} \approx 27\,\%$ at $P_{\mathit{1064,tot}} = 18.5\,\mathrm{W}$ or $P_{\mathit{532}} = 5\,\mathrm{W}$.

Shortly after the provision of the revised pump laser by *IBL*, the laser delivered a full average output power of around $P = 43\,\mathrm{W}$ at $532\,\mathrm{nm}$, which corresponds to a pulse energy of $E = 172\,\mathrm{mJ}$. The precise value depends on several conditions. First, the measured average output power depends on the power meter that is used. It was found that one power meter[9] showed a to some extent constant deviation of $\Delta P = -2.5\,\mathrm{W}$ from another model[10]. The here mentioned power values for the *IBL* laser correspond to the *Coherent* power meter. Moreover, a daily variation of the output power was determined ($\Delta P \approx \pm 1\,\mathrm{W}$). The cause of this variation can be the laser or the power meter itself. For the *Coherent* power meter, a total accuracy (sensor and display accuracy) is specified with $3\,\%$, corresponding to $\Delta P = \pm 1.3\,\mathrm{W}$ at a measured power of $P = 43\,\mathrm{W}$. Finally, the laser has a certain warm-up time. During this phase, which lasts approximately $1\,\mathrm{hour}$, the output power is exceeded by more than $1\,\mathrm{W}$. In Figure 3.3 a long-term measurement of the output power is plotted. The power was logged immediately after the

---

[9] *Coherent*, LM100-HTD with FieldMaster GS

[10] *Ophir*, FL250A-SH-V1 with Laserstar

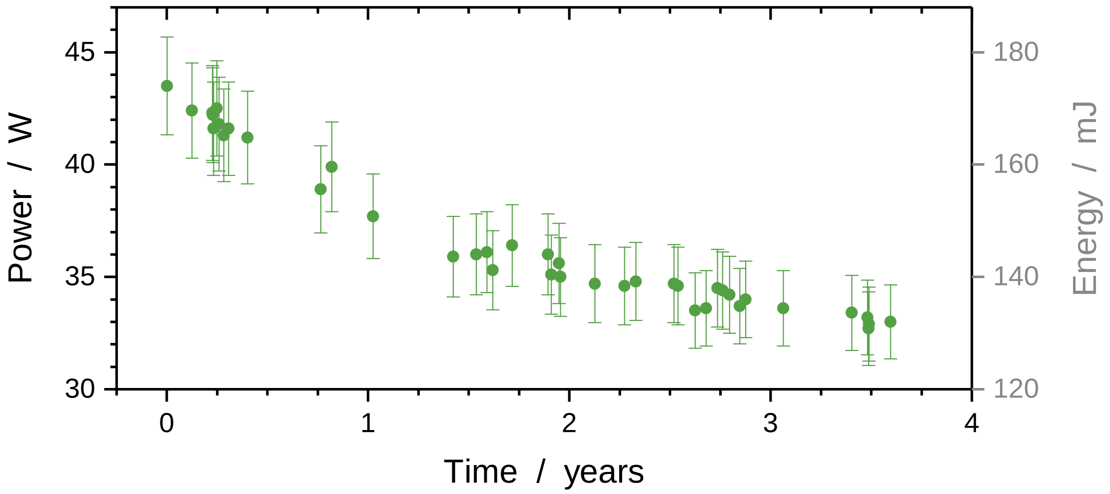

Figure 3.4: Maximum average output power at 532 nm of the *IBL* pump laser over the years. The degradation was strongest during the first one and a half years.

laser was completely powered up. Additionally, the temperature was measured with a logger[11], which was put inside the laser case. The plot shows the overshoot during the warm-up and how power and temperature then settle to a constant value.

In the course of time, the full output power gradually decreased. While sometimes this was preceded by a crash of the laser (a sudden failing of all electrical components, with the need of a complete restart), or a transport of the Hohenheim-DIAL to a campaign site, in other occasions no specific reason for the power drop off could be identified. Every power drop off amounts to 0.5 W to 1 W. Figure 3.4 shows the available full output power over the total operational time of the laser. It is a rough illustration only, as the power values also vary due to the above-mentioned reasons, and as the operational time of the laser was logged manually. After almost four years of operation, after the *IBL* laser was replaced by a new pump laser, a full output power at 532 nm of $P = 33\,\mathrm{W}$ was left.

The pulses of the laser were analyzed by detecting a fraction of the radiation with a photodiode[12] and coupling it with $50\,\Omega$ impedance to an oscilloscope[13]. The measured pulse shape (see Figure 3.5) is similar to a Gaussian function but overlain by a more or less complex structure of oscillations. The structure is due to competition of two or more modes in the resonator, manifesting as beat notes in the laser pulse [58]. Computing a fast Fourier transform of the pulse signal with the mode beating provides the frequency of the resonator's free spectral range (FSR), and thus, enables to determine the (optical) length of the resonator. For a ring resonator,

$$\Delta\nu_{FSR} = \frac{c}{L}\,. \tag{3.3}$$

From $\Delta\nu_{FSR} = (246 \pm 2)\,\mathrm{MHz}$ then follows $L = (1.22 \pm 0.01)\,\mathrm{m}$. This complies with the

---

[11] *Voltcraft*, DL-120TH

[12] *Thorlabs*, DET10A/M

[13] *Tektronix*, DPO 4104B ($1\,\mathrm{GHz}$, $5\,\mathrm{GS/s}$)

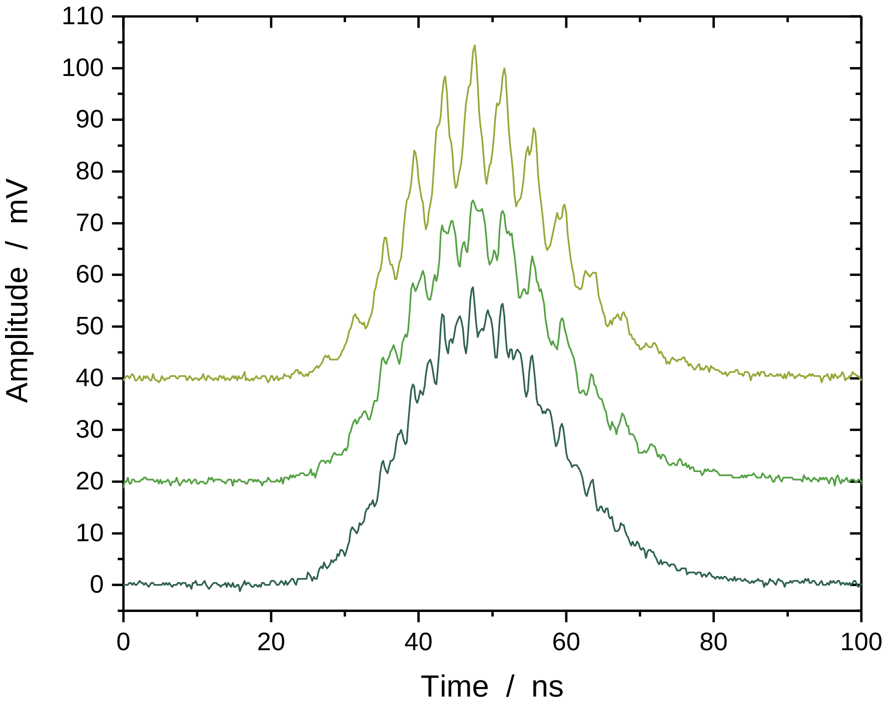

Figure 3.5: Different laser pulses of the *IBL* laser at the same operation power of $P \approx 33\,\mathrm{W}$ at $532\,\mathrm{nm}$, measured with a photodiode (shifted amplitudes for clarity). The beat note structure on the pulses varies according to the temporary mode competition situation in the resonator.

geometrically measured resonator length $L_{geo} = (1.07 \pm 0.03)\,\mathrm{m}$ keeping in mind that there are many and long elements in the resonator which have a refractive index $n > 1$ and thus, increase the optical length. The pulse duration can directly be obtained from the pulse shape. At the average output power of $P = (33.0 \pm 1.7)\,\mathrm{W}$, the full-width half-maximum of the pulse was determined to $\Delta t = (24 \pm 3)\,\mathrm{ns}$. With this parameter and the pulse energy $E = (132 \pm 7)\,\mathrm{mJ}$, the peak power of a single pulse can be calculated according to Equation (2.2) to $\hat{P} = (5.5 \pm 0.8)\,\mathrm{MW}$.

3.2.3 Beam Quality and Propagation

A first estimate for the beam quality of the pump laser can be assessed through the beam profile directly after the laser output, close to the case. Figure 3.6 shows the $532\,\mathrm{nm}$-beam profile at a distance of $z \approx 685\,\mathrm{mm}$ from the laser exit aperture, and at the full output power of the laser (where only the weak reflected beam from three uncoated wedges was directed onto the camera[14]). At the camera location the 2σ-beam width (radius) was $w = 2.7\,\mathrm{mm}$. The beam is dominated by the higher order transverse mode TEM_{01*}, also called donut mode. The intensity distribution only slightly deviates from a full circular symmetry (roundness of 0.97). But even a

---

[14] *Ophir / Spiricon*, SP620U

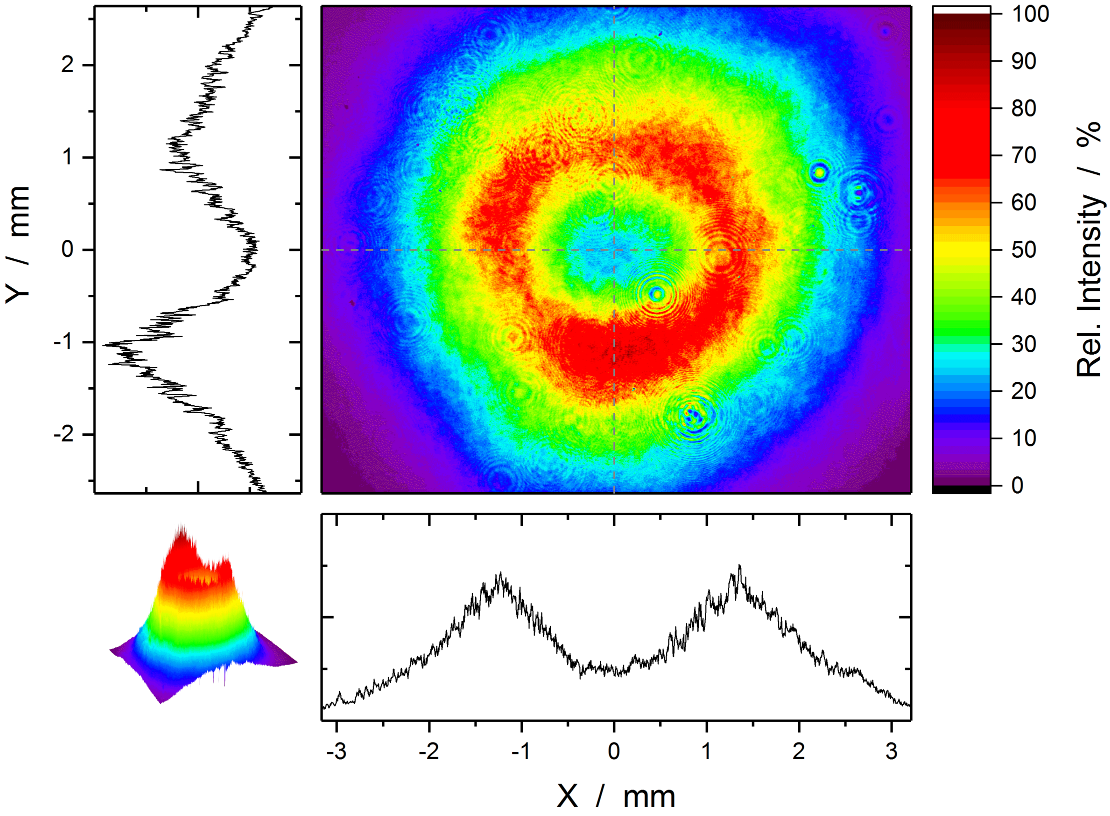

Figure 3.6: Beam profile of the *IBL* laser at a distance $z \approx 685\,\mathrm{cm}$ from the laser exit aperture and at full power operation. The profile shows the main presence of the donut mode TEM_{01*} in the $532\,\mathrm{nm}$-laser beam, but without the complete intensity decrease in the center and a slightly higher intensity in the lower part of the circular distribution. The speckles in the image are dirt particles on the neutral density filters of the camera, as has been verified by rotating the filters.

small deviation can escalate to a clear asymmetric profile when focusing the beam, as shown in Figure 3.7. It is favorable for the beam profile to not contain any hot spots, which could cause damage on the optics.

The shape of the intensity distribution remains nearly constant over the range of different pump powers. This particularly applies to the power range $P_{532} \gtrsim 8\,\mathrm{W}$, at which the Ti:sapphire laser is operated. Only at very low powers of the pump laser the beam profile changes notably. This indicates, that at this point the rods in the pump chambers have not yet reached their designed thermal lens. In view of the temporal development of the beam profile, it was found that it also stays almost unchanged. After a long-term measurement of over $6\,\mathrm{hours}$ for the above-mentioned arrangement, only a small increase of the asymmetry of the intensity distribution was noticed. More obvious was the conduct of the pointing stability. Over the $6\,\mathrm{hours}$ of measurement, the location of the centroid shifted by $\Delta x = 0.15\,\mathrm{mm}$ in the plane parallel to the optical table and by $\Delta y = 0.24\,\mathrm{mm}$ in the perpendicular plane, corresponding to $\approx 5\,\%$ and $\approx 9\,\%$ of the beam radius, respectively. Likewise, over the four years of operation of the *IBL* pump laser, the beam profile remained the same. Interestingly, neither the power drop off mentioned in the previous section had an influence on the beam profile. This suggests, that the power drop off (particularly, a crash of the laser) was most probably not caused by a failure of a laser diode in one of the pump chambers. A complete failure of a laser diode would have affected the homogeneity of the Nd:YAG crystal pumping in the corresponding pump chamber and this directly would have influenced the beam profile.

An M^2 analysis[15] of the beam yielded values of $M_x^2 = 1.90$ and $M_y^2 = 1.77$. The resulting beam waists (radii) from the analysis were $w_{0,x} = 2.36\,\mathrm{mm}$ and $w_{0,y} = 2.32\,\mathrm{mm}$. The divergences (half angle) were $\theta_x = 0.14\,\mathrm{mrad}$ and $\theta_y = 0.13\,\mathrm{mrad}$. The experimental M^2 values comply with what one would expect from theoretical calculation [99]; for higher transverse circular modes, also known as Laguerre-Gaussian modes, the beam quality is given by

$$M_{m,p}^2 = 2m + p + 1\ . \tag{3.4}$$

The donut mode has the mode indices $m = 0$ and $p = 1$, and thus $M_{0,1}^2 = 2$. The smaller experimental values can be attributed to the fact that the measured beam profile is not completely a TEM_{01*} donut mode, but partially also contains the fundamental transverse mode TEM_{00} (the intensity in the center of the beam does not entirely descend to zero). In comparison to the former Nd:YAG-MOPA the M^2 values have significantly improved. Previously, for a configuration of the laser that delivered approximately the same output power, the beam quality was $M_x^2 = 3.9$ and $M_y^2 = 4.3$ [25]. Therefore, a higher pump efficiency of the Ti:sapphire laser can be expected, and actually is the case, as will be shown in Chapter 5.7.2.

A beam profiler was also used in combination with a polarizer to determine the ratio of linear polarization of the pump laser. The linear polarizer in front of the camera was rotated to maximum and minimum transmission of the (low power) probe beam. The respective intensities were captured with a camera because of its higher sensitivity and determined by adding up the values of all pixels. The ratio was then calculated to be $I_{max}/(I_{max} + I_{min}) > 99.7\,\%$.

3.2.4 Mode Matching to Ti:sapphire Laser

Section 3.1 explained that, since the Ti:sapphire crystal is end-pumped, in order to get the highest efficiency of radiation transfer, a specific intensity distribution of the pump beam is required and an ideal spatial overlap with the Ti:sapphire laser resonator mode inside the crystal has to be achieved. In reality, the available pump beam mode differs significantly from the theoretically desired one. By using one or more lenses it is possible to attain a certain redistribution of the intensity in the beam profile, as well as an adaptation of beam parameters (e.g., width and divergence). However, the accomplishment of all properties at once, can pose a great challenge. In particular, the redistribution of the intensity at a fixed beam width is limited, as it is dependent on the given original beam quality. A further demand is to keep the number of lenses as low as possible, as every additional optical element implicates power losses—despite coatings for low back reflection—and represents a potential source for misalignment. Finally, there are some geometrical restrictions for the placement of the lens(es). In the setup of the Ti:sapphire laser

---

[15] *Ophir / Spiricon*, M^2-200 (Accuracy of mentioned values, typical 5 %)

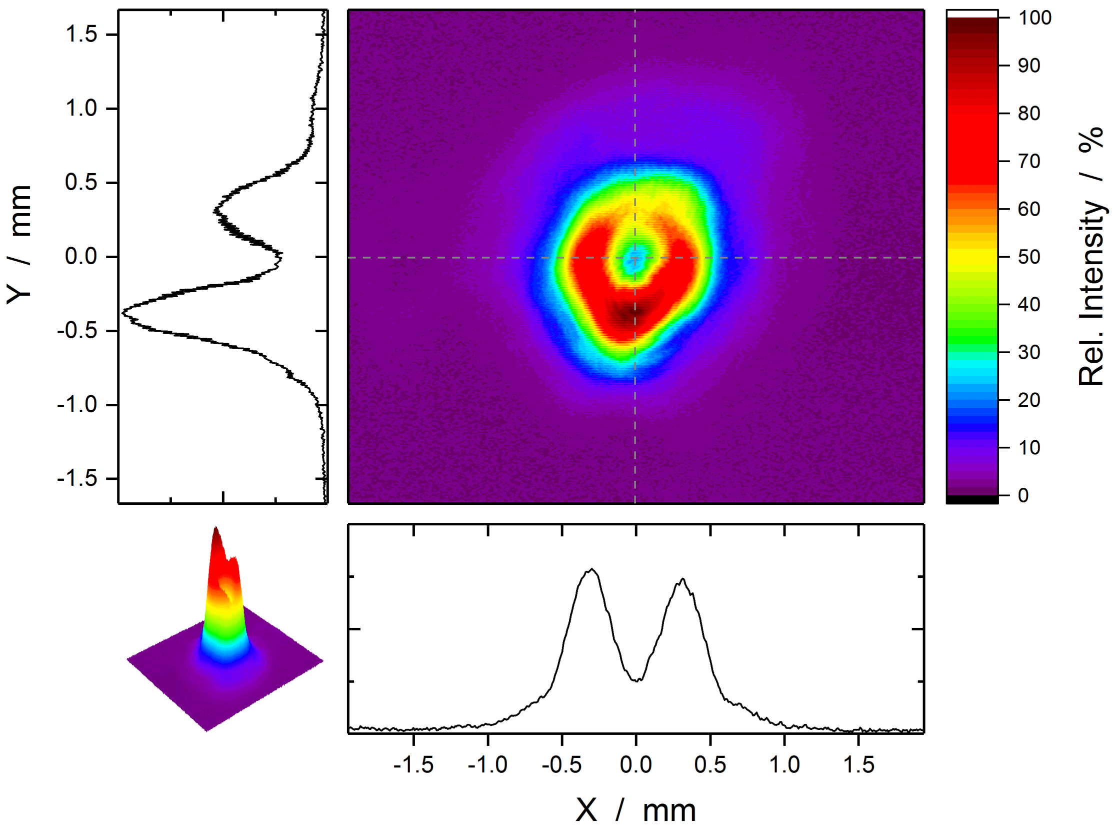

Figure 3.7: Beam profile of the *IBL* pump laser after propagation through the beam adaption lens. The distance behind the lens where the image was captured corresponds to the position of the Ti:sapphire crystal in the laser setup. There, the beam width of the pump beam is approximately as large as the Ti:sapphire laser mode (see the text for the parameter values). The circular intensity distribution has become more asymmetric.

(see Figure 5.7 in Chapter 5) the placing of the lens(es) is restricted to a distance between $685\,\mathrm{mm}$ to $885\,\mathrm{mm}$ from the crystal. A trade-off between all these issues has to be found, or at least a choice has to be made, for which property to prioritize.

First and foremost, the adaption of the beam width of the pump laser to the Ti:sapphire beam width at the end-surfaces of the laser crystal is performed. There, the beam radius is $w \approx 0.7\,\mathrm{mm}$, as will be shown in Section 5.2.1. The small divergence and the large beam radius that were found for the *IBL* laser in the previous section, encourage to find a suitable mode matching with one lens only. Thus, different lenses were tested, with focal length values related to the possible placing distances of the lens. For every lens, the beam width and intensity distribution were measured with a camera[16] and profiling software[17] at different distances behind

---

[16] *Pulnix*, TM-6EX

[17] *Ophir / Spiricon*, LBA-400PC (v4.26)

the lens. Eventually, a plano-concave lens[18] with a focal length $f = +1118\,\mathrm{mm}$ at $532\,\mathrm{nm}$ was selected. The lens was placed at a distance of $z = (750 \pm 30)\,\mathrm{mm}$ from the crystal, or $z = (725 \pm 25)\,\mathrm{mm}$ from the exit aperture of the pump laser. Figure 3.7 depicts the beam profile that results at the end-surface of the Ti:sapphire crystal. The mean beam radius of the profile is $w_{pump} = 0.76\,\mathrm{mm}$, being slightly larger than the Ti:sapphire laser beam. Due to the focusing, the profile becomes more asymmetric, manifesting itself in an increased intensity in the lower part and a reduced intensity in the higher part of the donut. The ellipticity also has increased (roundness of 0.81). Certainly, this beam profile is not ideal for pumping, and this was one of the main reasons why another pump source was later employed in the Ti:sapphire laser system. Nevertheless, it represents an improvement of the situation in comparison to the former pump laser, which suffered from hot spots in the profile. Here, none of them are present. Therefore, the Ti:sapphire crystal and further optics are not endangered by the pump beam when the power level is increased to high values. As a result, the pump beam width is adapted reasonably well to the radius of the laser mode at the crystal with one single lens.

3.2.5 Spectral Characteristics

Although the pumping of Ti:sapphire may not be very demanding in terms of spectral properties, the results of a wavelength meter measurement shall be given here. They can be a valuable information if the *IBL* laser comes into operation for other applications. The same wavelength meter model[19] was used which normally characterizes the Ti:sapphire laser performance. The pump laser radiation in the green spectral region was measured. The result for the (vacuum) wavelength was $\lambda = (532.212 \pm 0.015)\,\mathrm{nm}$, and for the linewidth $\Delta\nu = (13 \pm 5)\,\mathrm{GHz}$. The latter value lies above the maximum bandwidth limit (8 GHz) of the instrument which is considered as reliable by the manufacturer. Hence, the result should be treated with caution. The lower limit for the bandwidth is estimated from the pulse length via the time–bandwidth product (Equation 2.15). With the pulse length being $\Delta t = (24 \pm 3)\,\mathrm{ns}$ (see Section 3.2.2) the lower bandwidth limit is $\Delta\nu = (18 \pm 3)\,\mathrm{MHz}$. This value expresses which minimum linewidth would be possible in case of a single-frequency operation of the laser.

---

[18] *Laser Components*, AR/AR1064+532 PLCX-25.4/515.1UV ($f_{nom} = +1000\,\mathrm{mm}$)

[19] see footnote 75 on page 132

3.3 *PLA* Pump Laser

While the output power of the previous pump laser continuously degraded over the years, the development of the Ti:sapphire laser moved forward and with it the endeavor of achieving higher output powers. At a certain point the maximum available output power for pumping was reached and thus, the output power of the Ti:sapphire limited accordingly. That is why, from 2015 on, a new Nd:YAG laser is used as pump source. This laser is a customized development of *Proton Laser Applications* (*PLA*). Again, the architecture of the Nd:YAG laser is a master-oscillator power-amplifier system, that is fully diode-pumped and frequency-doubled. *PLA* works closely with the company *Monocrom*[20], which had already delivered laser diode modules for the *IBL* laser, and now produces the entire pump chambers. Two main aims were set to the new Nd:YAG-MOPA: to provide a higher average output power ($P_{532} > 50\,\mathrm{W}$), and a beam profile close to the ideal top-hat intensity distribution. In addition, improvements of the laser control software with better monitoring and logging possibilities were requested. As far as possible, a better overall efficiency and a more compact construction, was favored, too. Since the *PLA* laser is to some extent similar to the *IBL* laser, the differences to the latter will be emphasized in this section.

3.3.1 Setup

Compared to the *IBL* laser, the setup of the *PLA* laser is simplified in many aspects. The layout of the laser head is composed of the master oscillator, only one amplifying stage, the second harmonic generation, and finally the distribution and measurement of the output power (see Figure 3.8). For reasons of convenience and compactness, the manufacturer chose a linear resonator design for the master oscillator. A curved mirror, with a $4\,\mathrm{m}$ convex radius of curvature and highly reflective at $1064\,\mathrm{nm}$, as well as a plane mirror with a reflectivity of $R = 25\,\%$, serving as output coupler, form the linear resonator. The resonator includes two pump chambers of the same model[21]. According to the manufacturer, they contain a Nd:YAG crystal rod of $5\,\mathrm{mm}$ diameter and $80\,\mathrm{mm}$ length, with a doping degree of $0.6\,\mathrm{at\%}$. The crystal is water-cooled and side-pumped by a total of 36 laser diodes, arranged in six stacks around the crystal, each with six laser diodes bars. Furthermore, the resonator includes the Q-switch (Pockels cell), a quartz rotator, and a shutter. A Faraday isolator installed after the oscillator prevents potential feedback from the following amplifying stage.

The amplifying stage begins with a pair of lenses that adapt the beam for the single pass amplification through two pump chambers. The first pump chamber[22] provides a higher pumping power of the laser diodes ($150\,\mathrm{W}$ instead of $100\,\mathrm{W}$). The Nd:YAG crystal rod contained therein is longer ($100\,\mathrm{mm}$ length) and has lower doping degree ($0.4\,\mathrm{at\%}$). The second pump chamber is identical to the pump chambers in the oscillator. Between the two pump chambers, a quartz rotator is situated.

After the amplification another pair of lenses adapts the beam, now for the frequency conversion. It is followed by a zero-order half-wave plate. One nonlinear potassium titanyl phosphate (KTP) crystal is used for the second harmonic generation. The crystal has a dimension of

---

[20] *Monocrom*, Spain

[21] *Monocrom*, PH3600 series

[22] *Monocrom*, PH5400 series

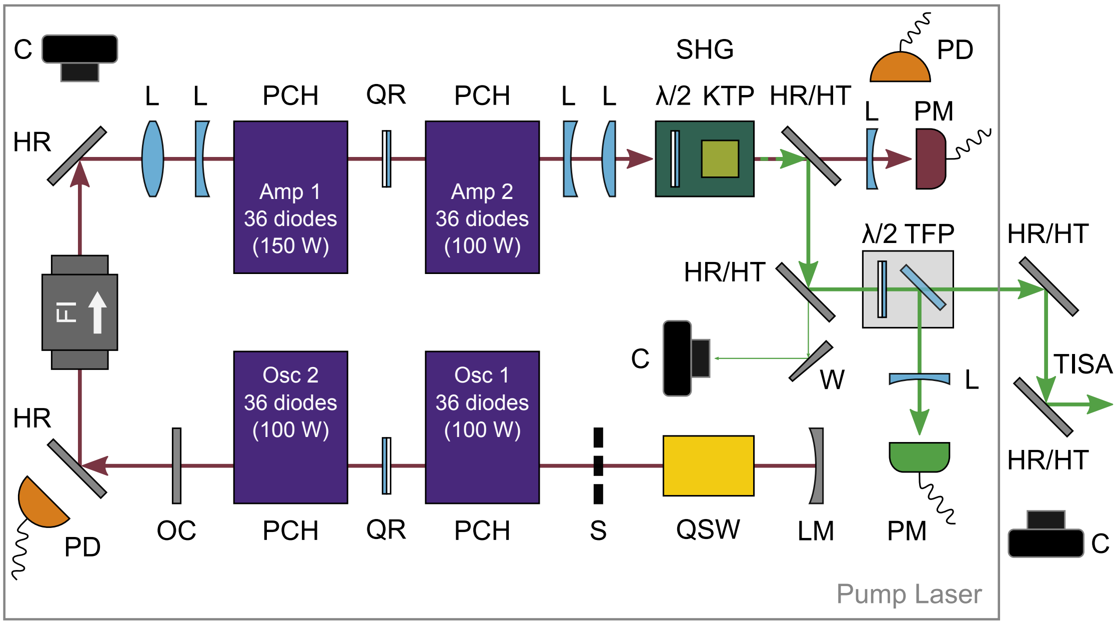

Figure 3.8: Setup of the *PLA* pump laser. The Nd:YAG MOPA architecture consists of a linear laser resonator as master oscillator (Osc) and a linear stage as power amplifier (Amp). Here, a potassium titanyl phosphate (KTP) crystal is used for the second harmonic generation (SHG). The arrangement behind it has been specifically implemented to regulate the pump power with a motorized half-wave plate ($\lambda/2$) and a thin-film polarizer (TFP), as well as to monitor the idle green and infrared power for analysis. LM – laser end mirror, PCH – pump chamber (with number of laser diodes and power pumping the Nd:YAG rod), W – wedge, further abbreviations see Figure 3.1.

$8\,\mathrm{mm} \times 8\,\mathrm{mm} \times 8\,\mathrm{mm}$ and is temperature stabilized to $T \approx 40\,°\mathrm{C}$. The residual fundamental radiation ($P_{1064,res}$) is separated from the second harmonic (P_{532}) with a dichroic mirror. By this, the infrared radiation is transmitted through the mirror, and directed onto a power meter[23].

As final step, the $532\,\mathrm{nm}$-radiation passes a motorized polarization rotator, which—combined with a thin-film polarizer—enables to only send a certain percentage of output power out of the laser case, while the rest is directed onto another internal power meter[24]. The percentage which is sent out is linearly p-polarized ($P_{532,p}$), and is either used for pumping the Ti:sapphire laser or—when characterizing the *PLA* laser—measured with yet another external power meter. The percentage remaining in the laser case is linearly s-polarized ($P_{532,s}$). The power meters and the polarization controller were implemented as a special suggestion of this thesis' author. Simultaneous monitoring of these powers provides information about the performance of the laser during operation. The information is not only obtained from the directly measured values, but also, by derivation of further parameters:

---

[23] *Standa*, UP19K-150W-H5-D0

[24] *Standa*, 11PMK-150W-H5

- The total fundamental power $P_{1064,tot}$ is calculated from the sum of all measured powers,

  $$P_{1064,tot} = P_{532} + P_{1064,res} = P_{532,p} + P_{532,s} + P_{1064,res} \ , \tag{3.5}$$

  and expresses the stability of the originally produced power, i.e., the laser in general.

- The frequency conversion efficiency is obtained as usual by the ratio of the entire power in the green spectral region and the total power in the infrared,

  $$\eta_{SHG} = \frac{P_{532}}{P_{1064,tot}} \ . \tag{3.6}$$

- The parameter S_1 of the normalized Stokes vector [99] gives a clue to the development of the linear polarization in front of the motorized polarization rotator. It assumes values from $S_1 = -1$ (totally s-polarized light) to $S_1 = +1$ (p-polarized) and is calculated by

  $$S_1 = \frac{P_{532,p} - P_{532,s}}{P_{532,p} + P_{532,s}} \ . \tag{3.7}$$

To obtain an unambiguous information about the power evolution, it is not enough to investigate only one of the measured powers. For instance, a decrease of the power at $532\,\mathrm{nm}$ could originate from a decrease of the SHG conversion efficiency or from a loss of original laser power.

In the end, most notably for pumping the Ti:sapphire laser is the knowledge about the behavior of $P_{532,p}$. Obviously, this quantity cannot be measured while the Ti:sapphire crystal is pumped. Therefore, the other parameters cannot be deduced and no statement about the related properties can be made. However, under the assumption of a constant polarization, it is possible to draw some conclusions. The course of $P_{532,p}$ then correlates with $P_{532,s}$, and both powers only differ in their absolute value. Together with the measured $P_{1064,res}$ it is possible to determine how η_{SHG} changes. The assumption of a constant linear polarization is generally plausible due to the birefringent nature of the nonlinear conversion process, albeit there are sources for depolarization related to phase mismatch as well [85, 100].

To get an estimate of the magnitude of $P_{532,p}$ during operation of the Ti:sapphire laser, the following action is taken. At the beginning, or for short moments during operation, the motorized polarization controller is set to the polarization position at which the whole second harmonic power is directed onto the internal power meter. Thus, at this moment $P_{532} := P_{532,s}$. Thereupon, the pump power is obtained by $P_{532,p} = P_{532} - P_{532,s}$, where $P_{532,s}$ then is the measured power. Since P_{532} can change with ongoing operation time, the procedure should be repeated after a while, at least at the end of operation. Another beneficial side effect of this arrangement for power distribution and measurement is, that the beam, which is sent out and used for pumping, is transmitted through the thin-film polarizer. Hence, the required p-polarization for the Ti:sapphire crystal pumping is ensured.

By default, two cameras[25] have been installed in the laser to monitor the $1064\,\mathrm{nm}$-beam behind the oscillator and the $532\,\mathrm{nm}$-beam behind the harmonic separation. The image acquisition is implemented in the software and the images are logged every minute. Likewise, the power

---

[25] see footnote 5 on page 30

measurements are implemented in the software. Unfortunately, the values are stored without decimal places (rounding). Changes in the power can thereby only be identified afterwards, when differences of over $1\,\mathrm{W}$ occur. A future update of the software should allow to save the values with full precision.

The required space by the pump source has been reduced with the *PLA* laser. The dimension of the laser head's case is $1.1 \times 0.6 \times 0.3\,\mathrm{m}^3$. The smaller size is due to the linear resonator design and the simple need of only one amplifier stage. The weight of the laser head is approximately $100\,\mathrm{kg}$. Great advancements have been achieved for the electronics. The high voltage power supply and the driver of a pump chamber are now completely included in the pump chamber. As a result, long power and signal lines are omitted, which improves signal quality for the laser diodes and reduces strong signal noise emitted to surrounding devices. Another major advantage consists in the removal of the external drivers, importantly reducing the space. Thus, in the 19-inch rack, only the central control unit (4U height[26]) and the chiller (12U height) have to be accommodated. The weight of both is approximately $65\,\mathrm{kg}$, according to the manufacturer. The chiller is a water-water cooler[27] and set to a temperature of $28\,°\mathrm{C}$. The total power consumption of the laser operating at full power is specified by the manufacturer with $3\,\mathrm{kW}$. The UPS of the Hohenheim-DIAL measured a power consumption of about $8.4\,\mathrm{kW}$. Other devices than the pump laser were switched off as far as possible. However, the air–water heat exchanger of the DIAL had to remain running, as well as a computer and an oscilloscope for monitoring, consuming itself $\approx 4.2\,\mathrm{kW}$. Thus, the wall-plug efficiency was $\eta_{wp} \approx 1\,\%$.

3.3.2 Power Characteristics

While developing the *PLA* laser, the question arose whether to keep the same pulse repetition rate ($f_{rep} = 250\,\mathrm{Hz}$) or to increase it. Since the energy per pulse is one of the first parameters to be limited by the component's damage threshold, increasing the repetition rate is the next possibility to achieve higher average output powers. Generally, the DIAL requirements allow for repetition rates $f_{rep} > 250\,\mathrm{Hz}$. If the pulse energy is the same, then higher repetition rates are even preferred (mainly due to a better spatial resolution for scanning measurements). On the other hand, fast pulse repetition frequencies set high standards to other devices of the transmitter or the receiver of the DIAL. This was discussed in detail in Chapter 2.2.1. In the end, it was decided to increase the repetition rate to $f_{rep} = 300\,\mathrm{Hz}$, so that it does not cause any inconvenience for the DIAL system but enables higher average output powers.

The control of the laser power is similar to the method of the *IBL* laser. The delay times of the laser diode pulses relative to each other are altered, while the pulse durations stay at fixed values. The pulses of the laser diodes in the two pump chambers of the oscillator are triggered at the same time. The time delay of all other trigger signals is relative to this point. To power the laser up, first, the delay time of the Q-switch trigger signal is reduced. Then, the delay time of one of the amplifier's pump chamber is decreased, and finally, also the delay time of the last pump chamber is decreased. The maximum output power is reached at $t_{Qsw} = 70\,\mu\mathrm{s}$, $t_{amp,1} = 30\,\mu\mathrm{s}$, $t_{amp,2} = 20\,\mu\mathrm{s}$. In contrast to the *IBL* laser, here, the delay time values can only be changed gradually by the end user, and the values of the pulse duration cannot be accessed

---

[26] rack unit: $1\mathrm{U} \mathrel{\widehat{=}} 1.75\,\mathrm{inches} = 44.45\,\mathrm{mm}$

[27] *Termotek*, P330

at all (are known to the manufacturer only). The amount of power that is effectively sent out and directed to the Ti:sapphire laser, is ultimately regulated by the aforementioned motorized polarization rotator.

Turned up to full output power, the *PLA* laser originally delivered over $P_{532} = 60\,\mathrm{W}$ ($E_{532} = 200\,\mathrm{mJ}$) at $532\,\mathrm{nm}$ with a residual infrared (IR) power of $P_{1064,res} = 50\,\mathrm{W}$ ($E_{1064,res} = 167\,\mathrm{mJ}$), and thus an original fundamental power (before the SHG) of $P_{1064,tot} = 110\,\mathrm{W}$ ($E_{1064,tot} = 367\,\mathrm{mJ}$). The highest power values obtained with the *PLA* laser were around $P_{532} = 63.2\,\mathrm{W}$ ($E_{532} = 211\,\mathrm{mJ}$) with an original fundamental power of $P_{1064,tot} = 116.8\,\mathrm{W}$ ($E_{1064,tot} = 389\,\mathrm{mJ}$). Again, the precise value depends on conditions which were already discussed in Section 3.2.2. The pump power values stated here refer to the *Standa* power meter that is installed in the *PLA* laser, except otherwise noted. By comparing the measured values to the measurement of other power meters[28,29], a measurement uncertainty of $5\,\%$ has been established, being a little above the value specified by the manufacturer. With a newly acquired power meter[30] values close to the *Standa* power meter have been measured, thus, confirming its use.

The efficiency of the second harmonic generation at full output power is $\eta_{SHG} \approx 54\,\%$. When comparing the conversion efficiency of the *PLA* laser and the *IBL* laser, different values of the original IR power have to be borne in mind, due to the nonlinearity of the conversion process. The higher efficiency of the *PLA* laser is therefore mainly attributed to its higher output power. For a direct comparison, the laser power can be set as close as possible to the full output power value of the *IBL* laser ($P_{532} = 43\,\mathrm{W}$), within the bounds of the software control possibilities. At the measured powers of $P_{532} = 43.8\,\mathrm{W}$ and $P_{1064,res} = 56.9\,\mathrm{W}$ the efficiency is $\eta_{SHG} \approx 43\,\%$. This is lower than the SHG conversion efficiency of the *IBL* laser. To pump the Ti:sapphire laser usually a setting of the *PLA* laser was chosen, at which it does not operate at its maximum, but at which still more power is available than necessary. The reasons for this were to take care of the laser's condition and to avoid wasting resources. At this setting, the output power is $P_{532} \approx 57\,\mathrm{W}$, the residual IR power $P_{1064,res} \approx 48\,\mathrm{W}$, and the conversion efficiency $\eta_{SHG} \approx 54\,\%$.

To analyze the long-term behavior of the laser power, the three power values $P_{532,p}$, $P_{532,s}$, and $P_{1064,res}$ were simultaneously measured. The motorized polarization rotator was set in such a way that the most part ($\approx 80\,\%$) of the output power at $532\,\mathrm{nm}$ was sent out of the laser, where it was logged with the *Coherent* power meter. The values of the internal power meters were logged on a regular basis with the *PLA* laser software, but also manually, to acquire the full measurement precision. In this way, all the further characterizing parameters mentioned in Section 3.3.1 can be obtained. The measurement was started right after the laser was completely powered up and lasted over $6\,\mathrm{hours}$.

In Figure 3.9, the measured quantities and the deduced parameters $P_{1064,tot}$, η_{SHG}, and S_1 are plotted. The powers in the green ($P_{532,p}$ and $P_{532,s}$) show similar behavior. They remain almost constant. Towards the end of the measurement period a slight decrease is observed. The residual infrared power of the frequency conversion process ($P_{1064,res}$) changes more markedly. It rises

---

[28] *Ophir*, FL250-RP-v1 with VEGA (P/N: 7Z01560)

[29] *Coherent*, LM100-HTD with FieldMax TOP

[30] *Ophir*, FL250A-BB-55-PPS with NovaII

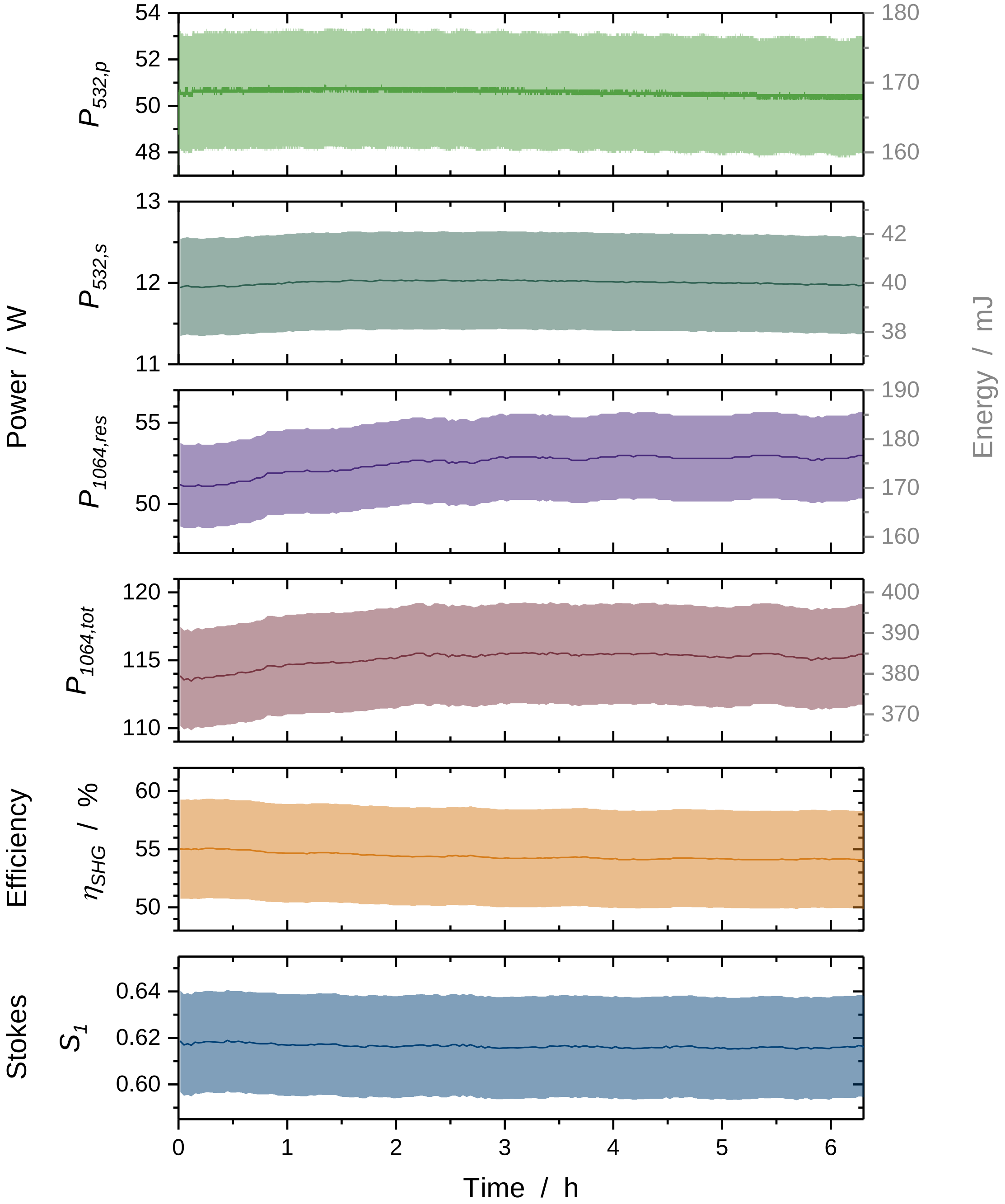

Figure 3.9: Analysis of the power behavior of the *PLA* pump laser for a 6 hours-operation period. The powers $P_{532,p}$, $P_{532,s}$, and $P_{1064,res}$ (upper three panels) have been measured. From this, the power $P_{1064,tot}$, the conversion efficiency η_{SHG}, and the Stokes vector parameter S_1 (lower three panels) have been calculated. The filled area of the curves represents the uncertainty of the corresponding parameter.

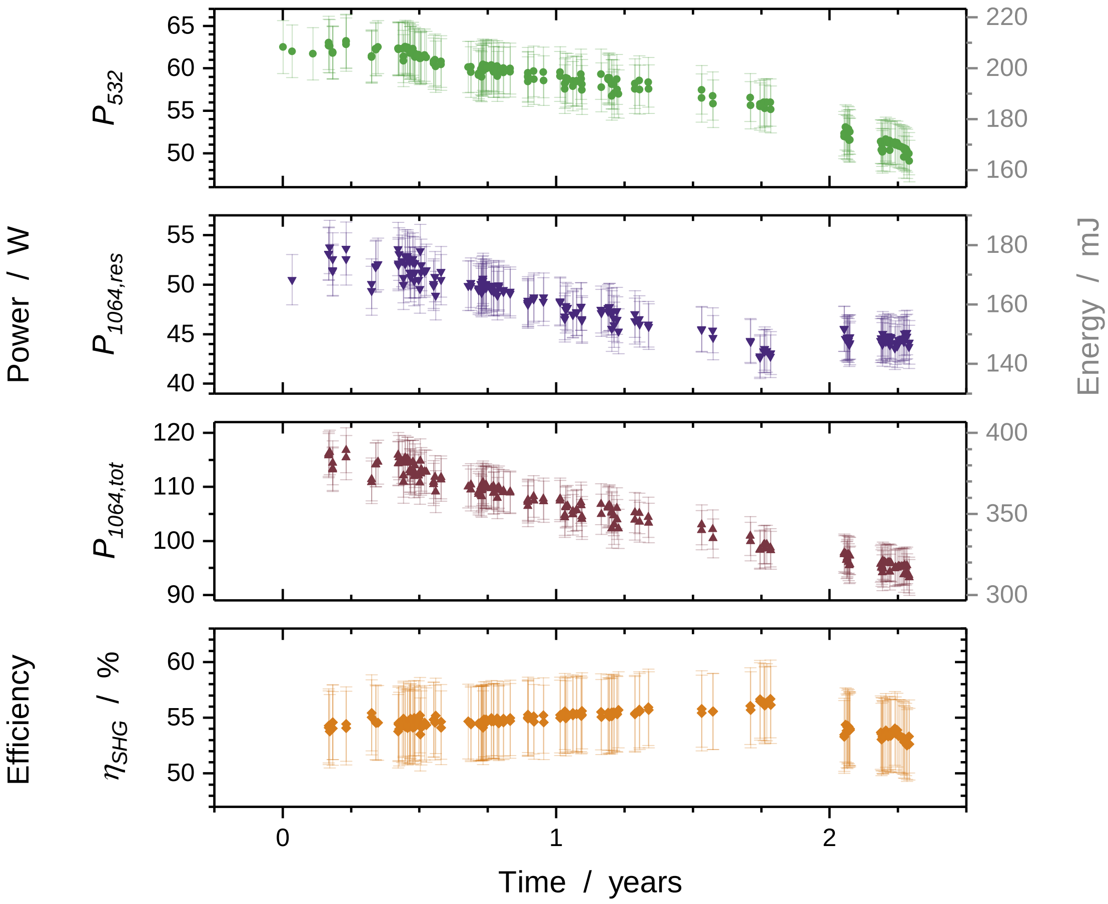

Figure 3.10: Evaluation of maximum power performance of the *PLA* pump laser over the years. The parameters P_{532} and $P_{1064,res}$ were measured. From these, $P_{1064,tot}$ and η_{SHG} were calculated. The total laser power decreased constantly. From the second year on, additionally, the SHG efficiency degraded.

particularly within the first two hours. In sum, the total fundamental power ($P_{1064,tot}$) increases, akin to $P_{1064,res}$. Hence, there is a general warm-up process that influences the MOPA's performance. As the plot for η_{SHG} reveals, the second harmonic generation becomes less efficient for longer operation. This contrasts with the increase of the total laser power but has a stronger effect. Consequently, the fairly constant behavior of the powers at $532\,\mathrm{nm}$ with the lessening at the end can be explained. No significant change is visible for the Stokes parameter S_1, demonstrating a constant polarization for the $532\,\mathrm{nm}$-radiation behind the SHG, and allowing for a deduction of $P_{532,p}$ from $P_{532,s}$. In conclusion, most important for pumping the Ti:sapphire laser is the power stability of the *PLA* laser. During long-term operation, it experienced a decrease of $1\,\%$ to $3\,\%$ in the pump power.

Over the past few years, the maximum output power declined also for the *PLA* laser. The regular measurement of both, P_{532} and $P_{1064,res}$, allowed to determine $P_{1064,tot}$ as well as η_{SHG}

(see Figure 3.10). As a result, it was found that the decrease originates from a drop of the total power of the laser, whereas the frequency-doubling efficiency was nearly stable with a slight tendency to increase. Only during the second year, after a longer overseas transport to a field campaign site, the SHG seems to have been affected. Responsible for the decrease of the total laser power, $P_{1064,tot}$, could be a disadjustment of the oscillator, or a deterioration of the laser diodes in the pump chambers. Meanwhile, the maximum available output power for pumping is $P_{532} \approx 50\,\mathrm{W}$, still being more than what is necessary for the Ti:sapphire laser. A verification of the *PLA* laser adjustment and checking its SHG crystal might regain a better performance.

The pulse properties are quite similar to the *IBL* laser and have been determined in the same manner. The shape of the pulse again resembles a Gaussian function, superimposed with beat notes. The fast Fourier transform of the pulse signal now yielded $\Delta\nu_{FSR} = (184.5 \pm 2.5)\,\mathrm{MHz}$ for the free spectral range of the resonator. For a linear resonator, the relationship with the (optical) resonator length is

$$\Delta\nu_{FSR} = \frac{c}{2\,L}\,, \tag{3.8}$$

so that follows $L = (812 \pm 12)\,\mathrm{mm}$. As expected, the geometrical length of the resonator is smaller than the optical length, $L_{geo} = (625 \pm 20)\,\mathrm{mm}$. The pulse properties were measured at the parameter setting of the *PLA* laser which is used for pumping the Ti:sapphire laser. At the time of the measurement and for this setting, the entire power at $532\,\mathrm{nm}$ was $P = (51.8 \pm 2.6)\,\mathrm{W}$, and the pulse energy $E = (173 \pm 9)\,\mathrm{mJ}$. A pulse length (FWHM) of $\Delta t = (14 \pm 2)\,\mathrm{ns}$ was measured, and from this a peak power of $\hat{P} = (12.3 \pm 1.9)\,\mathrm{MW}$ results. The pulse-to-pulse energy stability was measured with respect to the trigger signal of the oscillator's pump chambers. For samples of 1000 pulses, the standard deviation of the pulse area was divided by its mean value. This lead to values of $\Delta E = 2.4\,\%$ to $3.8\,\%$. The time jitter of the pulse emission was measured, too. The difference between the shortest and the longest delay time was found to be $t_{max} - t_{min} \approx 25\,\mathrm{ns}$.

With the power-distribution-and-measurement arrangement inside the *PLA* laser, on the one hand, a linear polarization is already ensured by the thin-film polarizer, on the other hand, the ratio of linear polarization of the output beam is easily measured. The power was distributed such that it was maximum on the internal power meter, $P_{532,s} = (52.5 \pm 2.7)\,\mathrm{W} > 49.7\,\mathrm{W}$. Then, the residual exiting power was measured with a sensitive power meter[31], $P_{532,p} = (148 \pm 20)\,\mu\mathrm{W} < 200\,\mu\mathrm{W}$. Hence, the ratio of linear polarization was $\gg 99.9\,\%$.

3.3.3 Beam Quality and Propagation

Another major progress for the pump source of the Ti:sapphire laser consists of the *PLA* laser's beam quality. The aim of the development was to attain a top-hat beam profile, and this was largely realized, as will be demonstrated below. Figure 3.11 depicts the beam profile of the $532\,\mathrm{nm}$-laser radiation at the power setting for pumping the Ti:sapphire laser ($P_{532} \approx 55\,\mathrm{W}$). The monitoring camera[32] was placed behind a highly reflective bending mirror at a distance of $z = (443 \pm 10)\,\mathrm{mm}$ from the exit aperture of the laser case (camera at bottom right in Figure 3.8). The intensity distribution can be described as a combination of a Gaussian and

---

[31] see footnote 23 on page 69

[32] see footnote 5 on page 30

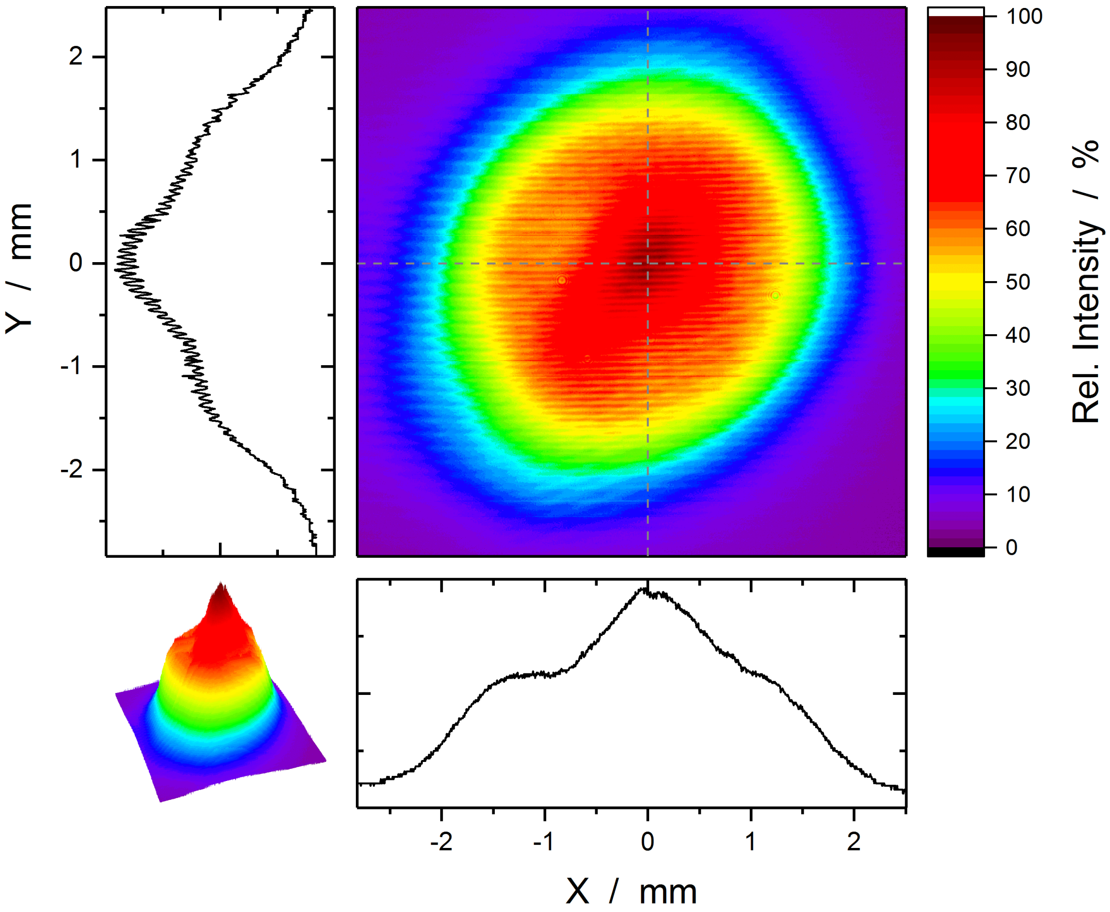

Figure 3.11: Beam profile of the *PLA* laser, at a distance $z = (443 \pm 10)\,\mathrm{mm}$ from the laser exit aperture, and for the operation setting $P_{532} \approx 55\,\mathrm{W}$. The intensity distribution is a kind of (assorted) higher-order Gaussian function(s). Due to electromagnetic interference there were horizontal lines scrolling through the image (notable also in the y-cross section); this is an artifact of the camera, not a feature of the beam.

a top-hat beam profile. It is predominately homogenous, but has a tapered intensity rise in the middle. The evaluated[33] mean 2σ-beam radius is $w = 1.8\,\mathrm{mm}$. The beam has a circular symmetry with a moderate ellipticity (roundness 0.77). It is understood that no hot spots exist in the beam profile. Although at this location the profile differs from an ideal top-hat, this changes when the beam is focused (see next section).

Analogous to the *IBL* laser, for output powers $P_{532,p} \gtrsim 8\,\mathrm{W}$, the change of the intensity distribution of the *PLA* laser beam is marginal. It was found that the diameter of the beam varies a little; when powering the laser up from 57 W to 62 W, the diameter increased by $\approx 5\,\%$. This is convenient, as it somehow relieves the concomitant rise of power density ($\mathrm{W/cm^2}$). Likewise,

---

[33] *TU Berlin*, Beam Analyser (v1.5)

when laser operation lasted more than a few hours, a small, but nonessential transformation of the beam profile was observed. The asymmetrical and inhomogeneous parts of the beam profile then tend to be more accentuated.

From an M^2 analysis[34] of the beam, the values $M_x^2 = 26$ and $M_y^2 = 29$ were obtained. The resulting beam waists (radii) from the analysis were $w_{0,x} = 1.72\,\mathrm{mm}$ and $w_{0,y} = 1.84\,\mathrm{mm}$. The divergences (half angle) were $\theta_x = 2.6\,\mathrm{mrad}$ and $\theta_y = 2.7\,\mathrm{mrad}$. The high experimental M^2 values can be attributed to the fact that for a top-hat beam profile in theory the M^2 factor is infinite, as discussed in Section 3.1. The beam waists are comparable to the results of the *IBL* laser. In contrast, the beam divergences of the *PLA* laser are huge. This presumably originates from the adjustment of the beam adapting lenses right in front of the frequency conversion. The high divergence indicates, that for the mode matching of the beam to the Ti:sapphire laser mode, one lens is not sufficient.

3.3.4 Mode Matching for Ti:sapphire Laser

Primary goal of the beam adaption of the *PLA* laser is the accordance of the pump beam with the beam of Ti:sapphire laser at its crystal end-surfaces. Beyond that, the pump beam should remain reasonably constant along its propagation through the laser crystal, i.e., have a Rayleigh length much larger than the crystal length. The beam radius of the pump laser is chosen to be slightly bigger than the Ti:sapphire laser beam radius. This is supported by the consideration of the top-hat beam profile, thermal effects, and meanwhile, the possibility of pumping with substantial higher powers.

Initially, it was attempted to achieve the desired beam adaption with one lens, just like for the *IBL* laser. However, a suitable lens could not be identified. Either the focal length of the lens was too large to scale down the pump beam to the requested size of $w_{pump} \approx 0.9\,\mathrm{mm}$, or it was too short to produce the focal plane within the distance required for placing the lens inside of the Ti:sapphire laser setup. In addition, the lenses with short focal lengths generated a caustic with a significant change of the beam width over small propagation distances, i.e., with a short Rayleigh length z_R. The high divergence of the original laser beam impedes the generation of small beam sizes at large distances. Thus, it is not possible to mode-match the *PLA* laser beam with only one lens.

By using a pair of lenses, the beam adaption capabilities are much more comprehensive. Knowing the initial beam parameters, the parameters that the beam shall be transformed into, and some boundary conditions, the focal lengths of the lenses can be determined. The formalism of Gaussian beam propagation (see Chapter 5.2) through a lens with consideration of the M^2 factor is suited for the calculation [101, 102]. A boundary condition for the calculation is the separation distance of the two lenses. Furthermore, it has to be considered at which distance from the Ti:sapphire crystal the telescope has to be placed and the space that is required. As telescope layout the Galileo design (one concave and one convex lens) is preferred. In contrast to the Kepler design (two convex lenses), it is more compact and does not run the risk of creating a focal point of very high energy density between the two lenses. It is important to take the beam quality factor M^2 into consideration, since the beam profile is a top-hat, and its propagation

---

[34] *Ophir / Spiricon*, M^2-200s (Accuracy $\pm 5\,\%$ typical, $\pm 12\,\%$ waist location and Rayleigh length typical)

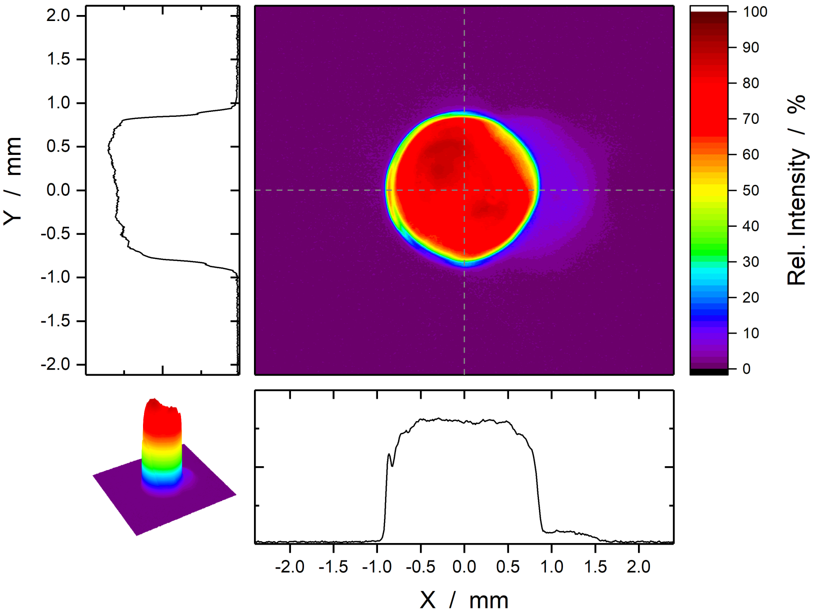

Figure 3.12: Beam profile of the *PLA* pump laser after adaption with a beam-reducing pair of lenses. The *PLA* laser was operated in the setting with $P_{532} \approx 55\,\mathrm{W}$, being the configuration that is used to pump the Ti:sapphire laser crystal (with a fraction $P_{532,p}$ of this power). The image was captured at a distance behind the lenses which corresponds to the crystal's location. A ghosting effect is perceived to the right of the beam profile and originates from a reflection at the back surface of the auxiliary bending mirror for the measurement.

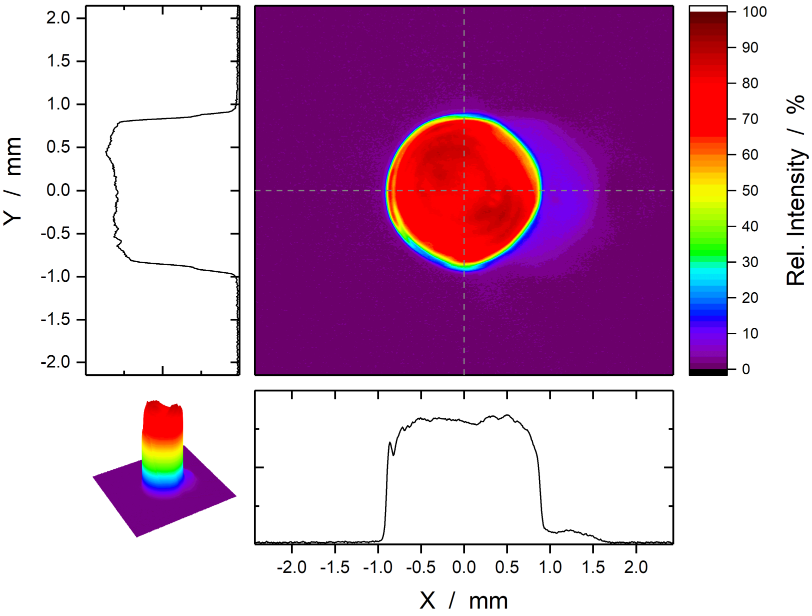

Figure 3.13: Same as Figure 3.12, but for an operation power setting of $P_{532} \approx 62\,\mathrm{W}$.

differs strongly from a Gaussian beam.

A solution with very good experimental feasibility was found for the following configuration. The focal lengths for the first[35] and the second lens[36] are $f_1 = -84\,\mathrm{mm}$ and $f_2 = +112\,\mathrm{mm}$, respectively. Both lenses are separated by a distance of $l_{12} = (55 \pm 1)\,\mathrm{mm}$ and placed at a distance of $z = (712 \pm 5)\,\mathrm{mm}$ from the Ti:sapphire crystal, or $z = (818 \pm 7)\,\mathrm{mm}$ from the exit aperture of the *PLA* laser. Interestingly, the sequence of arrangement of the lenses is reverse as expected from geometrical optics and common beam reducers, where the concave lens follows after the convex lens. Yet, only with this configuration the correct beam adaption was obtained.

In the experiment, the telescope is adjusted in such a way that the waist of the generated caustic is situated on the end-surfaces of the Ti:sapphire crystal. From there on, (i.e., inside the crystal and behind) the pump beam propagates with its beam width becoming only larger. This provides the advantage that any unintended, further concentration of energy afterwards is avoided. Figures 3.12 and 3.13 show the beam profile at the crystal end-surface for a power setting of $P_{532} \approx 55\,\mathrm{W}$ and $P_{532} \approx 62\,\mathrm{W}$, respectively. They demonstrate that the intensity distribution is nicely represented by a top-hat profile, where at full power operation the profile is even closer to theory. The respective 2σ-beam radii were measured[37,38] to be $w_{pump} = 0.94\,\mathrm{mm}$ and $w_{pump} = 0.96\,\mathrm{mm}$, both having a roundness of 0.97. Here, by turning up to full power the radius increased by $\approx 3\,\%$.

The M^2 analysis of the adapted beam behind the telescope at $P_{532} \approx 55\,\mathrm{W}$ delivered the values $w_{0,x} = 0.83\,\mathrm{mm}$ and $w_{0,y} = 0.78\,\mathrm{mm}$ for the radii at the beam waist, $\theta_x = 6.2\,\mathrm{mrad}$ and $\theta_y = 5.9\,\mathrm{mrad}$ for the half angle divergence, as well as $M_x^2 = 30$ and $M_y^2 = 27$. It is noticeable, that the values for the beam waist and the beam quality are a little different to the previously mentioned w_{pump} and M^2, although they are still in the same order of magnitude. An explanation could be, that the M^2-device's accuracy may be reduced for such higher-order transverse beam modes.

Concerning the pointing stability of the beam profile at the crystal surface, a measurement over a time period of $2\,\mathrm{hours}$ was executed at the usual power setting. The overall-movement of the intensity centroid was $\Delta x < 0.01\,\mathrm{mm}$ and $\Delta y < 0.02\,\mathrm{mm}$, corresponding to $\approx 1\,\%$ and $\approx 2\,\%$ of the beam radius, respectively. While in the horizontal direction this was more like a random walk, in the vertical direction a drift upwards was recognized. The change of the distribution of the intensity was negligible.

3.3.5 Spectral Characteristics

As for the *IBL* laser, the frequency properties of the *PLA* laser were determined based on long-term measurements with the wavelength meter. Here, individual measurements of the $1064\,\mathrm{nm}$- and the $532\,\mathrm{nm}$-radiation were performed. The (residual) infrared radiation was analyzed for a time period of $5\,\mathrm{hours}$ (see Figure 3.14) with the laser running at full output power. The measurement started with a wavelength at $\lambda_{vac} \approx 1064.440\,\mathrm{nm}$. Together with the warm-up

---

[35] *Laser Components*, AR/AR1064+532 PLCC-25.4/38.6UV ($f_{nom} = -75\,\mathrm{mm}$)

[36] *Laser Components*, AR/AR532 PLCC-25.4/51.5UV ($f_{nom} = +100\,\mathrm{mm}$)

[37] *Pulnix*, TM-7EX/CN

[38] see footnote 17 on page 38

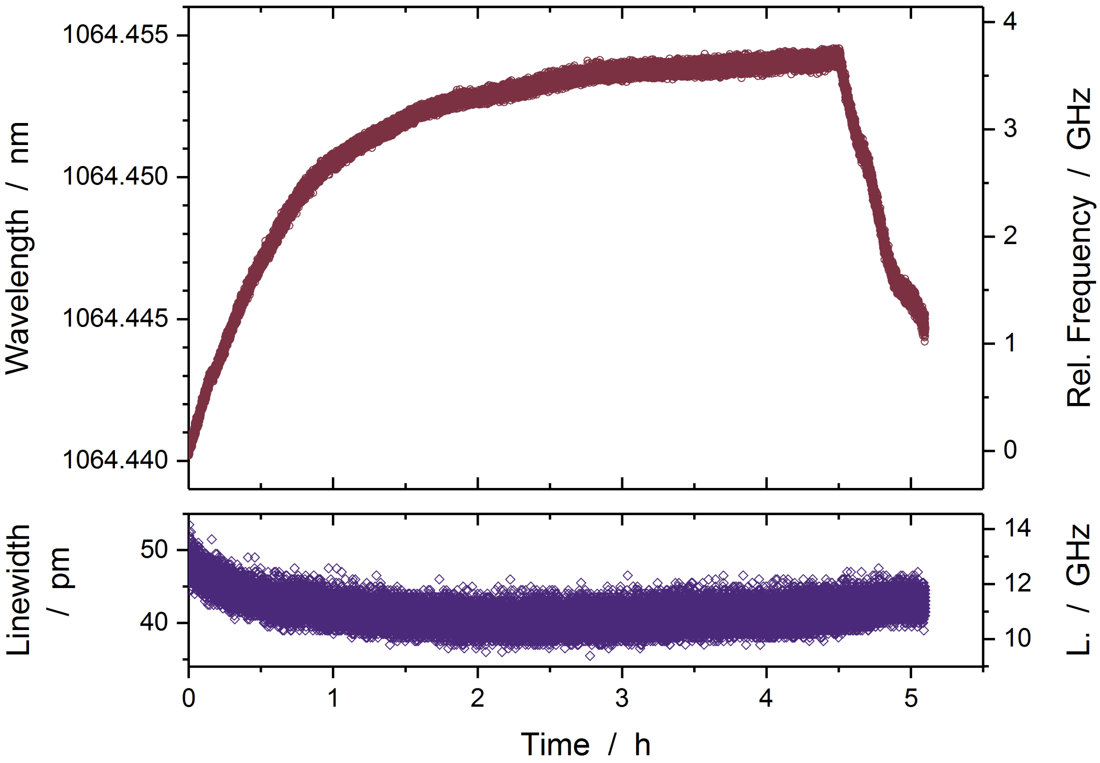

Figure 3.14: Wavelength and linewidth behavior of the *PLA* laser for a long-term measurement of the residual infrared radiation. In the beginning, a drift, attributed to a warm-up of the laser, was present. At 4.5 hours, the laser case was opened, resulting in a release of the accumulated heat and a drift backwards. The laser operated at full output power.

procedure of the laser, the wavelength drifted away from this value, especially during the first hours. After $4.5\,\mathrm{hours}$ of measurement, the wavelength was $\lambda_{vac} \approx 1064.454\,\mathrm{nm}$. Thus, the total wavelength drift was $\delta\lambda \approx 14\,\mathrm{pm}$ or $\delta\nu \approx 3.7\,\mathrm{GHz}$. A warm-up phase was also observed for the linewidth. Then, it settled down to a value of $\Delta\lambda = (42 \pm 3)\,\mathrm{pm}$ or $\Delta\nu = (11 \pm 1)\,\mathrm{GHz}$. It has to be pointed out, that for the last $36\,\mathrm{minutes}$ of the long-term measurement the cover of the laser case was removed. This was done intentionally to investigate the consequence of the removal of accumulated heat and increased air swirling. As can be seen in the figure, the wavelength drift is reversed by the action, and the drift runs faster, too. The cause for the gradual deviation of the wavelength can be challenging to identify. Presumably, the source is to be found in the oscillator of the *PLA* laser, but the specific component is unknown. The quick change after opening the cover suggests that the thermal effect might be related to a disadjustment of the resonator mirrors. In contrast, the laser crystals are precisely temperature-controlled by the water cooler ($\Delta T = 0.1\,\mathrm{K}$).

The wavelength meter measurement for the frequency-doubled radiation showed the following results. In order to investigate the behavior of the equilibrated state of the laser (without a drift caused by thermal effects) more closely, the measurement was started after the laser had

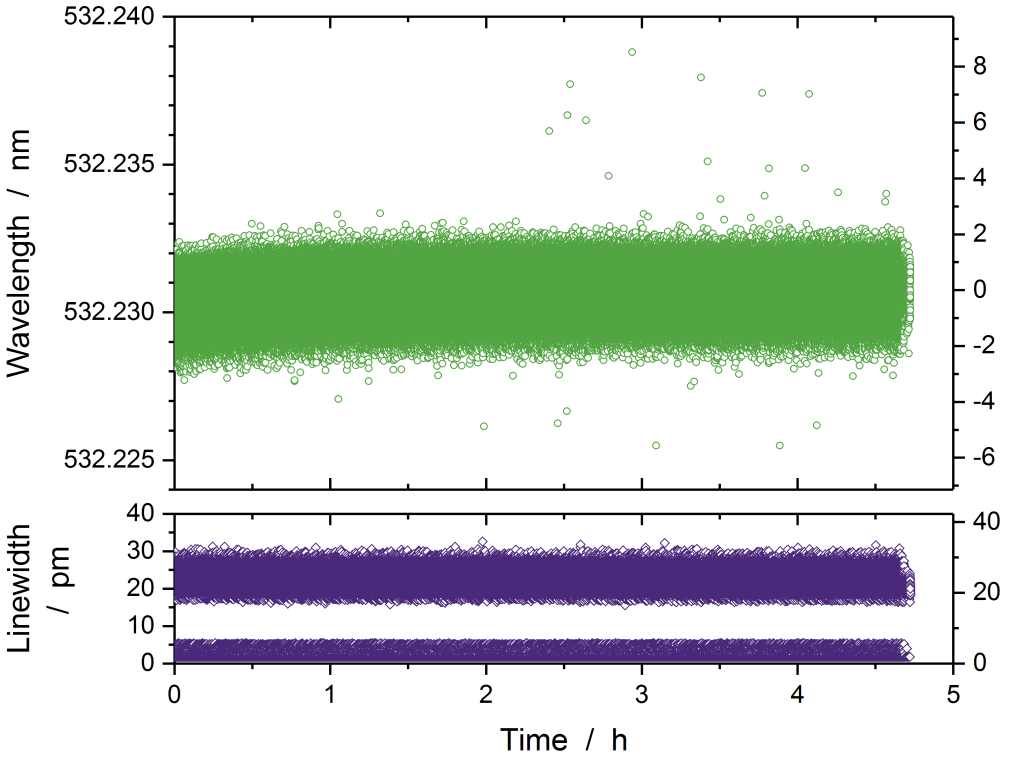

Figure 3.15: Wavelength and linewidth measurement of the *PLA* laser's $532\,\mathrm{nm}$-radiation. The laser was turned on three hours before. A minor remaining drift due to the warm-up phase was present in the first hour. The linewidth graph shows that broad- and narrowband laser pulses appeared.

been operating already for three hours. Figure 3.15 shows this measurement which almost lasted $5\,\mathrm{hours}$. At the beginning, a small drift of the wavelength could still be noticed. Apart from that, the laser pulses gathered around the mean value of $\lambda_{vac} = 532.2308\,\mathrm{nm}$. The standard deviation from this mean value was $\delta\lambda = 0.526\,\mathrm{pm}$ or $\delta\nu = 557\,\mathrm{MHz}$. However, the figure demonstrates that the vast majority of laser pulses occur within $\delta\lambda \approx \pm 2\,\mathrm{pm}$ or $\delta\nu \approx \pm 2.1\,\mathrm{GHz}$. From all measured laser pulses (in total $5\,216\,254$), less than $1.5\,\%$ were outside the range from $531\,\mathrm{nm}$ to $533\,\mathrm{nm}$ (mainly located around $534.6\,\mathrm{nm}$). These pulses were excluded from the statistics, as it was assumed that they were misinterpreted or underexposed interference patterns of the wavelength meter. The values for the linewidth lied below $\Delta\lambda = 35\,\mathrm{pm}$ or $\Delta\nu = 37\,\mathrm{GHz}$. Some pulses occurred with a much lower linewidth, indicating that the laser was partially operating in a narrowband mode. Again, it should be remembered that these values exceed the specified maximum bandwidth limit of the wavelength meter and should not be regarded as completely reliable.

To improve these spectral characteristics, the oscillator of *PLA* laser could be injection seeded and actively stabilized. In doing so, even single-frequency operation could be achieved. According to the time–bandwidth product (Equation 2.15) and the measured pulse width of

$\Delta t = (14 \pm 2)\,\mathrm{ns}$, the narrowest possible bandwidth would then be $\Delta\nu = (32 \pm 5)\,\mathrm{MHz}$ at $\lambda = 532\,\mathrm{nm}$.

CHAPTER **4**

Injection Seeders

In the Ti:sapphire laser system of the Hohenheim-DIAL, the frequency behavior is substantially controlled by injection seeding. The technique of injection seeding has proven to be very effective and reliable when it comes to precisely selecting the wavelength of operation and to narrowing the emission bandwidth of pulsed lasers or optical parametric oscillators (OPO), see e.g., [103–111]. In combination with an active resonator stabilization of the pulsed laser, it is possible to obtain single-frequency operation (see references in Chapter 5.6.2). In fact, only since the application of injection seeding in laser transmitters, did DIAL become a feasible lidar method [43].

As differential absorption lidar requires the operation at two wavelengths, the question arises whether to use two independent sources for seeding, or one source emitting alternately at two frequencies. For the system described in this thesis, two independent seed sources are used, for various reasons. Depending on the laser type, the frequency tuning or modulation range of one laser is limited and typically below the spectral distance of the chosen online and offline wavelengths. Disregarding this limit, a potentially necessary stabilization of the seeder's frequency may be more complex, when the laser switches between two wavelengths. Generally, two independent lasers provide more flexibility and tuning capabilities. A conceivable scenario in which the offline frequency stays at a fixed value while the online frequency is tuned (e.g., with a triangle signal as described in Chapter 6.2.2) is easily realized. In terms of risk of failure, using two seed sources can be an advantage. A failure of one of the lasers does not automatically mean a complete failure of the injection seeding, and hence of the frequency control of the DIAL. With one remaining seed source, an emergency operation is still possible (for instance, with an alternately online-seeded and unseeded laser transmitter). This is important when repairing or exchanging the damaged seed source would take too much time, e.g., during intensive observation periods of a field campaign, or even impossible, as in satellites. A drawback of two independent seed sources might consist in higher expenses and additional amount of space. In any case, an adequate instrumentation to switch between the two wavelengths is necessary as well.

In the course of time, the injection seeding system of the Hohenheim-DIAL was subject to continued development. Originally having been developed at the *DLR* [112] and applied in the DIAL transmitter before 2010, the first major change was the substitution of the prior external-cavity diode lasers (ECDL) by distributed-feedback (DFB) laser diodes [113]. Simultaneously, the feasibility of an electro-optic deflector as online–offline switch was investigated. In this work, more changes with even major effects were performed. They consist, among other things, in the replacement of the DFB lasers with next-generation ECDLs, and the implementation of a more precise stabilization concept with versatile tuning capabilities. These changes led to an extensive improvement of the injection seeding system and represent one of the key achievements of this work.

This chapter is organized as follows. In the first section, a brief review of injection seeding theory is given. The setup of the seeding system is presented in the second section. Then, the components are treated in detail in separate sections. The frequency reference and control concept is explained in the third section. The fourth section deals with the diode lasers, and the fifth section with the online–offline switch. In an additional section, the power budget for the whole injection seeding path is analyzed. The last section describes how the mode matching to the Ti:sapphire laser is accomplished.

4.1 Theory of Injection Seeding

Injection seeding describes a technique where the beam of a laser with low power, but favorable spectral characteristics is coupled into the resonator of a laser with a comparatively high power but moderate spectral performance. The first laser is termed seed laser or master laser, while the second is referred to as power oscillator or slave laser. Usually, the power oscillator is a pulsed laser that is seeded with a continuous-wave laser (albeit other configurations exist). By injecting the output of the seed laser into the power oscillator, the laser action evolves from the seeded longitudinal mode, in contrast to the natural laser evolution which grows from vacuum or spontaneous emission. Eventually, the laser operation of the power oscillator will be at the seed laser mode, or, if the condition for resonance at this mode is not met, at the longitudinal mode(s) that are closest. Thus, through the master laser, a frequency control of the slave laser is achieved.

The number of excited longitudinal modes, the resulting laser bandwidth, and the spectral purity (i.e., the ratio between the laser output at the seed frequency and the total generated laser output including frequencies not corresponding to the seed laser) are properties that express the accomplishment of the seeding. They depend on the spectral properties of the master laser itself, the fulfillment of longitudinal resonance in the oscillator, but also on a certain effectiveness of injection. N. P. BARNES and J. C. BARNES formulated the concept of an injection seeding threshold [114]. It is defined by parameters that attribute to the coupling of the seed into the resonator of the slave laser combined with the injected power. Coupling parameters of the modes are the width and the location (both longitudinally and transversely) of the beam waist, as well as the direction of propagation. In [31], the power that is required for injection seeding of the Hohenheim-DIAL transmitter was determined based on modified rate equation modeling.

Last, it should be noted that the term injection locking is also mentioned in the literature, however, different definitions are used. On the one hand, it is used, when both master and slave laser have a continuous-wave emission, and the slave laser potentially also retroacts on the master laser [58, 85]. On the other hand, in [114] it describes “instances where the seed pulse

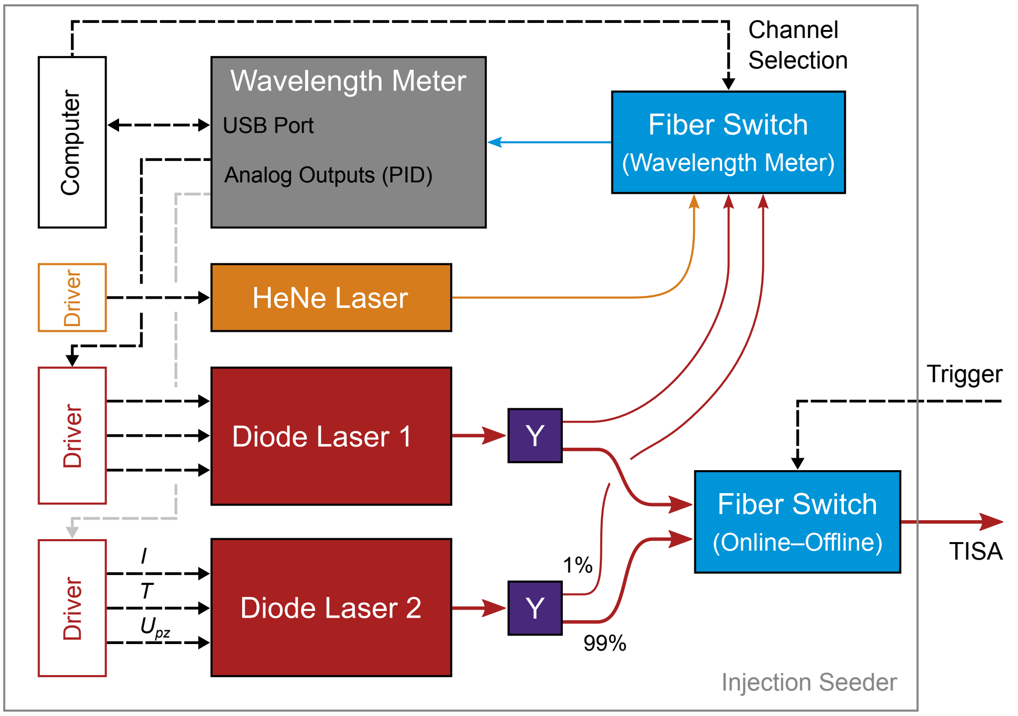

Figure 4.1: Setup of the injection seeding system for the laser transmitter. The image shows the situation for the new stabilization concept, where the feedback loop to the diode lasers is realized with the analog output signal of the wavelength meter. Solid arrow lines symbolize waveguided laser beams. Dashed lines indicate electrical connections. The grayed-out connection will be implemented in the future. Y – bifurcated fiber (with output power ratio), I, T, U_{pz} – regulation of diode laser current, temperature, and voltage (for ECDL-piezo actuator), respectively.

exactly matches the frequency of the resonant mode" (p. 2676), and thus indicates a single-frequency operation of the power oscillator. In this work, the latter definition is used.

4.2 Setup of the Seeding System

An overview of the injection seeding system is given in Figure 4.1. The single components are presented in detail in the following sections of this chapter. Two independent diode lasers are the seed sources of the system. The specific type of diode lasers applied are described in Section 4.4. The diode lasers include a temperature stabilization, an optical isolator, and a fiber coupler. With corresponding drivers, the current, the temperature, and the piezo voltage (if available) are controlled. The laser light is coupled in each case into a bifurcated fiber[1] (also designated as Y-fiber) that splits the light with a power ratio of 99:1. The output with the main part of the power is connected to a 2-to-1 fiber switch. The fiber switch selects between the inputs of the two diode lasers and only transmits the light of one of them. Thus, it takes the

---

[1] *Evanescent Optics*, 954PS

role of the online–offline switch (see Section 4.5). The output of the switch is connected to a $5\,\mathrm{m}$-long fiber[2] that guides the seed laser light to the setup of the Ti:sapphire laser.

Information about the operation frequencies of the diode lasers is obtained from a wavelength meter. For this, the minor part of laser power ($1\,\%$) from the Y-fiber is directed for both diode lasers to a 4-to-1 fiber switch[3]. The output of this switch is connected via a mating sleeve and a singlemode fiber[4] to the wavelength meter. A third input of the fiber switch is utilized for a frequency-stabilized helium–neon laser. This laser is needed to regularly calibrate the wavelength meter, hence, acting as frequency reference. The remaining fourth input of the fiber switch is currently not used. Wavelength meter and fiber switch are controlled from a computer. The computer includes a PCI card[5] which sends a signal to the 4-to-1 fiber switch in order to select the fiber input channel transmitted to the wavelength meter.

By monitoring with the wavelength meter, it is not only possible to determine the operation frequencies, but also to give feedback to the diode lasers. The communication with the diode laser drivers is performed either via the computer, or directly from the wavelength meter. This way, a feedback loop to control the frequencies of the diode lasers is realized. The frequency reference and control procedure is explicitly detailed in the following section.

In the setup, all fiber components and cables guiding the essential power fraction for seeding are polarization maintaining. This is mandatory, as in the path of the seeder beam at the Ti:sapphire laser setup, polarization selective elements are available (Section 4.7). The paths that conduct the power fraction for monitoring comprise standard singlemode fibers and components. Likewise, all fiber ends have FC/APC connectors, except for some special cases (e.g., the wavelength meter input stipulates a FC/PC connector).

The injection seeding system is housed in two identical 19-inch racks[6] with $0.5\,\mathrm{m}$ height and $0.8\,\mathrm{m}$ depth. To isolate the optical instruments from vibrations, they are mounted on a damped optical table and are kept separately from the electronics. The space of one rack is occupied by the diode laser drivers and the computer. The optical table with the instruments and the remaining electronic parts (e.g., the HeNe laser driver) are installed in the second rack.

4.3 Frequency Reference and Control

The adherence of the frequency specifications of the laser transmitter is vital for differential absorption lidar, as already pointed out before. The relative change of frequency might be paramount, but also the absolute frequency value is important. While the frequency stability affects the precision of the determined atmospheric variable, the absolute values have influence on the accuracy of the measurement. Thus, especially for the online frequency, it is necessary to know exactly at which position of a (water-vapor) absorption line the laser is set.

The absorption lines of water vapor vary depending on the conditions of the atmosphere (temperature, pressure, etc). Therefore, the precise control and knowledge of the laser frequency

---

[2] *OZ Optics*, PMJ-3A3A-850-5/125-3A-5-1

[3] *Sercalo Microtechnology*, SN-1x4-4N

[4] *Nufern*, 780HP (FC/APC–FC/PC)

[5] *National Instruments*, PCI-6221-37

[6] *Knürr*, DoubleProRack 9HE T800 1.243.809.1

alone, does not guarantee that the DIAL measurement is executed strictly at the calculated absorption line position. For this purpose, the absorption line of interest would have to be analyzed experimentally first, for instance, with a special DIAL measurement, where the online frequency is tuned over the absorption line (see Chapter 6.2.2). Nevertheless, even when the exact position on the absorption line is unknown, it is advised to determine the absolute value of the emission frequency of the transmitter as best as possible, since it is a basis parameter for all further DIAL evaluation.

In the laser transmitter of the Hohenheim-DIAL, the frequency control is realized via multiple instances. The Ti:sapphire oscillator acquires its frequency properties from the diode lasers of the injection seeding system. The diode lasers' frequency, in turn, is monitored and regulated by way of the wavelength meter. The wavelength meter, on the other hand, is calibrated with the helium–neon laser. The helium–neon laser represents the top of the frequency control procedure and marks the absolute frequency standard of the entire DIAL system. Together with the wavelength meter, it plays a crucial role for the adherence of the frequency requirements of the system. Obviously, all frequency control instances preceding the Ti:sapphire laser need at least to fulfill the stated requirements, or even exceed them.

4.3.1 Helium–Neon Laser

The helium–neon laser[7] employed in the injection seeding system utilizes a stabilization technique based on dual longitudinal mode comparison [115]. According to the manufacturer's device certificate, the emission frequency is $\nu = 473\,612\,516.0\,\mathrm{MHz}$ corresponding to a vacuum wavelength of $\lambda = 632.990\,995\,5\,\mathrm{nm}$. The laser features two operation modes: amplitude stabilizing or frequency stabilizing. The frequency-stabilized mode of operation is selected, providing a frequency stability of better than $\delta\nu = \pm 9.5\,\mathrm{MHz}$. The certificate also states that a warm-up time of approximately $30\,\mathrm{minutes}$ is required to achieve this performance. The output power of the HeNe laser is $P \approx 1\,\mathrm{mW}$ and is directly coupled into the fiber-end of one of the 4-to-1 fiber switch's inputs. During this work the laser had to be exchanged once due to end of lifetime. The lifetime of the laser tube is typically specified with $30\,000\,\mathrm{hours}$.

4.3.2 Wavelength Meter

The wavelength meter[8] of the seeding system is composed of Fizeau interferometers which are temperature controlled and do not contain any mechanically moving parts. Hereby, precise measurements of the wavelength are possible, specified by the manufacturer with an absolute accuracy of $60\,\mathrm{MHz}$ and a resolution (wavelength deviation sensitivity) of $10\,\mathrm{MHz}$ [116]. The calibration certificate of the device showed that the accuracy and precision were well below these specification limits.

To stay within these specifications, the wavelength meter has to be calibrated regularly. Although a time period of $\leq 14\,\mathrm{days}$ would conform with the manufacturer's statement, during field campaigns the calibration period is much more frequent. During intensive observation periods a calibration or a reference measurement with the HeNe laser was performed at least twice

---

[7] *SIOS Meßtechnik*, SL 03

[8] *HighFinesse / Ångstrom*, WS7 with Double-PID Laser Control option

a day. It was found that from the beginning to the end of a measurement day ($\approx 7\,\mathrm{hours}$) the HeNe laser frequency typically deviates by up to $\nu_{max} - \nu_{min} \approx 50\,\mathrm{MHz}$. This value constitutes the combined drift of HeNe laser and/or wavelength meter.

The wavelength meter is connected via a USB port to a computer, where it is controlled by the supplied software. The software provides an application programming interface, which enables directly reading out the measured wavelength in a self-developed program and process this information further to realize a feedback control of the diode laser's operation frequency. The method how it is actuated on the diode lasers is described in the next section.

The quality of the frequency control and stabilization of the diode lasers depends on the overall regulation speed, which is limited primarily by the diode laser drivers and by the data acquisition speed of the wavelength meter. For the DFB laser diodes, the communication between computer and diode laser drivers was performed with RS-232 interfaces. Obviously, the data rate of this interface is not very fast, hence, representing the bottleneck in the feedback control procedure. For this reason, in the course of the development of the injection seeding system, special emphasis was put on improving regulation speed.

The modernized concept includes analog output channels of the wavelength meter, which can be connected to the current or the piezo voltage modulation input of the ECDL drivers. Thus, the overall regulation speed is not limited by the transfer rate of the regulation signal and is predominantly given by the acquisition speed of the wavelength measurement. The manufacturer claims that the measurement speed (the data acquisition in conjunction with the wavelength calculation) is up to $400\,\mathrm{Hz}$, providing a strong computer hardware.

As the wavelength meter can measure only one laser at a time, the stabilization or generally the frequency control can only be (actively) performed during the measurement of the corresponding laser. When more than one laser source is to be involved in the control process, a suitable time distribution has to be chosen, to consecutively select all lasers with the 4-to-1 fiber switch. In this case, the response time of the fiber switch is negligible, because with $\approx 1\,\mathrm{ms}$ it lies below the measurement speed of the wavelength meter.

4.4 Diode Lasers

Diode lasers have ideal properties for injection seeding. Among the spectral properties, the advantages are single-frequency operation with narrow linewidth and good frequency stability (or at least feasible means by which it can be achieved), as well as frequency tuning capabilities. Besides, diode lasers are compact, robust, and belong to lasers with the highest wall-plug efficiency. With several tens of mW, the output power of diode lasers is sufficient for injection seeding. Still, it is important to consider the power losses on the path to the pulsed laser resonator, and for increasing operation power even more seed power is preferable.

As mentioned in the introduction of this chapter, the ongoing development of the seeding system comprised exchanging the diode lasers. Within the scope of this work, two types of diode lasers came into operation: diode lasers based on DFB (distributed feedback) laser diodes, and state-of-the-art ECDLs (external-cavity diode lasers). The former consist of self-made housings with temperature stabilization for the DFB laser diode and include components for the following fiber coupling. These diode lasers were substituted by the ECDLs to obtain higher seeding powers and an improved frequency stability.

To begin with, only one of the DFB lasers was replaced by an ECDL, allowing for a direct performance comparison. One field campaign of the DIAL (see Chapter 6.1.1) was completed with this configuration, setting the ECDL to the online frequency, and the DFB laser to the offline frequency of water vapor. Afterwards the second DFB diode laser was exchanged with an identical ECDL model. The replacement of the diode lasers implied the change of the (current and temperature) drivers, as well as of the regulation signal for frequency control.

4.4.1 DFB Lasers

The DFB lasers have been extensively described in a dedicated publication [113]. Therefore, only a brief review of their characteristics shall be given here. The distributed feedback laser diodes[9] were technically designed to emit laser light at a wavelength of $815\,\mathrm{nm}$. Due to the manufacturing process, some laser diodes are produced with wavelengths deviating from the design point randomly. The employed DFB laser diodes in this work were especially selected from such a charge, operating in the range from $\lambda = 817.7\,\mathrm{nm}$ to $819.0\,\mathrm{nm}$.

The maximum output power of the laser diode was $P = 50\,\mathrm{mW}$ to $60\,\mathrm{mW}$, depending on the specific laser diode. After fiber coupling of the laser radiation and transmission through all fiber components, a power of $P \approx 12\,\mathrm{mW}$ remained at the Ti:sapphire laser setup. The control of the laser diode current and temperature with corresponding drivers[10] allowed for a single-frequency operation by finding appropriate current–temperature value pairs. Likewise, the operation frequency could be tuned by changing the current or the temperature. The search for suitable current–temperature value pairs, especially with a wide tuning range, sometimes turned out to be challenging. Fine adjustment of the frequency was performed by manipulation of the laser current only.

The feedback control of the DFB lasers was realized with a *LabVIEW* program. The program accessed the measured wavelength, determined the deviation from the set value, calculated the corrected current, and sent this value via the RS-232 interface to the diode laser driver. Subsequently, the program switched to the next monitoring signal and actuated in the same manner for the second DFB laser. Occasionally the frequency of the HeNe laser was also monitored and taken into consideration for the determination of the correction signal. The switching alternated consecutively so that the monitoring time was distributed in $\approx 40\,\mathrm{s}$ for every DFB laser and $\approx 2\,\mathrm{s}$ for the HeNe laser. Because of the slow transfer rate via the RS-232 cable the regulation speed was not very fast and not very much correction steps could be run. Nevertheless, a frequency stabilization was achieved, that enabled DIAL measurements, though it was more difficult to obtain single-frequency operation of the Ti:sapphire laser.

Stabilizing the frequency of the DFB lasers to a constant value resulted in a frequency distribution around the set value that followed by good approximation a Gaussian function with a half width at half maximum of $\delta\nu \approx 6.7\,\mathrm{MHz}$. The linewidth of the DFB lasers was determined with a heterodyne beat note measurement to be $\Delta\nu \approx 4.6\,\mathrm{MHz}$ (FWHM). Two figures showing the long-term frequency behavior (passive and active) of the DFB laser in comparison with the ECDL are available in the next section.

---

[9] *SRI International / Sarnoff*, SAR-815-DFB

[10] *Thorlabs*, PRO800 with ITC8022 modules

4.4.2 External-Cavity Diode Lasers

In the last years, commercially available external-cavity diode lasers have reached the next level of development. Considerable technological improvement has been achieved with respect to their stability against temperature variations and acoustic noise in the environment. While previous ECDLs[11,12] in the Hohenheim-DIAL trailer exhibited a certain sensitivity to these disturbances, the next-generation model[13] comes up with a newly developed opto-mechanical setup, eliminating this deficit. The setup is still designed in a Littrow configuration with a piezo-controlled grating, a mount with actively-stabilized temperature, and an integrated fiber coupling. A Fabry–Pérot laser diode is installed, normally operating around $\lambda = 830\,\mathrm{nm}$. Coarse tuning of the wavelength is carried out with a screw on the laser head, addressing the range $\lambda = 814\,\mathrm{nm}$ to $830\,\mathrm{nm}$.

Together with an advanced diode laser driver[14] the ECDL is now well suited for operation in the trailer. The driver is equipped with current, temperature, and piezo controller, along with analog inputs. The analog inputs act on the laser diode current or the piezo voltage, hence, fine-tuning the operation frequency of the ECDL. The maximum mode-hop-free tuning range of the ECDL is $\approx 20\,\mathrm{GHz}$ depending on the chosen current–temperature value pair and the tuning speed. For slow tuning speeds (e.g., with a period of $\approx 1\,\mathrm{s}$), it was more challenging to find a suitable current–temperature value pair with a large mode-hop-free tuning range than for tuning speeds with a period of $0.1\,\mathrm{s}$, or even $0.02\,\mathrm{s}$.

The diode laser driver contributes to the enhanced performance of the ECDL due to its low noise levels. The specified low frequency current noise of the ECDL driver is $< 50\,\mathrm{nA}$ (at $0.1\,\mathrm{Hz}$ to $10\,\mathrm{Hz}$), and the current noise density is $280\,\mathrm{pA}/\sqrt{\mathrm{Hz}}$ (at $1\,\mathrm{kHz}$) [117]. In contrast, for the DFB laser, the remaining frequency instability and the linewidth could be attributed to the current noise ($\approx 2\,\mu\mathrm{A}$) of its driver [113].

Two identical ECDL models were acquired. Some characterization parameters showed small differences for each ECDL, which can be mainly traced back to the inherent variations of the laser diodes. If not stated otherwise, the differences are negligible, and a mean value is given.

Power Characteristics and Limits

The maximum output power of the external-cavity diode lasers is $P_{max} \approx 100\,\mathrm{mW}$ at a current of $I_{max} \approx 160\,\mathrm{mA}$ and a temperature of $T = 20\,^{\circ}\mathrm{C}$. The precise values depend on the individual ECDL and on the coarsely-set wavelength, which is naturally associated with the gain of the laser diode. The variations through this are $\Delta P_{max} \leq \pm 5\,\mathrm{mW}$ and $\Delta I_{max} \leq \pm 2\,\mathrm{mA}$.

Indeed, the diode lasers have to be operated at lower output powers. This has two reasons. First, some of the succeeding fiber components accept powers only up to a certain value without being damaged. In the injection seeding system, the foremost limiting constituent is the online–offline fiber switch, having a damage threshold of $P_{limit,fs} \approx 50\,\mathrm{mW}$. Despite substantial power losses in front of the fiber switch (primarily caused by the coupling into the fiber), the remaining

---

[11] *TOPTICA Photonics*, DL 100

[12] *Sacher Lasertechnik*, TEC500 Lion

[13] *TOPTICA Photonics*, DL pro

[14] *TOPTICA Photonics*, DLC pro

power at the fiber switch can still be too high for an operation of the ECDL at its maximum output power. The subject of power losses in the seeding system with respect to all incorporated elements is discussed in detail in Section 4.6.

The second reason for lowering the ECDL output power is that frequency tuning is linked to a change of current (due to the feed forward[15]) and thereby also to a change of power. Thus, it has to be ensured that over the whole frequency tuning range neither the current surpasses the current limit of the laser diode nor the power exceeds the damage threshold of the fiber switch. In practice this means that the current value at constant frequency has to be set such that it corresponds to the center frequency of the tuning range. Obviously, a larger tuning range demands a lower center current and, hence, results in a lower output power at the center frequency. A trade-off between large tuning range and high output power has to be found.

Taking these aspects into account, the ECDLs are operated at an output power of $P = (82 \pm 5)\,\mathrm{mW}$, where the values for the current and temperature are different for each laser due to the distinct operation frequencies (on- and offline). The feed forward factor of the ECDLs is $(0.60 \pm 0.09)\,\mathrm{mA/V}$. Then, a tuning range of $\approx 20\,\mathrm{GHz}$ is feasible and the resulting power at the Ti:sapphire laser setup is $P = (20 \pm 2)\,\mathrm{mW}$. Although the ECDLs are operated at a constant frequency during a DIAL measurement, a tunability must be given to quickly address a potential change of atmospheric conditions. Finding a suitable current–temperature value pair together with a mode-hop-free tuning range (at slow tuning speeds) can also be time taking for the ECDL. Furthermore, it was observed that a suitable configuration did not persist but was lost from time to time (after some weeks). A clear reason for this could not be identified, however, a certain correlation with strong changes of environmental pressure or temperature was noted.

According to the manufacturer's data sheet the laser threshold is $I_{ths} = (30 \pm 1)\,\mathrm{mA}$ and the slope efficiency is $\eta_{slope} = (0.81 \pm 0.02)\,\mathrm{W/A}$ [117]. From measurements of the output power *versus* the current of the ECDL, both parameters were ascertained experimentally. While the laser threshold gave consistent result, a comparison of the slope efficiency is inapplicable, because the power could not be measured at the same position (i.e., inside of the diode laser, behind the grating or in front of the optical isolator and the fiber coupler). In this case, the power was measured after fiber coupling and transmission through a fiber. The resulting slope efficiency varied from $0.39\,\mathrm{W/A}$ to $0.44\,\mathrm{W/A}$, depending on the fiber coupling efficiency.

Frequency Characteristics

The passive frequency stability gives a first impression on how the ECDL performs in the surrounding it is exposed to. The term passive refers to the frequency behavior of the laser without the (active) feedback control loop by the wavelength meter and without the regulation signal acting on the grating piezo voltage nor the diode current. Nevertheless, the temperature stabilization of the ECDL, also being an active control process, is always functioning since an operation of the laser diode without it would lead to a destruction due to overheating.

In the Hohenheim-DIAL trailer, the passive frequency stability was analyzed for time periods of several hours. Figure 4.2 shows the frequency behavior of the ECDL for a measurement of more than $3\,\mathrm{hours}$ together with a similar measurement previously performed for the DFB

---

[15] in the so-called *feed forward* method, the laser diode current is changed simultaneously with the orientation angle of the piezo-mounted grating to extend the mode-hop-free tuning range of the ECDL

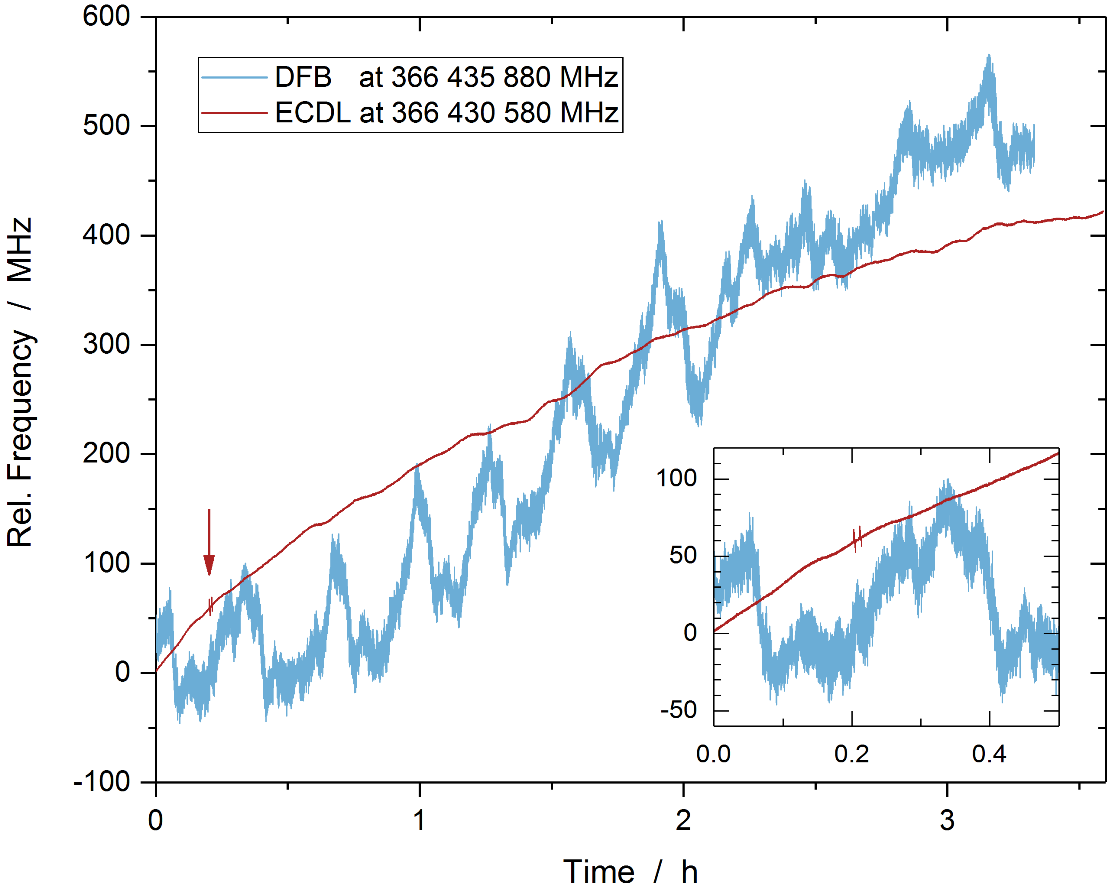

Figure 4.2: Frequency behavior of the distributed-feedback (DFB) laser and the external-cavity diode laser (ECDL) operating in the DIAL system without frequency control (passive stability). The measurements were carried out at different dates, but under similar conditions. For both diode lasers, the frequency drifted away in the course of time. For the ECDL, apart from the drift, only small variations of the frequency are observed. It exhibits significantly less frequency noise, whereby small external disturbances can be recognized. The tiny peaks marked with the arrow were caused by opening the door of the laboratory compartment.

laser. The measurements were started after an initial running of the diode lasers to establish a single-frequency state. The operation frequencies were set to values on the slope (DFB laser) and on the peak (ECDL) of the absorption line of water vapor, thus, being online frequencies of the DIAL system.

The figure shows that the frequency of both diode lasers drifted away from its starting value in the course of time. The drift is about as large for the ECDL as for the DFB laser. It should be kept in mind that such frequency drifts also depend on the environmental conditions. Hence, for a more significant comparison in this regard, the different diode lasers would have to be measured simultaneously. Much more striking and important is that the frequency behavior of the ECDL is extremely calm in comparison to the DFB laser. While the DFB laser's frequency curve exhibits clearly visible oscillations and noise, the curve of the ECDL is smooth and has only a minor variability. Especially the noise reduction on short time scales is advantageous for the performance of the entire laser system. Quick frequency jumps are the most difficult to counteract for the feedback control loop of the injection seeder, in particular when the regulation speed is slow. As a consequence, these frequency jumps are transferred to the Ti:sapphire laser, making it more difficult for its active resonator stabilization to follow the seeding mode and, thus, to maintain single-frequency operation. The low frequency noise of the ECDL enabled to a great extent the improvement of the frequency stability of the Ti:sapphire laser (see Chapter 5.7.3). It even led to a precision level which revealed minimal disturbances in the laboratory; the highlighted two peaks in Figure 4.2 were caused by opening and closing the entrance door. This could be identified and reproduced in further measurements. It is assumed that the opening/closing of the door causes an over/under pressure in the laboratory compartment for which the diode laser is sensitive.

Since the drifts (and for the DFB laser also the oscillations) in the frequency are in excess of the requirements for water-vapor DIAL ($\delta\nu < 210\,\mathrm{MHz}$, or even $< 60\,\mathrm{MHz}$), an active stabilization is necessary. The feedback loop for active frequency control is realized in the following way. The regulation signal of the wavelength meter is connected to one of the "Fine In" inputs of the ECDL driver, which is set such that the input acts on the piezo voltage of the grating. Thereupon, the diode current is adjusted automatically by the driver in correspondence to the piezo voltage with the implemented feed forward function. The equivalence of the input signal amplitude and the applied piezo voltage is set through a conversion factor. As the wavelength meter's regulation signal has a voltage range of $\approx \pm 4\,\mathrm{V}$ with a step resolution of $0.5\,\mathrm{mV}$, the conversion factor influences which frequency tuning range can be accessed and how fine it can be regulated. To stabilize the frequency to a constant value, a high resolution is preferred (i.e., steps with small frequency changes), where it is still possible to compensate for the abovementioned passive frequency drifts. For frequency tuning operation the resolution is decreased in favor of a larger tuning range.

The computation of the error value and the adequate correction signal in the feedback loop is executed by the wavelength meter software with an integrated proportional–integral–derivative (PID) controller. Proper PID parameters are determined beforehand with a PID simulator by running a test signal. They are contingent on the measurement cycle time and the control function that is applied on the laser. With a new computer hardware, measurement speeds from $\approx 100\,\mathrm{Hz}$ to over $300\,\mathrm{Hz}$ were achieved, depending on the computer load. The resulting regulation is significantly faster than the previous system. The software enables various frequency control functions. Among these are the regulation to a constant value, as well as linear, sine, triangle, exponential and step functions. The functions can be combined in a user defined manner, yielding even more complex frequency control abilities.

The active frequency stability was characterized, again, with long-term measurements in the Hohenheim-DIAL trailer. A 9-hours measurement of the ECDL and an over 7-hours measurement of the DFB laser, performed on different dates, are illustrated in Figure 4.3. The respective frequencies were stabilized to a constant value of $\nu = 366\,430\,000\,\mathrm{MHz}$ (corresponding to a vacuum wavelength of $\lambda = 818.143\,869\,\mathrm{nm}$) for the ECDL, and $\nu = 366\,438\,227\,\mathrm{MHz}$ ($\lambda = 818.125\,501\,\mathrm{nm}$) for the DFB laser. The figure also includes the ECDL's regulation signal

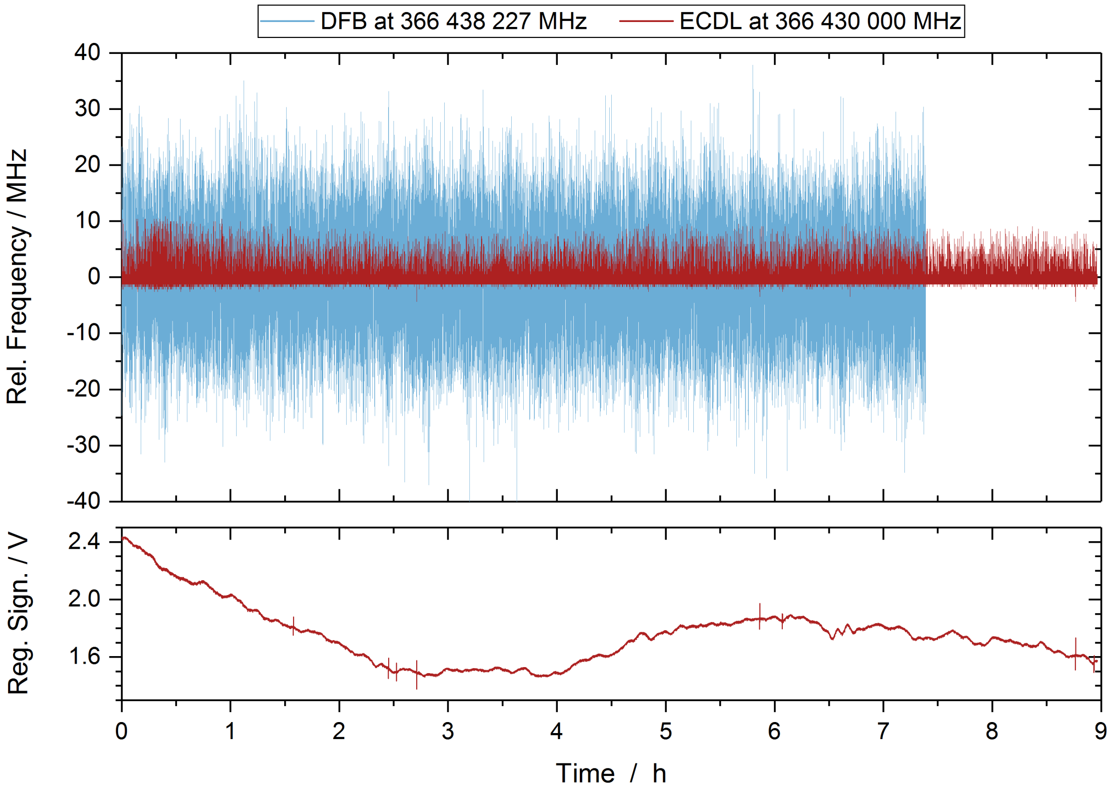

Figure 4.3: Frequency measurements with active stabilization for the DFB laser and the ECDL. The measurements took place in the Hohenheim-DIAL on different dates. The corresponding regulation signal of the ECDL's feedback loop is depicted below. The frequency distribution of the ECDL is lower spread than the DFB, and asymmetric, according to the electrical polarity and the value of the regulation voltage. The active stabilization compensated for long-term drifts and medium-term variations of the frequency. Short-term disturbances (the tiny peaks in the regulation signal) could only be corrected marginally.

generated by the wavelength meter. The measurements demonstrate that the frequency of the diode lasers stayed constant with a statistical distribution around the set value. The long-term drift and the medium-term variations of the frequency were eliminated. Only the (short-term) frequency noise persists. Here once more, the ECDL shows smaller deviations than the DFB laser. Note, that due to the representation of the measurement as a continuous line, large frequency deviations become more visible. However, the occurrence of measurement points close to the set frequency is much higher. The statistical evaluation of the ECDL data gives a standard deviation of $1\sigma = 0.32\,\mathrm{MHz}$. This value is clearly below the resolution limit of the wavelength meter (cf. Section 4.3.2). Therefore, it can be stated that the new frequency regulation concept exploits the maximum possible stabilization performance.

Interestingly, it can be observed that the frequencies are distributed more to one side of the set value (positive values on the relative frequency scale). This is confirmed by a skewness of 3.8

in the statistics and attributed to the regulation voltage. It was found in further measurements that the asymmetry of the distribution changed its side when the regulation signal crossed the zero voltage. Likewise, the skewness increased the higher the absolute value of the regulation voltage. There is a presumption that this is a peculiarity either of the wavelength meter's analog output signal, or of the ECDL driver's input signal conversion. The logged regulation signal visualizes, beside the activity of the feedback control loop, that again some external disturbances were noticed. As a closer investigation of the frequency at the instant of the disturbances showed, some of these could only be compensated partially, but not eliminated completely. Overall, the performance represents a great improvement of the injection seeding system, enhancing also the spectral characteristics of the Ti:sapphire laser. In Chapter 5.7.3 a frequency measurement is presented (while the ECDL was injection-seeding the Ti:sapphire laser) with similar results also showing the histogram of the frequency distribution (Figure 5.22). The evaluation of the DFB laser data yielded a standard deviation of a $1\sigma = 8.7\,\mathrm{MHz}$, being slightly larger than the value determined in Section 4.4.1.

For DIAL measurements the calibration with the HeNe laser and the stabilization of the second diode laser is also necessary. However, as the switching of the monitoring signal for the wavelength meter has to be controlled manually at the moment, most of the time it was decided to stabilize the ECDL which is operating at the online frequency. The switching to the other lasers for monitoring, calibration, or stabilization is executed only at selected instances (at the beginning, in a few cases during the measurement, and at the end). This is justified by the fact that the absorption of water vapor does not change significantly at an offline wavelength region and within the range of the passive frequency drifts of the diode lasers (see Figure 3 of reference [47]). The method was successfully applied during the field-campaigns SABLE and LAFE (see Chapter 6.1.1). In future, the consecutive switching through all monitoring signals, the calibration, and the stabilization of both diode lasers should be accomplished automatically. For this purpose, the wavelength meter was already upgraded with a second analog regulation output. The development of a *LabVIEW* program which executes the mentioned tasks is outstanding.

The linewidth of the ECDL was measured with a scanning, confocal Fabry–Pérot interferometer[16]. The available model has a free spectral range of $\Delta\nu_{FSR} = 7.5\,\mathrm{GHz}$ and a finesse of $\mathcal{F} > 200$. The measured linewidth corresponded to the instrumental linewidth $\Delta\nu_{FPI} < 37.5\,\mathrm{MHz}$. This measurement was solely intended to verify that the linewidth was sufficiently narrow for the application of a water-vapor DIAL. A future precise determination with a beat note measurement should yield much smaller values. The manufacturer specifies the linewidth to be below $1\,\mathrm{MHz}$ [117].

4.5 Online–Offline Switch

The employment of two independent diode lasers for alternating injection seeding at online and offline frequency demands a technique able to select the laser radiation of the two sources. This technique, which can be a single device or an optical arrangement with multiple items, is referred to as the online–offline switch.

---

[16] *Coherent*, Laser Spectrum Analyzer System (33-6131-001)

The online–offline switch has to fulfill three main features. First, it has to transmit the laser radiation of the selected seed source while blocking the other source as good as possible. The required high value of the spectral purity for a DIAL transmitter, $99.9\,\%$, is equivalent to a suppression ratio of $30\,\mathrm{dB}$ (i.e., a crosstalk[17] of $-30\,\mathrm{dB}$). Second, a fast switching time between the two states is necessary. For an alternating operation at every laser pulse, the duration of the switching process has to be at least quicker than half the repetition rate of the pulses. Stabilizing the cavity of the pulsed laser to the seed calls for an even faster response of the switch. Indeed, the shorter the switching time, the more time is left for stabilization, and hence, a single-frequency operation of the pulsed laser is more likely to be attained. Third, the online–offline switching must not affect the adjustment of how the seed laser beam is injected into the cavity. If the adjustment is altered from the optimal mode matched situation, injection seeding becomes less effective. Ideally, online and offline laser beams propagate identically in space behind the switch.

For the most part of this work a 2-to-1 fiber switch was employed as online–offline switch. Prior to this, a switching technique based on an electro-optic deflector (EOD) was studied and came into operation. In this technique, the online and the offline seed laser beams are simultaneously directed through the EOD crystal, propagating crosswise in free space. By applying a changing high voltage to the crystal, both beams are deflected from side to side, where the middle position is picked to be further directed to the Ti:sapphire laser resonator. The arrangement and its characteristics are described in more detail in [113]. Here, only the results are summarized, and some additional information is given.

The crystal of the EOD[18] has an anti-reflective coating, providing $99\,\%$ transmission of the incident optical power. A high voltage supply[19] drives the crystal with $\pm 2.5\,\mathrm{kV}$, resulting in a total beam deflection angle of $7.5\,\mathrm{mrad}$. The switching time was measured to be $\approx 8\,\mu\mathrm{s}$ from $10\,\%$ to $90\,\%$ of the signal intensity and conversely. These rise and fall times were limited by the response time of the high voltage driver. The optical arrangement with the EOD as online–offline switch led to a crosstalk with values ranging from $-27.6\,\mathrm{dB}$ to $-35.3\,\mathrm{dB}$.

The spatial overlap of both seed laser beams subsequently injected into the resonator depends on the adjustment of the deflecting beams. While in principle it is possible to achieve a sufficient spatial overlap, the adjustment can be rather time-consuming. Moreover, the adjustment depends on the deflection angle of the beams, which in turn correlates sensitively with the amplitude of the applied high voltage. The driver providing the high voltage, thus, has to reproduce the amplitude with high precision. For the used driver, the repeatability posed a considerable challenge, especially, as long-term operation involved several failures of the built-in tubes responsible for the high voltage generation. An exchange of the tubes, in most of the cases, implied a variation of the amplitude set, and hence, made a readjustment of the beams necessary. The overall laborious handling of the arrangement with the EOD as online–offline switch, caused above all by the high voltage driver, motivated the revision of the switching technique.

Emphasizing the demand of high spatial overlap and the ease of handling, gives rise to the use of a fiber-integrated multiplexer. It is immediately evident that for a fiber switch the spatial

---

[17] The term crosstalk refers to the residual signal from the channel not selected. Crosstalk values in dB are negative, but often only absolute values are given.

[18] *Leysop*, ED3-820

[19] *Leysop*, 5000 series amplifier

propagation of the outgoing beams is identical. The adjustment is reduced to a minimal effort, consisting only in connecting the fibers together properly. On the other hand, fiber switches might have some limitations with respect to other parameters. A prior fiber switch employed in the seeding system showed deficiencies in its long-term operation and crosstalk [25, 112, 113].

The fiber switch[20] of the present system is a fiber-coupled opto-mechanical switch realized in micro-electro-mechanical system (MEMS) technology. The switch, having two input and one output channels, is complemented as a special feature with polarization maintaining fibers. Simple $5\,\mathrm{V}$ DC voltages serve as electrical power supply and to select the switch state. Thus, a TTL trigger signal can directly be set to the control pins. The fiber switch accepts a maximum optical input power of approximately $50\,\mathrm{mW}$ without getting damaged. This represents a limitation in the injection seeding system, if the diode lasers deliver higher powers (see Sections 4.4.2 and 4.6). By the transmission through the fiber switch, the laser radiation experiences some considerable power loss, depending on the fiber channel. The transmission was measured by the manufacturer to be $85\,\%$ (insertion loss $0.7\,\mathrm{dB}$) and $74\,\%$ ($1.3\,\mathrm{dB}$).

The switching behavior was investigated at typical DIAL operation conditions. An online–offline TTL trigger signal with a period time of $8\,\mathrm{ms}$ was applied to the switch, corresponding to half of the repetition rate of the Ti:sapphire laser pulses when pumped with the *IBL* laser ($f_{rep} = 250\,\mathrm{Hz}$). The laser light of one diode laser was sent through the fiber switch and detected with a photodiode[21]. The signals were recorded with an oscilloscope[22] at high sampling rate. Figure 4.4 shows how the photodiode signal follows the trigger signal. Right after the leading and falling edges of the trigger, there is a small delay of $\approx 150\,\mu\mathrm{s}$ until the fiber switch reacts. This time lag is uncritical as it can be considered by a delay generator when producing the trigger signal. The effective rise and fall times of the fiber switch signal are about $1.5\,\mathrm{ms}$, where both response times are not perfectly equal. The individual values depend on the switching states, but also on the chosen starting and ending signal levels. The same conditions have influence on the crosstalk, which is determined by the ratio of the two signal levels.

For a precise evaluation, the measured raw signal of the photodiode was smoothed with a Savitzky–Golay filter. The low and high signal levels were calculated from the mean of the values within the last $1\,\mathrm{ms}$ before the trigger edge. In analogy to the EOD switch, the switching times were determined first between signal levels of $10\,\%$ and $90\,\%$. The result was a rise time of $t_{rise} = (0.44 \pm 0.05)\,\mathrm{ms}$ and a fall time of $t_{fall} = (0.48 \pm 0.05)\,\mathrm{ms}$. A signal ratio of $-30\,\mathrm{dB}$ was achieved from the low signal level up to a level of $99.9\,\%$ within $t_{rise} = (1.27 \pm 0.10)\,\mathrm{ms}$, or from the high signal level down to a level of $0.1\,\%$ within $t_{fall} = (1.71 \pm 0.20)\,\mathrm{ms}$. To determine the crosstalk, the signal powers were measured at constant state with a power meter[23]. The crosstalk was $(-63 \pm 5)\,\mathrm{dB}$ for one channel and $(-61 \pm 4)\,\mathrm{dB}$ for the other. In comparison, the values measured by the manufacturer were $-77\,\mathrm{dB}$ and $-72\,\mathrm{dB}$, respectively.

These values show that the fiber switch provides excellent low crosstalk capabilities. However, it has to kept in mind that to achieve these values a certain switching time is necessary, being in the order of the repetition rate of the laser pulses. Nevertheless, the stabilization process might not require such low crosstalk values so that it can be initiated already earlier and more

---

[20] *Sercalo Microtechnology*, SN-1x2-6N-PM

[21] see footnote 12 on page 34

[22] see footnote 13 on page 34

[23] *Coherent*, LM2-VIS with FieldMaster GS

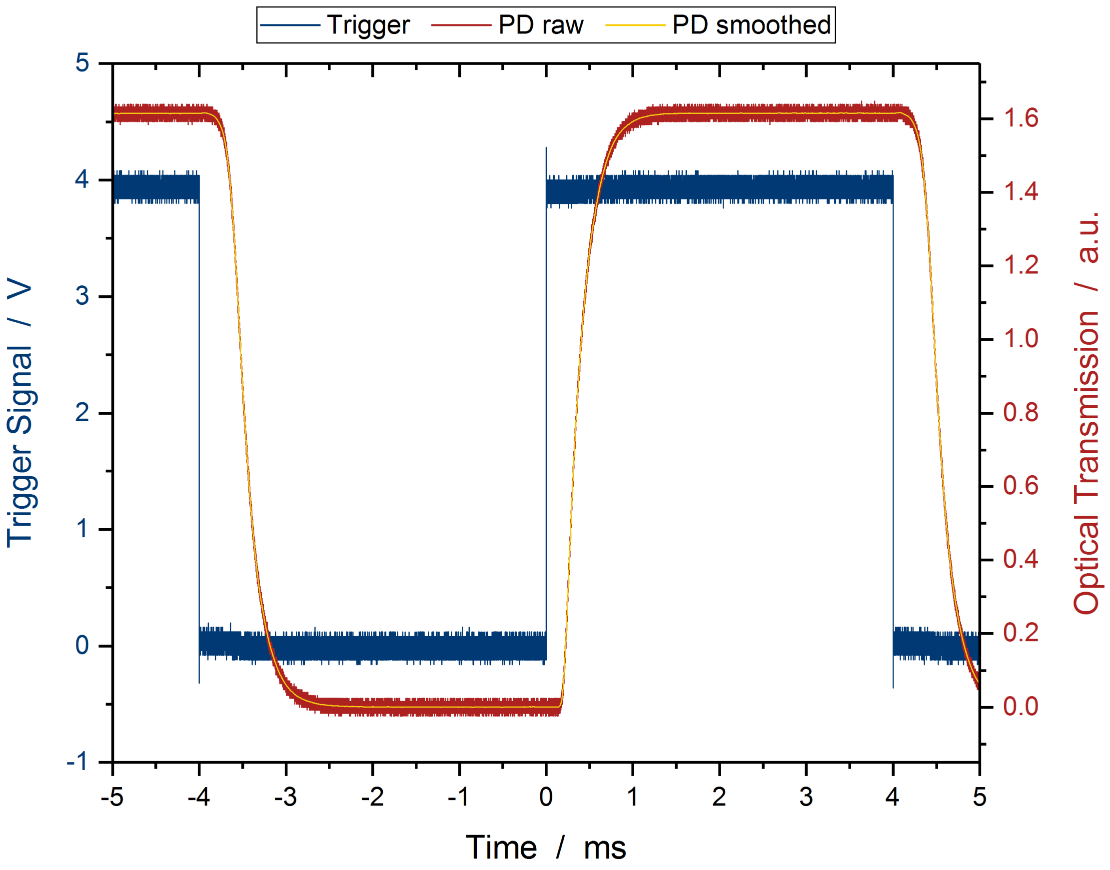

Figure 4.4: For the determination of the response time of the fiber switch, the optical transmission signal detected by a photodiode (PD) was measured together with the applied trigger signal. There is a time lag until the fiber switch reacts, and the actual phase where the transmission channel is switched. The raw signal of the photodiode was smoothed to precisely evaluate the switching times.

time for the stabilization process is available. On the contrary, it is essential that the crosstalk is low when the laser pulse builds up. As indicated above, this requires an elaborate trigger concept (see Chapter 5.8). During field operation of the Hohenheim-DIAL, the performance of the fiber switch was very satisfactory, especially because of its unparalleled performance with regard to the spatial overlap of the output beams. One last aspect to be considered is that the fiber switch has only a limited amount of switching operations. The manufacturer specifies as typical 1 billion cycles. So far, after several campaigns with many intensive observation periods, this durability limit has not been reached.

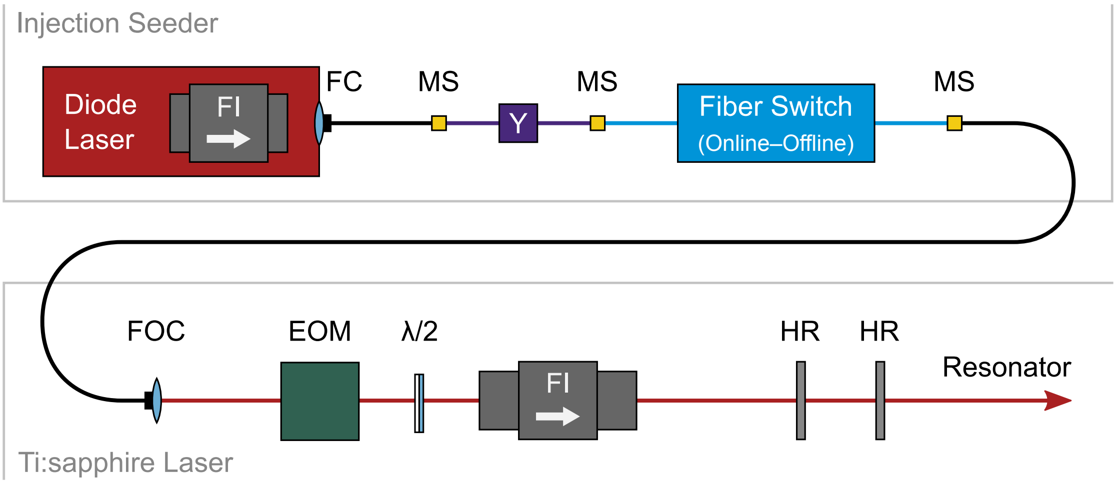

Figure 4.5: Simplified illustration of the injection seeding path, stringing together all components relevant for a power loss consideration. EOM – electro-optic modulator, FC / FOC – fiber (output) coupler, FI – Faraday isolator, $\lambda/2$ – half-wave plate, HR – highly reflective mirror at $820\,\mathrm{nm}$, MS – mating sleeve, Y – bifurcated fiber; branching fibers not shown.

4.6 Power Losses in the Injection Seeding Path

When pulsed lasers with high energies are injection seeded, the availability of enough seed power becomes eminently important to ensure that the desired laser mode prevails over the others. Starting from the seed laser diode, the coherent radiation propagates through several components, experiencing more or less power losses until finally reaching the Ti:sapphire laser resonator. There, only a minor fraction of the initially emitted power is left. Thus, it is worth to have a closer look at the injection seeding path and all relevant components with respect to its power transmission ratio $T = P_{out}/P_{in}$, or to the insertion loss $L(\mathrm{dB}) = 10\log_{10}[P_{in}/P_{out}]$. This helps in understanding the residual power at the end of the seeding path and identifying sources for further optimization. Having said that, the setup here already represents an optimized system state, without any non-essential parts and by partial renunciation of an easier handling.

The whole injection seeding path can be grouped in two segments: the part of the seeder system, until the laser light reaches the Ti:sapphire laser setup and which almost only consists of a propagation through fiber components, as well as the remaining part until the resonator mirror of the Ti:sapphire laser, where the seed is injected. Figure 4.5 depicts the path with its two segments and all denominated components causing power losses. In Table 4.1 the corresponding transmission and insertion loss are listed. The information on the devices was either obtained from specification or measurement by the manufacturer or from an own measurement. Beginning with the power emitted by the basic diode laser (i.e., leaving out the integrated optical isolator and the fiber coupling yet), the resulting power values behind all succeeding components is calculated with the transmission ratio. The power values are listed for three scenarios and will be discussed later on in this section.

Component	Transmission	Insertion Loss	Power (behind component)			
			Case 1	Case 2	Present Case	
			Calculated	Calculated	Calculated	Measured
Laser Diode			(100 ± 5) mW	(96 ± 5) mW	(81.9 ± 5.0) mW	
Faraday Isolator	(84.0 ± 5.0) %	(0.76 ± 0.26) dB	(84 ± 7) mW	(81 ± 7) mW	(68.8 ± 5.9) mW	
Fiber Coupler	(64.0 ± 5.0) %	(1.94 ± 0.34) dB	(54 ± 6) mW	(52 ± 6) mW	(44.0 ± 5.1) mW	(34.5 ± 3.0) mW
Y-Fiber: Fraction	(99.0 ± 0.3) %	(0.04 ± 0.02) dB	(53 ± 6) mW	(51 ± 6) mW	(43.6 ± 5.1) mW	
Y-Fiber: Loss	(96.6 ± 3.3) %	(0.15 ± 0.15) dB	(51 ± 6) mW	(49 ± 6) mW	(42.1 ± 5.1) mW	
Mating Sleeve	(87.1 ± 8.0) %	(0.6 ± 0.4) dB	(45 ± 7) mW	(43 ± 7) mW	(36.7 ± 5.6) mW	
Fiber Switch	(79.4 ± 5.5) %	(1.0 ± 0.3) dB	(36 ± 6) mW	(34 ± 6) mW	(29.1 ± 4.9) mW	(23.7 ± 3.0) mW
Mating Sleeve	(87.1 ± 8.0) %	(0.6 ± 0.4) dB	(31 ± 6) mW	(30 ± 6) mW	(25.4 ± 4.9) mW	
Fiber	(99.5 ± 0.2) %	(0.02 ± 0.01) dB	(31 ± 6) mW	(30 ± 6) mW	(25.3 ± 4.9) mW	
Fib. Outp. Coupl.	(99.6 ± 0.1) %	(0.02 ± 0.01) dB	(31 ± 6) mW	(29 ± 6) mW	(25.2 ± 4.8) mW	(22.0 ± 0.5) mW
Electr.-Opt. Mod.	(99.5 ± 0.5) %	(0.02 ± 0.03) dB	(31 ± 6) mW	(29 ± 6) mW	(25.0 ± 4.8) mW	(21.9 ± 0.5) mW
Half-Wave Plate	(99.8 ± 0.4) %	(0.01 ± 0.02) dB	(31 ± 6) mW	(29 ± 6) mW	(25.0 ± 4.8) mW	
Faraday Isolator	(86.0 ± 6.0) %	(0.66 ± 0.31) dB	(26 ± 6) mW	(25 ± 6) mW	(21.5 ± 4.4) mW	(19.7 ± 0.5) mW
Mirror 1	(98.3 ± 0.2) %	(0.07 ± 0.01) dB	(26 ± 6) mW	(25 ± 5) mW	(21.1 ± 4.3) mW	
Mirror 2	(99.0 ± 1.0) %	(0.04 ± 0.05) dB	(26 ± 6) mW	(25 ± 5) mW	(20.9 ± 4.3) mW	(19.6 ± 0.5) mW
Total	(25.5 ± 5.0) %	(5.93 ± 0.85) dB				

Table 4.1: Listing of transmission and insertion loss for the components of the injection seeding path. The optical power behind every component was calculated for three scenarios (described in the text). For the third scenario (present case) individual comparison measurements were made, that is why these values are given with a higher precision.

For the injection seeding system, the components mostly attributing to the power losses are the optical isolator together with the fiber coupling inside the diode laser. Although the insertion losses are high in comparison to other constituents, they lie within a usual range for the specific component. Other significant power losses occur due to the fiber switch and the mating sleeves connecting the fiber ends. The insertion loss of the fiber switch is listed in the table with $L = (1.0 \pm 0.3)\,\mathrm{dB}$, as it is different for each fiber channel ($0.7\,\mathrm{dB}$ and $1.3\,\mathrm{dB}$). The mating sleeves represent an element with very irregular power loss. In an individual measurement series with different models[24] and by plugging and unplugging two fibers several times, it was found that the insertion loss varies between $0.3\,\mathrm{dB}$ and $0.7\,\mathrm{dB}$. The information given by the manufacturer on the mating sleeves is ambiguous; values of $< 0.5\,\mathrm{dB}$, $< 1.0\,\mathrm{dB}$, and even $> 1.0\,\mathrm{dB}$ are mentioned. Moreover, the fiber manufacturer also provides some information, specifying insertion loss values of typically $< 0.6\,\mathrm{dB}$ and maximum $0.85\,\mathrm{dB}$. Finally, for the calculation a value of $L = (0.6 \pm 0.4)\,\mathrm{dB}$ was chosen. The attenuation losses inside the fibers themselves have also been considered in the calculation, even though they are rather small ($<$ $3\,\mathrm{dB/km}$).

The injection seeding path at the Ti:sapphire laser setup involves comparatively few power losses. The most notable component is the Faraday isolator, which is a two-stage model providing high optical isolation. Previously, the electro-optic modulator (EOM) also caused some power losses, but in the meantime, it was replaced by a different model with a suitable anti-reflective coating. Likewise, the other parts were optimized to provide high transmission or reflection for the bending mirrors at the end of the path. More details on these components can be found in the following section, as well as Chapter 5.3. The overall transmission efficiency for the injection seeding path is $T_{total} = (25.5 \pm 5.0)\,\%$.

The first calculation scenario is intended for the case that the ECDL operates at its maximum output power. While the power originating from the basic ECDL is then $P_{max} = (100 \pm 5)\,\mathrm{mW}$, the complete ECDL (including optical isolation and fiber coupling) yields $P = (53.8 \pm 5.9)\,\mathrm{mW}$, exceeding the damage threshold of the fiber switch. The situation at the point directly in front of the fiber switch is decisive. There, the power is still too high taking the margin of error into consideration. Hence, the power has to be decreased.

To be definitely below the damage threshold, a reduction of the original power to merely $P = (96 \pm 5)\,\mathrm{mW}$ is sufficient. This is represented in the second scenario. In this case, as the power behind the fiber coupling is still over $50\,\mathrm{mW}$, one strongly relies on the further losses appearing before the radiation reaches the fiber switch. At the end, for injection seeding of the Ti:sapphire laser resonator a power of $P = (24.5 \pm 5.0)\,\mathrm{mW}$ would theoretically be available.

When frequency tuning is considered, the central frequency power value has to be lower, corresponding to the tuning amplitude and the feed forward factor. The third case illustrates the experimentally chosen situation of being safe against damages while enabling tuning possibilities. Here, the originally emitted power was $P = (81.9 \pm 5.0)\,\mathrm{mW}$. The precise value depends on the chosen current–temperature value pair, i.e., the specific frequency that shall be addressed, and the accomplishment of mode-hop-free tuning operation. From the calculation results a power of $P = (20.9 \pm 4.3)\,\mathrm{mW}$ at the end of the seeding path. For this last scenario, measurements have been made to compare how well the theoretical values could be achieved.

---

[24] *Thorlabs*, ADAFCPM2 and ADAFC3

The measured values lie below the calculated values, but within the error estimation. The deviations can be attributed to the imprecise knowledge of the fiber coupling efficiency and to the insertion loss of the mating sleeves.

In conclusion, for injection seeding with the current setup configuration a power in the range of $P = 17\,\mathrm{mW}$ to $20\,\mathrm{mW}$ directly in front of the Ti:sapphire laser resonator was obtained. The limiting component in the path is the damage threshold of the 2-to-1 fiber switch. As long as this limit remains, a higher output power than $\approx 100\,\mathrm{mW}$ provided by the ECDLs is not reasonable. For future models of the fiber switch, it would be particularly desirable to have a lower insertion loss. Besides, more injection seeding power can only be obtained by improving the transmission efficiency in the seeding path *behind* the fiber switch. However, except for the mating sleeve, the losses in this section are already quite low. A solution to avoid the power losses due to the interconnections of the fibers would consist in splicing both fiber ends together. This can be very challenging for polarization-maintaining fibers and would compromise the flexibility to quickly exchange parts (e.g., in case of damage or end of lifetime) or to use different fiber collimators for test and alignment purposes (see next section).

4.7 Mode Matching for Ti:sapphire Laser

Mode matching of the seed laser beam to the Ti:sapphire laser resonator mode is crucial for an effective injection seeding. In contrast to the adaption of the pump laser beam, injection seeding asks for a seed laser beam whose beam parameters are matched very closely to the ones of the Ti:sapphire laser mode. These parameters are the beam width at the laser crystal and at the waist, the location of the waist, the divergence (if not dealing with Gaussian beams), as well as the direction of beam propagation [114]. The particular parameters will be addressed in the following. The subject is treated restricting to the configuration with the fiber switch as online–offline switch. Since the Ti:sapphire laser resonator mode and the injected seed laser beam (exiting from a polarization-maintaining singlemode fiber) correspond to (or at least are very close to) the fundamental mode TEM_{00}, the approach is based on Gaussian beams and the paraxial approximation[25].

The longitudinal location and the width of the beam waist are beam parameters that rely on the specific design and operation condition of the Ti:sapphire laser resonator, as will be demonstrated in Chapter 5.2. To obtain the perfect mode-matched situation, it is necessary to restrict to a certain design operation power. At powers deviating from the design point, injection seeding of the Ti:sapphire laser is still possible, though it may be less efficient. With higher operation powers the laser resonator mode becomes more and more asymmetric, and—when including a cylindrical compensating lens—even astigmatic[26]. Hence, the laser mode is different in both planes of the beam, the sagittal and the tangential plane[27]. Therefore, it is almost impossible to maintain an impeccable mode-matched beam at reasonable effort; a compromise for the parameters has to be found. The analysis and measurements in Chapter 5.2 and 5.7.1, respectively, led to the decision to match the seeder beam parameters to the following values. The beam radius

---

[25] see footnote 6 on page 85

[26] see footnotes 9 and 10 on page 94 for a differentiation of the terms asymmetry and astigmatism

[27] see footnote 7 on page 94

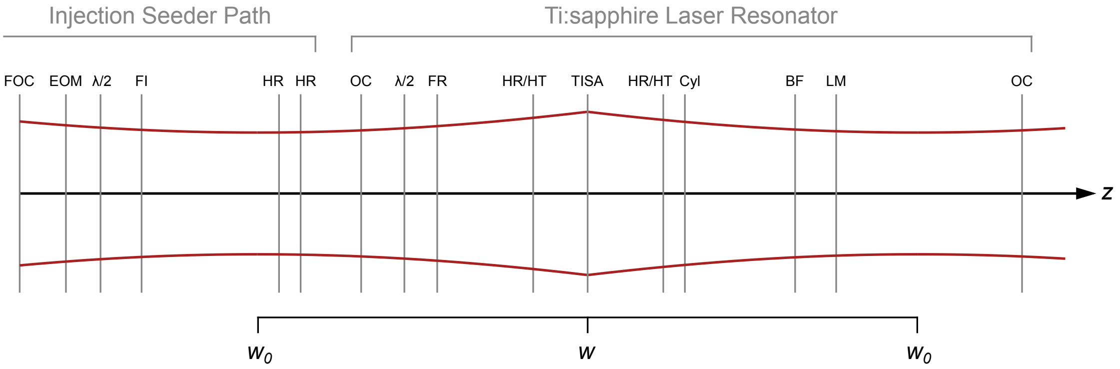

Figure 4.6: One-dimensional projection of the seed laser beam propagation along the free-space injection seeder path and into the resonator of the Ti:sapphire laser. The beam passes several components; the corresponding positions are marked. The caustic was plotted, emphasizing the beam waist (in reality, the change in beam width is barely noticeable). The beam waist is located at half resonator length-distance in front and behind the thermal lens of the Ti:sapphire crystal (TISA). Abbreviations see Figures 4.5 and 5.7.

at the laser crystal should be $w = 0.7\,\mathrm{mm}$. The location of the beam waist should correspond to the waist location of the Ti:sapphire laser mode in the sagittal plane (y-direction; resonator design calculation with the thermal lens only), being located at $z_{0,y} = 800\,\mathrm{mm}$ in front of the laser crystal. There, the beam width should be adapted to a radius of $w_{0,y} \approx 0.61\,\mathrm{mm}$.

The beam waist location of the seed laser beam has to be at the same position as the waist of the Ti:sapphire resonator mode would be, if theoretically propagating backwards, starting from the laser crystal, towards the fiber output coupler of the seed laser. This location lies outside the laser resonator, approximately $z = (252 \pm 20)\,\mathrm{mm}$ in front of the output coupler mirror, as Figure 4.6 depicts. The length from the beam waist position to the laser crystal apparently corresponds to half of the resonator length.

The accordance of the seed laser's beam to the above-mentioned parameters has to be achieved by a suitable beam adaption. Similar to the adaption of the pump laser beam, it aims at keeping the number of additional lenses for this purpose to a minimum. As the seed laser beam is brought to the Ti:sapphire laser setup via a waveguide and coupled out through a fiber collimator, one adjustment option is already given. The focal length of the fiber collimator lens and its translation adjustment determine the propagation of the outcoupled beam. Fiber collimator models with lenses of different focal lengths are available, so that a focusing beam or a beam of almost constant width can be generated. Two models for these two cases were used and compared. They were selected in consultation with the manufacturer who provides formulas to calculate the resulting beam parameters [118], as well as a closed-source components file for the optical design program *Zemax*.

The first fiber collimator model[28] has a lens with a focal length $f_{coll} = +3.1\,\mathrm{mm}$, and is intended to generate a focused beam, matching primarily $w_{0,y}$ and $z_{0,y}$ of the Ti:sapphire laser mode. The theoretical calculation yields a spot radius of $w_{spot} \approx 0.58\,\mathrm{mm}$ at a distance of

---

[28] *Schäfter+Kirchhoff*, 60FC-4-A3.1-02

$z_{spot} = 650\,\mathrm{mm}$ for the employed fiber[29] with a mode field diameter $MFD = 5.5\,\mu\mathrm{m}$, and $\lambda = 818\,\mathrm{nm}$. The spot radius computed with *Zemax* was slightly larger, $w_{spot} \approx 0.61\,\mathrm{mm}$, fitting precisely to $w_{0,y}$. The fiber collimator was collocated approximately at the distance z_{spot} in front of the beam waist location aimed for and adjusted with a beam profiler positioned there. The adjustment represented a challenge. For one thing, the handling of the fiber collimator's adjustment screw was not sufficiently sensitive. Additionally, the beam profiler was not able to register small location variations (i.e., variations of the beam width) at the required precision level. For verification, the beam profile of the seeder was measured at the location of the Ti:sapphire crystal. It was found that the beam width was much larger there ($w \approx 1.5\,\mathrm{mm}$) than the desired value of $w = 0.7\,\mathrm{mm}$. In this respect, the result was unsatisfactory.

The second fiber collimator model[30] was chosen primarily to match the beam width at the position of the Ti:sapphire laser crystal. With a lens of focal length $f_{coll} = +7.5\,\mathrm{mm}$, the resulting beam[31] propagates within a working range $A = 1.95\,\mathrm{m}$ with an almost constant beam radius of $w \approx 0.71\,\mathrm{mm}$, according to the calculation. The measurement of the beam profile at a corresponding distance of the laser crystal confirmed this (see Figure 4.7). The 2σ-beam radius was $w = (0.70 \pm 0.01)\,\mathrm{mm}$. Thus, a high intensity overlap of seeder and laser mode was achieved. The use of this model is supported by the fact that the sagittal Ti:sapphire laser mode already exhibits a low divergence, where the value of $w_{0,y}$ is very close to w. Furthermore, the resulting beam of this model allows for a more precise mode matching of the lateral and angular parameters. These are essential for injection seeding [114].

During high power operation of the Ti:sapphire laser, both fiber collimator models were tested. While for both of them injection-seeded, single-frequency operation was achieved, the second model lead to a slightly higher frequency stability. Therefore, this fiber collimator is preferred for permanent operation. The first collimator model was kept in the setup with an additional fiber[32] as backup. It can be used optionally by connecting the fiber to the output at the rack of the seeding system, and by inserting a flipping mirror, thus, replacing the normal path of the seed laser beam (see Figure 5.7 on page 98).

The transverse position of the beam waist and the direction of beam propagation are mode matching parameters addressed by classical alignment methods. Several irises and monitoring cameras are used to mark the position of the Ti:sapphire laser beam at different points in space. Usually these elements are positioned behind the resonator mirrors (see Figure 5.7 and description in Chapter 5.3). Then, the seed laser beam is aligned via two mirrors (a so-called Z-stage) such that it hits the same irises and position on the monitoring cameras. The two mirrors are situated as final elements of the injection seeding path, directly in front of the resonator's output coupler. As the total bending angle of the two mirrors is less than $180°$, one of the mirrors[33] has a coating for an exceptional angle of incidence $AOI = (60 \pm 5)°$, while the other mirror[34] has the standard $45°$-AOI coating.

The alignment of the seed laser beam has to be done while the Ti:sapphire laser is not oper-

---

[29] see footnote 2 on page 58

[30] *Schäfter+Kirchhoff*, 60FC-4-A7.5-02

[31] by the manufacturer also named as pilot beam

[32] *OZ Optics*, PMJ-3A3AF-850-5/125-3A-5-1

[33] *Laser Components*, HR820/60±5 PW1025UV

[34] *CVI / Melles Griot*, TLMB-800-45-1025

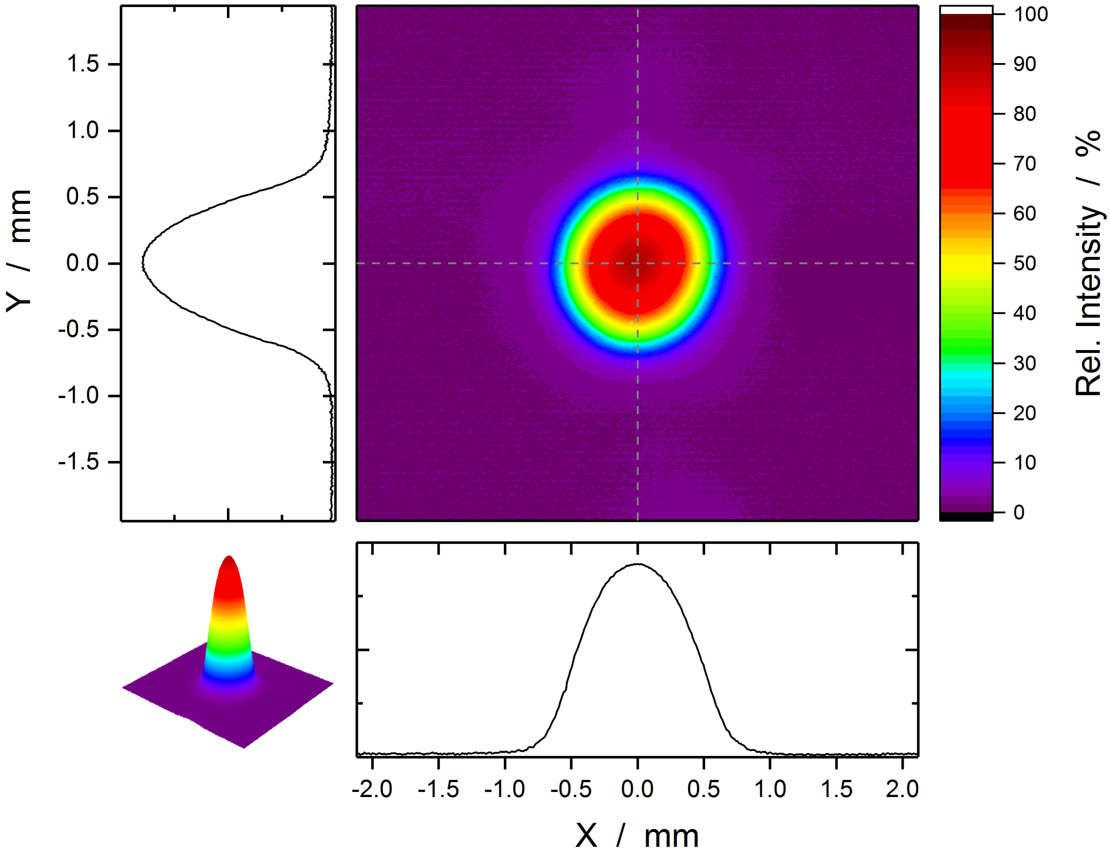

Figure 4.7: Beam profile of the mode-matched seed laser, captured at a distance corresponding to the location of the Ti:sapphire crystal. Since the seeder beam is brought to the laser setup with polarization-maintaining singlemode fibers, the resulting mode coincides well with TEM_{00}.

ating. During operation, the seeder cannot be distinguished from the pulsed laser beam. On the other hand, the Ti:sapphire crystal is still pumped close to the lasing threshold to sustain at least a weak thermal lens. Consequently, the beam in the cavity converges and the alignment is facilitated. This is also the case for the alignment approach where the cavity of the Ti:sapphire laser is ramped with a piezo and the transmission signal of the seeder is observed behind the cavity mirror with a photodiode. The transmission peaks, following an Airy function of a Fabry–Pérot interferometer, are maximized by adjusting the two earlier mentioned mirrors (without changing the adjustment of the resonator mirrors themselves). With a divergent beam the transmission peaks would be broader and weaker.

CHAPTER 5

Ti:sapphire Laser

In the previous two chapters, two important parts of the laser transmitter were treated. The pump source supplies the laser system with energy and provides the pulsed, high power operation. The injection seeders are necessary to enhance the spectral properties and select the emission frequency. The central part of the laser system is the Ti:sapphire laser, which is discussed in this chapter. Although the other lasers of the system are indispensable in their task, the Ti:sapphire laser takes the principal role of the transmitter. It does not only act as a frequency converter or as a simple amplifier. It is the true laser that produces the coherent radiation which is sent into the atmosphere.

The development of a laser which pursues specific and high goals (e.g., as defined in Chapter 2.2.1) is a process with several iterative stages. First, there is the theoretical analysis and simulation of the performance depending on the laser parameters. It is accompanied by the choice and design of the resonator. Then, the experimental realization consisting in the construction and alignment of the constituents follows. Finally, the fine adjustment and the characterization of the laser operation must be dealt with. Every step gives feedback on an optimized accomplishment of the current and also the previous development stages.

For the recent development of the Ti:sapphire laser, it was possible to draw on the results of the preceding studies by WAGNER and SCHILLER. Simulations consisting of four modules were carried out: thermal modeling (heat transfer in the laser crystal and formation of the thermal lens), resonator design (beam propagation and stability considerations), performance modeling (rate equations and efficiencies), as well as spectral modeling (injection seeding and spectral purity) [30, 31]. The first experimental realization was performed, including comparisons with the simulations and inaugural measurements with the Hohenheim-DIAL [25, 26]. In addition, due to the widespread use of Ti:sapphire lasers, abundant information can be found in the literature. However, as in this work a higher performance level was to be reached, and as dealing with an uncommon energetic operation domain, further investigation or an iterative trial at certain development stages was inevitable. Some of the theoretical analysis is revisited here, inasmuch as it is directly connected to the experimental implementation (e.g., the resonator design). For other subjects, the approach concentrates on the results of measurements (e.g., the determination of thermal lens). Essentially, the final state is described, while discussing significant intermediate examinations, limits, and breakthroughs.

This chapter begins with a report on the laser medium Ti:sapphire to provide essential information on the material and the laser physics. For the initial design of the resonator, calculations based on ray matrices were made and further attributes assessed. In the following, the entire laser setup is presented. First, the realization of the key functions is described in detail. Then, the laser operation is successively characterized. The chapter closes with the description of the devices used for triggering the DIAL measurement.

5.1 Ti:Al_2O_3

Titanium sapphire (or short, Ti:sapphire) was employed as laser active medium for the first time in 1982 by MOULTON [119, 120] (for this section also see references [85, 121]). The chemical formula of the material reads Ti:Al_2O_3 and indicates that it consists of the host crystal Al_2O_3 (more commonly known as sapphire) which is doped with Ti^{3+} ions, replacing a few of the aluminum ions. Ti^{3+} belongs to the transition metal ions, and has the electron configuration of an argon atom with a single 3d electron extra,

$$1s^2\,2s^2\,2p^6\,3s^2\,3p^6\,3d^1 = [Ar]\,3d^1. \tag{5.1}$$

Hence, only one electron remains in an incomplete shell. It determines the significant energy levels of the ion, facilitating the analysis and further advantages. For the free ion, the energy level is five-fold degenerate. Inside the host crystal, the unshielded 3d electron of the ion interacts with the surrounding electrostatic crystal field. The energy levels split into a ground-state triplet $^2T_2$ and into an excited-state doublet ^2E. Between these two levels the lasing transition occurs. The incorporation of the titanium ion in sapphire further affects the energy levels. During an excitation or a relaxation process, the ion is displaced causing vibrations on the host lattice. The lattice vibrations (phonons) in combination with the electronic energy levels lead to a multitude of transition energies. From originally discrete energy levels result energy bands, both for the ground and the excited state. Such band structures are often referred to as vibronic energy states.

The laser operation then proceeds as follows (see Figure 5.1). At first, the titanium ion is excited from its ground state by pumping to one of the higher vibronic levels of the ^2E state. Quick vibrational relaxation populates the lowest level of the band. Through emission of a photon the ion passes over to one of the upper vibronic levels of the ground state $^2T_2$. Again, relaxation of vibration brings the ion to the bottom level. The sequence represents a four-level system in laser dynamics theory.

Due to the vibronic bands of the excited state and the ground state, the spectra for absorption and emission, respectively, are extraordinarily broad. Both spectra are shown in Figure 5.2. The absorption spectrum lies in the blue-green region with a peak at $\lambda \approx 490\,\mathrm{nm}$. The emission radiation ranges from approximately $670\,\mathrm{nm}$ to $1070\,\mathrm{nm}$ and peaks near $790\,\mathrm{nm}$. This is one of the main advantages of titanium-doped sapphire. The outstandingly wide emission spectrum enables laser operation for numerous applications (see below). The broad absorption spectrum also suggests a variety of pumping possibilities. However, a comparatively short fluorescence lifetime[1] of the material of $\tau = 3.2\,\mu s$ makes flashlamp pumping inefficient. Therefore,

---

[1] time for a spontaneous decay of the lasing transition, i.e., without stimulation

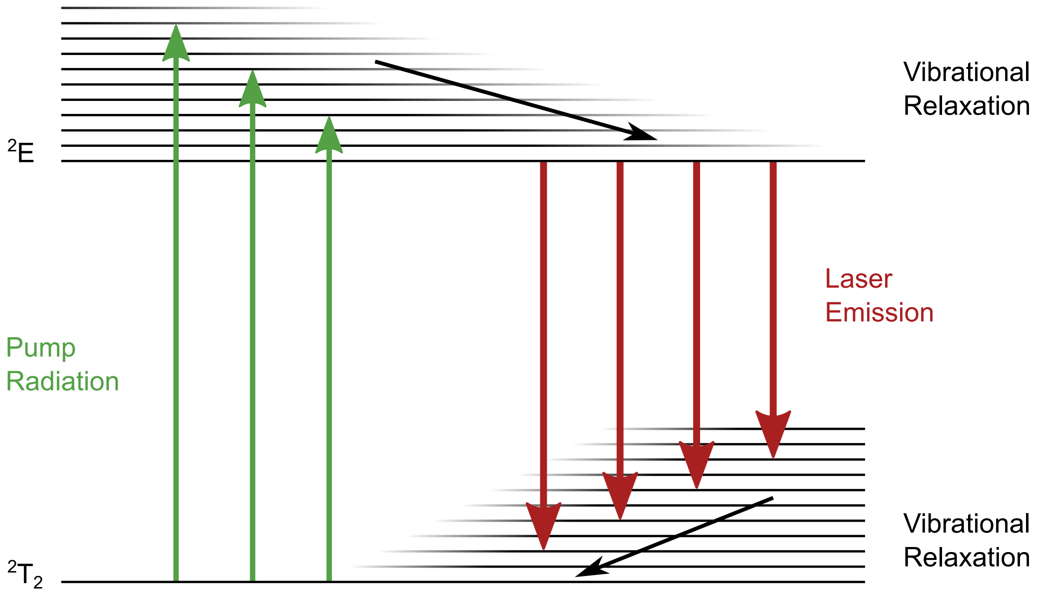

Figure 5.1: Simplified energy-level diagram of Ti:Al_2O_3. The vibronic energy states of the laser material give rise to broad spectra of the optical transitions [85].

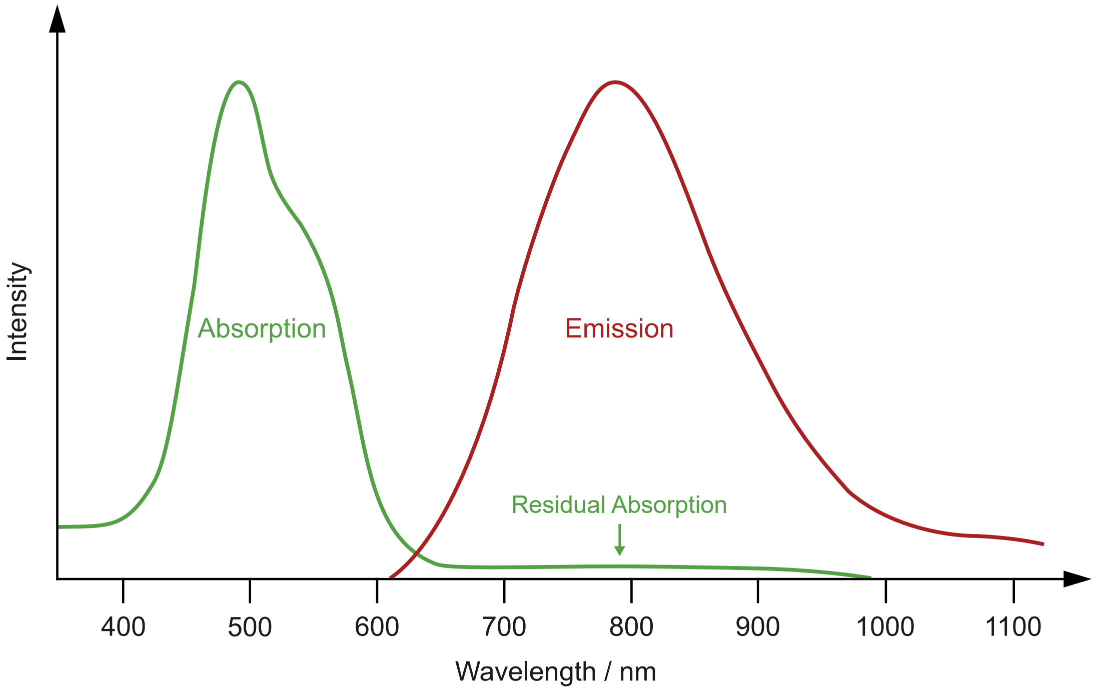

Figure 5.2: Absorption and emission spectrum of titanium-doped sapphire. A minor residual absorption in the emission band can occur if Ti^{3+}–Ti^{4+} pairs appear in the laser crystal [121].

frequency-doubled neodymium-based lasers or still gas lasers (with argon ions or copper vapor as medium) are used in most cases. Applying laser diodes or fiber lasers as pump source is currently in developmental stage [83,84,122]. Favorable for an efficient laser operation of Ti:$\mathrm{Al_2O_3}$ is its large gain cross section[2] of $\sigma = 3\text{–}4 \times 10^{-19}\,\mathrm{cm}^2$. Moreover, no excited-state absorption can occur. This denotes an undesirable absorption of the pump or the laser radiation caused by potential transitions to other, higher energy levels. As in Ti:sapphire no levels above the ^{2}E state exist, this is not an issue.

The absorption and the emission bands are well separated from each other in the spectrum, additionally contributing to an effective laser. An impairment might be the presence of weak residual absorption at the emission wavelengths. In Figure 5.2 it is depicted as a long, constant wing of low intensity at the right-hand side of the pump band. When doping sapphire with titanium ions (around $0.1\,\%$ by mass), not only Ti^{3+} but also Ti^{4+} ions can appear. Responsible for the residual absorption, though, are Ti^{3+}–Ti^{4+} pairs whose formation comes along with them [123]. The solution consists in reducing the amount of Ti^{4+} in the crystal as best as possible. Advanced crystal growth techniques as the Czochralski, the vertical-gradient-freeze, or the heat-exchanger method have realized this [124–126]. To characterize the quality of the crystal in this regard, a figure of merit (FOM) is used. It is defined as the ratio of the crystal's absorption coefficients α for the pump wavelength (e.g., $\lambda = 532\,\mathrm{nm}$) and the emission wavelength (e.g., $\lambda = 800\,\mathrm{nm}$),

$$FOM = \frac{\alpha_{532}}{\alpha_{800}}\,. \tag{5.2}$$

Typically, titanium–sapphire crystals have a FOM above 100, where values from about 300 on mark crystals with (very) high quality. When comparing FOM values, one has to keep in mind that different pump and emission wavelengths may have been used.

The material properties of Ti:sapphire, such as the mechanical and thermal behavior, are quite advantageous. These are largely defined by the host material, sapphire. The material parameter values found in the literature differ somewhat according to the crystal quality, its doping level, and to which direction of the crystal axis they refer. Table 5.1 sums up these quantities. They are based on the information from the manufacturer[3] of the crystals used in this work. Particularly noteworthy are the supreme hardness and rigidity, the thermal conductivity, which is high among laser media, and the low thermal expansion. The possibility to attain a high surface quality makes the material even more insusceptible. The damage threshold is estimated to be $10\,\mathrm{J/cm^2}$ or higher [127, 128]. In this thesis, the Ti:sapphire crystal resisted the highest pump power of the *PLA* laser without any damage. With the laser characteristics presented in Chapter 3.3, a maximum pump fluence[4] of $(3.5 \pm 0.3)\,\mathrm{J/cm^2}$ at $532\,\mathrm{nm}$, with $14\,\mathrm{ns}$-pulses and a homogenous top-hat profile was determined, for a single surface of the crystal. Therefore, titanium-doped sapphire is very robust and well suited for high power laser operation. More parameters of the optical properties are detailed in Section 5.4 (absorption coefficients α and FOM) and Section 5.7.1 (thermo-optic coefficient $\mathrm{d}n/\mathrm{d}T$).

Today, titanium–sapphire lasers exist in many application areas and in different operating modes. Two principal domains result from the broad emission band of the gain medium. First,

---

[2] simply put, the probability for stimulated emission

[3] *GT Advanced Technologies / Crystal Systems*, USA

[4] see Subsection *Discussion* on page 93 for the term fluence

Parameter	**Symbol**	**Value**
Density	ρ	$3.98\,\mathrm{g/cm^2}$
Hardness, Mohs scale	HM	9
Hardness, Knoop scale	HK	1525–2000
Young's modulus	E	$345\,\mathrm{GPa}^*$
Bulk modulus	K	$379\,\mathrm{GPa}^*$
Specific heat capacity	c	$774\,\mathrm{J/(kg\,K)}^*$
Molar heat capacity	C_{mol}	$78\,\mathrm{J/(mol\,K)}$
Thermal conductivity	κ	$44\,\mathrm{W/(m\,K)}$
Thermal diffusivity	a	$14 \times 10^{-6}\,\mathrm{m^2/s}$
Thermal expansion	α_l	$8.4 \times 10^{-6}\,\mathrm{K^{-1}}$
Refractive index	n	1.76
Brewster's angle	θ_B	60.4°

Table 5.1: Mechanical, thermal, and optical properties of Ti:Al_2O_3. The values were obtained from or by calculation of crystal specifications [127]. The asterisk marks values available only for undoped sapphire. As host material it shows similar behavior.

tunable laser operation over a wide range is possible. This enables to tune the emission wavelength continuously and in addition gives access to a large wavelength region. By means of nonlinear frequency conversion, the spectral range can be expanded even more [33]. The lasers operate in continuous-wave or pulsed mode. Therefore, they are utilized as a flexible source of coherent radiation (e.g., [34, 129]). Second, broad emission bandwidth gives rise to the generation of ultrashort pulses. By using mode-locking techniques, pulse durations down to femtoseconds (fs) can be achieved. On the one hand, such short pulse durations are necessary to investigate processes at corresponding time scales. On the other hand, they allow to reach extremely high peak powers at the terawatt (TW) or yet the petawatt (PW) level. The Ti:sapphire medium then often acts in an amplifier configuration. Depending on the application, these systems work at pulse repetition frequencies of a few single pulses or in the order of MHz–GHz. The research field of ultrashort physics has become so extensive that at this point only the general literature shall be referenced [85, 121, 130].

5.2 Resonator Design

The resonator of a laser defines its mode(s) of operation. More specifically, it determines the field distribution and the propagation of the oscillating electromagnetic wave. In laser theory, the electromagnetic wave is treated in separate components, the longitudinal and the transverse modes. This is supported by the fact that the different laser performance properties can usually be assigned to one of the two components. While the spatial characteristics can be categorized under the transverse modes, the spectral characteristics are mainly attributed to the longitudinal modes. Thus, elemental properties of the generated radiation depend on the resonator design. Note that, in contrast, the parameters of the resonator (e.g., the length of the cavity) may influence both mode types. Without specific arrangements, the laser normally operates at several of these modes, the designated eigenmodes [85].

The objective of the design is to build a resonator that produces laser radiation according to the requirements discussed in Chapter 2.2.1. In summary, the resonator of the Ti:sapphire laser must be capable of high power and spectrally pure laser operation, and at the same time be efficient and robust. This is addressed by the following concept.

The design is based on a dynamically stable resonator [131–134]. In such resonators, the laser oscillation becomes stable at a certain focal length of an occurring thermal lens. High optical powers usually involve the formation of a thermal lens in materials which absorb part of the energy as heat. The thermal gradient in the medium causes a variation of the refractive index (by change of temperature and by stresses), as well as a geometrical distortion (of length and surface curvature). As a result, a beam propagating through the material shows the same behavior as if propagating through a lens. From all effects of the heat dissipation, the temperature dependent variation of the refractive index accounts most [135]. The focal length of the thermal lens is contingent on the deposited heat and thereby on the optical power. Hence, thermal lenses in cavities are normally undesirable, as they change the configuration, introducing a function of power. However, it is possible to take advantage of the thermal lens, using it explicitly as the beam-contracting element of the cavity. The point of operation where the resonator becomes nearly insensitive to the change of the thermal lens, is called dynamically stable.

In the titanium–sapphire laser a thermal lens arises in the active crystal due to the end-pumping at high powers. The thermal lens acts as a positive (focusing) lens. For the resonator, planar mirrors are chosen to provide the feedback for the stimulated light amplification. Thus, the thermal lens of the Ti:sapphire crystal represents, for a start, the sole focusing element of the cavity. Together with the cavity length, it determines the eigenmode of the resonator. For a full description, the relation between the focal length of the thermal lens and the pump power has to be known. Simply put, the higher the pump power, the shorter the focal length of the thermal lens. Consequently, an increasing power modifies the eigenmode such that its beam width is reduced more and more. Eventually, the energy of the laser is concentrated on such a small area that a compensating element is necessary to avoid optical damage. An analysis of the implementation of an additional negative (diverging) lens is imperative if higher powers are intended.

Furthermore, the laser should operate in single mode and at single frequency[5]. This provides the required spectral purity and efficiency. With regard to the spatial modes, a kind of mode iris has to be applied to impose operation at the fundamental mode only. Here, the beam of the pump laser itself acts as an iris. By virtue of the end-pumping configuration with an adapted beam, the gain along the transverse plane is delimited. Higher order transverse modes—having larger beam widths—experience no gain, and thus, cannot start to oscillate. It is an essential advantage of laser resonators that the spatial mode of operation can be controlled. For the selection of a single longitudinal mode other steps have to be taken. A skillful choice of the cavity length is made as it determines the free spectral range, i.e., the separation of the longitudinal modes in the spectrum. Moreover, frequency selection methods are involved, where an active stabilization

---

[5] in this thesis the term *single mode* refers to the fundamental transverse mode (TEM_{00}), whereas *single frequency* means exclusively one longitudinal mode

maintains the resonance condition.

Altogether, a preceding theoretical analysis of the fundamental eigenmode is crucial for the development of the laser resonator. The calculation is performed using the formalism of ray transfer matrices with Gaussian beams. The final purpose is to identify the dynamically stable point or a configuration that enables operation close to it. *A priori*, the calculation and the solution do not fix the *type* of resonator (i.e., its layout, reflectivity of mirrors, etc). However, the mentioned criteria contribute to the decision of the resonator type.

5.2.1 Eigenmode, Variation of the Thermal Lens, and Dynamical Stability

The calculation of the eigenmode of the resonator is based on a combined description of the laser beam as an electromagnetic wave and as a ray path from geometrical optics (both in paraxial approximation[6]) [58, 136–138]. The latter considers the passage of a light ray through optical elements as a transformation which is mathematically represented by a matrix

$$\mathbf{M} = \begin{pmatrix} A & B \\ C & D \end{pmatrix} . \tag{5.3}$$

The matrix linearly maps the ray vector, consisting of two components—the distance w and the angle θ to its propagation axis at a certain position z. Different optical structures are defined by the items $ABCD$. A ray transfer matrix can symbolize individual but also a sequence of optical elements. Particularly, it opens up the study of periodical propagation, as it is the case in resonators.

From the wave equation results, as elementary solution, a wave with a Gaussian intensity distribution in the transverse profile, and a slowly changing phase front while traveling. The spatial aspects of this Gaussian beam are summarized in a complex beam parameter q,

$$\frac{1}{q(z)} = \frac{1}{R(z)} - i \, \frac{\lambda}{\pi \, w(z)^2} . \tag{5.4}$$

It is characterized by the radius of curvature R of the wavefront, and the width w of the beam. The two parameters evolve as a function of the location z according to the equations

$$R(z) = z \left(1 + \frac{{z_R}^2}{z^2} \right) , \tag{5.5}$$

$$w(z)^2 = {w_0}^2 \left(1 + \frac{z^2}{{z_R}^2} \right) . \tag{5.6}$$

The course of the beam width along its propagation direction has a minimum, so-called beam waist w_0. Often, the place of the waist is declared as the origin, $z = 0$. Otherwise its position is given by a value z_0. Then, z has to be replaced by $z - z_0$ in the equations above. The width w

---

[6] The paraxial approximation assumes that the transverse intensity distribution (x–y plane) varies only slowly with the propagation distance z of the beam. In the region close to the optical axis—the so-called paraxial region—the dependence of the transverse wave amplitude on z is negligible. This is valid for waves traveling at small distances w and small angles θ to the propagation axis.

is usually measured at $1/e$ of the electrical field's amplitude. In the following, all widths refer to the radius of the beam. The distance from the waist to the position where the width increases by a factor of $\sqrt{2}$ is determined by the Rayleigh length,

$$z_R = \frac{\pi\, {w_0}^2}{\lambda}\ . \tag{5.7}$$

In the far-field, the beam progressively spreads. There, the divergence can be quantified by the (half) aperture angle of the beam,

$$\theta = \frac{\lambda}{\pi\, w_0}\ . \tag{5.8}$$

A Gaussian beam is unique for given wavelength λ, and either w_0, z_R, or θ.

The propagation of a Gaussian beam through optical structures can be associated with the $ABCD$ matrix formalism (see Appendix A.1). In a resonator, the laser beam experiences a periodic run through a total set of elements. Thus, a total matrix, comprising one round trip of the beam, is assigned to a specific resonator configuration. The condition of stability claims that the parameters of the wave remain the same for periodic propagation. This declared self-consistency, finally, provides the solution of the resonator's eigenmode, where the handling with a Gaussian beam reveals the fundamental mode. If the evaluation is executed without defining the resonator configuration, i.e., using the (unspecified) matrix (5.3), a general expression for the eigenmode is obtained. The related beam parameters are

$$R = \frac{2B}{D-A}\ , \tag{5.9}$$

$$w^2 = \pm\frac{\lambda}{\pi}\,\frac{2B}{\sqrt{4-(A+D)^2}}\ , \tag{5.10}$$

$$z = \frac{A-D}{2C}\ , \tag{5.11}$$

$${w_0}^2 = \pm\frac{\lambda}{\pi}\,\frac{\sqrt{4-(A+D)^2}}{-2C}\ , \tag{5.12}$$

where R and w correspond to the plane from which the round-trip propagation starts/ends. Hence, this plane is located at distance z from the beam waist w_0. To get real solutions the term under the square root must be nonnegative, $4-(A+D)^2 \geq 0$. The condition possibly unveils more interesting information.

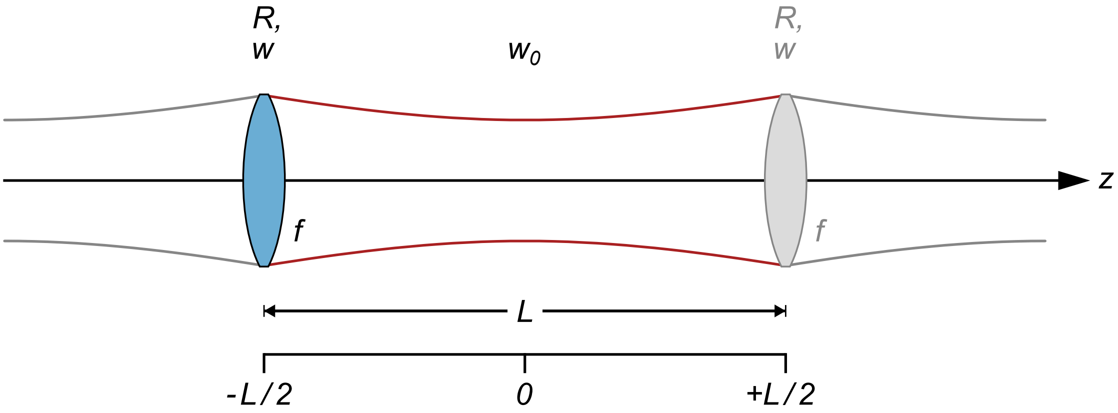

Figure 5.3: Illustration of the periodic propagation scheme and the caustic of the fundamental eigenmode for a resonator with one lens. If the focal length is variable (e.g., due to a thermal lens in the laser crystal) the mode volume changes, but the location of the waist remains constantly in the middle of the free-space propagation.

Ring Resonator with One Lens

A simple—or maybe even the easiest—configuration of a ring resonator consists of one lens and a spacing before and/or after it. Let f be the focal length of the (focusing) lens, and L the entire (optical) length of the cavity for one round trip. When choosing the scheme of periodic passage such that the input and output plane of the transfer are immediately in front of the lens, the total matrix of the configuration reads

$$\mathbf{M}_{tot1} = \begin{pmatrix} A & B \\ C & D \end{pmatrix} = \begin{pmatrix} 1-\frac{L}{f} & L \\ -\frac{1}{f} & 1 \end{pmatrix} . \tag{5.13}$$

The derivation of the matrix can be found in Appendix A.2. Using Equations (5.9) to (5.12) the beam parameters of the fundamental eigenmode yield

$$R = 2f \; , \tag{5.14}$$

$$w^2 = \frac{\lambda}{\pi} \frac{2Lf}{\sqrt{4Lf - L^2}} = \frac{\lambda}{\pi} \frac{1}{\sqrt{\frac{1}{Lf} - \frac{1}{4f^2}}} \; , \tag{5.15}$$

$$z = \frac{L}{2} \; , \tag{5.16}$$

$$w_0{}^2 = \frac{\lambda}{\pi} \sqrt{Lf - \frac{L^2}{4}} \; . \tag{5.17}$$

The equations demonstrate the dependence of the parameters on the resonator length and the focal length of the lens. It is of particular interest when these quantities vary. With its thermal

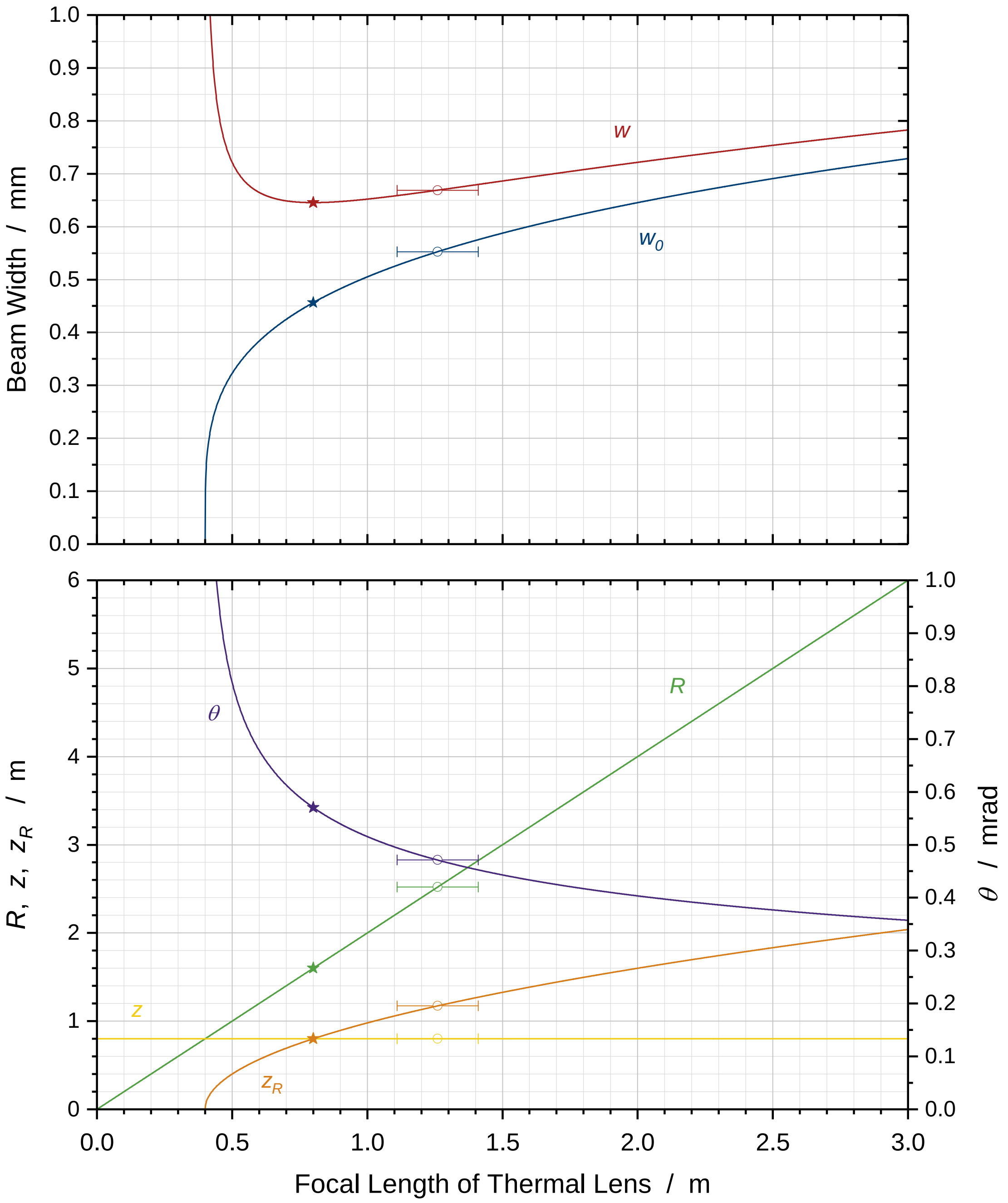

Figure 5.4: Parameters of the fundamental eigenmode for a ring resonator configuration with one (thermal) lens as a function of its focal length f. **Top:** Beam width w at the laser crystal, and waist w_0 (both radii). **Bottom:** Radius of curvature R at crystal position, distance z to waist location, Rayleigh length z_R, and far-field divergence angle θ. The constants for the plot are $L = 1.6\,\mathrm{m}$ and $\lambda = 818\,\mathrm{nm}$. The dynamically stable point is marked with $\star$. The circle with the error bar indicates the situation for the sagittal plane of the realized laser operation at $10\,\mathrm{W}$.

lens of the laser crystal, the Ti:sapphire laser presents such a situation. If no other beam transforming elements are involved, the resonator corresponds to the configuration discussed here. The cavity has a fixed length L and the focal length of the thermal lens varies with the pump power, $f = f_{th}(P_{pump})$.

The values of the radius of curvature R and the beam width w (Equations 5.14 and 5.15) are obtained for the position directly in front of the thermal lens, i.e., at the laser crystal. It can be noted that the distance z to the location of the waist w_0 is independent of f (Equation 5.16). Therefore, the waist always lies at the "middle" of the cavity length. Figure 5.3 illustrates this with a plot of the eigenmode's caustic. Attention has to be paid to the origin of the axis for the propagation direction. It might be confusing that the beam waist is defined to be at $z = 0$, whereas the calculation of the ray transfer matrix begins with the lens.

The influence of a changing thermal lens is evaluated in Figure 5.4. The course is traced as a function of the focal length f for the beam widths w and w_0, as well as for the parameters R, z, z_R and θ, respectively. The latter two were calculated with the help of Equations (5.7) and (5.8). For a growing thermal lens (i.e., a shorter focal length) both beam widths, the Rayleigh length, and the divergence, approach a vertical asymptote. This becomes clear by looking at the square root term of the corresponding equations. The aforementioned condition for the radicand gives $f \geq L/4$.

The curve of the beam waist w_0 reveals how the minimum beam size decreases as the thermal lens gets stronger. This allows to calculate the laser beam's fluence and find a critical value for the focal length, which should not be lower in order to avoid optical damage. Certainly, the positions where optical components are placed within the beam caustic stipulate the definite limit.

Of special interest in the progression of w is the passage through a valley. The minimum is the desired dynamically stable point of operation. As is well known, it can be determined by

$$\frac{\partial w}{\partial f} = 0 \, . \tag{5.18}$$

This condition leads to a solution $f^\star$ of the focal length, which can be inserted into the other equations to obtain the value of the parameters at this point. For Equation (5.15) the result is a focal length of

$$f^\star = \frac{L}{2} \, , \tag{5.19}$$

and hereby follow the beam widths

$$w^{\star 2} = \frac{\lambda}{\pi} \, L \, , \tag{5.20}$$

$$w_0^{\star 2} = \frac{\lambda}{\pi} \, \frac{L}{2} \, . \tag{5.21}$$

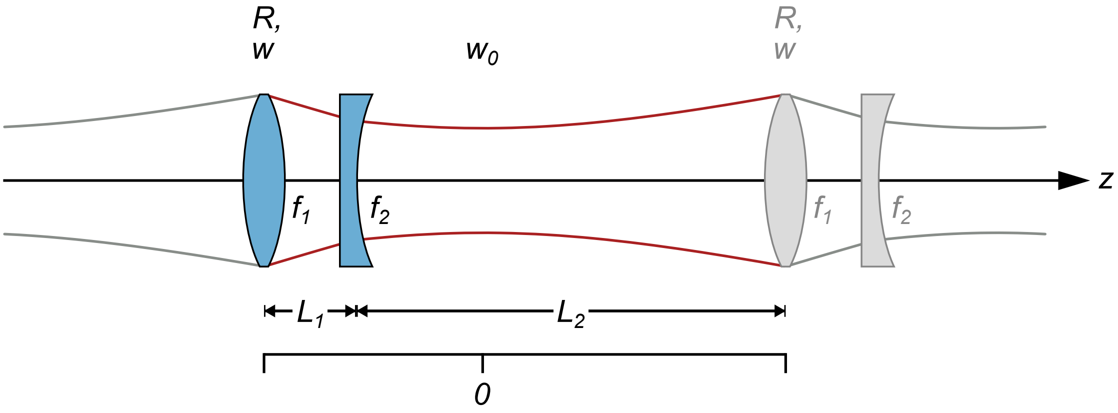

Figure 5.5: Schematic representation of the eigenmode's periodic propagation in a resonator configuration with two lenses. The second diverging lens is installed to compensate for the strong focusing of the primary (thermal) lens at high powers. Now, a variation of the thermal lens' focal length f_1 also causes a displacement of the waist. The image depicts the case described in the text, where the waist is shifted a little towards the lenses.

Ring Resonator with Two Lenses

The singular behavior of the eigenmode's beam parameters at short focal lengths impedes the application of powers at which the thermal lens becomes that strong. This calls for an additional element in the resonator to compensate the intense focusing of the eigenmode. The integration of a second lens modifies the beam caustic, pushing the boundary of destructive energy density a little farther.

For the calculation of the ray transfer matrix the circumstances may be as follows (see Figure 5.5). The propagation starts at the primary (thermal) lens of focal length f_1. At a distance L_1 behind this lens, the second lens of focal length f_2 is placed. The remaining distance of the resonator cycle is denoted with L_2. Thus, the entire (optical) length of the resonator is $L = L_1 + L_2$. The total matrix of the described sequence turns out to be (see Appendix A.2 for details)

$$\mathbf{M}_{tot2} = \begin{pmatrix} A & B \\ C & D \end{pmatrix} = \begin{pmatrix} 1 - \frac{L}{f_1} - \frac{L_2}{f_2} + \frac{L_1 L_2}{f_1 f_2} & L - \frac{L_1 L_2}{f_2} \\ -\frac{1}{f_1} - \frac{1}{f_2} + \frac{L_1}{f_1 f_2} & 1 - \frac{L_1}{f_2} \end{pmatrix} . \tag{5.22}$$

The matrix already indicates that the solution for the fundamental eigenmode is more extensive. Inserting the $ABCD$ elements into the general equations for the beam parameters results in long terms. That is why they are not listed here but in Appendix A.3. The condition for dynamical stability reduces the complexity somewhat. Again, the aim is to find the situation for which the change of the beam width w disappears (or, is small) against a variation of the focal length f_1 of the thermal lens,

$$\frac{\partial w}{\partial f_1} = 0 . \tag{5.23}$$

In comparison to the resonator with one lens, there are two more variables in the equations now. Consequently, for the calculation of a complete solution, two additional quantities must be known. According to the ones given, the equations are rearranged. Three scenarios are demonstrated in order of successive derivation.

First, if f_2, L_1, and L_2 (thus, also L) are predefined, the dynamically stable point $(f_1^\star \,|\, w^\star)$ is obtained by

$$f_1^\star = \frac{L - \frac{L_1 L_2}{f_2}}{2 - \frac{L}{f_2}} \,, \tag{5.24}$$

$$w^{\star 2} = \frac{\lambda}{\pi} \left(L - \frac{L_1 L_2}{f_2} \right) \,. \tag{5.25}$$

Second, for given f_2, $w^\star$, and L, dynamical stability is achieved when the thermal lens has the focal length and the distance to the compensating lens of, respectively,

$$f_1^\star = \frac{\pi}{\lambda} \frac{w^{\star 2}}{2 - \frac{L}{f_2}} \,, \tag{5.26}$$

$$L_1 = \frac{L}{2} \pm \sqrt{\left(\frac{L}{2}\right)^2 + f_2 \left(\frac{\pi}{\lambda} w^{\star 2} - L\right)} \,. \tag{5.27}$$

Third, provided that the values for $f_1^\star$, $w^\star$, and L are fixed, then

$$f_2 = \frac{L}{2 - \frac{\pi}{\lambda} \frac{w^{\star 2}}{f_1^\star}} \,, \tag{5.28}$$

$$L_1 = \frac{L}{2} \pm \sqrt{\left(\frac{L}{2}\right)^2 + \frac{L\left(\frac{\pi}{\lambda} w^{\star 2} - L\right)}{2 - \frac{\pi}{\lambda} \frac{w^{\star 2}}{f_1^\star}}} \,. \tag{5.29}$$

In any case the corresponding beam parameters at the dynamically stable point can be calculated ultimately with

$$w_0^{\star 2} = \frac{\lambda}{\pi} \frac{L - \frac{L_1 L_2}{f_2}}{1 + \left(1 - \frac{L_1}{f_2}\right)^2} = \frac{w^{\star 2}}{1 + \left(1 - \frac{L_1}{f_2}\right)^2} \,, \tag{5.30}$$

$$z^\star = \frac{L - \frac{L_1 L_2}{f_2}}{1 - \frac{L_1}{f_2} + \frac{1}{2 - L_1/f_2}} = \frac{\lambda}{\pi} \frac{w^{\star 2}}{1 - \frac{L_1}{f_2} + \frac{1}{2 - L_1/f_2}} \,, \tag{5.31}$$

$$R^\star = L_2 + \frac{L_1}{1 - \frac{L_1}{f_2}} \,. \tag{5.32}$$

The third of the mentioned instances applies to the operation at a certain (pump) power. In such a design scenario the focal length of the thermal lens, the beam width on the laser crystal, and the resonator length are predetermined. The equations (5.28) and (5.29) then deliver the

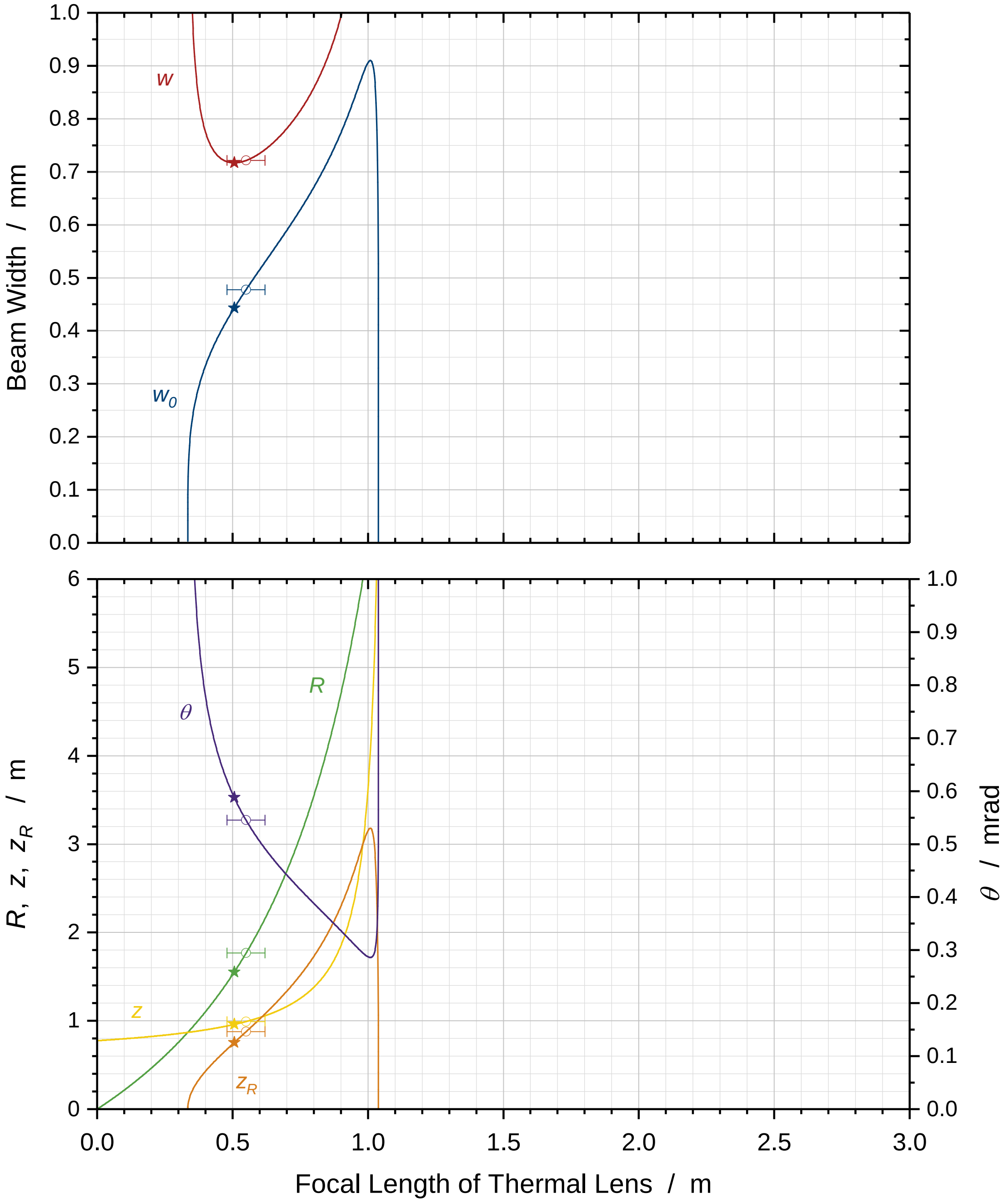

Figure 5.6: Eigenmode parameters for the two–lens ring resonator configuration discussed in the text, as a function of the thermal focal length f_1. **Top:** Beam width w at the laser crystal, and waist w_0 (both radii). **Bottom:** Radius of curvature R at crystal position, distance z to waist location, Rayleigh length z_R, and far-field divergence angle θ. The dynamically stable point is marked with $\star$. The circle with the error bar indicates the situation for the tangential plane of the realized laser operation at 10 W.

information which focal length is needed for the second lens and where it has to be located in the cavity.

An experimental scenario is represented by the first case. The focal length and the position of the compensating lens are subject to practical realization. For the focal length values at incremental steps are usually offered by the lens suppliers. Also, the installation of the lens in the experiment is not possible at arbitrary positions, e.g., due to collision with other objects. Hence, if these parameters are preset, the equations (5.24) and (5.25) determine which focal length of the thermal lens and beam width at crystal will result for dynamical stability.

Analogous to the one–lens resonator it is possible to analyze, for an experimental configuration where f_2, L_1, and L_2 are fixed, the function of the beam parameters against the thermal lens' focal length. For this purpose, the principal equations of the eigenmode parameters (see Appendix A.3) were used. Figure 5.6 shows the resulting curves of the beam widths (w, w_0) and the other parameters (R, z, z_R, θ). The constants were $f_2 = -842\,\mathrm{mm}$, $L_1 = 230\,\mathrm{mm}$, and $L_2 = 1370\,\mathrm{mm}$. This configuration corresponds to the setup that later came into operation.

Most noteworthy are the following differences of the resonator with a compensating lens and the previous configuration. The minimum of w turns up at the design focal length of the thermal lens or according to the setting of the second lens. The beam widths are raised to some extent (cf. top panel of Figure 5.4) for the same focal length values. This is especially true for the waist and discussed further in the next section. Besides, the values of the beam widths are nonsingular only within an explicit zone of the focal length of the thermal lens. This zone delimits the stable operation of the resonator. The extent is considerably narrower than the interval $[\frac{L}{4}, +\infty)$ for the one–lens resonator. On that account it is understood that the configuration of a resonator with two lenses is conceived to operate at (or close to) a design point of power. A formula that specifies the extent of the zone can be found in [138, 139]. Moreover, it should be noted that the location of the beam waist in the resonator now depends on the thermal focal length. The waist position is slightly shifted away from the "middle" of the cavity as is also depicted in the caustic plot of Figure 5.5.

Discussion

High power operation of a laser is limited by the intensity or the fluence of its beam inside the resonator. The optical components of the resonator withstand until a maximum value is reached. For the power–energy–time domain of the pulsed lasers treated here, the fluence is more likely the limiting factor. Being defined as an energy density relative to the cross-sectional area of the beam, it increases if the beam width gets smaller (or if the energy is raised of course). The exact beam width, in turn, depends on the place in the cavity. Speaking of the entire caustic in the resonator, the expression mode volume is utilized. The analysis showed that the volume of the fundamental eigenmode decreases for an augmenting thermal lens. The latter again, increases with the power.

Thus, to achieve high power laser operation, the first step is to keep the thermal lens low, i.e., at large focal lengths. This is approached by efficient cooling of the laser crystal (see Section 5.4). Furthermore, the equations show that a large mode volume is generally obtained for a long resonator length. The choice of a long resonator length competes with the available space and the objective of spectrally far-separated longitudinal modes (see next section). A trade-off between these interests is necessary. Beyond that, the contraction of the eigenmode is counteracted by the two–lens resonator configuration. The compensating lens extends the critical power limit. However, it also represents an additional element causing losses. As a consequence, the laser threshold is raised, and higher pump powers are needed to obtain the same output power.

It is important to mention that Ti:sapphire crystals in so-called Brewster-cut exhibit a thermal lens of different focal length for the tangential and the sagittal plane[7]. The shape of such crystals is from top view[8] that of a parallelogram where the end surfaces are cut at Brewster's angle. Due to refraction of the tangential component of the laser beam and the concomitant twofold shearing, this beam width component is expanded inside the crystal. The expansion factor equals the refractive index of Ti:sapphire. As the sagittal component is not affected, an originally circular beam profile in the crystal becomes elliptical. It is demonstrated that ultimately this causes a thermal lens where the focal length is shorter in the tangential plane than in the sagittal plane [30, 129]. An individual analysis for each plane is necessary. Different focal lengths of the thermal lens lead to a fundamental eigenmode that is asymmetric[9], and for the two–lens resonator configuration also astigmatic[10].

As will be shown later, for the Ti:sapphire laser it is sufficient to compensate the eigenmode contraction in the tangential plane only to achieve laser operation at the aspired average output power,. The implemented compensating lens is cylindrical. Therefore, the tangential component of the eigenmode is described by the configuration of a resonator with two lenses, and the sagittal component by a resonator with one single (thermal) lens. Of key significance at this point is that both states are interrelated by the condition

$$w_x := w_y \ , \tag{5.33}$$

which declares that at the position of the thermal lens (i.e., at the laser crystal) the beam width is as big in the tangential plane as in the sagittal plane. This ensures that the pumping efficiency is the same in both planes, assuming a circular beam profile of the pump laser beam. Basically, the implementation of the cylindrical lens is the solution to counterbalance the different focal lengths in the two planes of the thermal lens.

In practice, this cannot be achieved perfectly. The experimental settings of the cylindrical lens will slightly deviate from the theoretically determined ones, for the above-mentioned reasons. As a result, the condition (5.33) is fulfilled approximately. In the end, an output beam of elliptical profile emerges, which should not be of concern for the lidar application. Note also that an exact operation at the dynamically stable point is not always feasible for both eigenmode components simultaneously. While the tangential resonator configuration is systematically designed for, in the sagittal plane it might occur that the beam's critical energy density is reached before the ideal stability point $f^\star$ is attained. However, in the curve progression of the beam

---

[7] In this thesis the tangential plane is equivalent to the plane parallel to the optical table, or the horizontal direction, also denoted with x. The sagittal plane is perpendicular and equivalent to the vertical direction, also denoted with y.

[8] view of the x–z plane

[9] asymmetry means unequal waist width components, $w_{0,x} \neq w_{0,y}$

[10] astigmatism signifies dissimilar locations of the waist components, $z_{0,x} \neq z_{0,y}$

width w, the valley around $f^\star$ is quite broad, and the effect due to deviations of the focal length is minor.

For the present setup of the titanium–sapphire laser the following values are calculated (the nominal wavelength being $\lambda = 818\,\mathrm{nm}$). A cavity of total length $L = 1.6\,\mathrm{m}$ is chosen. The one–lens resonator configuration provides insight to the general dynamic of the laser and describes the eigenmode in the sagittal plane (Figure 5.4). The stability point is at the focal length $f^\star_{th,y} = +800\,\mathrm{mm}$ (Equation 5.19). For it, the beam radius at the laser crystal is $w_y = 0.65\,\mathrm{mm} \approx 0.7\,\mathrm{mm}$ (Equation 5.20). As estimated in Chapter 3.1, to achieve a laser output power of $P = 10\,\mathrm{W}$, a pump power of $P_{pump} \approx 40\,\mathrm{W}$ is necessary. The characterization of the thermal lens shows that at this pump power level the focal length is $f_{th,y} \approx +960\,\mathrm{mm}$ in the sagittal plane, and $f_{th,x} \approx +425\,\mathrm{mm}$ in the tangential plane (Section 5.7.1). Due to the short focal length in the tangential plane, the mode volume then becomes so small that the fluence exceeds the damage threshold of the Ti:sapphire laser's constituents.

That is why a compensating lens is introduced to the tangential plane of the eigenmode. Using $f_{th,x}$ and condition (5.33) in Equations (5.28) and (5.29), the parameters for the cylindrical lens are calculated to obtain dynamical stability in the tangential plane at the design power. The aimed focal length is $f_{cyl} = -879\,\mathrm{mm}$ and the lens must be placed at distance $L_1 = 13\,\mathrm{mm}$ in front or behind the thermal lens. The focal length of cylindrical lenses available through manufacturers are very close to the intended value. The most expedient model[11] has a focal length of $f_{cyl} = -842\,\mathrm{mm}$ at $\lambda = 820\,\mathrm{nm}$. In contrast, the physical position cannot be realized (explanation of the setup in Section 5.3). The least distance between the thermal and the cylindrical lens that is put into practice is $L_1 \approx 230\,\mathrm{mm}$. As the real parameters of the compensating lens deviate from the ideal ones, the behavior of the tangential beam parameters over the thermal focal length is reanalyzed with the two–lens resonator configuration (Figure 5.6). Dynamically stable operation is obtained now for $f^\star_{th,x} = +506\,\mathrm{mm}$ (Equation 5.24), yielding the beam radius $w^\star_x = 0.72\,\mathrm{mm}$ at the laser crystal (Equation 5.25). This value of the tangential focal length of the thermal lens was attained at a pump power $P_{pump} \approx 34\,\mathrm{W}$. For this power, the sagittal focal length was $f_{th,y} \approx +1153\,\mathrm{mm}$, yielding a beam radius at the laser crystal of $w_y = 0.66\,\mathrm{mm}$. Moreover, with the beam waist widths being $w_{0,x} = 0.46\,\mathrm{mm}$ and $w_{0,y} = 0.54\,\mathrm{mm}$, the mode volume approaches a demanding small size. The total efficiency of the laser resulted to be higher than expected, and thus, the laser output power of $P = 10\,\mathrm{W}$ was achieved at pump powers very close to this design point (Section 5.7.2).

5.2.2 Resonator Type

While in the previous section the resonator *configuration* described which beam focusing elements are incorporated in the cavity and at which distance to each other they are placed, the resonator *type* shall refer to the geometrical layout of the mirrors that form the cavity. Although the resonator configuration fully defines the transverse field distribution and the propagation of the laser eigenmode, the choice of type still has serious impact on the laser action. The Ti:sapphire laser is set up in a folded four-mirror, unidirectional-ring resonator geometry (see Figure 5.7). This section explains why this resonator type is optimal for the required operation.

---

[11] see footnote 65 on page 125

The arguments are drawn from references [58] and [140].

In linear resonators the propagation (back and forth) of the laser light causes a standing wave. This way, inside the gain medium the saturation degree varies along the longitudinal axis. It is minimal at the spots of the wave nodes. The phenomenon is called spatial hole burning and basically has two consequences. On the one hand, it provokes mode competition of adjacent longitudinal modes, as they benefit from the unsaturated regions. On the other hand, if these modes are otherwise inhibited, the extraction efficiency of the medium is lower. Ring resonators with unidirectional propagation of the laser beam do not experience spatial hole burning. The wave continuously travels through the active medium and generates a homogenous gain. One longitudinal mode prevails over its adjacent ones and harvests more power output. Hence, single-frequency operation at high powers is easier and even more efficient in unidirectional ring resonators.

The resonator structure of a ring circulating only in one direction has further advantages. The extension of the optical ray paths across the laser mirrors towards the outside of the cavity shows that outgoing and incoming paths are separate (i.e., not coaxial). On the one hand, this eliminates feedback to a different source being injected into the resonator, as for injection seeding. On the other hand, it provides additional opportunities to monitor the laser light of the resonator. Another feature of ring resonators is an increased misalignment insensitivity. Despite small perturbations in the tangential plane the round-trip path of the beam stays closed. Moreover, the stability zone of a variable thermal lens as discussed in the previous section is twice as wide for a ring resonator than for a linear configuration [138, 139]. In general, ring cavities have a free spectral range twice as large as a linear cavity of same length (cf. Equation (3.3) with (3.8) on pages 34 and 47, respectively). For an (optical) length $L = 1.6\,\mathrm{m}$ of a ring resonator the spectral separation of the longitudinal modes is $\Delta\nu_{FSR} \approx 187\,\mathrm{MHz}$.

There are few disadvantages of the unidirectional ring type. The intricacy of the arrangement can be greater. Nevertheless, the technical effort of linear resonators that apply special propagation schemes to overcome spatial hole burning is similar. The circulation of a beam in a ring furthermore induces astigmatism due to the off-axis reflection on the mirrors. Finally, the laser light is amplified only once per round-trip in the gain medium. In comparison to a linear resonator with identical parameters the pump power must be higher to compensate the lower gain and to obtain equal output power. Viewed differently, the ring resonator experiences an overcoupling of the intracavity power as the light encounters the output coupler two times for the same gain. By adapting the reflectivity of the output coupler appropriately, the laser power recovers the same output level.

The issues are handled as follows. The cavity layout consists of four mirrors: three highly reflecting mirrors, and one output coupler. The mirrors are arranged in such manner that the ring is folded, and the ray path has the form of a bow-tie, lending the name[12] to this layout. For this geometry, the angle of incidence on the mirrors is small and the effect of astigmatism minor or even nonexistent. Additionally, the folding of the ring enables a longer resonator length while maintaining the needed area. Section 5.5 describes how the unidirectional laser emission in the ring is enforced.

The selection of a suitable reflectivity value of the output coupler relies on the simulations

---

[12] sometimes it is also referred to as “X” or “folded-Z” shaped resonator

by WAGNER. In the performance model, the dependency of the laser output pulse energy on the output coupler reflectivity and the pump pulse energy was analyzed. It revealed an optimum extraction efficiency at reflectivities $R = 50\,\%$ to $70\,\%$ for the relevant pump powers [30]. The decision for an output coupler reflectivity of $R = 60\,\%$ is in line with the optimum extraction efficiency, but the value is slightly reduced in favor of an eased fluence of the laser beam inside the resonator. Merely at the beginning of the laser development, an output coupler with $R = 80\,\%$ was used as it lowers the laser threshold, making the first-time adjustment, to obtain resonance, easier. The finesse and the cavity linewidth ensuing from the mirror reflectivities are determined in Section 5.6.2.

5.3 Laser Setup

The setup of the titanium–sapphire laser was realized according to the insights from the resonator design and the best possible practical implementation. Prior to the assemblage, the setup was constructed as a computer-aided design (CAD) model to test the arrangement of the components, considering the experimental constraints, i.e., space consumption and mounting options. Pictures of the CAD model can be found in Appendix C. A schematic drawing of the Ti:sapphire laser setup is presented in Figure 5.7.

The principal element is the resonator. The bow-tie layout of the cavity has a shorter arm at the bottom and a longer arm at the top. The Ti:Al_2O_3 crystal is located in the middle of the short arm. The laser crystal is built into a specially developed cooling mount (detailed in the next section) and pumped from both end-surfaces. For efficient laser operation the pump beam must propagate coaxially with the laser beam inside the crystal. Outside of the crystal, the dispersion of the beams only occurs at large distances. Therefore, the beams travel close to each other and the pump beam has to be directed through the laser mirror. On that account the coating of the two laser mirrors[13] at the bottom side of the cavity is dichroic—highly reflective at the laser wavelength and anti-reflective at the pump wavelength.

In the upper part of the bow-tie cavity, the laser mirror on the left-hand side is mounted on a piezo actuator. The piezo actuator is used to finely adjust the cavity length and maintain single-frequency laser-resonance. The chosen model[14] has an inner hole, serving as clear aperture to monitor the optical leakage signal of the resonator. As the laser mirror is attached to the piezo actuator, size and weight of the optic are adapted. In contrast to all other mirrors and lenses in the setup which are of $1\,\mathrm{inch}$ diameter, this mirror has a diameter of $1/2\ \mathrm{inch}$. The mirror[15] possesses a (single) high reflectivity coating at the laser wavelength. The fourth of the cavity mirrors located on the right-hand side is the output coupler[16]. Its reflectivity is $R = 60\,\%$ as stated before. The incoming beam path through the output coupler is used to inject the seed laser.

In the diagonal beam paths of the bow-tie cavity further optical elements are arranged. A half-wave plate and a Faraday rotator are the principal components ensuring unidirectional beam

---

[13] *Laser Components*, HR820HT532/10/AR PI1025UV (10°-AOI coating)

[14] *Physik Instrumente (PI)*, PICA Thru Ring Actuator P-010.00H

[15] *Laser Components*, HR820 PW0504UV

[16] *Laser Components*, PR815/60/AR PI1025UV

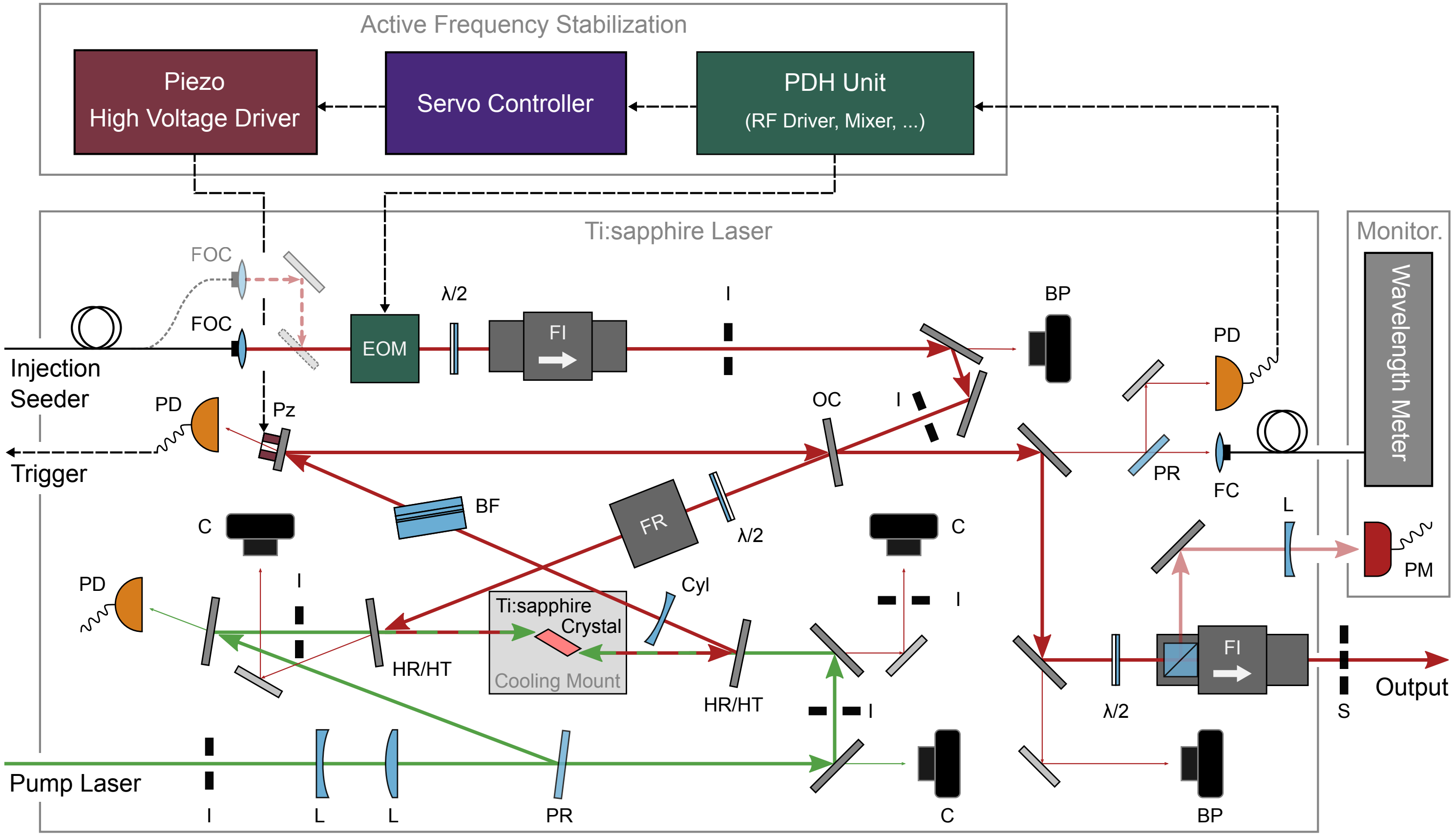

Figure 5.7: Setup of the Ti:sapphire laser. BF – birefringent filter, BP – beam profiler, C – camera, Cyl – cylindrical lens, EOM – electro-optic modulator, FC / FOC – fiber (output) coupler, FI / FR – Faraday isolator/rotator, HR/HT – mirror with highly reflective coating at $818\,\mathrm{nm}$ and anti-reflective coating at $532\,\mathrm{nm}$, I – adjustment iris, L – lens, $\lambda/2$ – half-wave plate, OC – output coupler, PD – photodiode, PM – power meter, PR – partially reflective mirror, PDH – Pound–Drever–Hall, Pz – laser mirror mounted on piezo actuator, RF – radio frequency, S – shutter. Unmarked mirrors are highly reflective at the wavelength of the corresponding laser beam. A few secondary monitoring devices have been omitted in this figure. Solid lines indicate optical paths. Dashed lines indicate electrical connections.

propagation in the ring resonator (see Section 5.5). For the control of the laser emission frequency, in addition to injection seeding, a birefringent filter comes into operation. It assumes the task of coarsely or pre-selecting the wavelength. The complete method of frequency selection including the single-frequency control is explored in Section 5.6. Last, the cylindrical lens is placed in the resonator to render possible higher output powers.

Generally, the optical elements in the resonator should be positioned in such manner that the distance to the location of the eigenmode's beam waist is maximized. In doing so, the local values of the fluence, and thus, the risk of optical damage are decreased. From the resonator design calculations and geometrical measurements, it was found that the beam waist is located approximately in the middle between the piezo mirror and the output coupler. That is why this arm of the bow-tie resonator is conceived longer and does not contain any optical components. The half-wave plate and the Faraday rotator are situated in the diagonal path heading towards the laser crystal as their influence on the beam direction is negligible or only moderate. Hence, the adjustment of this primary section is simplified. On the contrary, the birefringent filter causes a significant offset of the beam ray. The mount of the filter is quite bulky and installed in the opposite diagonal path. With regard to the cylindrical lens, the ideal position determined by the condition of dynamical stability represents a challenge. Theoretically, the compensating lens would have to be placed in close proximity to the thermal lens. On the one hand, this is hindered by the extent of the crystal cooling mount or even by the crystal length itself. On the other hand, the lens must withstand the additional optical power of the pump beam that is directed through it. Cylindrical lenses with a corresponding dichroic anti-reflective coating[17] were tested in action but could not resist the joint high power density. Although uncoated lenses would possibly endure these power levels, they have not been taken into consideration as it would entail too many losses in the resonator. In the end, high power laser operation was successful when positioning the cylindrical lens on the diagonal ray path behind the thermal lens, still at the shortest possible distance to it. Different lens models were applied (see Section 5.7.2), with a coating which is anti-reflective at the laser wavelength only.

In the lower area of the setup, the pump laser beam is directed to the Ti:sapphire crystal. At first, the pump beam is adapted to the Ti:sapphire laser mode with a lens combination according to the pump laser employed (refer to Chapters 3.2.4 and 3.3.4). Subsequently, the pump beam is divided into two beams of half power, which are directed onto each side of the crystal end-surfaces. The arrangement of the bending mirrors might appear peculiar, but results from spatial constraints and the intention of avoiding unessential mirrors. Then again, both partial beams should be fully and individually adjustable, calling for two mirrors for each branch. In the left branch the angle of incidence on the partially reflective mirror[18] and the bending mirror[19] is close to the mirrors' normal vector, $AOI \approx 6°$. For the right branch the reflection on the bending mirrors[20] is at the common AOI of $45°$. The mirrors (except the partially reflective mirror) are highly reflective at $532\,\mathrm{nm}$ and highly transmissive at $1064\,\mathrm{nm}$ to filter out residual infrared radiation. The position of the mirrors is arranged in such way that the length of the two branches is identical. This guarantees that the adapted pump beam mode impacts equally on

---

[17] *Laser Components*, AR/AR818+532 RCC25.4-25.4-362.6UV, and -340.0UV (both IBS1)

[18] *CVI / Melles Griot*, PR1-532-50-1025

[19] *CVI / Melles Griot*, LWP-0-R532-T1064-PW1-1025-UV-S

[20] *Laser Components*, HR532HT1064/45/BAR PW1025UV

both sides of the laser crystal. The length of these branches determines a minimum distance for the mode matching of the pump beam and positioning of the lens combination, as discussed in the corresponding chapter.

The injection seeding path (or, more precisely, the final segment of it) is found at the top of the Ti:sapphire laser setup. Chapter 4.7 already described that the laser radiation of the seeders is brought to the setup via a fiber and a collimator. Two versions thereof are available. Details about the used model and the related longitudinal mode-matching as well as the two mirrors at the end of the path, used for the lateral and angular mode matching, can be found in the referred chapter. Along the path, the beam passes through three further elements. The electro-optic modulator (EOM) is part of the frequency stabilization technique. The following half-wave plate[21] changes the linear polarization from the vertical s-state, required by the EOM, to the horizontal p-state. The subsequent Faraday isolator is a two-stage model[22] with an optical isolation $\geq 60\,\mathrm{dB}$. It ensures once again the protection of the sensitive seed lasers against unexpected returning strong pulses of the Ti:sapphire laser. A positive side-effect of the two-stage isolator is that the orientation of the beam's linear polarization is the same after the transmission as at the entry. Thus, it conforms to the p-polarized resonator eigenmode.

The output beam of the Ti:sapphire laser is directed via several bending mirrors[23] out of its enclosure. It passes a half-wave plate[21], a Faraday isolator[24] and a shutter[25]. This Faraday isolator now the Ti:sapphire laser from harm of potential back-reflections by succeeding optics. The combination of the half-wave plate and the first polarizing beam splitter cube (PBSC) of the isolator allows to regulate the amount of power being sent into the atmosphere. The half-wave plate is carried by a motorized rotation mount[26]. Thereby, the output power can be controlled remotely without having to access the inside of the body housing. The remaining power (i.e., the percentage that is separated by the PBSC) is deviated towards a power meter. Beforehand, the beam is widened by a plano-concave lens[27] to extensively illuminate the detector area.

Several photodiodes and cameras are situated throughout the setup. They are mainly used for comprehensive monitoring of the pump, seed, and laser operation. An exception are two detectors, crucial for the system operation itself. One is located behind a bending mirror at the output area and measures the signal of the (injected plus reflected) seed laser beam which carries the information on the resonance condition of the cavity. The signal is generated with the help of the EOM and electronic devices. The latter also interpret the received signal and produce a correction voltage for the piezo to ultimately stabilize the cavity to the seeder frequency (Section 5.6.2). The other important photodiode[28] is situated behind the piezo mirror. During DIAL measurements it detects the Ti:sapphire laser pulse to trigger the acquisition of the lidar signal (Section 5.8). A photodiode positioned behind a cavity mirror in extension of the (forward) propagating resonator beam can also be utilized for the adjustment of the resonator. Then, a ramp

---

[21] *Thorlabs*, WPH05M-808

[22] *Qioptiq / Linos*, DLI 1

[23] high reflectivity models from *CVI / Melles Griot* and *Laser Components*

[24] *Qioptiq / Linos*, FI-600/1100-5SI

[25] see footnote 14 on page 22

[26] *Thorlabs*, PRM1/MZ8E

[27] *Thorlabs*, LC1715-B ($f_{nom} = -50\,\mathrm{mm}$)

[28] see footnote 12 on page 34

voltage is applied to the piezo and the transmission signal through the mirror is observed with the photodiode. Another detector of the same model collects the leakage light behind one of the pump beam bending mirrors to catch the pulse signal of the pump laser.

An essential camera is the beam profiler[29,30] which monitors the output beam of the titanium–sapphire laser. During laser operation, it is permanently in use. When performing the mode-matching adjustment of the seed laser beam, the camera is highly valuable as well. The distance of the camera to the output coupler equals the distance from there to the laser crystal. Hence, the camera shows the seeder's beam profile at the crystal. The accordance with a previously captured profile of the Ti:sapphire laser beam can be easily determined. The adjustment is executed with the help of more cameras[31] placed behind the resonator mirrors. The reference direction of the Ti:sapphire laser beam is additionally fixed with irises in front of the cameras. In a similar manner, the pump and the seeder beam profile are supervised. Again, the cameras are installed behind bending mirrors of the corresponding path, with optionally one advanced camera model[32] at disposal. The cameras are also beneficial when checking for optical misalignment after a transportation of the DIAL trailer.

All components are mounted on a separate optical table[33] and covered by a casing built by *IPM*. The total dimensions are $1.20 \times 0.60 \times 0.25\,\mathrm{m}^3$. The side panels provide various apertures for cable entry and beam ejection on different places (during development, for characterization measurements, or other purposes). If necessary, the panels can also be removed individually. In the setup, attention was paid to employing mounts of particular sturdiness. For example, the models of the mirror mounts[34] feature a very low thermal expansion. For the same reason, mirrors and lens optics of the material fused silica were favored to the greatest possible extent. Only a small number of optics are made of the substrate material BK7. The coatings of the optics are optimized for high powers. Photos of the setup are presented in Appendix D.

5.4 Crystal Cooling Mount

With the Ti:Al_2O_3 crystal being the core component of the whole laser system, the mechanical structure carrying the crystal assumes paramount significance. This is due to its principal function as cooler besides the actual task of being a mount. Efficient cooling is important because it affects the thermal lens in the crystal. The formation of the thermal lens can be diminished by maximizing the heat dissipation. In this regard, the properties of the crystal material are already advantageous. Titanium-doped sapphire exhibits a high thermal conductivity and diffusivity (see Table 5.1 on page 83) in comparison to other laser materials [121, 141]. For the cooling mount, a high heat dissipation requires three things: a good contact with the crystal surface, a high thermal conduction inside of the mount's material, and a method to (quickly) remove the heat from the mount.

---

[29] see footnote 16 on page 38

[30] see footnote 17 on page 38

[31] see footnote 5 on page 30

[32] Cinogy, CinCam CMOS-1202 with RayCi v2.3.7

[33] *Qioptiq / Linos*, G437811911 (*TMC* Series 78 CleanTopII Breadboards)

[34] *Newport*, Suprema SN100 series

In its function as mount the construction has to enable a precise adjustment. Necessary adjustments are the transverse central position and the angle of incidence of the laser beam on the crystal. This is particularly true for the Brewster-cut crystal shape, applying to all crystals used for this laser. Here, it is helpful that the cooling mount allows to monitor the beam which is reflected at the crystal end-surface. At Brewster's angle the reflection ideally vanishes (or becomes minimal in reality). Specially designed irises that are optionally attached to the mount can assist the beam adjustment procedure. Self-evidently, the cooling mount must provide a robust fixation of the crystal. The alignment must be constant despite the thermal influence. Moreover, it is desirable that the construction can be disassembled piecewise. In the event of a sub-component replacement (e.g. due to failure), the adjustment should not be lost completely. Protection against dust is also preferable as the cleaning of the small crystal surface is difficult and hazardous.

Considering all these aspects, different crystal cooling mounts were developed. Originally, the construction was designed at the *National Center for Atmospheric Research (NCAR)* in Boulder, Colorado, USA. It is based on the concept of mounting the laser crystal between two clamp shells, which are each cooled by a Peltier device that, in turn, removes the heat via water-cooled metal blocks. The design was slightly adapted for the former laser transmitter of the Hohenheim-DIAL. As part of this work, the crystal cooling mount was developed further with substantial changes to the design. The optimization was performed, *inter alia*, with respect to material choice, mounting form, and crystal surface contact. It is important to mention that crystals with two different shape types of the cross-sectional area (circular-cut and square-cut) were investigated. Therefore, two essential constructions of the crystal cooling mount are presented. The components were manufactured at the institute's mechanic workshop.

5.4.1 Circular-cut Crystal

The first Ti:sapphire crystal cooling mount of the two presented versions is shown as a CAD model in Figure 5.8. The collocation of the constituting parts resembles the form of a tower or a sandwich. The design results from the necessity that the ray reflected at the crystal surface should not be blocked or cut off by parts or edges of the mount itself. By arranging the clamp shells horizontally this can simply be realized with a recess. As a consequence, the remaining components are organized in a stack, similarly above and below the clamp shells.

In this version of the cooling mount, laser crystals with a circular cross-sectional area came into operation. Two crystals of the same type are available. The manufacturer[35] specifies a diameter of $(7.00 \pm 0.01)\,\mathrm{mm}$ and a (path) length of $20\,\mathrm{mm}$. The figure of merit is stated to be $FOM > 250$, where the absorption coefficient at the pump wavelength is $\alpha_{532} = 1.84\,\mathrm{cm}^{-1}$. This gives a low-power single-pass absorption of $LPSP = 97.5\,\%$.

The clamp shells are made of aluminum (see Appendix C for technical drawings). The bore hole in which the crystal is placed must fit precisely to the crystal diameter. Therefore, several copies of the parts were manufactured, and subsequently, the bore hole and the crystal measured[36]. The measurement confirmed the accuracy of the Ti:sapphire crystals' diameter and revealed the most suitable clamp shell pair. To improve the surface contact with the crystal and to

---

[35] see footnote 3 on page 82

[36] *Zeiss*, Prismo MPS with Calypso v4.4.04.01 (accuracy $\pm 1\,\mu\mathrm{m}$)

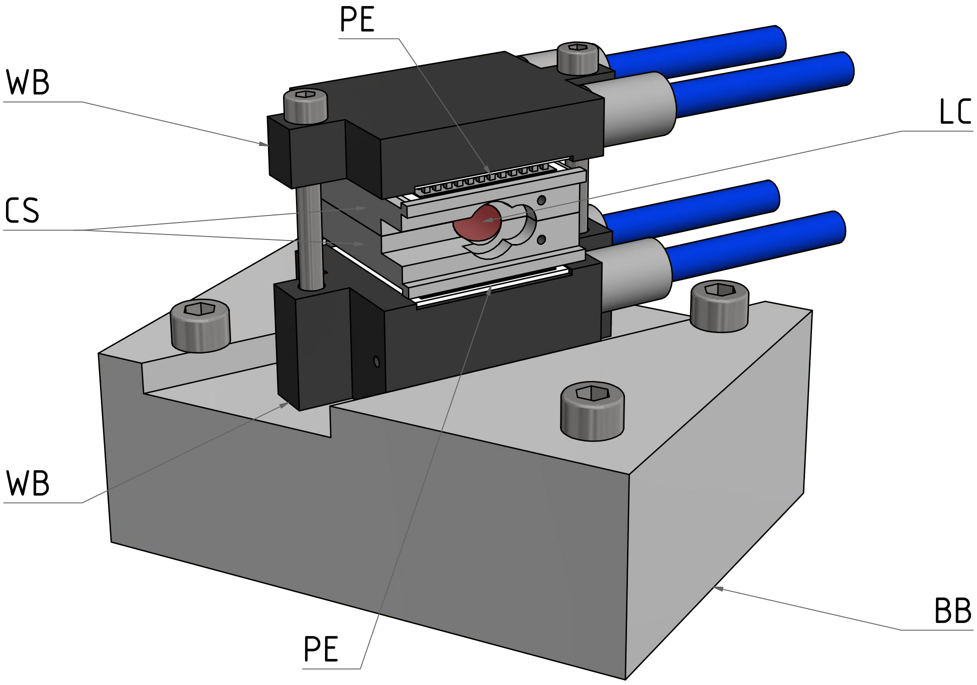

Figure 5.8: Version of the crystal cooling mount with a stack design and a Ti:sapphire crystal of circular cross-sectional area. BB – base block, CS – clamp shell, LC – laser crystal, PE – Peltier module, WB – water-cooled metal block. The blue cylinders represent water tubes.

compensate irregularities of the bore hole, the corresponding areas of the clamp shells (cylinder envelope) were coated with a thin layer of fine gold by a company[37]. The total thickness of the layer is approximately $15\,\mu\mathrm{m}$. The clamp shells are bolted together by two small screws and two guide pins.

On both sides of the clamp shells a Peltier module[38] is seated. The thermoelectric coolers are connected in parallel and driven by a temperature controller[39]. It regulates the current of the Peltier modules to achieve a constant temperature of the clamp shells, and thus, of the laser crystal. The sensor is a resistance thermometer[40] which is inserted into a small hole close to the crystal in one of the clamp shells. The temperature is set to $T \approx 18\,°\mathrm{C}$. On the reverse side of each Peltier device a metal block is mounted. Through these blocks flows water cooled by a chiller[41] to approximately the same temperature. At the interface of the thermoelectric coolers and of the temperature sensor a thermal paste[42] is used. In contrast to a thermal adhesive tape, the paste enables flexible disassembling of the parts later on, and what is more, it does not

---

[37] *Doduco*, Germany

[38] *Quick-Cool*, QC-127-1.0-3.9M

[39] *AMS Technologies*, Alimentation peltier 2410

[40] *B+B Thermo-Technik*, 0364 0012 (Pt100/B, $d = 1.8\,\mathrm{mm} \times 6\,\mathrm{mm}$, Glass)

[41] *Laird Technologies / Melcor*, MRC300DH2-HT-DV; later *Termotek*, Piko 302

[42] *B+B Thermo-Technik*, 0554 0034 (Heat-conductive paste, WLC)

modify the height of the construction.

The entire stack rests on a base block of stainless steel and is fastened by two long screws. Stainless steel has relatively low thermal conductivity ($\kappa \approx 25\,\mathrm{W\,m^{-1}\,K^{-1}}$) and thermal expansion ($\alpha_l \approx 11 \times 10^{-6}\,\mathrm{K^{-1}}$), isolating the construction from the optical table and minimizing deformation. The height of the cooling mount is designed for a beam height of $60\,\mathrm{mm}$ (central position on the crystal). For the fine adjustment of the beam incidence and position on the crystal, specially made irises can be fixed at the clamp shells.

The experience with this cooling mount version, provided the following observations. During installation, the circular-cut laser crystal was rotated around its central axis to the correct position (p-polarization). Monitoring the reflection on the crystal surface of the pump beam (at low power) was helpful for this purpose. The procedure was much easier for this design, the crystal resting on the lower sub-components, as compared to the version where the clamp shells are oriented vertically. However, the accomplishment of a perfect crystal orientation was time consuming. Additionally, when screwing down the construction, the adjustment was slightly altered. This was probably caused by a compression of the thermoelectric coolers. Likewise, loosening the screws again (e.g., for the exchange of a sub-component) called for a readjustment of the laser and pump beam. Overall, the possibility of monitoring the reflected beams at the crystal end-surfaces led to more accurate adjustments (see Section 5.5), and hence, a better laser performance.

5.4.2 Square-cut Crystal

To continue improving the heat dissipation, further modifications of the cooling mount were made. Extra focus was given to the crystal's surface contact and the thermal conductivity of the clamp shells. A laser crystal with plane lateral surfaces could be more convenient, as in practice a higher and a uniform contact pressure are thus enabled. To determine this, two new Ti:sapphire crystals with a square cross-sectional area were ordered. The dimensions are similar to the circular-cut crystal. The edge length of the square is $(6.99 \pm 0.02)\,\mathrm{mm}$, and the path length is $(20.03 \pm 0.03)\,\mathrm{mm}$. The crystals were grown by the previously mentioned manufacturer. It specifies a figure of merit of $FOM = 424$ and $FOM = 320$, with a pump wavelength absorption coefficient of $\alpha_{532} = 1.72\,\mathrm{cm^{-1}}$ and $1.80\,\mathrm{cm^{-1}}$, respectively. The corresponding low-power single-pass absorption is $LPSP = 96.8\,\%$ and $LPSP = 97.3\,\%$. The higher FOM values are attributed to a now improved production quality. In the current setup, the crystal with the higher FOM is installed.

The square shape of the laser crystals requires, of course, a complete redesign of the clamp shells (for technical drawings, see Appendix C). In this construction, a possibility was envisaged to gently increase the contact pressure. The new development of the cooling mount also offered the opportunity to implement changes suggested by earlier findings. Figure 5.9 depicts the CAD model of the elaborated construction, being the version in use at present. It is particularly remarkable that the lower clamp shell now rests on dedicated pillars in the form of a bridge. This has the advantage that its position is fixed independently of the thermoelectric coolers and the water-cooled blocks. Therefore, it is possible to disassemble the latter without affecting the

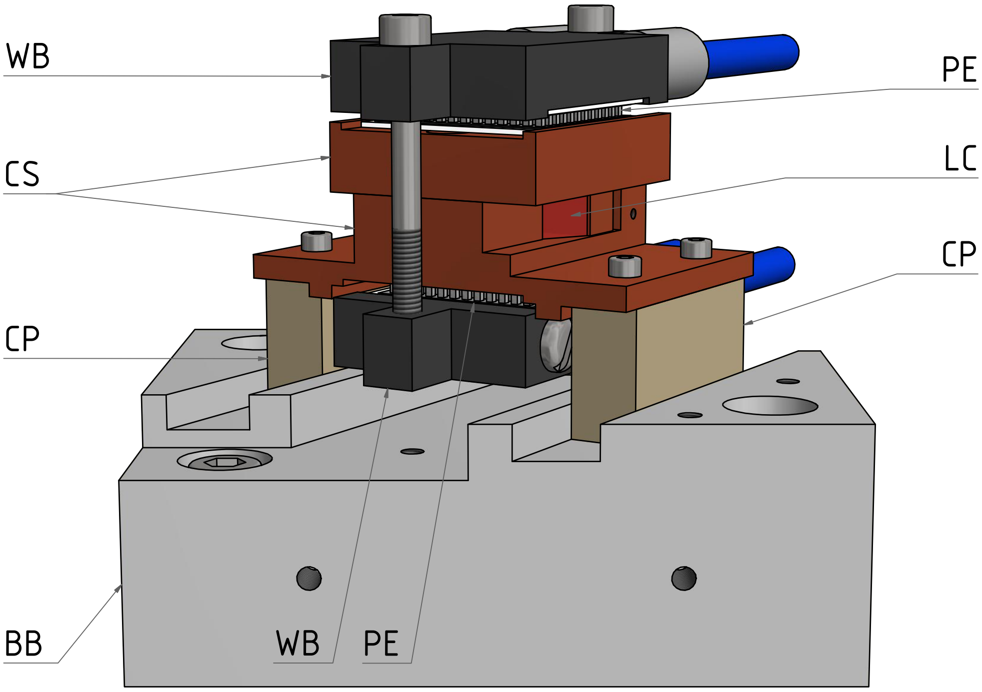

Figure 5.9: Version of the crystal cooling mount with a bridge design and a Ti:sapphire crystal of square-cut cross-sectional area. CP – ceramic pillars, further abbreviations see Figure 5.8.

alignment of the crystal or the beam adjustments. The pillars are made of a ceramic material[43] offering excellent thermal isolation ($\kappa \approx 1.5\,\mathrm{W\,m^{-1}\,K^{-1}}$) and low thermal expansion ($\alpha_l \approx 8.1 \times 10^{-6}\,\mathrm{K^{-1}}$). The base block is adapted to the construction and therefore also usable for the previous design. With screws and through holes in the pillars, the lower clamp shell is fastened to the base block. The sub-components for temperature regulation (Peltier devices, sensor, controller) remain unchanged, the water-cooled metal blocks are adapted marginally.

The clamp shells are designed in such manner that the crystal is tightened separately in the horizontal and the vertical plane with two adjusting screws in each case. The following approach simultaneously ensures a non-damaging pressing on the crystal and a high thermal conductivity. The clamp shells are produced from a copper alloy[44], because it has a higher thermal conductivity than aluminum. For the same reason, the areas of the clamp shells that come into contact with the Ti:sapphire crystal are now coated with silver. Silver possesses supreme thermal conductivity ($\kappa \approx 429\,\mathrm{W\,m^{-1}\,K^{-1}}$) and diffusivity ($a \approx 172 \times 10^{-6}\,\mathrm{m^2/s}$), while providing a comparable softness to gold. The layer thickness of the coating is $50\,\mathrm{\mu m}$. When pressing on the crystal, it is intended that the silver layer deforms first, and afterwards the copper solid together with the (partially) spring-loaded screws. Once again, the material properties of Ti:sapphire are expedient in this respect. It has high hardness and strength parameters (see Table 5.1), protecting

---

[43] *MCI*, Macor

[44] *Schreier Metall*, CuTeP (CW118C, DIN EN 12164)

the crystal from mechanical damage.

Obviously, the square-cut crystal cannot be rotated around its longitudinal axis. One has to rely on a perfectly upright construction and a proper crystal shape. Otherwise, the fine adjustment of the polarization orientation has to be accomplished by other means. The structure of the design features a high rigidity and proved robust. The effect of the modified construction on the thermal lens of the laser crystal was studied by comparing the focal length measurements (see Section 5.7.1).

5.5 Unidirectional Propagation

In ring cavities it is distinguished between two traveling directions of the wave. One is defined as the forward propagation, the other as the backward propagation. Usually, in a ring resonator only one-way propagation of the laser eigenmode is desired so that the output beam and power leave the cavity in only one direction. For the titanium–sapphire laser the unidirectional propagation is achieved by injection seeding and through individual components of the resonator, described below. In fact, injection seeding implies preferential laser evolution at the corresponding beam propagation direction. Thus, injection seeding alone could be sufficient. Nevertheless, as dealing with high laser powers and as the seeding switches between two sources (online and offline diode laser), the enforcement of uni-directionality by a supplementary scheme is very advisable.

The components ensuring unidirectional propagation are a half-wave plate, a Faraday rotator, and optics oriented at Brewster's angle through which the eigenmode propagates. The latter are the Ti:sapphire crystal and the birefringent filter. Their tilted interfaces act as linear polarizer, since at Brewster's angle only p-polarized light is transmitted without losses. The half-wave plate and the Faraday rotator change the polarization orientation in a suitable manner and thereby allow forward propagation is allowed, while backward circulation is inhibited.

The change of the polarization orientation in the resonator can be expressed by simple formulas. Let α be the angle (in degrees) that describes the state of orientation in space of the beam's linear polarization at a certain location. A half-wave plate changes the orientation of polarization such that it is flipped around the (fast) crystal axis [142]. If ω denotes the angle of the half-wave plate's crystal axis in the same coordinate system, the transformation function reads,

$$f_{HWP}(\alpha) = \alpha + 2(\omega - \alpha) = 2\omega - \alpha \, . \tag{5.34}$$

The Faraday rotator leads to a rotation of the polarization by an angle ρ,

$$f_{FR}(\alpha) = \alpha - \rho \, . \tag{5.35}$$

This definition (the minus sign) assumes that the device has a left-handed rotation. Both transformation functions apply to both forward and backward direction. Yet, the combination of the two components induces a distinction of forward and backward propagation as the corresponding total transformations have different function composition,

$$f_{fwd}(\alpha) \;=\; f_{FR}\left(f_{HWP}(\alpha)\right) \;=\; (2\omega - \alpha) - \rho \;=\; 2\omega - \rho - \alpha \, , \tag{5.36}$$

$$f_{bwd}(\alpha) \;=\; f_{HWP}\left(f_{FR}(\alpha)\right) \;=\; 2\omega - (\alpha - \rho) \;=\; 2\omega + \rho - \alpha \, . \tag{5.37}$$

The equations can be used to find a configuration of the parameters ω and ρ which results in unidirectional propagation. To this end, the conditions

$$f_{fwd}(\alpha) = \alpha \; , \tag{5.38}$$

$$f_{bwd}(\alpha) = \alpha + 90^\circ \; , \tag{5.39}$$

must hold. They claim that the polarization orientation after forward transmission is equivalent to the initial state, whereas in backward direction it concludes in a perpendicular state, being blocked by the polarizer. Applying the conditions to equations (5.36) and (5.37) gives the solution $\omega = \alpha + 22.5^\circ$ and $\rho = 45^\circ$. Given that the forward-propagating, p-polarized eigenmode is defined to be $\alpha = 90^\circ$, the optical axis of the half-wave plate has to be set to $\omega = 112.5^\circ$. Of course, there are also more equivalent solutions.

The consequences of a deviation from the ideal configuration is studied next. Since the half-wave plate is put into a rotation mount[45], the orientation of its optical axis can be adjusted. Thanks to the new design of the cooling mount, fine adjustment is possible by monitoring and minimizing the reflection at the Ti:sapphire crystal end-surface. Therefore, it is assumed that the best orientation is always attained, and a corresponding error is not present or negligible, $\Delta\omega = 0$. The rotation angle ρ is predetermined by the Faraday effect, according to the relation $\rho = \mathcal{V}\, d\, B$. Here, $\mathcal{V}$ and d are the Verdet constant and the length of the medium, respectively, through which the light propagates, and which is exposed to a magnetic field B [142]. Even though the parameters are matched to the application during manufacture, deviations may occur. For instance, the Verdet constant varies with the wavelength and the temperature. Hence, an error $\Delta\rho$ is introduced for the Faraday rotator. It is easily seen from Equations (5.36) and (5.37) that this leads to a deviation from the desired orientation transformation of the same amount in both, the forward and the backward direction. By adjusting the half-wave plate, it is possible to assign the deviations to only one direction, but a total discrepancy of $2\Delta\rho$ remains. Consequently, losses arise, either due to the presence of residual laser operation in backward direction or caused by the imperfect orientation relative to p-polarization in forward direction. In the latter case, according to Malus' law, the intensity is decreased by the factor $\cos^2(2\Delta\rho)$. The rotator models that came into operation (see below) have deviations of up to $\Delta\rho = \pm 2^\circ$ causing $\approx 0.5\,\%$ power losses.

The model[46] of the half-wave plate almost always sustained the high intracavity powers. In contrast, the Faraday rotator turned out to be a critical element. When approaching the limiting peak power densities, the rotator was often the part of the resonator being damaged. Relocating the rotator skillfully enabled to pass by the incurred damaged spots. Moreover, different models were tested. The model[47] coming into operation most of the time, is specified with a damage threshold of $500\,\mathrm{MW/cm^2}$, or $5\,\mathrm{J/cm^2}$ in $10\,\mathrm{ns}$. The mean value of the experimentally determined peak power densities was $\approx 478\,\mathrm{MW/cm^2}$, or $\approx 14.3\,\mathrm{J/cm^2}$ in $30\,\mathrm{ns}$. A second model[48] with a damage threshold specification of $300\,\mathrm{MW/cm^2}$, or $3\,\mathrm{J/cm^2}$ in $10\,\mathrm{ns}$, in prac-

---

[45] Thorlabs, RSP1/M

[46] see footnote 21 on page 100

[47] *Leysop*, FOI-5/57-AR820 (excluding polarizers)

[48] *Qioptiq / Linos*, FR-810-5SV

tice was damaged at $\approx 268\,\mathrm{MW/cm^2}$, or $\approx 8.0\,\mathrm{J/cm^2}$ in $30\,\mathrm{ns}$. A third model[49] has been installed in the setup recently. The specifications for the damage threshold are similar to the ones of the first model. Experimental damage values still have to be determined. However, the model resists laser operation at the $10\,\mathrm{W}$ output power level.

It has to be pointed out that the experimental values of destruction were derived from the maximum output power being measured. The true values the Faraday rotators were exposed to might be higher if there are losses in the cavity, e.g., due to the above-mentioned reasons. Then again, it is difficult to tell whether a lower damage value can be ascribed to a (larger) deviation of the ideal rotation angle, $\rho = 45°$, or to a crystal that actually endures less. The manufacturers have various suppliers for the terbium gallium garnet (TGG) crystals, which are commonly used in the Faraday rotators. Differences in quality (crystal purity) might play a considerable role. Initially, it was also considered to apply rotators with a lower angle of rotation ρ in favor of a shorter TGG crystal. This could have helped with the thermal load caused by the high powers, but since further deviations of $\Delta\rho$ lead to substantial losses in the resonator, the idea was dismissed.

Finally, thermal lensing effects in TGG crystals have been reported, e.g., [143–145]. So far, this has not been taken into account in the resonator design calculations. However, for the high power values that have been reached with the Ti:sapphire laser, the generation of a thermal lens in the Faraday rotator might become relevant. A rough estimation of the resulting focal length of the thermal lens in the TGG crystal is made with Equation (5.53), which is discussed in more detail in Section 5.7.1. The material constants assumed are the thermal conductivity $\kappa = 7.4\,\mathrm{W\,m^{-1}\,K^{-1}}$ [145], the thermo-optic coefficient $\mathrm{d}n/\mathrm{d}T = 20 \times 10^{-6}\,\mathrm{K^{-1}}$ [145], the absorption coefficient $\alpha = (0.0015 \pm 0.0005)\,\mathrm{cm^{-1}}$ [143–145], and the rod length $l = (5 \pm 1)\,\mathrm{cm}$. At a laser output power of $P = (10.0 \pm 0.5)\,\mathrm{W}$, the intracavity power is $P_{ic} = (25.0 \pm 1.3)\,\mathrm{W}$ which is the incident power for the heating process without any reduction[50] $P_h = P_{ic}$, and the mean beam radius at the Faraday rotator is $w = (0.60 \pm 0.05)\,\mathrm{mm}$. This yields a thermal lens focal length $f = (2.2 \pm 0.9)\,\mathrm{m}$ of the TGG crystal. The value is in the order of magnitude where a slight influence on the eigenmode might be given. In the future, it would be interesting to investigate this further and evaluate potential countervailing measures (for instance, cooling of the Faraday rotator, or modification of the resonator configuration).

5.6 Frequency Selection and Control

As was described in Section 5.1 the gain spectrum of titanium-doped sapphire is, by nature, very broad and has a peak at $\approx 790\,\mathrm{nm}$. Narrowband operation of the laser plus emission off the gain peak (close to $818\,\mathrm{nm}$), therefore, call for frequency selection methods. The concept in this system is similar to the one of the previous Hohenheim-DIAL transmitter [25, 26]. In the first instance, the emission spectrum is restricted to a smaller range around the operation wavelength. This pre-selection is accomplished by a tunable, intracavity birefringent filter. Then, injection seeding of the resonator reduces the bandwidth further (down to orders of the frequency scale, or

---

[49] *Electro-Optics Technology (EOT)*, HP-05-R-818

[50] there is no optical conversion process for the transmitted laser beam, and the losses at the surfaces are considered to be very low, due to anti-reflective coating

a few laser modes only), and actually assumes the task of frequency control (precise selection or tuning). Finally, a locking technique actively stabilizes the cavity via the piezo-mounted mirror, ensuring single-frequency operation of the laser.

5.6.1 Coarse Wavelength Selection

To obtain laser operation at a wavelength off the Ti:sapphire gain peak and to decrease the number of effective modes of the free-running laser, a birefringent filter is installed within the cavity. Such a bandpass filter consists of multiple crystalline, birefringent, and plane-parallel plates, placed to have beam incidence at Brewster's angle. By rotating the plates around its normal axis, the passband wavelengths can be tuned. Birefringent filters have proven to be a suitable frequency (pre-)selective element in pulsed Ti:sapphire and other lasers [17,22,126,139, 146–148]. Alternative elements (e.g., etalons, prisms, or diffraction gratings) were considered to be less convenient for the intended application. Either they are too sensitive for small changes of the incident angle, not resistant against the high optical power densities, entail more transmission losses, or require an unfavorable cavity layout.

The transmission characteristic of a birefringent filter can be analyzed theoretically with the Jones-matrix formalism; see e.g., [149–152]. A first insight is provided by the calculation for a single-pass propagation through the filter. However, the situation might be different if the filter is applied inside a resonator. Then, the transmission behavior not only depends on the specific configuration (number, thickness, and orientation of the plates) of the birefringent filter, but also on further polarizing elements included in the cavity. The calculation helps identifying an appropriate filter configuration, though the equations can become very extensive.

The birefringent filter of the present laser is the one used in the former Hohenheim-DIAL transmitter. SCHILLER determined the configuration with the above-mentioned formalism [25]. According to his findings, a previously acquired filter was modified by the manufacturer[51]. Since then, the filter consists of four quartz crystal plates with the respective thicknesses, $8\,\mathrm{mm}$, $0.5\,\mathrm{mm}$, $1\,\mathrm{mm}$, and $2\,\mathrm{mm}$, in the order of propagation direction. The plates have a rectangular shape of dimension $19\,\mathrm{mm} \times 25\,\mathrm{mm}$. They are assembled together and mounted in a precision rotary holder[52]. The optic axis (slow axis) of the crystal plates lies in the surface plane and is parallel to the short edge.

Adequate rotation angles of the birefringent plates leading to wavelength selection close to $818\,\mathrm{nm}$ were assessed by the manufacturer with the optical design program *Zemax*. The calculus of the software is based on a single-pass transmission through the filter. Two essential orientations were found: $\phi \approx 30^\circ$, and $\phi \approx 61^\circ$, where ϕ is the angle of the optic axis to the normal of the plane of incidence. Figure 5.10 shows the single-pass transmission function of the p-polarized fraction for the two cases. Such a calculated function merely represents the ratio of the intensities in front and behind the birefringent filter. The laser gain, further polarizing elements, and losses in the resonator alter the absolute intensity curve. Nevertheless, the calculation provides an estimate for the location of the principal and secondary transmission maxima. The curves show that the transmission of the secondary peaks is mostly lower at the rotation angle $\phi \approx 61^\circ$. Hence, this setting would be preferable, as it prevents laser evolution at other than the

---

[51] *Bernhard Halle Nachfl.*, Germany

[52] *CVI / Melles Griot*, 07HPT735

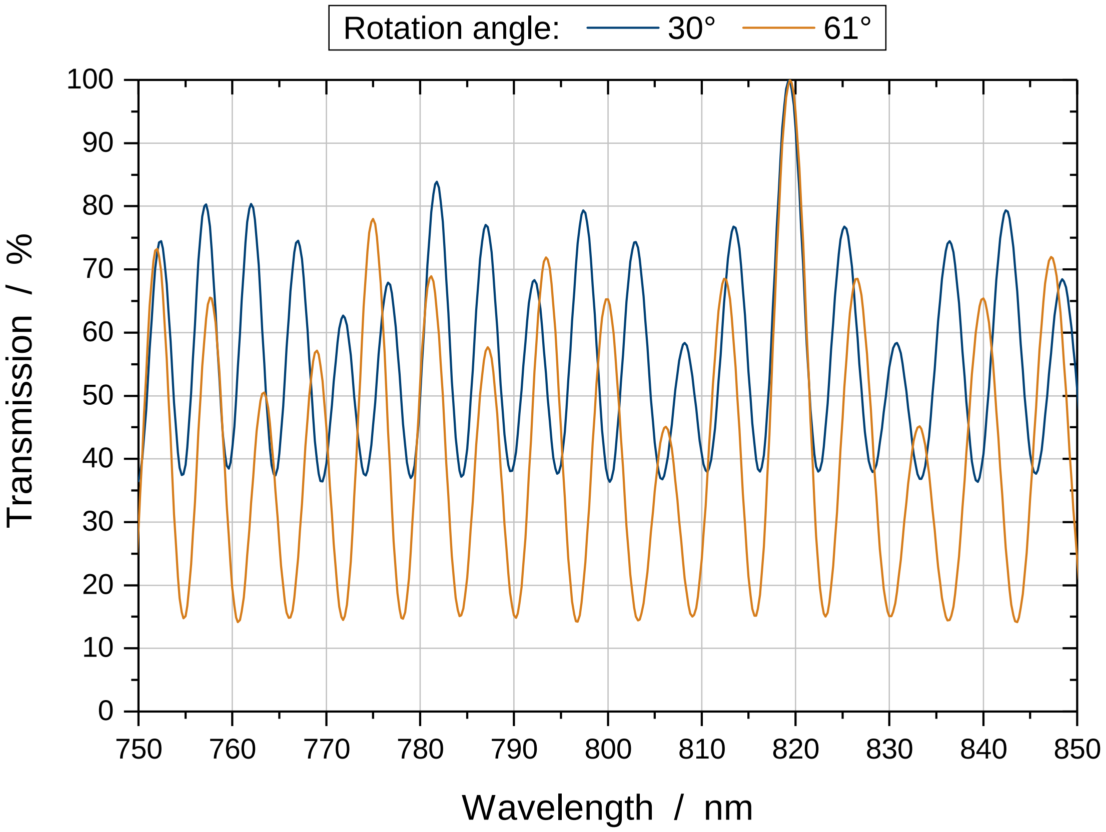

Figure 5.10: Calculated transmission function of the four-plate birefringent filter for the two rotation angles yielding a primary peak at the desired operation wavelength of $\lambda \approx 818\,\mathrm{nm}$.

desired wavelength more effectively. Unfortunately, the aperture of this birefringent filter was too tight at this angle (due to the rectangular shape of the plates), and for the experiment the angle $\phi \approx 30°$ had to be chosen. This issue will be reconsidered in Section 5.7.3. The values of the rotation angles were confirmed in the experiment. The free spectral range of the birefringent filter is $\Delta\lambda_{FSR} \approx 111\,\mathrm{nm}$.

5.6.2 Precise Frequency Control and Active Stabilization Technique

Beyond the pre-selection of the operation wavelength, injection seeding significantly intensifies the frequency selection and the narrowing of the bandwidth. The ability to precisely change the frequency, enables (alternate) switching to different nearby locations in the frequency spectrum, or to continuously tune over a certain frequency range. Since the output of the Ti:sapphire laser is pulsed, the term continuously has to be understood as a sampling of the spectrum, where the resolution is defined by the tuning speed and pulse repetition rate.

Injection seeding without further steps of resonator stabilization is still insufficient to fulfill the requirements for water-vapor DIAL. Therefore, a technique is necessary that actively adapts the cavity length to the frequency of the seeder to keep the cavity at resonance and ultimately achieve single-frequency laser operation. The method of active resonator stabilization employed here follows the Pound–Drever–Hall (PDH) technique [153, 154], which is based on phase modulation. The application of this technique was demonstrated for the first time in a pulsed Tm:LuYAG laser by WULFMEYER *et al.* [155, 156], and later also implemented in a Nd:YAG master oscillator [97, 98, 157] as well as in the previous Ti:sapphire laser transmitter of the Hohenheim-DIAL [25, 26]. There are also other techniques to actively stabilize the frequency of pulsed lasers, e.g., through minimization of the pulse build-up time [158], by ramping the cavity length [159, 160], or via polarization spectroscopy [161].

The advantages of the PDH technique are the following. It provides an error signal with a zero crossing at resonance informing the direction in which the cavity length has to be corrected. The slope of this signal is very steep enabling a quick reaction to disturbances. The correction is performed almost instantly and continuously, as the signal is permanently present (except for the short period after the laser pulse emission when the detector is saturated by the high pulse intensity). Moreover, the choice of the modulation frequency allows to define the capture range of the error signal. The phase modulation technique is insensitive to small variations of the wavelength, polarization, or alignment. Thus, it is particularly suitable when the system is exposed to harsh environments. The additional need of an electro-optic modulator in the setup is opposed by only one necessary detector.

Theoretical Review of Ring Cavity Interference and the PDH Technique

The information about the resonance condition of the cavity with respect to the frequency of the injected seeder beam—the so-called error signal—is won from the phase modulation of the incident wave and the detection of the reflection signal of the cavity. The theoretical description below was derived from the references [162, 163]. First, the wave interference of the four-mirror ring-cavity is considered. Then, the phase modulation and detection is treated.

The reflection signal of the cavity is a superposition of the fraction which is directly reflected at the mirror where the beam is coupled into the cavity and the fractions returning from the inside of the cavity. In analogy to the analysis of a Fabry–Pérot interferometer, the (complex amplitude of the) reflected electromagnetic wave E_r can be expressed by the incident wave E_i and a complex reflection coefficient $r_{ring}(\omega)$ of the four-mirror ring-cavity,

$$E_r = r_{ring}(\omega)\, E_i \; , \tag{5.40}$$

with

$$r_{ring}(\omega) = \frac{r_1 - (r_1^2 + t_1^2) r_2 r_3 r_4\, e^{-i\omega L/c}}{1 - r_1 r_2 r_3 r_4\, e^{-i\omega L/c}} \; . \tag{5.41}$$

Here, r_1 and t_1 are the reflection and transmission coefficients of the output coupler mirror. The reflection coefficients of the remaining mirrors are r_2, r_3, and r_4. The frequency of the seed laser is declared by $\omega = 2\pi\nu$, and L is the cavity length.

Likewise, it is possible to determine the transmitted wave E_t through the cavity, i.e., behind the other besides the output coupler. The equations are found in Appendix A.4. For the intensity of the transmitted part, $I_t \propto E_t E_t^*$, results the well-known Airy function. The resonance lines of the cavity have a full width at half maximum given by

$$\Delta\nu_{cav} = \frac{1 - r_1 r_2 r_3 r_4}{\pi\sqrt{r_1 r_2 r_3 r_4}}\frac{c}{L} \,. \tag{5.42}$$

The finesse is equivalent to ratio of the free spectral range and the cavity linewidth,

$$\mathcal{F} \equiv \frac{\Delta\nu_{FSR}}{\Delta\nu_{cav}} = \frac{\pi\sqrt{r_1 r_2 r_3 r_4}}{1 - r_1 r_2 r_3 r_4} \,. \tag{5.43}$$

The main difference to the usual Fabry–Pérot interferometer are the additional reflection coefficients, which can be summarized into one substitute reflection coefficient $\tilde{r}_2 := r_2 r_3 r_4$, and the length of the ring cavity that is twice the linear cavity length, $L = 2\tilde{L}$. What is more, the reflection coefficient of the output coupler mirror is considerably lower than for the other mirrors. As a consequence, the cavity linewidth becomes large with respect to the free spectral range. In other words, the finesse of the cavity is not very high. For the mirror configuration of the Ti:sapphire laser ($r_1 = \sqrt{60\,\%}$, $r_2 = r_3 = r_4 \approx \sqrt{99.8\,\%}$, and $L = 1.6\,\mathrm{m}$) the resonance linewidth of the cavity is $\Delta\nu_{cav} \approx 15\,\mathrm{MHz}$, and the finesse $\mathcal{F} \approx 12$.

The phase of the electromagnetic wave of the seeder is modulated before it encounters the cavity. Hence, the incident wave can be written as

$$E_i = E_0\, e^{i[\,\omega t\, +\, \beta\cos(\Omega t)\,]} \,, \tag{5.44}$$

where E_0 represents the complex amplitude of the original (unmodulated) wave, Ω denotes the modulation frequency, and β is the strength or depth of modulation, also called modulation index. This expression can be expanded into a power series and rearranged in terms of Bessel functions[53],

$$E_i = E_0 \left[J_0(\beta)\, e^{i\omega t} + J_1(\beta)\, e^{i(\omega+\Omega)t} - J_1(\beta)\, e^{i(\omega-\Omega)t} + \,\ldots \right] . \tag{5.45}$$

From this representation it is apparent that the wave consists of a carrier with frequency ω and sidebands at (multiples of) the modulation frequency Ω around this carrier. The contribution of each constituent is determined by the Bessel functions, which in turn depend on the modulation depth. With increasing modulation index more power of the electrical field is transferred from the carrier into the sidebands, exciting also higher orders. If the modulation is weak ($\beta < 1$), only the carrier and the two sidebands at the frequencies $\omega + \Omega$ and $\omega - \Omega$ become relevant and the higher order terms can be neglected.

According to Equation (5.40) the wave reflected by the cavity is obtained by multiplying each constituent of the incident wave (5.45) with the complex reflection coefficient (5.41) at corresponding frequency,

$$\begin{aligned} E_r \approx E_0 \Big[\, & r_{ring}(\omega)\, J_0(\beta)\, e^{i\omega t} + r_{ring}(\omega+\Omega)\, J_1(\beta)\, e^{i(\omega+\Omega)t} \\ & - r_{ring}(\omega-\Omega)\, J_1(\beta)\, e^{i(\omega-\Omega)t} \Big] . \end{aligned} \tag{5.46}$$

---

[53] The Bessel functions of the first kind are $J_n(\beta) = \sum_{k=0}^{\infty} \frac{(-1)^k}{k!\,\Gamma(k+n+1)} \left(\frac{\beta}{2}\right)^{2k+n}$, with the gamma function $\Gamma(n) = (n-1)!$

The detector measures the current of the photodiode which is proportional to the intensity of the electromagnetic field, $I_r \propto E_r E_r^*$. Therefore, the resulting signal becomes

$$\begin{aligned} I_r \propto \{ \quad & J_0^2\,|r_{ring}(\omega)|^2 + J_1^2\,|r_{ring}(\omega+\Omega)|^2 + J_1^2\,|r_{ring}(\omega-\Omega)|^2 \\ & + J_0 J_1\, r_{ring}(\omega)\, r^*_{ring}(\omega+\Omega)\, e^{-i\Omega t} \\ & - J_0 J_1\, r_{ring}(\omega)\, r^*_{ring}(\omega-\Omega)\, e^{i\Omega t} \\ & + J_0 J_1\, r^*_{ring}(\omega)\, r_{ring}(\omega+\Omega)\, e^{i\Omega t} \\ & - J_0 J_1\, r^*_{ring}(\omega)\, r_{ring}(\omega-\Omega)\, e^{-i\Omega t} \\ & + J_1^2\, r^*_{ring}(\omega+\Omega)\, r_{ring}(\omega-\Omega)\, e^{-i2\Omega t} \\ & - \; J_1^2\, r_{ring}(\omega+\Omega)\, r^*_{ring}(\omega-\Omega)\, e^{i2\Omega t} \quad \}\,. \end{aligned} \tag{5.47}$$

This signal includes the constant components of the three initial frequencies (of the carrier and the two sidebands), as well as mixed terms oscillating at the frequencies Ω and 2Ω. The latter are beat notes between the carrier and the sidebands, respective between the two sidebands themselves. The beat notes with the frequency Ω inform on the resonance condition of the cavity with respect to the wave of frequency ω. They are isolated from the other components (particularly the 2Ω-beat notes) with the help of a low-pass filter. The essential term is

$$\begin{aligned} I_\Omega \;\propto\; J_0 J_1 \{ \quad & \left[r_{ring}(\omega)\, r^*_{ring}(\omega+\Omega) - r^*_{ring}(\omega)\, r_{ring}(\omega-\Omega) \right] e^{-i\Omega t} \\ & + \left[r^*_{ring}(\omega)\, r_{ring}(\omega+\Omega) - r_{ring}(\omega)\, r^*_{ring}(\omega-\Omega) \right] e^{i\Omega t} \quad \}\,. \end{aligned} \tag{5.48}$$

The expression can be rewritten into a different form, using the relation $z\, e^{-i\Omega t} + z^*\, e^{i\Omega t} = 2x\cos(\Omega t) + 2y\sin(\Omega t)$, where $z = x + i\,y$. Then,

$$I_\Omega \;\propto\; J_0(\beta)\, J_1(\beta)\, [\, A\cos(\Omega t) + D\sin(\Omega t)\,]\ , \tag{5.49}$$

with

$$A = \; 2\,\Re\mathrm{e}\left[\, r_{ring}(\omega)\, r^*_{ring}(\omega+\Omega) - r^*_{ring}(\omega)\, r_{ring}(\omega-\Omega)\,\right]\ , \tag{5.50}$$

$$D = 2\,\Im\mathrm{m}\left[\, r_{ring}(\omega)\, r^*_{ring}(\omega+\Omega) - r^*_{ring}(\omega)\, r_{ring}(\omega-\Omega)\,\right]\ . \tag{5.51}$$

Further evaluation of the factors A and D usually comprises the simplification of the complex reflection coefficient. It is approximated by assuming that the cavity is symmetric (all reflection coefficients are equal) and has a high finesse. These assumptions are not—or only partially—applicable here. The use of the general equation (5.41) is possible but entails a more extensive calculation which shall not be presented here. It is shown that for low modulation frequencies, $\Omega \ll \Delta\nu_{cal}$, the signal I_Ω is mainly determined by the term with the factor A, whereas for high modulation frequencies, $\Omega \gg \Delta\nu_{cal}$, the D term dominates [163].

The signal is demodulated by mixing (multiplying) it with the local oscillator signal of the phase modulator. It is important to note that the two terms of Equation (5.49) are in phase opposition due to the cosine and sine functions. Thus, the mixer balances the terms according to the relative phase to the local oscillator. An additional phase shifter accounts for unequal delays of the signal paths in the experiment and allows to select one of the two terms. The term oscillating in phase with the modulator is referred to as absorption signal A, since it is sensitive to the amplitude variations caused by the cavity. The term oscillating out of phase is named the dispersion signal D, exhibiting a similar shape with a bipolar slope at the resonance frequency. The slope is very steep and ideal to be used as error signal for the stabilization of the cavity. Both signals are scaled with $J_0 J_1$ which becomes maximum for the modulation index $\hat{\beta} \approx 1.08$.

Experimental Realization and Comparison

For the Ti:sapphire laser in this work, key parameters of the PDH technique were reconsidered and the hardware nearly completely exchanged. A modulation frequency of $\Omega = 80\,\mathrm{MHz}$ was chosen, which is higher than for the former configuration ($\Omega = 40\,\mathrm{MHz}$). This was motivated by the fact that the condition $\Omega \gg \Delta\nu_{cal}$ is fulfilled in a better way. Hence, the dispersion term has a stronger contribution in the error signal, as discussed above. Additionally, a higher modulation frequency increases the capture range of the error signal. With $80\,\mathrm{MHz}$, the range towards one detuning side is only slightly lower than half of the free spectral range and therewith almost as wide as for the error signal of the Hänsch–Couillaud technique. A wide capture range is important as the injection seeding is switched between online and offline diode laser. Although the offline frequency is set in such manner that the difference to the online frequency corresponds to an integer number of the cavity's free spectral range, the situation may occur when the frequencies drift apart on the detuning scale.

The phase modulation of the seeder wave is performed by transmitting the beam through an electro-optic modulator (EOM). The acquired model[54] consists of a MgO:LN crystal with $5 \times 5\,\mathrm{mm}^2$ aperture and an anti-reflective coating ($R < 0.5\,\%$) for $\lambda = 650\,\mathrm{nm}$ to $950\,\mathrm{nm}$. Due to the optimized aperture and coating the seeder power loss was diminished. The EOM provides a tunable resonance frequency from $\approx 70\,\mathrm{MHz}$ to $97\,\mathrm{MHz}$ and a bandwidth of $\approx\ 800\,\mathrm{kHz}$ [164].

Furthermore, the improvement of signal quality (noise reduction) was a concern. A fast transimpedance amplified photodiode is used as detector. The model[55] has a detection bandwidth of up to $100\,\mathrm{MHz}$ and a low noise level. While the electronics previously consisted of a discrete setup with individual components, now a device which integrates all necessary components for the generation and detection of the PDH signal in one single unit comes into operation. This keeps the signal paths short, making the device less susceptible to noise. The unit[56] comprises the radio-frequency (RF) driver for the EOM, and the circuitry for the phase sensitive detection (splitter, low-pass filter, phase shifter, and mixer, amongst others). The RF driver produces up to $22\,\mathrm{dBm}$ of power output and is tunable from $0.1\,\mathrm{MHz}$ to $200\,\mathrm{MHz}$. For the stabilization an RF power of $17\,\mathrm{dBm}$ is used, yielding a modulation index of $\beta \approx 0.47$. Being lower than the value of highest effect, $\hat{\beta} \approx 1.08$, this setting was chosen because the slope of the error signal was tested to be perfectly sufficient for the stabilization. Additionally, the transfer of too much power into the sidebands is unfavorable as this power is reflected by the cavity, reducing the effective power for the seeding process. The frequency was adjusted together with the EOM at the factory to the desired value. The driver unit provides a function to automatically track the resonance frequency of the EOM during operation. In this way, modulation fluctuations caused

---

[54] *Qubig*, EO-T80M5-NIR

[55] *Qubig*, PD-AC100Si

[56] *Qubig*, Advanced Driver Unit (ADU)

by thermal drifts are avoided. The unit is housed in a shielded enclosure preventing that the RF signal is dispread unintentionally and that other electromagnetic disturbances are captured. By means of the new detector and the electronics unit the signal-to-noise ratio of the error signal was considerably enhanced.

Finally, the error signal is passed to a servo controller. The device[57] is equipped with a proportional-integral controller and supplementary signal-processing components (filters, attenuators, ampflifiers, etc). The settings of the servo allow manipulating the error signal to form an appropriate correction signal. Optionally, the device can sample and hold the correction signal following an external trigger. The output is connected to a high-voltage amplifier[58] which drives the piezo actuator[59]. In [25], SCHILLER estimated the response frequency for the same combination of piezo actuator and fixed cavity mirror as well as for this high-voltage amplifier model. He found that the response was limited by the latter to a frequency of $f \approx 3\,\mathrm{kHz}$. This value was verified by the adjustment of the servo's corner frequency, being the same in the present setup. The piezo actuator in combination with its driver has a maximum displacement which corresponds to approximately 12 times the free spectral range. The output voltage of the servo controller, however, is restricted in such way that three times the free spectral range is covered during stabilization. This restriction is acceptable because a larger displacement of the piezo actuator affects the adjustment condition for laser resonance when the thermal lens is present. The mentioned devices are depicted in Figure 5.7 of the Ti:sapphire laser setup.

Owing to the low finesse of the cavity, the error signal as a function of the detuning differs somewhat from the more common picture of three superposed, sharply-defined dispersion curves. In order to assess which signal shape can be expected from the experiment, the error signal was calculated for the corresponding parameters of the cavity and the modulation. Additionally, the transmission intensity of the modulated seeder wave through the cavity was computed. The calculation was realized with a *Mathematica* program supplied by the manufacturer of the PDH devices and adapted to the aforementioned cavity configuration. Figure 5.11 shows the obtained theoretical transmission intensity as well as the PDH error signal for the two cases of modulation depth, $\beta = 0.47$ and $\beta = 1.08$. Not surprisingly, the transmission peaks appear with a broad linewidth according to an Airy function of low finesse. For the lower modulation index, $\beta = 0.47$, the sidebands on the left and right of each peak are hardly visible. For $\beta = 1.08$, the sidebands are very high, as expected. The error signal turns out to be smoothed, without its distinctive side peaks, but still featuring some bucklings. The latter become more pronounced for the higher modulation index. Most crucial is the bipolar slope at resonance, which is steep even for the case of lower modulation depth.

The measurement of these signals was carried out by ramping the cavity length, i.e., applying a linearly increasing voltage to the piezo actuator. Both error signal and piezo voltage were taken from corresponding monitor outputs of the servo controller and the high-voltage amplifier. For the measurement, the seeder beam was used while the Ti:sapphire crystal was being pumped just below the laser threshold. As already discussed at the end of Section 4.7, this leads to a beam propagation and interference corresponding closer to the resonator's eigenmode. In Figure 5.12,

---

[57] *Sacher Lasertechnik*, LB2001

[58] *Physik Instrumente (PI)*, Piezo Amplifier Module E-507.00X

[59] see footnote 14 on page 97

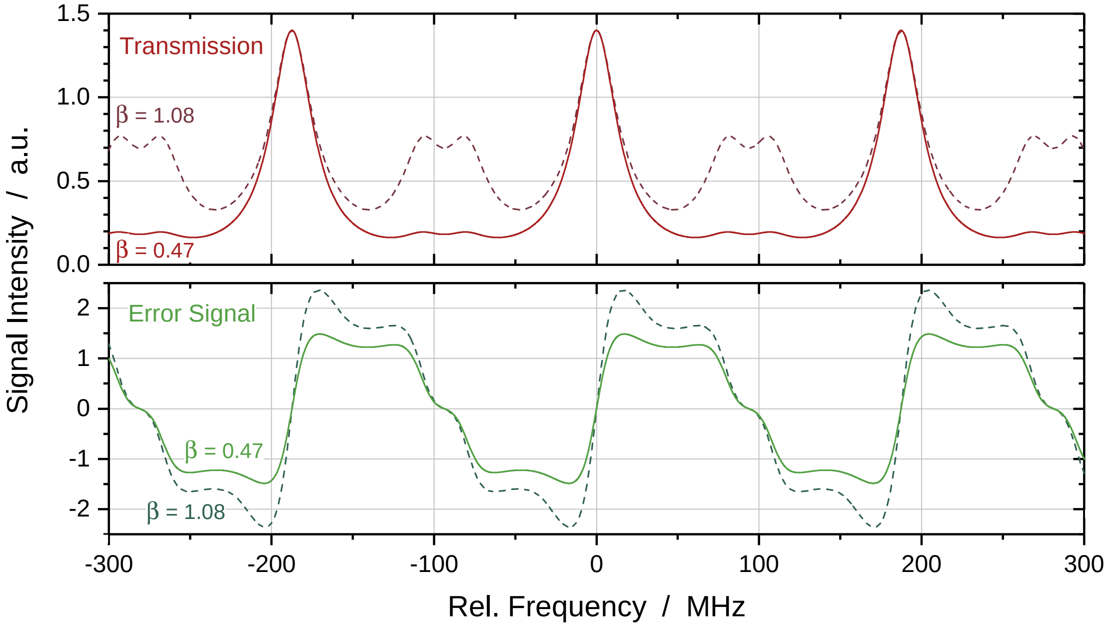

Figure 5.11: Calculated transmission and PDH error signal for the Ti:sapphire laser resonator. Two cases of different modulation index are depicted: the experimental realization ($\beta = 0.47$, solid line), and the modulation for which the error signal is highest ($\beta = 1.08$, dashed line).

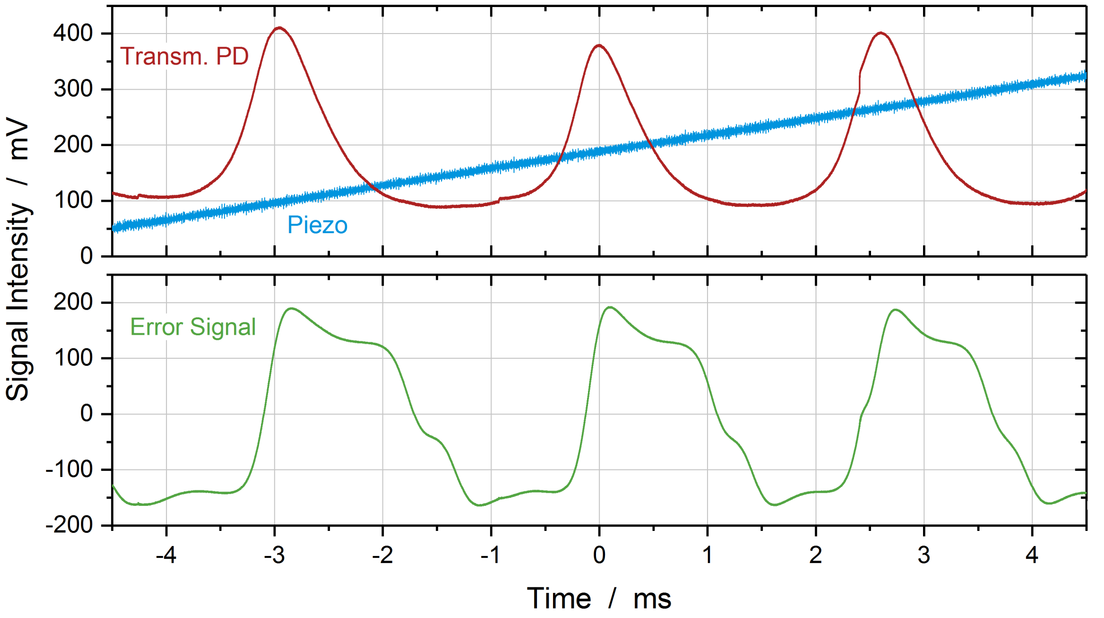

Figure 5.12: Laser cavity transmission signal of the seeder beam, measured with a photodiode (Transm. PD) while ramping the piezo voltage and resulting PDH error signal. The three minor discontinuities in the transmission signal were caused by parasitic light of the pump pulses.

the resulting signals are plotted. They match well with the calculated curve progressions. In comparison, the transmission peaks are broader, and the sidebands are not discernible. In the measurement it was also observed that the peaks were partly askew, with varying maximum intensities. The error signal also exhibits a slight asymmetry, still being very similar to the theoretical curve. These differences are explained by the fact that at the pumping level below laser threshold, the thermal lens is too weak, and the ideal mode-matched condition of the seeder beam is not yet given. Conversely, when the pumping of the crystal was completely omitted, the transmission peaks got even wider and the error signal turned out to be greatly smoothed. Finally, a shift between the transmission peaks and the zero crossing of the error signal is noticed. However, in an individual measurement of the reflection signal a minor shift was present as well. The reason for this could be a residual amplitude modulation of the EOM [162, 165]. The phenomenon can introduce a small detuning—or frequency offset—from the seeder frequency. Nonetheless, the relative frequency stability is unaffected. Section 5.7.3 demonstrates that a high frequency stability of the Ti:sapphire laser was obtained.

5.7 Characterization

5.7.1 Thermal Lens

The focal length of the Ti:sapphire laser crystal's thermal lens was determined evaluating the change of the caustic of a probe beam propagating through the crystal. One of the seed laser beams was used as probe beam. After the passage through the Ti:sapphire crystal the beam was directed with two bending mirrors to an M^2 device[60]. From the M^2 analysis, the parameters of the caustic were obtained. The pump source was the *PLA* laser.

The measuring principle consists of the following procedure. First, the caustic of the probe beam is measured without pumping the crystal. Since in this case no thermal lens is present, the resulting beam parameters serve as reference for the subsequent calculation. Then, the pump power is gradually increased. For every step, a full M^2 measurement is performed, including the determination of all beam parameters. The successively increasing thermal lens affects the caustic of the probe beam. Putting the beam parameters of the reference measurement in relation with the parameters of the altered caustic, enables calculating the focal length of the thermal lens at the related pump power. The beam waist of the probe beam is located in front of the laser crystal. Thus, in the presence of the thermal lens, a second beam waist is generated behind the crystal. Having determined the beam parameters in front of the thermal lens (from the reference measurement) and behind, the focal length is calculated [102, 136] with

$$f = \frac{l_1 - l_2\, z_{R1}/z_{R2}}{1 - z_{R1}/z_{R2}}\ , \tag{5.52}$$

where l_1, l_2 are the distances from the location of the thermal lens to the beam waist in front and behind the lens, respectively, and z_{R1}, z_{R2} are the corresponding Rayleigh lengths, given by the widths of the beam waist and the wavelength, as defined in Equation (5.7).

---

[60] see footnote 34 on page 49

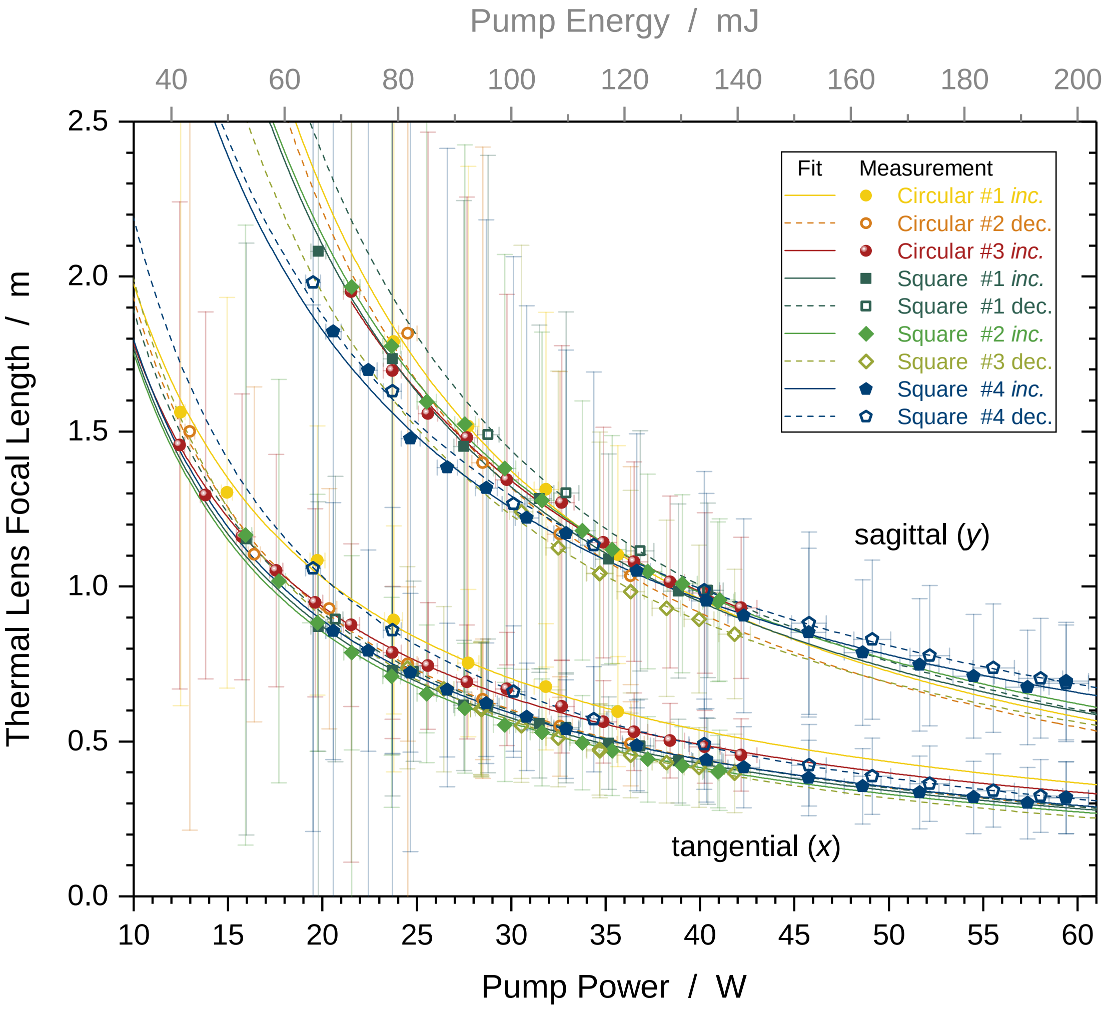

Figure 5.13: Measurement of the focal length of the Ti:sapphire crystal's thermal lens as a function of the pump power. Due to the Brewster geometry of the crystal, the focal length is different in the tangential and the sagittal plane. Several measurement series were carried out: for the cooling mount with the circular-cut and the square-cut crystal, for different M^2 device adjustments, as well as for increasing (inc.) and decreasing (dec.) pump power.

The alignment of the pump and the seed laser beam is identical to the situation during laser operation. Therefore, the method of measurement adequately reproduces the behavior of the thermal lens. During laser action the beam of the Ti:sapphire laser itself might have a minor influence on the generation of the thermal lens, too. From Equation (5.2) and the specified values for the crystals (see Section 5.4) follows $\alpha_{800} < 0.008\,\mathrm{cm}^{-1}$. The absorption at this wavelength is low, but the high intracavity power could cause an additional thermal load, as discussed for the Faraday rotator in Section 5.5. However, the measurement of the thermal lens during laser operation would be experimentally complex and limited to the maximum laser output power.

As is shown below, the characterization at higher powers is important, since the measurement errors are lower. The seed laser beam agrees well with a Gaussian beam, being confirmed by M^2 factors close to unity—even after propagation through the thermal lens (worst value of all measurements $M^2 = 1.25$)—and validating the application of Gaussian beam propagation laws. According to the astigmatic behavior of the thermal lens, it is distinguished between the tangential (x) and the sagittal (y) plane. For this measurement method it is beneficial to obtain the beam parameters from a systematically functioning device. A high repeatability is significant for the precision of the outcome.

Several measurement series have been carried out. Sequences for increasing and decreasing pump power were considered, different M^2 device adjustments, as well as both of the cooling mount constructions described in Section 5.4. In one case, data was also collected up to the maximum available pump power of $P \approx 60\,\mathrm{W}$ and back. In this measurement, the Ti:sapphire crystal in conjunction with the cooling mount also proved its capability to endure such high pump powers without damages. The obtained values of the focal length f were plotted against the pump power P. The results are depicted in Figure 5.13.

A curve of function $f(P) = a\,P^{\,b}$ was fitted to every series. Table 5.2 lists the resulting fit parameters, a and b. The fit function was chosen based on the thermal model of INNOCENZI *et al.* giving the equation for the effective focal length of an axially-pumped, cylindrical crystal rod [166],

$$f = \frac{\kappa\,\pi\,w^2}{(\mathrm{d}n/\mathrm{d}T)\;P_h}\,\frac{1}{1-\exp(-\alpha\,l)}\;. \tag{5.53}$$

Here, the crystal is parametrized by the thermal conductivity κ, the thermo-optic coefficient $\mathrm{d}n/\mathrm{d}T$, the absorption coefficient α, and the rod length l. The pump laser is implicated by the beam radius w and the power which is converted into heat P_h. The latter can be expressed with a heat conversion factor η_h and the (incident) pump power P by $P_h = \eta_h\,P$. The factor η_h, in turn, may be estimated by the Stokes efficiency (Equation 3.1) via $\eta_h = 1 - \eta_s$, as in [30], which represents the lower limit for η_h. Unlike Equation (5.53), an exponent b of the pump power P was implemented in the fit function. This allowed to find a theoretical relation following the experimental values more closely, because the primary objective of the thermal lens characterization was to precisely associate the focal length f to the pump power P. Nevertheless, further properties can be derived from the fit parameter a. It is assigned to

$$a = \frac{\kappa\,\pi\,w^2}{(\mathrm{d}n/\mathrm{d}T)\;\eta_h\;(1-\exp(-\alpha\,l))}\;. \tag{5.54}$$

Hence, by way of example, $\mathrm{d}n/\mathrm{d}T$ can be determined if the other values are known. For the calculation, the mean from the respective values of a for the tangential and the sagittal plane was taken. The reason was that the thermal model of INNOCENZI *et al.* described a simple cylindrical rod, without end-surfaces polished at Brewster's angle. The comparison of the model to a finite element analysis (FEA) with a Brewster-cut crystal demonstrated that Equation (5.53) provides a curve which lies between the curves of the tangential and the sagittal plane [30]. The constants $\kappa = 44\,\mathrm{W/(m\,K)}$, $\alpha_{532,c} = 1.84\,\mathrm{cm}^{-1}$, $\alpha_{532,s} = 1.72\,\mathrm{cm}^{-1}$, $l = 20\,\mathrm{mm}$, $w = (0.94 \pm 0.05)\,\mathrm{mm}$, and $\eta_h = 0.35 \pm 0.10$ were used. The indices c and s in the absorption coefficient at the pump wavelength α_{532} refer to the circular-cut and the square-cut

Measurement Series		Fit Parameter			
		Tangential (x)		Sagittal (y)	
		a (m/W)	b	a (m/W)	b
Circular # 1	inc.	17.2 ± 1.2	-0.94 ± 0.02	95.7 ± 20.6	-1.25 ± 0.07
Circular # 2	dec.	22.1 ± 1.3	-1.06 ± 0.02	100.3 ± 25.2	-1.27 ± 0.08
Circular # 3	inc.	15.2 ± 0.8	-0.93 ± 0.02	52.5 ± 5.2	-1.08 ± 0.03
Square # 1	inc.	18.7 ± 2.0	-1.02 ± 0.04	65.0 ± 9.7	-1.15 ± 0.05
Square # 1	dec.	21.1 ± 1.6	-1.05 ± 0.03	102.9 ± 21.6	-1.26 ± 0.06
Square # 2	inc.	19.2 ± 1.0	-1.04 ± 0.02	61.6 ± 3.6	-1.12 ± 0.02
Square # 3	dec.	27.6 ± 2.6	-1.14 ± 0.03	57.4 ± 6.8	-1.13 ± 0.04
Square # 4	inc.	18.4 ± 1.1	-1.01 ± 0.02	29.6 ± 2.7	-0.93 ± 0.03
Square # 4	dec.	26.5 ± 0.8	-1.08 ± 0.01	29.3 ± 1.2	-0.92 ± 0.01

Table 5.2: Resulting parameters of the function $f(P) = a\,P^b$ used for the fitting to the measurement series depicted in Figure 5.13.

crystal, respectively. The values are stated in the previous sections. The errors of w and η_h were estimated to cover different pump powers and consider a higher heat conversion. The results for $\bar{a}$, $\bar{b}$, and $\mathrm{d}n/\mathrm{d}T$ are listed in Table 5.3.

The following observations are made from Figure 5.13, and Tables 5.2 and 5.3. First of all, it should be noted that a clear distinction between the focal length values of the tangential and the sagittal plane is given. As expected, the thermal lens is stronger in the tangential plane due to the Brewster-cut of the crystal. Second, the inverse proportionality of the focal length as function of the pump power is readily observed. The fitted parameters b are close to -1, where the absolute values for the sagittal plane are slightly larger than for the tangential plane. Third, the uncertainty of the obtained values for the focal length increases for lower pump powers. This is attributed to a not very pronounced thermal lens at these powers. At larger focal lengths a fluctuation of the pump power comes stronger into effect. Additionally, the determination of the waist location becomes more difficult. That is why some outliers were removed from the measurement, most of them happening for focal lengths $f \gtrsim 2\,\mathrm{m}$. Fourth, the variation of the fit parameter $\bar{a}$, also results in different values for $\mathrm{d}n/\mathrm{d}T$. However, they are in the same order of magnitude and close to the value of undoped sapphire, $\mathrm{d}n/\mathrm{d}T \approx 13 \times 10^{-6}\,\mathrm{K}^{-1}$ which is found in the references [167, 168]. The uncertainties of the value are mainly caused by the error of η_h.

Finally, no clear conclusion can be drawn from the results whether one of the two crystal shapes or cooling mount types is more suitable. Within the error bars the focal length values are considered to be equivalent. This can be explained by the careful design and realization of the parts that clamp the crystal including the coating layer for both of the cooling mounts. Note that between measurements of increasing and decreasing pump power—without any further changes—differences in the results already occur. The cooling mount with the square-cut crystal was kept in the laser setup because of its mechanical advantages and the improved crystal quality.

Knowing the relationship between the pump power and the focal length of the thermal lens

Measurement Series		**Fit Parameter** $\bar{a}$	$\bar{b}$	**Thermo-optic Coefficient** $\mathrm{d}n/\mathrm{d}T$
Circular # 1	inc.	$(56.5 \pm 12.8)\,\mathrm{m/W}$	-1.09 ± 0.06	$(12.3 \pm 6.0) \times 10^{-6}\,\mathrm{K}^{-1}$
Circular # 2	dec.	$(61.2 \pm 15.7)\,\mathrm{m/W}$	-1.17 ± 0.07	$(9.9 \pm 5.0) \times 10^{-6}\,\mathrm{K}^{-1}$
Circular # 3	inc.	$(33.9 \pm 3.7)\,\mathrm{m/W}$	-1.00 ± 0.03	$(15.2 \pm 6.8) \times 10^{-6}\,\mathrm{K}^{-1}$
Square # 1	inc.	$(41.8 \pm 7.7)\,\mathrm{m/W}$	-1.08 ± 0.06	$(12.4 \pm 5.9) \times 10^{-6}\,\mathrm{K}^{-1}$
Square # 1	dec.	$(62.0 \pm 13.8)\,\mathrm{m/W}$	-1.15 ± 0.06	$(10.3 \pm 5.0) \times 10^{-6}\,\mathrm{K}^{-1}$
Square # 2	inc.	$(40.4 \pm 3.2)\,\mathrm{m/W}$	-1.08 ± 0.03	$(12.3 \pm 5.5) \times 10^{-6}\,\mathrm{K}^{-1}$
Square # 3	dec.	$(42.5 \pm 6.4)\,\mathrm{m/W}$	-1.14 ± 0.05	$(9.7 \pm 4.5) \times 10^{-6}\,\mathrm{K}^{-1}$
Square # 4	inc.	$(24.0 \pm 2.6)\,\mathrm{m/W}$	-0.97 ± 0.03	$(15.9 \pm 7.1) \times 10^{-6}\,\mathrm{K}^{-1}$
Square # 4	dec.	$(27.9 \pm 1.4)\,\mathrm{m/W}$	-1.00 ± 0.02	$(13.0 \pm 5.7) \times 10^{-6}\,\mathrm{K}^{-1}$

Table 5.3: Mean values of the fit parameters from the respective quantities of the tangential and the sagittal plane. By way of example, the thermo-optic coefficient $\mathrm{d}n/\mathrm{d}T$ was determined from the parameter $\bar{a}$ and the constants mentioned in the text. The parameter $\bar{b}$ is given for information only.

it is possible to represent the parameters of the resonator design as a function of the power rather than the focal length. To this end, the corresponding equations of Section 5.2.1 are composed via the focal length of the thermal lens with the now determined function $f(P) = a\,P^{\,b}$. For instance, the eigenmode's beam width at the laser crystal in the sagittal plane (Equation 5.15) becomes the composite function

$$w^2(f(P)) = \frac{\lambda}{\pi}\,\frac{2L\,a\,P^{\,b}}{\sqrt{4L\,a\,P^{\,b} - L^2}} = \frac{\lambda}{\pi}\,\frac{1}{\sqrt{\frac{1}{L\,a\,P^{b}} - \frac{1}{4a^2P^{2b}}}}\,. \tag{5.55}$$

In the same way, the composite functions for the tangential plane can be obtained by replacing f_1 in the equations of Appendix A.3. The beam width at the laser crystal w and at the waist w_0 are depicted in Figure 5.14 for the tangential and the sagittal plane, respectively. For the calculation of the curves the fit parameters of the measurement series were used. The other constants were chosen as described at the end of Section 5.2.1 ($\lambda = 818\,\mathrm{nm}$, $L = 1.6\,\mathrm{m}$, $f_{cyl} = -842\,\mathrm{mm}$, $L_1 = 230\,\mathrm{mm}$). The point of dynamical stability is marked in every curve. Additionally, the pump power range is highlighted for laser operation achieving 10 W output power. As can be seen, the variation of the measurement series becomes more apparent in the tangential plane. For the majority of the curves the dynamically stable operation in the tangential plane is close to or within the 10 W laser operation range. As expected, In the sagittal plane the dynamically stable points lie at much higher pump powers. Nonetheless, at laser operation of 10 W the deviation and change of the beam width w is very small.

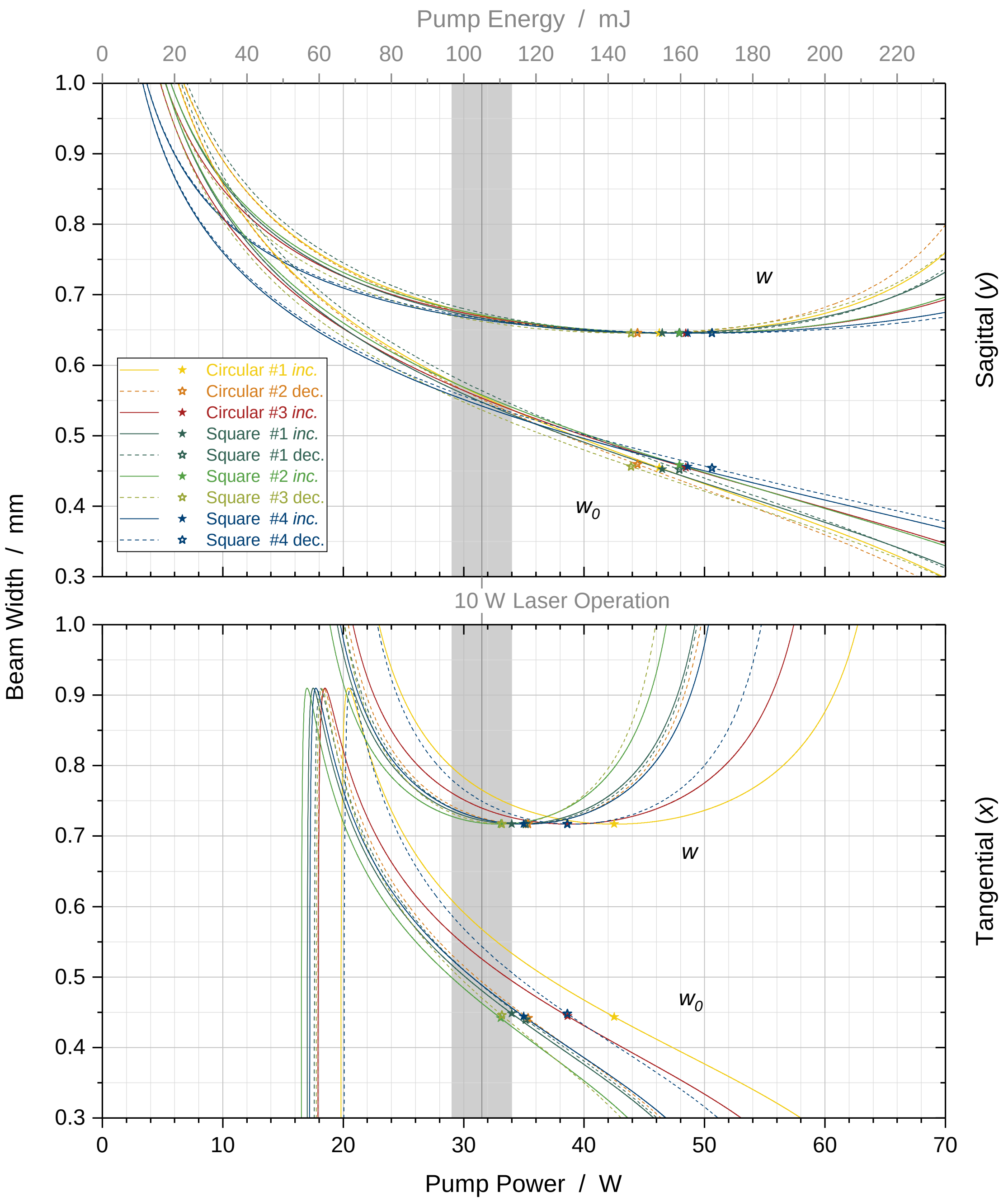

Figure 5.14: Beam radius w at the titanium–sapphire crystal and w_0 at the waist as a function of the pump power for the tangential and sagittal plane of the laser eigenmode. The curves were obtained by composition of the fit functions from the thermal lens measurement (Figure 5.13) with the corresponding equations of the resonator design (Section 5.2). The points of dynamical stability are marked with $\star$.

5.7.2 Average Power, Energy, Pulse Characteristics, and Polarization

In the course of the laser development process, operation with an ever higher output power was achieved. The principal steps in this regard consisted in modifying the resonator from the one–lens to the two–lens configuration and changing to a new pump source. In the meantime, the laser system already came into operation as transmitter of the Hohenheim-DIAL during several field campaigns. Thus, a higher maximum output power was gradually available for the campaigns (see Chapter 6.1.1). For all measurements presented in this section, the Ti:sapphire laser was injection seeded and actively frequency stabilized to the online diode laser.

Input–Output Power Curves

In the beginning, the *IBL* laser (Chapter 3.2) was used as pump source for the titanium–sapphire laser. Furthermore, the thermal lens was the only focusing element in the resonator, the design being as described in Section 5.3, but without the cylindrical lens. In this configuration, laser operation up to approximately $P = 7\,\mathrm{W}$ average output power was possible, corresponding to a pulse energy of $E = 28\,\mathrm{mJ}$ at $f_{rep} = 250\,\mathrm{Hz}$ repetition rate. A curve of the output *versus* pump power is presented in Figure 5.15. The pump power was determined beforehand by assigning the pulse delay values of the *IBL* laser's pump chambers to the delivered power at $532\,\mathrm{nm}$, as depicted in Figure 3.2 on page 32. The laser output data was recorded with the *Coherent* power meter[61]. In the following, unless otherwise indicated, a measurement uncertainty of $5\,\%$ is stipulated for all power values. This factor takes into account other power meter models that were also utilized. The fit of a line to the measured values yields a slope efficiency of $\eta_{slope} = (31 \pm 3)\,\%$. The first two measurement values were excluded from the fit since they were considered to be too close to the laser threshold at $P_{532,ths} = (8.5 \pm 1.0)\,\mathrm{W}$ pump power. The total laser efficiency (optical to optical conversion) was $\eta_{total} > 27\,\%$. At an average output power of $P_{max} \approx 7.16\,\mathrm{W}$ ($E_{max} \approx 28.64\,\mathrm{mJ}$) the Faraday rotator in the resonator was damaged. In this moment the rotator was exposed to an intracavity power of $P_{ic,max} \approx 17.9\,\mathrm{W}$ and the pulse length was $\Delta t \approx 29\,\mathrm{ns}$ (FWHM). From the caustic analysis of the fundamental eigenmode, the beam radius at the according position was calculated to be $w \approx 0.57\,\mathrm{mm}$ (Gaussian beam profile). Hence, the damage occurred at a peak power density of $\approx 475\,\mathrm{MW/cm^2}$ or a fluence of $\approx 14.1\,\mathrm{J/cm^2}$. The obtained maximum output power and the total efficiency are higher than for the previous laser transmitter ($P_{max} = 6.75\,\mathrm{W}$ and $\eta_{total} = 19\,\%$) [25,26]. Both are attributed to the improved pump beam quality of the revised *IBL* laser (see Chapter 3.2.3).

To compensate for the strong contraction of the eigenmode in the tangential (x) plane, a cylindrical lens was integrated in the laser resonator. The first model[62] which was applied has a nominal focal length of $f_{nom} = -750\,\mathrm{mm}$. The lens is made of the material BK7, resulting in nearly the same focal length at the laser wavelength, $f_{820} = -747\,\mathrm{mm}$. Apart from this modification, the setup was as before. Now a power output up to $P_{max} = 8\,\mathrm{W}$ ($E_{max} = 32\,\mathrm{mJ}$) without damage was achieved, which was only limited by the maximum available pump power. The measurement was verified with different power meters[63,64]. In some exceptions deviations

---

[61] see footnote 29 on page 44

[62] *CVI / Melles Griot*, SCC-20.0-381.4-C-633-1064

[63] see footnote 28 on page 44

[64] *Coherent*, LM30v with FieldMax TOP

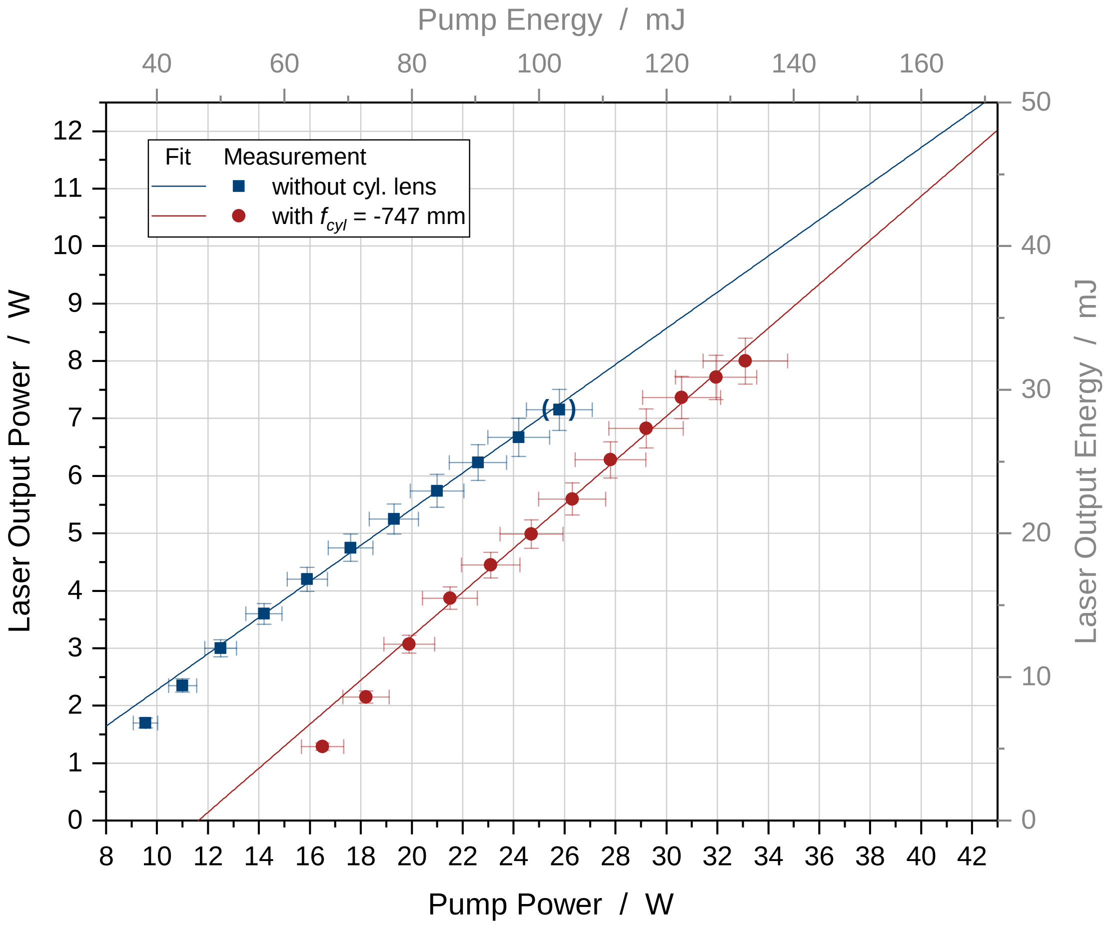

Figure 5.15: Average output power of the Ti:sapphire laser ($\lambda = 818\,\mathrm{nm}$) as a function of the pump power ($\lambda = 532\,\mathrm{nm}$). The pump source was the *IBL* laser. Two exemplary cases are shown: the resonator configuration with the thermal lens only (without cyl. lens), and the configuration with an additional cylindrical lens ($f_{cyl} = -747\,\mathrm{mm}$) installed in the resonator. The point in parenthesis was measured shortly before optical damage occurred.

up to $6\,\%$ between the devices were observed. For the performance curve (depicted in Figure 5.15) it is remarked that the output powers shifted towards higher pump powers. Laser emission was beginning at a pump power of $P_{532,ths} = 14.9\,\mathrm{W}$. The power shift is attributed to the cylindrical lens since it is an additional element in the resonator causing losses. The linear fit (again excluding the two values close to the laser threshold) gives a higher slope efficiency of $\eta_{slope} = (38 \pm 5)\,\%$. The total efficiency is lower due to the increased losses, $\eta_{total} \approx 24\,\%$.

With the *PLA* laser (Chapter 3.3), a pump source of considerably more average output power was provided (up to $P_{532} \approx 60\,\mathrm{W}$, i.e., $E_{532} \approx 200\,\mathrm{mJ}$ at $f_{rep} = 300\,\mathrm{Hz}$). This enabled achieving the aspired goal of a Ti:sapphire laser with $P = 10\,\mathrm{W}$ average output power, corresponding to a pulse energy of $E = 33.\overline{3}\,\mathrm{mJ}$. Additionally, the cylindrical lens was replaced by an en-

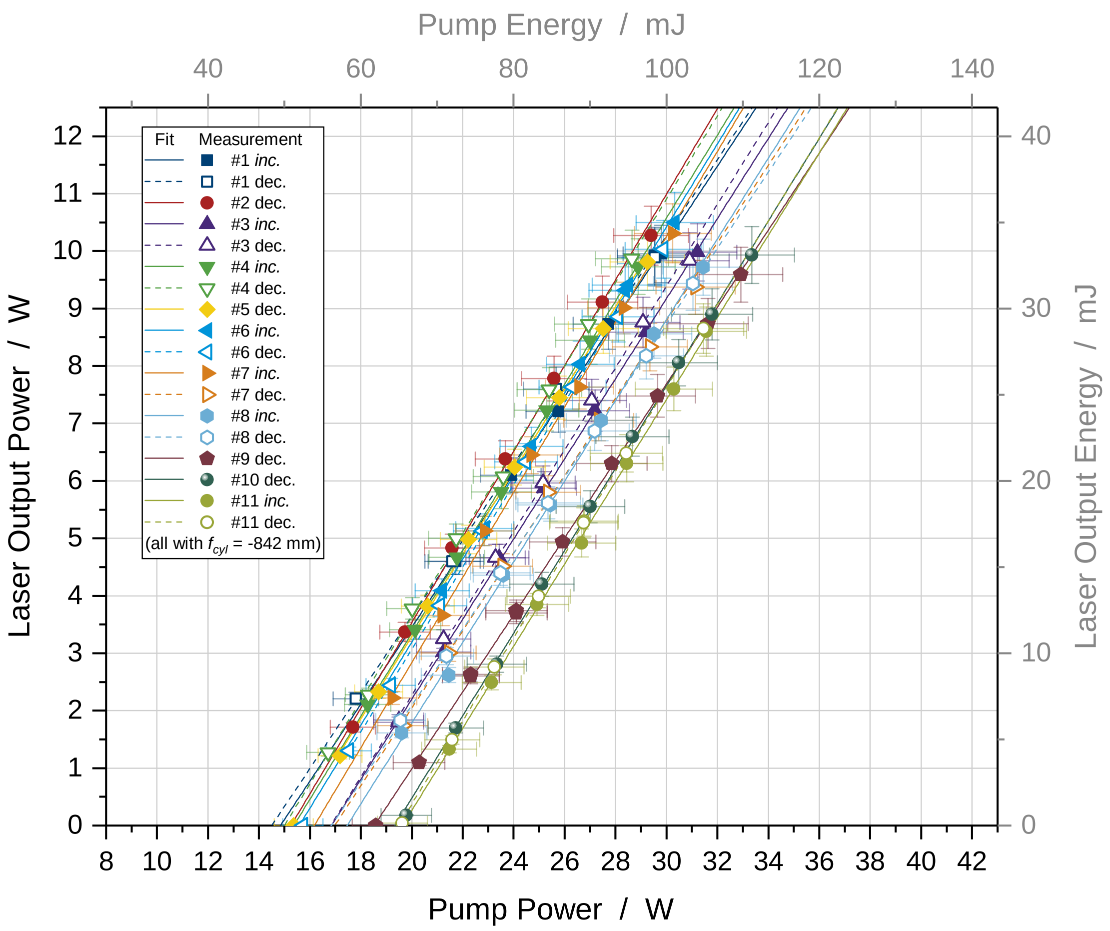

Figure 5.16: Input–output power measurements of the Ti:sapphire laser with the *PLA* laser as pump source. The cylindrical lens of focal length $f_{cyl} = -842\,\mathrm{mm}$ was installed in the resonator, representing the final configuration of the laser. Measurement series with increasing (inc.) and decreasing (dec.) power were carried out. Output power values $P < 1\,\mathrm{W}$ were excluded from the linear fits. The variations in the series are mainly explained by different laser adjustments.

hanced model[65] of same nominal focal length but made from fused silica. The focal length at the operation wavelength was now $f_{820} = -842\,\mathrm{mm}$. Owing to the internal power measurement arrangement of the *PLA* laser (described in Section 3.3.1) it was possible to obtain information on the pump power more directly. The output of the Ti:sapphire laser was measured with the *Ophir* power meter[66] and occasionally verified by the other models at disposal. Figure 5.16 shows performance curves for the mentioned configuration, representing the current development state. Cases for which the overall adjustment of the laser was not entirely optimized, e.g., due to temporary exchange and trial of different components, are also been included.

---

[65] *CVI / Melles Griot*, SCC-25.4-381.4-UV-700-900 ($f_{nom} = -750\,\mathrm{mm}$)

[66] see footnote 30 on page 44

Consequently, the values obtained from the linear fits vary. The laser threshold ranges from $P_{532,ths} = (14.5 \pm 3.3)\,\mathrm{W}$ to $(19.6 \pm 4.9)\,\mathrm{W}$, and the slope efficiency from $\eta_{slope} = (66 \pm 8)\,\%$ to $(75 \pm 9)\,\%$. The efficiency has risen significantly compared to the performance when using the *IBL* laser as pump source. This reflects the fact that the top-hat-like beam profile of the *PLA* laser (Section 3.3.3) leads to a much better spatial overlap for the radiation transfer. In this way, even less average power for pumping is needed ($P_{532} \approx 31\,\mathrm{W}$) to obtain a laser output power of $P = 10\,\mathrm{W}$ with the *PLA* laser, then to achieve the laser output of $P = 8\,\mathrm{W}$ with the *IBL* pump laser ($P_{532} \approx 33\,\mathrm{W}$). At the power level of $P = 10\,\mathrm{W}$ the total efficiency of the laser lies between $\eta_{total} = 29\,\%$ and $35\,\%$.

The availability of more pump power with the *PLA* laser offers the possibility for investigating how far the Ti:sapphire laser can be driven to its own damage threshold and how this limit can potentially be extended. That is why in further tests the pump power was intentionally increased until the Ti:sapphire laser power suddenly dropped, indicating a deterioration of an optical element. For the configuration with the cylindrical lens of focal length $f_{820} = -747\,\mathrm{mm}$ this value was reached at an average output power of $P_{max} = 10.69\,\mathrm{W}$. The lens itself was affected by the optical intensity (deduced peak power density $\approx 401\,\mathrm{MW/cm^2}$ and fluence $\approx 11.6\,\mathrm{J/cm^2}$). In the present configuration with the cylindrical lens of focal length $f_{820} = -842\,\mathrm{mm}$, laser operation without harm at a maximum output of $P_{max} = 10.5\,\mathrm{W}$ was achieved. Tentatively, other cylindrical lenses were implemented, the underlying idea being to increase the resonator's mode size. First, another cylindrical lens[67] with an even shorter focal length of $f_{820} = -561\,\mathrm{mm}$ replaced the preceding model. In this case, a maximum output power of $P_{max} = 11.19\,\mathrm{W}$ ($E_{max} = 37.3\,\mathrm{mJ}$) was reached. Once more, the anti-reflective coating of the lens manifested itself as the weak point (corresponding peak power density $\approx 415\,\mathrm{MW/cm^2}$ and fluence $\approx 11.8\,\mathrm{J/cm^2}$). During other attempts in this configuration, though, two different Faraday rotator models suffered burn patterns already at lower powers (see also Section 5.5). Subsequently, a cylindrical lens for the sagittal (y) plane was added. A model[68] with a moderately compensating focal length of $f_{820} = -1706\,\mathrm{mm}$ was chosen. As a result, the highest average output power was obtained, $P_{max} = 11.81\,\mathrm{W}$ ($E_{max} \approx 39.4\,\mathrm{mJ}$). The *Leysop* Faraday rotator endured up to a peak power density of $\approx 628\,\mathrm{MW/cm^2}$ and a fluence of $\approx 16.6\,\mathrm{J/cm^2}$. These values appear unusually high for the specified damage threshold of the device. However, optical damage values have a certain fluctuation. The input–output power curves for the latter two resonator configurations are plotted in Figure 5.17. The values in parenthesis were the highest measured values at the instant shortly before the damage took place. Note that for the configuration with $f_{820} = -561\,\mathrm{mm}$ alone, there are also measurement series which required higher pump powers. This is again attributed to a not perfectly optimized laser adjustment. Safe operation in the dual-cylindrical-lens configuration was possible at lower powers (e.g., $P = 11\,\mathrm{W}$). On the other hand, the laser exhibited an irregular movement in its beam position which was accompanied by a more active piezo regulation. The consequence was a stronger fluctuation of the output power. A lower variation of the output power ($\Delta P \lesssim \pm 0.5\,\mathrm{W}$) due to a change of the piezo voltage is also observed in the current laser configuration, most notably when operated away from the design point of dynamical stability. Here in contrast, the fluctuations are calm and do not affect

---

[67] *CVI / Melles Griot*, SCC-25.4-254.3-UV-700-900 ($f_{nom} = -500\,\mathrm{mm}$)

[68] *Laser Components*, AR/AR820 RCC25.4-25.4-772.6UV ($f_{nom} = -1500\,\mathrm{mm}$)

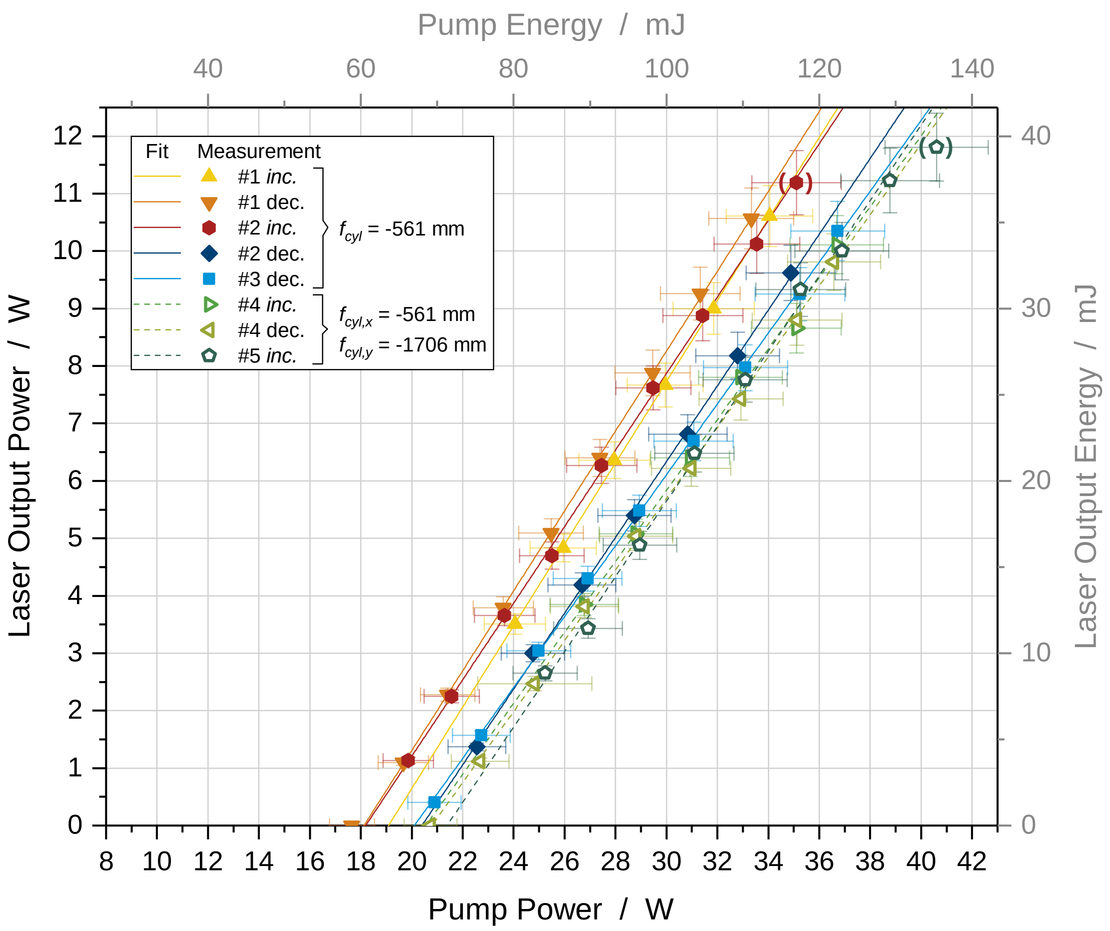

Figure 5.17: Power curves of the Ti:sapphire laser for two further resonator configurations which were experimentally tested to achieve a higher laser output. The points in parenthesis represent the maximum power values measured before optical damage occurred.

the remaining laser performance. The resonator configuration with only one compensating lens ($f_{820} = -842\,\mathrm{mm}$) proved itself during long-term operations of intensive observation periods with the Hohenheim-DIAL.

Pulse Characteristics

Similar to the pump laser (see Chapter 3.2.2 and 3.3.2), the pulses of the Ti:sapphire laser were analyzed with a fast detector[69] and a high-resolution oscilloscope[70]. The pulse characteristics depend on the laser power. The build-up time of the pulse, its width, and area were determined with the oscilloscope's integrated evaluation functions. Figure 5.18 shows the build-up time and the pulse duration as function of the laser output power. At every power value, except for the values $P > 10\,\mathrm{W}$, a statistic was run over approximately one minute corresponding to a sample of $18\,000$ pulses. For the measurement points $P > 10\,\mathrm{W}$, the period of the statistic was five to ten minutes (more than $100\,000$ pulses). Out of each sample the maximum and the minimum value were used for the y-error bars. By measurement of the pulse area, the energy stability from pulse to pulse was obtained. Dividing the standard deviation by the mean value of the pulse area gave $0.4\,\%$ to $0.7\,\%$ for the operation powers $P \geq 7\,\mathrm{W}$, and hence, an energy stability $\Delta E \geq 99.3\,\%$. At the lower powers, departing from the dynamically stable point, the stability decreased down to $\Delta E = 96.8\,\%$

Since the Ti:sapphire laser was injection seeded and actively frequency stabilized, the pulse showed a persistent smooth shape, close to a Gaussian function. This is illustrated in Figure 5.19 for the measurement point at $P = 10.25\,\mathrm{W}$, together with the pulse of the pump source which was acquired with an individual detector. The fit of a Gaussian function reveals that the laser pulse is somewhat askew, showing a prolonged decay. Note that already the pump pulse (envelope) possesses such an askew shape, probably being the cause. The skewness leads to a bias of the fitted function. Most notably, the center position of the function is slightly shifted to the right. That is why a second fit was executed with fixed values for the center position and the amplitude of the Gaussian function. The two fitted functions are plotted in the same figure. The resulting width (FWHM) of the fitted function without and with the fixed parameters is $\Delta t = (31.2 \pm 0.1)\,\mathrm{ns}$ and $\Delta t = (30.0 \pm 0.1)\,\mathrm{ns}$, respectively. The latter complies with the value determined by the oscilloscope, $\Delta t = (30.1 \pm 0.3)\,\mathrm{ns}$. However, the pulsed widths observed for the different resonator configurations deviated to a larger extent ($\approx 2\,\mathrm{ns}$) from the values discussed here. During online–offline operating mode, a small difference (around $5\,\mathrm{ns}$) in the build-up time between the online- and offline-seeded laser pulses was also observed. It was found that the appearance and the magnitude of this delay correlated with the detuning between the online and the offline frequency from an integer number of the cavity's free spectral range. Since the lidar measurement is triggered by the laser pulse, this delay or timing jitter originating from the pump pulse has no effect on the data acquisition.

The smooth pulse shape indicates that the laser is running at one single frequency. Provided that the pulses are Fourier transform-limited, the time–bandwidth product (Equation 2.15) gives a spectral linewidth of $\Delta\nu = (14.7 \pm 0.2)\,\mathrm{MHz}$. If the frequency stabilization of Ti:sapphire laser is deactivated the pulses recurrently exhibit a shape with a mode beating structure similar to the pump pulses. This was used to verify—via the fast Fourier transformation and Equation (3.3)—the free spectral range and the optical length of the cavity (cf. Section 5.2.2). The experimentally gained values are $\Delta\nu_{FSR} = (189.3 \pm 0.5)\,\mathrm{MHz}$ and $L = (1.584 \pm 0.005)\,\mathrm{m}$. The optical length of the resonator is slightly below the value used for the theoretical calculations,

---

[69] see footnote 12 on page 34

[70] see footnote 13 on page 34

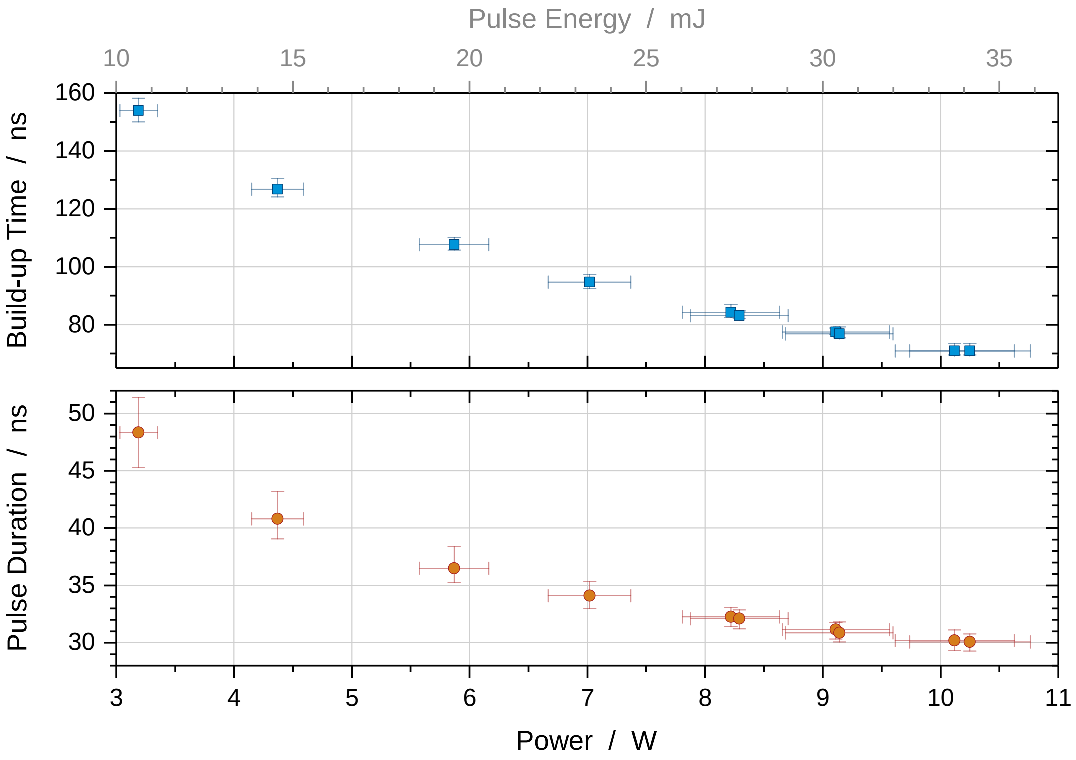

Figure 5.18: Build-up time and duration of the Ti:sapphire laser pulses as a function of its output power for the present resonator configuration.

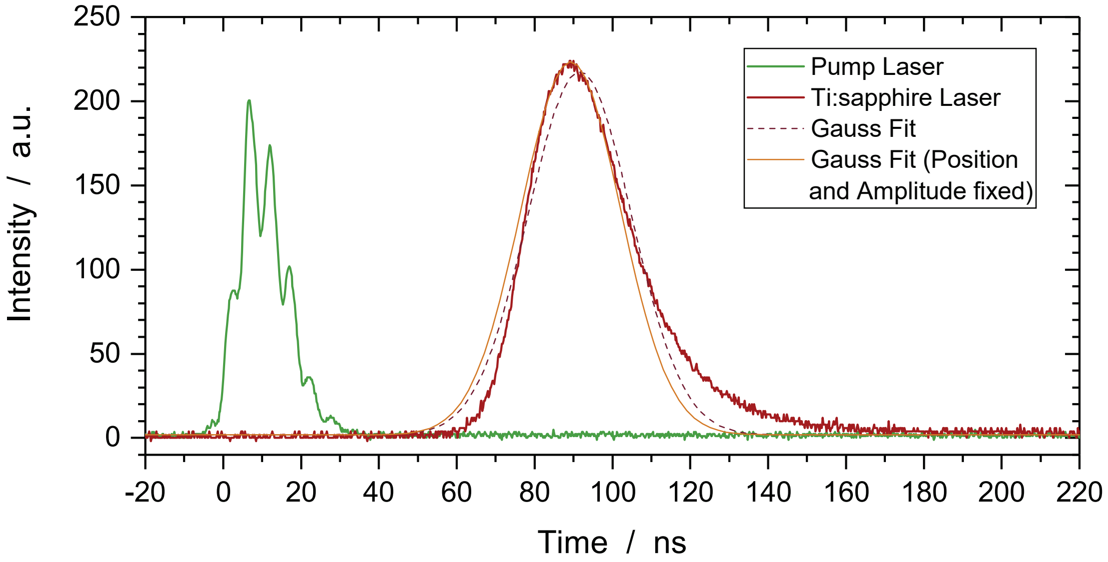

Figure 5.19: Pump pulse and Ti:sapphire laser pulse at the measurement point of $P = 10.25\,\mathrm{W}$. A Gaussian function without and with partially fixed parameters was fitted to the laser pulse.

$L = 1.6\,\mathrm{m}$. The geometrical resonator length was measured to be $L_{geo} = (1.53 \pm 0.01)\,\mathrm{m}$.

Polarization, Electrical Power Consumption

The ratio of linear polarization of the laser output was measured with the arrangement measuring and controlling the power which exits the casing (see Section 5.3). The almost completely p-polarized power and the residual s-polarized fraction were measured with the *Ophir* power meter and a sensitive power meter[71], respectively. The obtained polarization ratio values were $> 99.97\,\%$. Since the laser beam exits the casing through a Faraday isolator, the linear polarization is herewith ensured.

The electrical power consumption of the entire Ti:sapphire laser system is essentially given by the consumption of the pump laser (including the air–water heat exchanger in the energy compartment of the trailer for the water circulation). During operation of the laser system, the UPS of the Hohenheim-DIAL measured a power consumption of $\approx 9\,\mathrm{kW}$, being a bit higher then when only the pump laser was running ($\approx 8.4\,\mathrm{kW}$).

5.7.3 Spectrum, Frequency Stability, and Linewidth

The spectral properties of the Ti:sapphire laser radiation were investigated in different ways. With an optical spectrum analyzer, the emission spectrum was measured on a broad scale. For a fine analysis, a wavelength meter with extensive evaluation capabilities was used. The spectral purity and the frequency tuning were assessed during special DIAL measurements (see the next chapter).

Optical Spectrum Analyzer

The optical spectrum analyzer[72] (OSA) is specified to be sensitive over the wavelength range from $500\,\mathrm{nm}$ to $1000\,\mathrm{nm}$ with an accuracy of $\Delta\lambda < 0.6\,\mathrm{nm}$. A mere fraction of the laser light at the output of the Ti:sapphire laser was fiber-guided[73,74] into the OSA. Several spectra were collected: while the laser was injection seeded, as well as in a free-running mode (i.e., without seeding). With the help of the OSA, the adjustment of the birefringent filter was performed by monitoring the spectrum during unseeded laser operation. Furthermore, the measurement enabled to identify potential laser emission at other than the desired wavelength of $818\,\mathrm{nm}$. An exact comparability of the absolute intensity values is not guaranteed because the amplitude calibration of the OSA was due and the transmission through the (singlemode) fiber has a certain wavelength dependency. Spectra for the seeded and the free-running mode are presented in Figure 5.20. They were measured for a laser operation with an output power of $P \approx 2\,\mathrm{W}$.

The spectrum sweeps of the free running Ti:sapphire laser show a main intensity peak at $\lambda = 818\,\mathrm{nm}$, but around the wavelength $\lambda = 781\,\mathrm{nm}$ significant peaks are also present. Thus, it appears that the birefringent filter selects the principal wavelength of operation, though it does not succeed in completely suppressing the gain maximum of titanium-doped sapphire at

---

[71] see footnote 23 on page 69

[72] *Thorlabs*, CCS175/M

[73] *Nufern*, 780-HP

[74] *Thorlabs*, M14L01

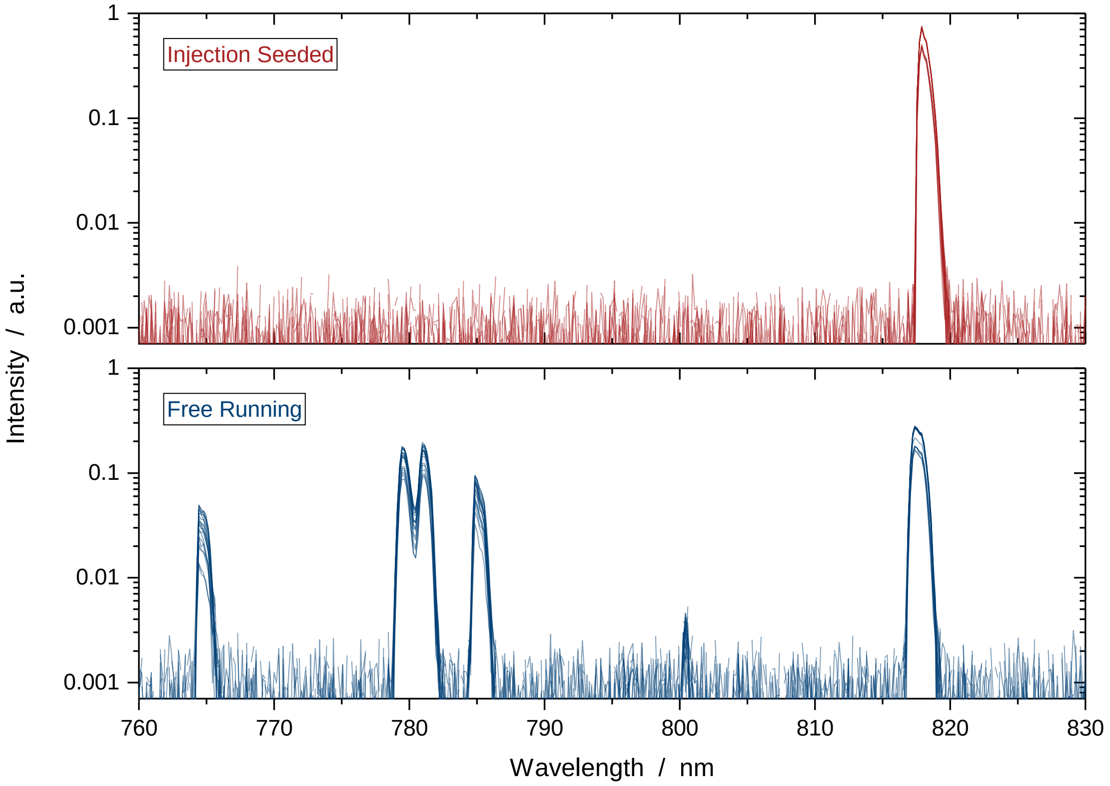

Figure 5.20: Spectrum of the Ti:sapphire laser with injection seeding and without (free running). Several sweeps of the optical spectrum analyzer were performed. The measurement was carried out to identify other than the main emission peak at $\lambda = 818\,\mathrm{nm}$. The intensity is plotted on a logarithmic scale. The absolute values of the amplitudes are not comparable (see text).

$\lambda = 790\,\mathrm{nm}$. To understand this, the calculated transmission curves of the birefringent filter (see Figure 5.10 of Section 5.6.1) are reconsidered. It is noticed that for the used filter setting ($\phi \approx 30°$) some of the secondary transmission peaks coincide with the location of the supplementary intensity portions measured. On the one hand, this could be an explanation for the occurrence of the unwanted intensity double peak at $\lambda \approx 781\,\mathrm{nm}$, and the peak at $\lambda \approx 786\,\mathrm{nm}$. On the other hand, it is unclear why these secondary peaks rise, while others, being also close to the gain maximum, can not ($\lambda \approx 797\,\mathrm{nm}$) or only hardly ($\lambda \approx 802\,\mathrm{nm}$) be observed. The theoretical model could have reached its limits here, as well.

The adjustment of the birefringent filter's rotation showed that either the left or the right part of the double peak at $\lambda = 781\,\mathrm{nm}$ quickly start to dominate if the main transmission peak of the birefringent filter at $\lambda = 818\,\mathrm{nm}$ is slightly adjusted towards smaller or larger wavelengths, respectively. Thus, for the fine adjustment two conflicting interests had to be compromised. The undesired intensity emission around $\lambda = 781\,\mathrm{nm}$ had to be kept at minimum (i.e. both parts of the double peak at approximately the same intensity level). What is more, the location of the main intensity peak had to allow both, online and offline seeding. Hence, the main intensity peak was set as close as possible to the online and the offline wavelength while the unwanted intensities were kept as low as possible.

When the laser resonator was injection seeded, no other intensity portions were detected apart from the peak at the seeder wavelength which became even more pronounced. This also holds for laser operation at higher powers as verified by corresponding measurements with the OSA. It was decided to refrain from high power operation without injection seeding due to the above findings which could have led to an uncontrolled or detrimental functioning of the laser. The spectrum during online or offline seeded laser operation distinguished itself by a marginal wavelength shift only. In comparison, the spectrum of the free-running mode exhibits a more distinct shift of the primary intensity peak, and in the opposite direction. However, this was considered as the best compromise. In conclusion, it could still be beneficial to develop an optimized birefringent filter in the future. To suppress the arising emission around $781\,\mathrm{nm}$, the design of the filter could be adapted either by a different arrangement of the birefringent plates (plate thickness, plate order), by adding additional ones, or increasing the aperture so as to access other rotation angles.

Wavelength Meter

The wavelength meter for the characterization of the Ti:sapphire laser is similar to the model installed in the seeding system (see Section 4.3.2). This model here[75] has even higher accuracy as well as linewidth measurement and external pulse triggering capabilities. The manufacturer specifies the following values [169]. In the wavelength range from $420\,\mathrm{nm}$ to $1100\,\mathrm{nm}$ the absolute accuracy is $30\,\mathrm{MHz}$ with a resolution (wavelength deviation sensitivity) of $5\,\mathrm{MHz}$. For the linewidth analysis the accuracy is $100\,\mathrm{MHz}$ (FWHM); the maximum bandwidth that the device can reliably interpret is $8\,\mathrm{GHz}$. As the device is controlled from a computer with strong hardware, the maximum data-acquisition and wavelength-determination speed ($400\,\mathrm{Hz}$) lies above the pulse repetition rate of the laser, enabling measurements for every single pulse. The latter requires special preparation of the software.

The wavelength meter is regularly used during laser operation to monitor the frequency-stable and narrowband emission. Only if this is confirmed, the laser is turned up to its highest power. It is understood that the Ti:sapphire laser is then operated with the active stabilization technique since it provides the required single-frequency mode. The frequency performance of the Ti:sapphire laser is demonstrated in two exemplary cases, both having been executed at $P \approx 10\,\mathrm{W}$ power output. In the first case, the laser was continuously injection seeded with one diode laser only (stabilized to the online frequency). The measurement shows the achievable frequency stability with the present system configuration. The second case shows the behavior during a DIAL measurement. Thus, the injection seeding was alternately switched between the two diode lasers running at the online and the offline frequency. This measurement also includes instances where the Ti:sapphire laser cavity stabilization was reset, as well as manual readjustments of the offline frequency.

Figure 5.21 illustrates the measurement for which the Ti:sapphire laser was injection seeded with one diode laser. The diode laser was stabilized by means of the analog control output of

---

[75] *HighFinesse / Ångstrom*, WSU-30 with Linewidth Measurement and External Trigger options

the wavelength meter of the seeder system (see Chapter 4.3.2) to the constant (online) frequency $\nu = 366\,430\,000\,\mathrm{MHz}$ ($\lambda \approx 818.143\,869\,\mathrm{nm}$ in vacuum). The recorded frequency of the diode laser is plotted in the top panel of the figure. Beneath, the results for the Ti:sapphire laser are shown. The course of the frequency follows precisely the reference of the seeder. In the absolute value an offset $\bar{\nu}_{Tisa} - \bar{\nu}_{Seeder} \approx 32\,\mathrm{MHz}$ is noted. This could be explained either by the absolute accuracy of the wavelength meters or residual amplitude modulation of the EOM (as discussed at the end of Section 5.6.2). The measured linewidth (plotted in another panel of the figure) stayed—during the whole measurement—at the lowest value the instrument can resolve. Interestingly, the wavelength meter's software indicates this value as "$< 60\,\mathrm{MHz}$", although the minimum measurable linewidth is stated to be $100\,\mathrm{MHz}$. In the data file, a value of $\Delta\lambda = 0.14\,\mathrm{pm}$ is saved for the linewidth. Converted, this results in $\Delta\nu \approx 62.7\,\mathrm{MHz}$ which was plotted in the graph. According to the previous section (from the calculation via the pulse duration and time–bandwidth product) the linewidth would be well below these values. Even if the linewidth was $\Delta\nu = 100\,\mathrm{MHz}$, the requirements for a water-vapor DIAL were still comfortably met (cf. Table 2.1 on page 11). With the linewidth below the separation of the Ti:sapphire laser's longitudinal modes ($\Delta\nu_{FSR} \approx 189\,\mathrm{MHz}$) it can be noted that the laser operates at one single frequency. The frequency and linewidth behavior of the Ti:sapphire laser is insusceptible to a change of operation power, which was also verified experimentally. During the measurement, the output power was altered at the beginning from $P \approx 8.6\,\mathrm{W}$ to $P \approx 10\,\mathrm{W}$ and back towards the end (bottom panel of Figure 5.21).

The frequency stability was quantified with a statistical evaluation of the data and the corresponding histogram (see Figure 5.22). A total of 886 365 Ti:sapphire laser pulses were recorded over the entire measurement time. From these, 644 measurement points were classified as invalid by the instrument. When the software of the wavelength meter is unable to interpret the fringe pattern of its interferometers unambiguously, it stores a negative value in the data file. In an individual measurement (see below), analyzing the recorded interference patterns from pulse to pulse, it was found that the questionable patterns were underexposed. Therefore, it is unclear whether this truly originates from the Ti:sapphire laser, or is related to the instrument (e.g., due to inaccurate triggering). Supposing that all invalid measurement points are caused by the laser (pulses with a too broad bandwidth), more than $99.92\,\%$ of measurement points still represent pulses with narrowband laser operation. The standard deviation for all valid measurement points of the Ti:sapphire laser's frequency is $1\sigma = 0.67\,\mathrm{MHz}$, being only moderately larger than the corresponding standard deviation for the injection seeder (here, $1\sigma = 0.42\,\mathrm{MHz}$). The next larger standard deviation ranges are $2\sigma = 1.3\,\mathrm{MHz}$ and $3\sigma = 2.0\,\mathrm{MHz}$. These values are well below the resolution limit of the wavelength meter and demonstrate the achievement of a formidable stability. A few measurement points with higher frequency deviation from the mean value exist. The histograms visualize this in an enlarged display. In this measurement, the frequency of the injection seeder again exhibited an asymmetry in its distribution (skewness $\approx$ 12, excess kurtosis $\approx$ 355). The latter recurs for the Ti:sapphire laser, demonstrating that the pulsed laser closely follows the behavior of the master laser. However, the frequencies are distributed in slightly more uniform way around the mean (skewness $\approx$ 3, excess kurtosis $\approx$ 54). Generally, the high accordance supports the assumption that the Ti:sapphire laser's frequency stability is mainly determined by the performance of the injection seeder. It can be expected that the Ti:sapphire laser would become even more stable if the seeder system's fre-

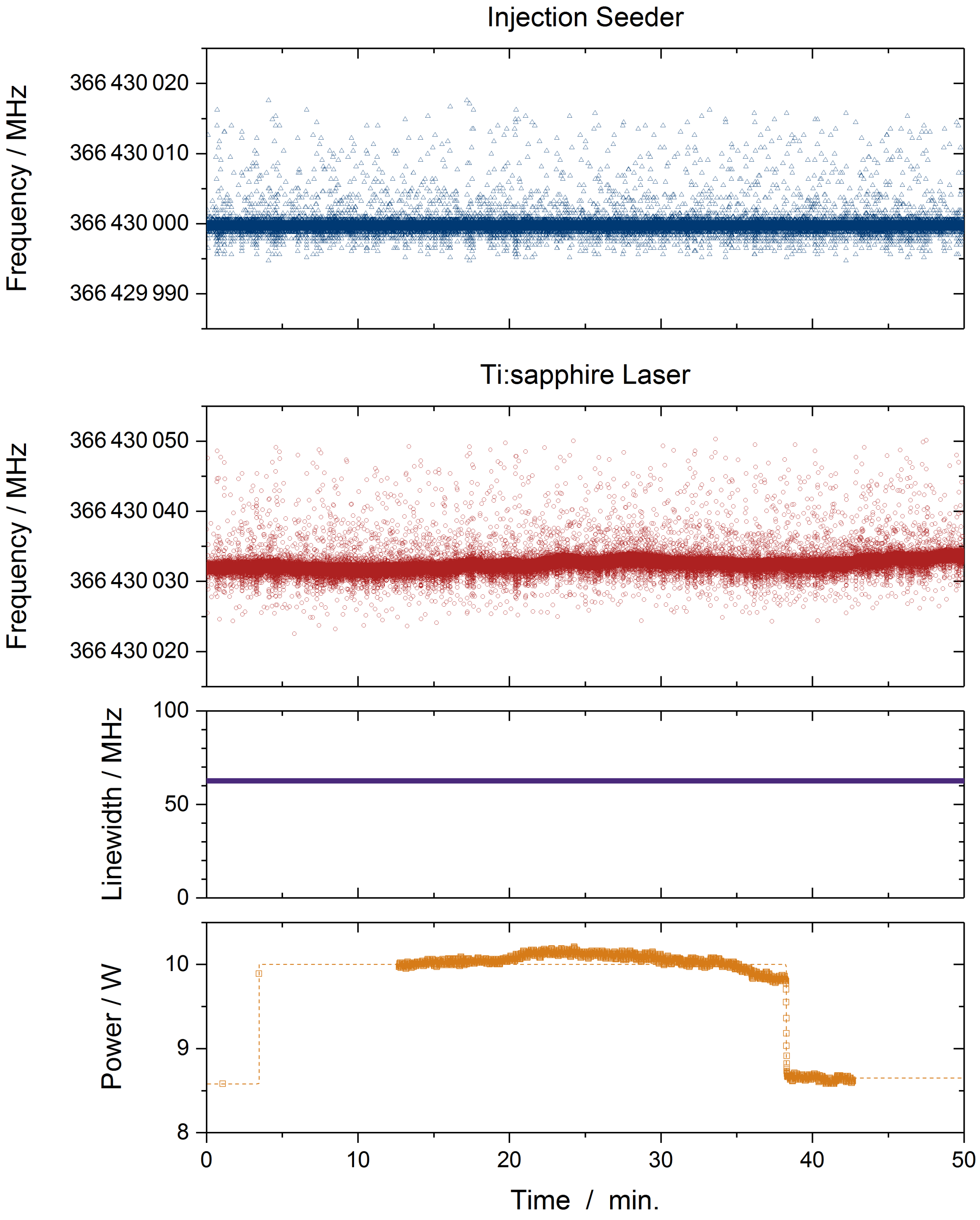

Figure 5.21: Measurement for the characterization of the frequency stability and linewidth of the Ti:sapphire laser. The laser was injection seeded with one diode laser at constant frequency. The power of the laser was changed at the beginning and towards the end of the measurement (indicated by the dashed line) to study a potential influence on the spectral properties.

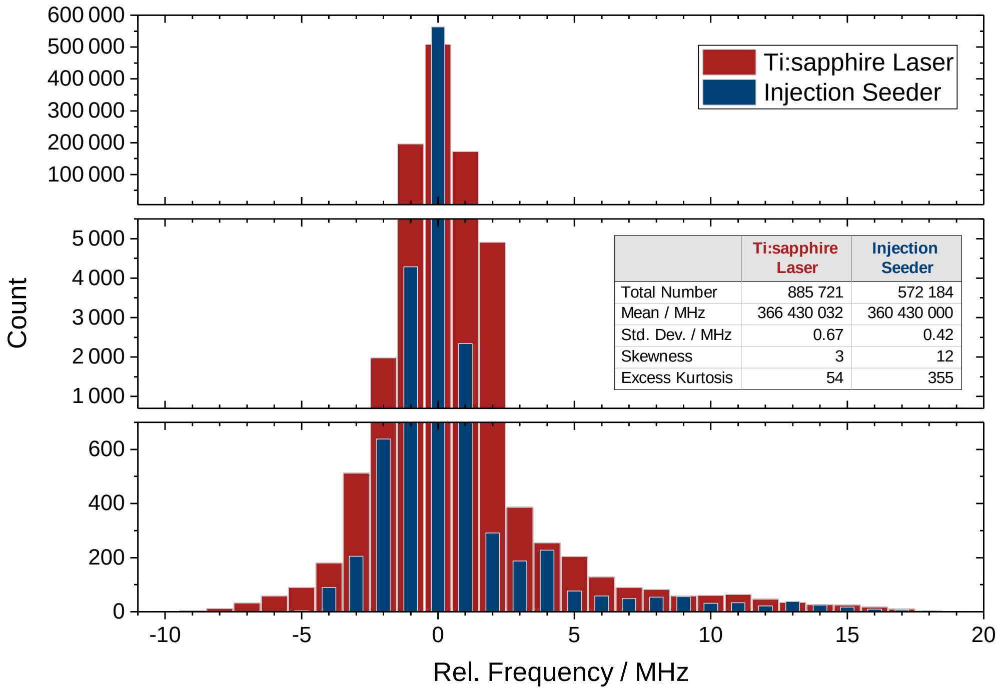

	Ti:sapphire Laser	Injection Seeder
Total Number	885 721	572 184
Mean / MHz	366 430 032	360 430 000
Std. Dev. / MHz	0.67	0.42
Skewness	3	12
Excess Kurtosis	54	355

Figure 5.22: Histograms of the frequency measurements presented in Figure 5.21. The bin size is $1\,\mathrm{MHz}$. The y-axis breaks have the same ending/starting values.

quency control would incorporate instruments with an even higher resolution. Clearly, this is beyond the scope of the requirements for a water-vapor DIAL transmitter.

Another analysis possibility of the wavelength meter is provided by the interference pattern of the installed Fizeau interferometers. The raw data of this pattern can be separately read out or recorded for a certain period on a single-shot basis. The intensity curve of the Fizeau wedge fringe pattern coarsely resembles the course of an Airy function (equally spaced, parallel fringes), but manifests in detail an asymmetry and secondary peaks [170, 171]. For the Ti:sapphire laser, the wavelength meter generally shows such a fringe pattern with clearly defined peaks (see top panel in Figure 5.23). The distance of the peaks corresponds to the free spectral range of the interferometer with fine resolution, $\Delta\nu_{FSR} = 2\,\mathrm{GHz}$. In a small number of cases, however, the pattern differs. The peaks have a lower intensity and are no longer smooth (middle panel in the figure). If the patterns become too low, the instrument cannot execute the calculation of the wavelength and the linewidth (designated as underexposed measurement). To find out how often each interference pattern occurs, or to give a representation for its stability during operation of the Ti:sapphire laser, the patterns were recorded in an additional measurement with constant online-frequency operation. Recording the data on a single-shot basis quickly consumes a lot of disk memory. For this reason, the record was restricted to a period of approximately $5\,\mathrm{minutes}$ or a total number of $83\,769$ pulses (file size $\approx\ 700\,\mathrm{MB}$). All patterns were evaluated by counting the occurrence of every pixel coordinate (intensity value *versus* pixel number of the array). The result is illustrated in the bottom panel in Figure 5.23, the counts

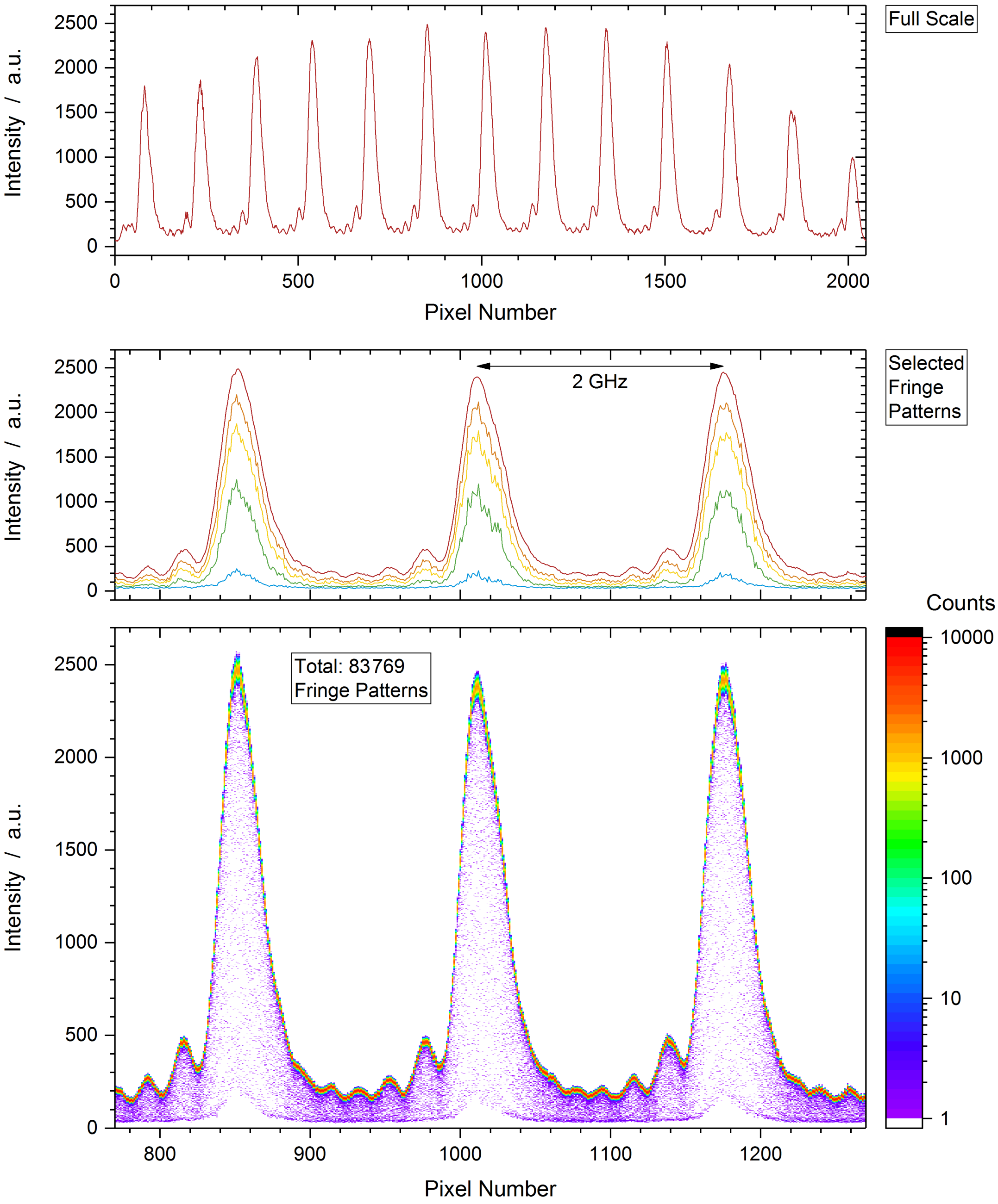

Figure 5.23: Interference pattern analysis of a pulse-to-pulse measurement of the Ti:sapphire laser with the wavelength meter. **Top:** Representative fringe pattern for one laser pulse of the fine-resolution interferometer at full scale. **Middle:** Selected fringe patterns with different peak intensities and altered shape occurring during the measurement. **Bottom:** Superimposed illustration of all measured fringe patterns. The occurrence of each point is colored with a logarithmic scale, starting from counts ≥ 1.

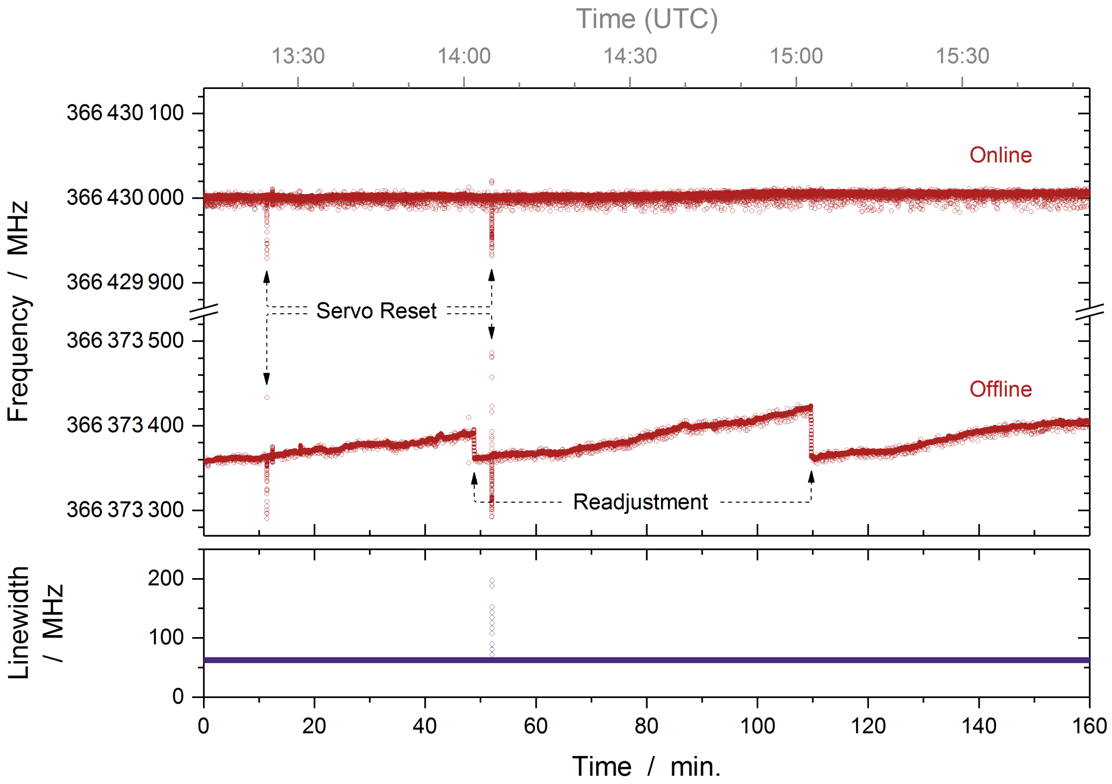

Figure 5.24: Frequency and linewidth measurement of the Ti:sapphire laser during operation of the Hohenheim-DIAL. The laser emission switches from pulse to pulse between online and offline frequency, following the alternate injection seeding with two diode lasers. The diode laser for the online frequency was stabilized to a constant value. The offline diode laser drifts and is readjusted from time to time to maintain a certain frequency relationship. Resetting the servo controller of the Ti:sapphire laser's active stabilization briefly leads to frequency deviations.

being color dependent. It can be recognized that fringe patterns with lower peak intensity are occasionally present. Still, the vast majority of patterns is concentrated in a narrow range. The variation is mainly given in the intensity (y-axis), whereas a change in the pixel number (x-axis) is hardly detected. The latter is related to the emission frequency of the laser, demonstrating again its high stability. In this measurement, from all measured laser pulses, 42 were classified by the instrument as underexposed. Hence, more than $99.94\,\%$ of the measurement points were evaluated by the instrument, all giving a linewidth below the resolution limit.

The progression of the Ti:sapphire laser frequency during a DIAL measurement is depicted in Figure 5.24. The laser operated with $P = 10\,\mathrm{W}$ average output power. Single laser pulses were emitted one by one at the online and offline frequency. With a pulse repetition rate $f_{rep} = 300\,\mathrm{Hz}$, the pulses at the online and offline frequency occur each for themselves every $6.\overline{6}\ \mathrm{ms}$. Hence, the Ti:sapphire laser was acting as defined by the alternate switching between the two diode lasers of the injection seeding system. One diode laser was permanently stabilized to the same online frequency as above. The other was initially set close to the offline frequency $\nu = 366\,373\,360\,\mathrm{MHz}$ ($\lambda \approx 818.270\,351\,\mathrm{nm}$), corresponding to a separation to the online frequency of 299 times a free spectral range of $\Delta\nu_{FSR} \approx 189.4\,\mathrm{MHz}$. In the course of the measurement, the offline frequency slowly drifted away from its starting value. This is not critical for the DIAL measurement, as explained at the end of Chapter 4.4.2. However, to maintain the condition of a frequency separation that is equal to an integer multiple of the resonator's free spectral range, the offline frequency was readjusted by changing the piezo voltage for the grating of the external-cavity diode laser. The readjustment, undertaken twice, is distinctly visible in Figure 5.24 as a sudden frequency change of the offline pulses. The action has no impact on the laser pulses at the online frequency.

Furthermore, there were situations during the measurement when the active frequency stabilization of the Ti:sapphire laser resonator was resetted. In the process of cavity regulation, the correction signal can trend towards the maximum or the minimum output voltage the servo controller can deliver. These situations usually arise for one-sided or permanent disturbances from the environment (e.g., major temperature variations or vibrations). Then, the correction signal has to be reinitialized to the central position of its regulation bounds. In the short moment the reset takes place, the resonator is not stabilized. That is why some laser pulses at both, the online and the offline frequency, deviate from their normal value. Two servo controller resets were performed during the measurement and are observed as laser pulses with frequency deviations $\lesssim 100\,\mathrm{MHz}$. Apparently, resetting the servo controller can have a more or less pronounced effect. While for the first reset the linewidth remained at the lowest measurable value, the second caused the emission of some laser pulses with increased bandwidth. It is assumed that this depends on the duration of the reset procedure which is done manually. Since the number of the deviating laser pulses is very low (in comparison to the high amount of stabilized pulses), the consequences for the DIAL measurement are minor or even negligible. Nonetheless, this is an option for potential improvement in the future.

During operation of the water-vapor DIAL, the moments of servo controller reset and offline diode laser readjustment are coordinated as best as possible with the instances when the DIAL measurement period is interrupted (e.g., for a change of the scan pattern). The atmospheric humidity data that was obtained with the Hohenheim-DIAL, while the here discussed frequency characterization was being executed, is presented in the next chapter (see Figure 6.1). Neither repercussions due to the readjustment of the offline frequency nor due to the resetting of the active stabilization could be identified. Finally, the statistical evaluation of solely the measurement points at the online frequency, for the time period without intervention (from minute 60 to 160), demonstrated that the frequency deviation from the mean is slightly larger ($1\sigma = 1.57\,\mathrm{MHz}$) to when the laser is operating at a constant seeder frequency. Still, the value is below the resolution limit of the wavelength meter. Thus, the alternate online–offline frequency switching has no significant effect on the stability performance of the system.

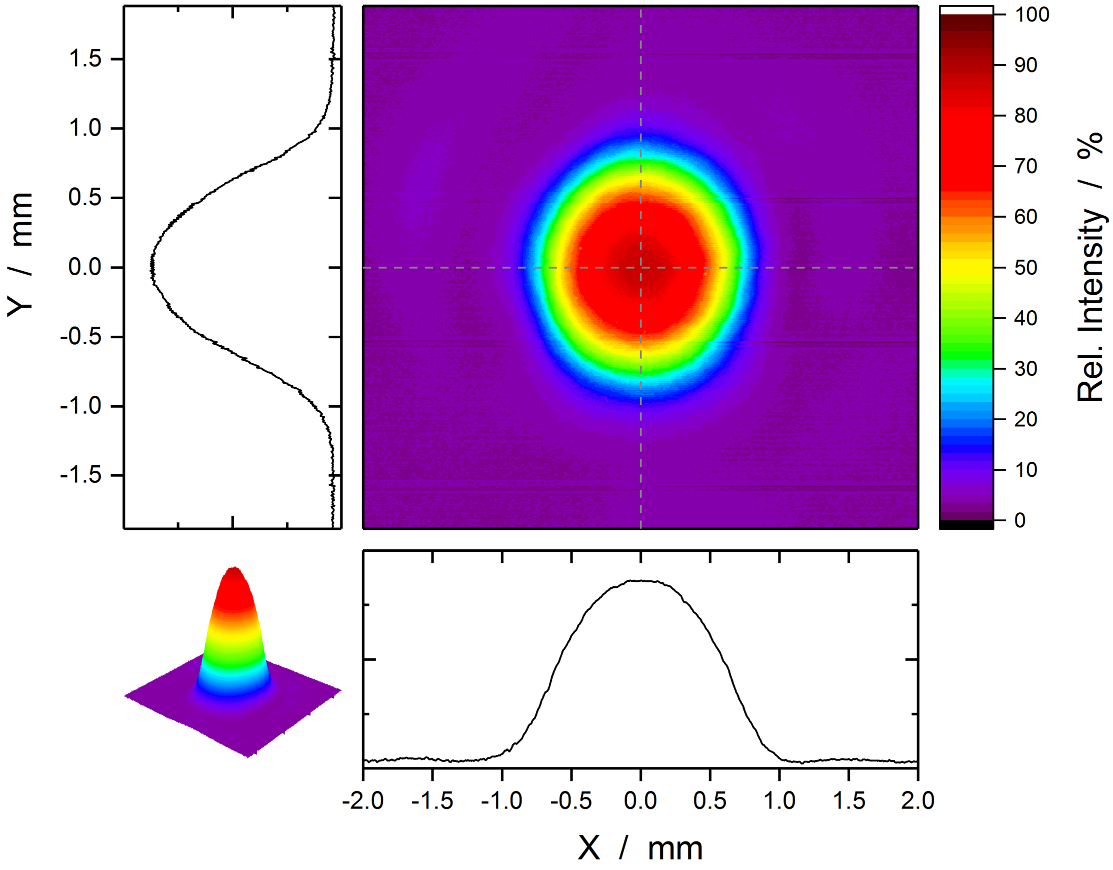

Figure 5.25: Beam profile of the Ti:sapphire laser in the resonator configuration without cylindrical lens, demonstrating a fundamental transverse mode (TEM_{00}). The image was captured with the camera at the output of the laser setup and at an operation power of $P = 4\,\mathrm{W}$. The weak horizontal lines are due to electromagnetic interference, i.e., an artifact of the camera and not a feature of the beam.

5.7.4 Beam Quality and Propagation

The end-pumping of the Ti:sapphire crystal with a beam that is adapted to the fundamental mode of the laser resonator entails operation in single mode. Therefore, the transverse mode accords with the TEM_{00} mode, which is permanently observed in the experiment. Only after one of the resonator optics suffered a burn pattern induced by too high intracavity powers, as discussed in Section 5.7.2, the laser mode converted to the higher order mode TEM_{01}.

The beam profile of the Ti:sapphire laser in the resonator configuration without cylindrical lens is shown in Figure 5.25. It was measured with the camera situated close to the exit aperture of the laser case (see Section 5.3 for the setup of laser and instruments). The distance of the camera to the waist of the eigenmode is $z \approx (801 \pm 9)\,\mathrm{mm}$. The beam profile was captured at an average output power of $P = 4\,\mathrm{W}$. A Gaussian intensity distribution is nicely represented. The 2σ-beam radii are $w_x \approx 0.92\,\mathrm{mm}$ and $w_y \approx 0.98\,\mathrm{mm}$, yielding a roundness of ≈ 0.93. Thus, in this resonator configuration (and at this output power) the laser mode's difference between sagittal and tangential plane is negligible. The values of the beam width are higher than expected, even considering that laser operation was at medium power, i.e., at a weakly present thermal lens. In a detailed analysis and using a second software[76] for comparison, it was found that the results varied depending on the background area which was included in the calculation. Indeed, operation of pulsed lasers involves intensive stray light. Despite a background correction, some remaining light around the beam profile is captured, affecting the beam width determination via the second moments. The manual evaluation delivered beam width values ranging from $w_x = 0.77\,\mathrm{mm}$ to $0.84\,\mathrm{mm}$ and from $w_y = 0.86\,\mathrm{mm}$ to $0.94\,\mathrm{mm}$.

With the implementation of the cylindrical lens ($f_{cyl} = -842\,\mathrm{mm}$) the eigenmode in the tangential plane is altered. Although the beam widths are—according to the resonator design (Equation 5.33)—approximately equal in both planes at the laser crystal, at all other locations they are dissimilar due to their distinct caustic (with now clearly differing waist sizes and locations). As a consequence, the measured beam profile has an elliptical appearance. Figure 5.26 displays the intensity distribution of the beam at $P = 10\,\mathrm{W}$ power output, detected with the same camera. Here, the beam radii are $w_x \approx 1.37\,\mathrm{mm}$ and $w_y \approx 0.92\,\mathrm{mm}$. Obviously, the roundness is reduced, being ≈ 0.67. Again, the individual analysis yielded smaller values of the beam widths, ranging from $w_x = 1.16\,\mathrm{mm}$ to $1.36\,\mathrm{mm}$ and from $w_y = 0.76\,\mathrm{mm}$ to $0.88\,\mathrm{mm}$. The remaining ellipticity can be explained by the fact that the implementation of the cylindrical lens was subject to experimental constraints, as already discussed. Hence, deviations from the ideal design configuration appear. Additionally, at the given operation power, the dynamically stable point is probably not yet completely reached. Consequently, at lower powers the beam becomes even more elliptical since operation moves further away from dynamical stability. Most important, the eigenmode of the laser is permanently still the fundamental mode, TEM_{00}.

The variation of the beam position was characterized in three forms. The first defines a slow drift due to heating effects, noticed for long-term operation. The second specifies the variation accompanied by the movement of the piezo-mounted cavity mirror, due to the active frequency stabilization. The third represents a continuous measurement which was evaluated statistically for quantification of the pointing stability. The long-term drift was evaluated by determination of the beam profile's centroid at the beginning and after $3.3\,\mathrm{hours}$ of laser operation. For the measurement, the piezo regulation was temporarily deactivated, whereby the piezo rested in a center position. The difference in the centroid coordinates was $\Delta x = (70 \pm 1)\,\mu\mathrm{m}$ and $\Delta y = (35 \pm 2)\,\mu\mathrm{m}$, corresponding to $(5.1 \pm 0.1)\,\%$ and $(3.8 \pm 0.2)\,\%$ of the beam radii, respectively.

The influence of the piezo movement was examined by manually applying a voltage that drove the piezo actuator to the maximum upper and lower regulation bound. It was observed that the corresponding change of the cavity length caused a dislocation of the beam position, essentially in the x-direction. From the center position to the upper regulation bound, the centroid of the intensity distribution shifted by $\Delta x \approx -180\,\mu\mathrm{m}$ (13.1 %). From the center position to the lower regulation bound, the centroid of the intensity distribution shifted by $\Delta x \approx 300\,\mu\mathrm{m}$ (21.9 %). In contrast, the y-dislocation was generally small, $\Delta y < 20\,\mu\mathrm{m}$ (2.2 %). Furthermore, in this connection the average output power varied in each case by $\Delta P \approx -1.1\,\mathrm{W}$. These values were measured at an output power of $P = 7.5\,\mathrm{W}$. A higher power level for this characterization

---

[76] see footnote 33 on page 48

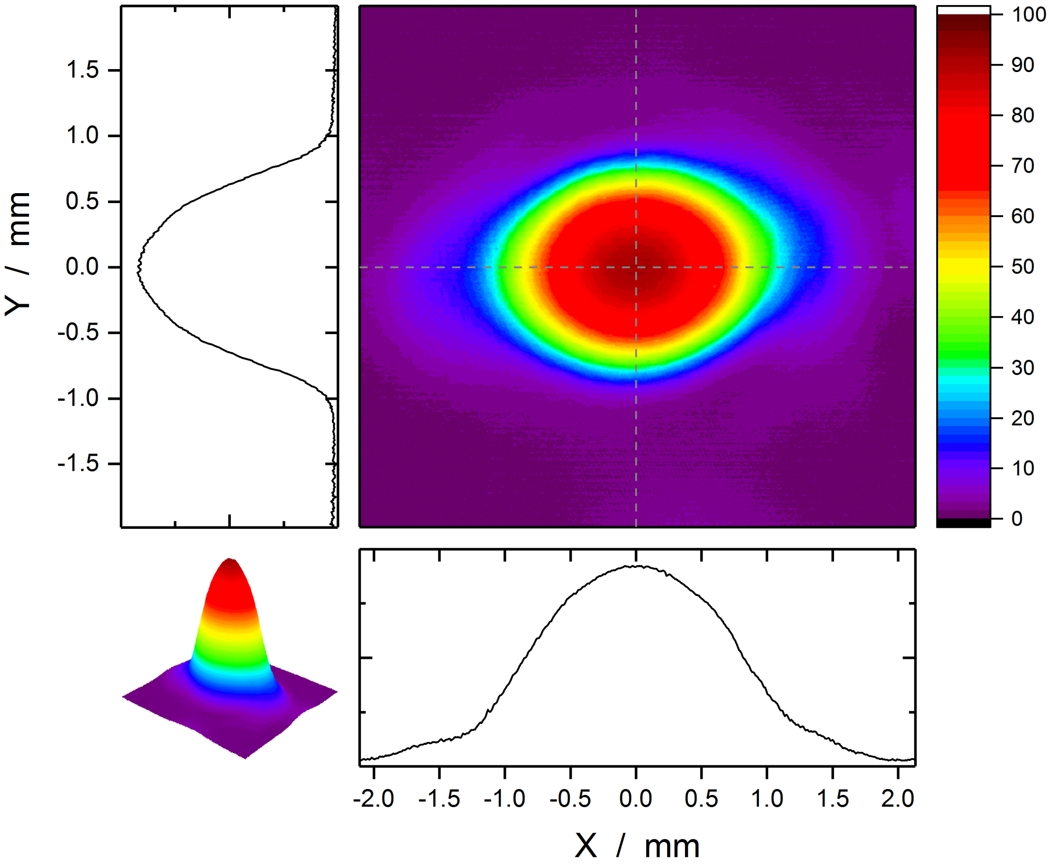

Figure 5.26: Beam profile of the Ti:sapphire laser with the cylindrical lens ($f_{cyl} = -842\,\mathrm{mm}$) installed in the resonator. The modified resonator configuration leads to noticeable different beam widths in the tangential (x) and the sagittal (y) plane. The increased mode volume enables high-power operation at $P = 10\,\mathrm{W}$ output.

was avoided in order to not risk a damage which could have been provoked by the enforced operation at the regulation bound. The results show that the maximum regulation bounds lead to a beam dislocation affecting the overlap with the pump beam, and thus, the efficiency of the laser. However, when operating the laser with the active frequency stabilization, the required regulation range is usually much lower than in these extreme cases. In the end, this depends on the severity of the external disturbances (vibrations, temperature variations, etc.) the laser is exposed to.

In Figure 5.27, the graphs of the output power as well as the x- and the y-coordinate of the beam centroid are plotted for a $20\,\mathrm{minutes}$-measurement at full power operation and with active frequency stabilization. A correspondence between the power and the beam position is seen mainly in the x-coordinate. With a certain retardation, the power follows the course of the x-centroid. Slow changes and also short-term position jumps are partially present. The y-coordinate of the beam centroid is much steadier. Here, a conclusive statement on whether there

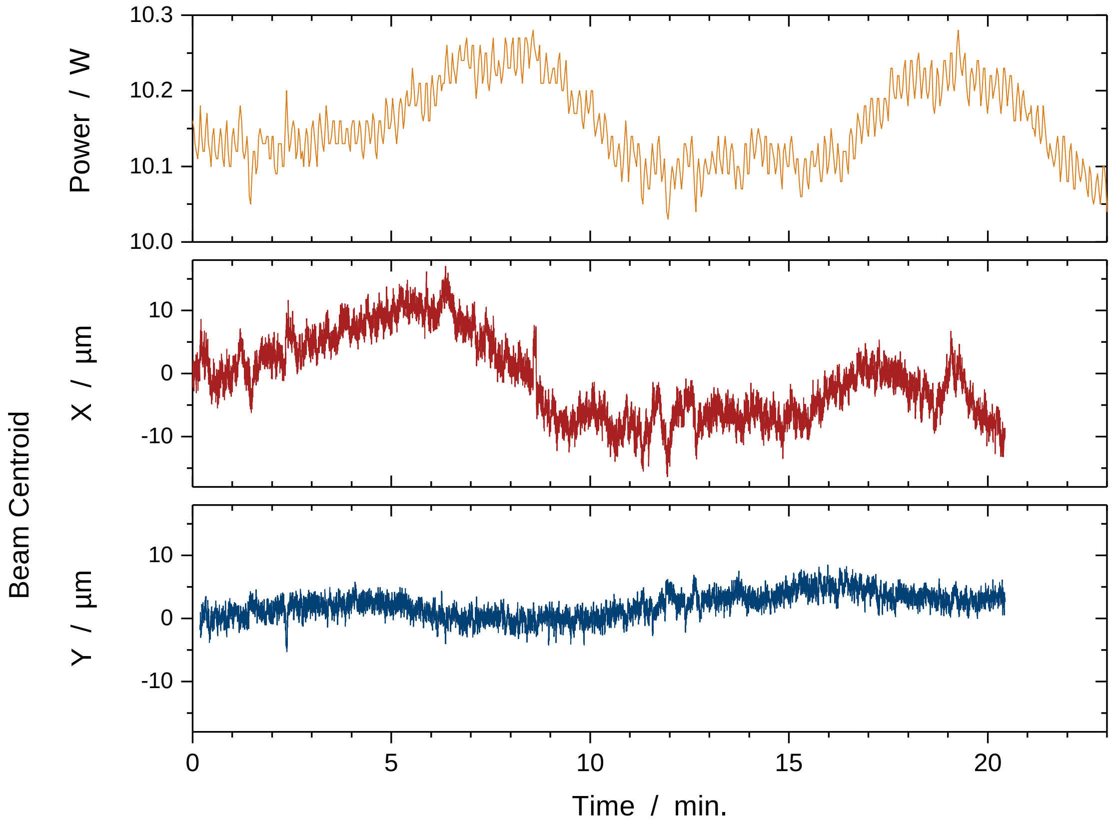

Figure 5.27: Power and beam stability measurement of the Ti:sapphire laser with active frequency stabilization. The regulation of the cavity length via the piezo-mounted mirror leads to a dislocation of the beam, mainly of the centroid's x-coordinate. This in turn goes along with a variation of the output power. The movement in the y-direction is comparatively small.

is a connection to the piezo movement or if this is an independent drift, cannot be made. The measurement statistics yielded a standard deviation of the beam position of $\Delta x = 7\,\mu\mathrm{m}$ and $\Delta y = 3\,\mu\mathrm{m}$, corresponding to $0.7\,\%$ and $0.4\,\%$ of the respective beam radius component. In terms of the determined beam divergence (see below) the pointing stability is $\Delta\theta_x = 3\,\mu\mathrm{rad}$ and $\Delta\theta_y = 2\,\mu\mathrm{rad}$. It should be pointed out that the change of the beam position has no severe consequences for the DIAL measurements. The accompanying variation of the power could have a minor impact on the lidar signal's maximum range at the most. Additionally, it needs to be mentioned that for the resonator configuration without cylindrical lens the change of beam position caused by the piezo movement was negligible in both x- and y-direction.

More insight into the beam quality and propagation was obtained by an M^2 analysis. At the $10\,\mathrm{W}$ operating state the results were as follows. The beam quality factor was $M_x^2 = 1.06$ in the tangential plane, and $M_y^2 = 1.02$ in the sagittal plane. The respective waist radii were determined to be $w_{0,x} = 0.61\,\mu\mathrm{m}$, and $w_{0,y} = 0.59\,\mu\mathrm{m}$. This yields a (half angle) divergence

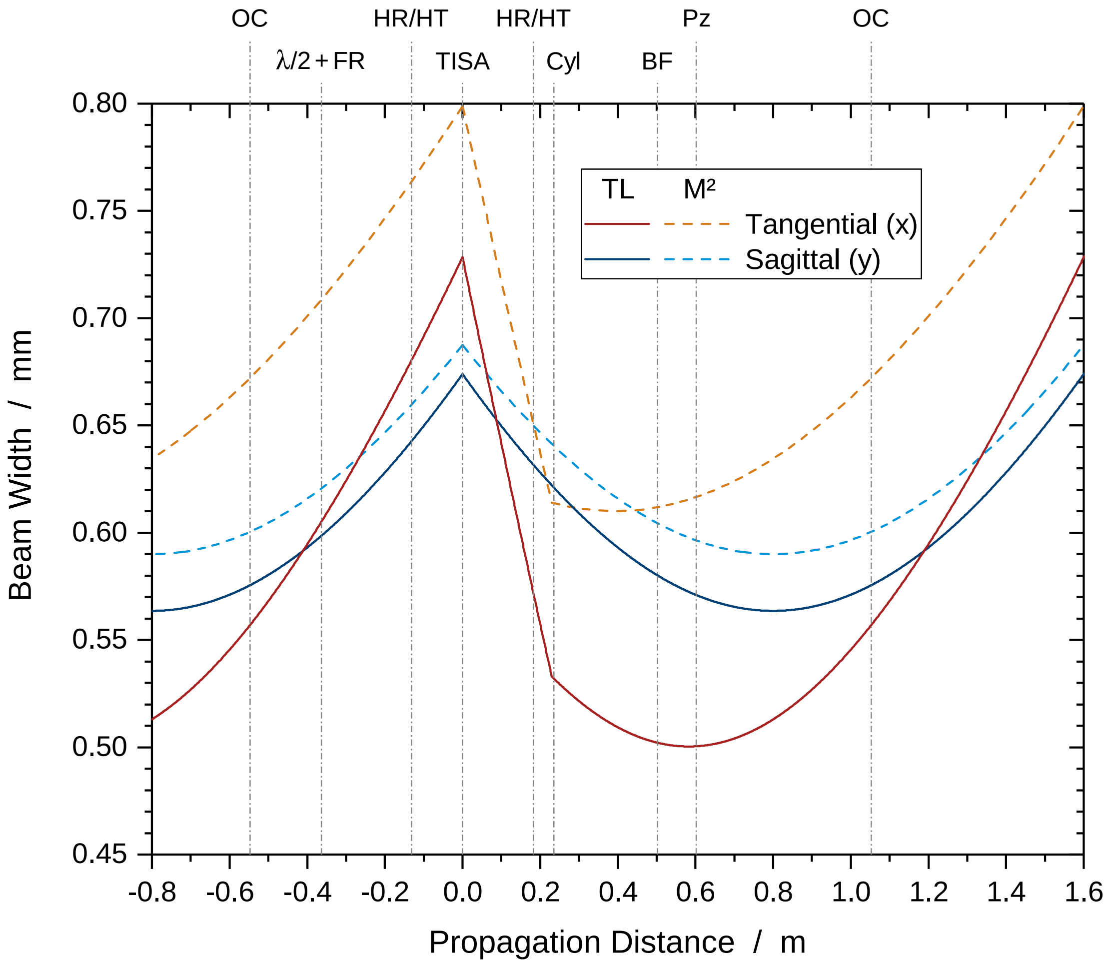

Figure 5.28: Course of the beam width of the Ti:sapphire laser is eigenmode in the tangential and the sagittal plane. The caustic was calculated once with the resonator design formalism of Section 5.2, and the thermal lens' focal lengths being determined via the pump power (TL, solid lines). Additionally, the caustic parameters were chosen according to the beam waist width from the M^2 measurement (M^2, dashed lines). See Figure 5.7 for the components' abbreviations.

of $\theta = 0.45\,\mathrm{mrad}$ for both planes. The measurement accuracy of the M^2 device[77] for the mentioned parameters so far is $5\,\%$. The precise retrieval of the waist locations posed a challenge. The reason was a higher uncertainty for this parameter by the instrument ($12\,\%$) as well as the accumulating errors in the measurement of the lengths from the device to the laser resonator. From the measurement results it was determined that the eigenmode's waists would be located at a distance of $z_x = (928 \pm 297)\,\mathrm{mm}$, and respectively $z_y = (233 \pm 214)\,\mathrm{mm}$, before the beam leaves the resonator through the output coupler. The beam parameters define a caustic which can be compared to the resonator mode given by the focal length of the thermal lens at

---

[77] see footnote 34 on page 49

the corresponding pump power. For $P_{532} \approx 30\,\mathrm{W}$, according to Section 5.7.1, the thermal lens' focal lengths are $f_{th,x} \approx +580\,\mathrm{mm}$ and $f_{th,y} \approx +1330\,\mathrm{mm}$. With the resonator design calculations, the related caustic for the tangential and sagittal plane was plotted (see Figure 5.28). Likewise, the caustic for the M^2 analysis was depicted, using parameters that yield equivalent waist widths. The positions of the resonator's constituents were marked in the figure as well. It can be seen that the beam mode representing the M^2 measurement is larger. Similar reasons as discussed for the beam profiles may have an impact here. Therefore, it is assumed that the approach via the focal length measurement of the thermal lens is more accurate.

The M^2 analysis was also carried out at lower output powers of the Ti:sapphire laser. Table B.1 in Appendix B.1 lists the essential beam parameters for different power levels. The results show that there is only partial agreement with the quantities derived from the resonator design calculations. On the one hand, the values for the sagittal plane follow the expected behavior. For instance, the beam width of the waist becomes smaller with increasing power (cf. Figure 5.14), although the values tend to be slightly larger. On the other hand, the values for the tangential plane are contradictory to the theoretical behavior. The outcome for the tangential waist location appears to be too large as well. Best overall agreement is given for the powers close to $P = 10\,\mathrm{W}$.

5.8 Trigger Concept

Since lidar is a time-of-flight measurement at the speed of light, it is important to precisely determine the moment when the laser pulse is sent into the atmosphere. This moment initiates the time measurement which is later related to the range where the light is backscattered. The emission of laser pulses with different frequencies, according to the DIAL technique, also calls for a (frequency-) state definition for every laser pulse. Therefore, a concept for triggering the DIAL system adequately is necessary. In this work, the trigger sequence was revised, and some devices were replaced by improved ones.

Previously, the concept made use of a monitor signal of the pump laser's Q-switch trigger to activate the online–offline switching, as well as a photodiode, detecting the Ti:sapphire laser pulse and connected to a comparator device to start the registration of the lidar signal. This arrangement exhibited some drawbacks. Via the direct connection to the pump laser, electrical noise from the Q-switch and the pump chamber drivers was transferred to the data acquisition. Moreover, the (digital) trigger signal formed by the comparator device after passing a certain threshold of the laser pulse, deviated considerably from the ideal transistor–transistor logic (TTL) standard. Finally, between the two trigger sources (Q-switch and photodiode) a timing jitter existed.

The new trigger concept only uses the laser pulse detector as primary trigger source. All further trigger signals are derived from it (see Figure 5.29). Thus, the photodiode[78] optically measuring the Ti:sapphire laser pulse, acts as master device for the timing event. The photodiode is connected to a digital delay/pulse generator[79]. The latter produces TTL pulses with low jitter ($< 100\,\mathrm{ps}$, RMS) and of true rectangular shape, even if the original analog signal of

---

[78] see footnote 5 on page 30

[79] *Stanford Research Systems*, DG535

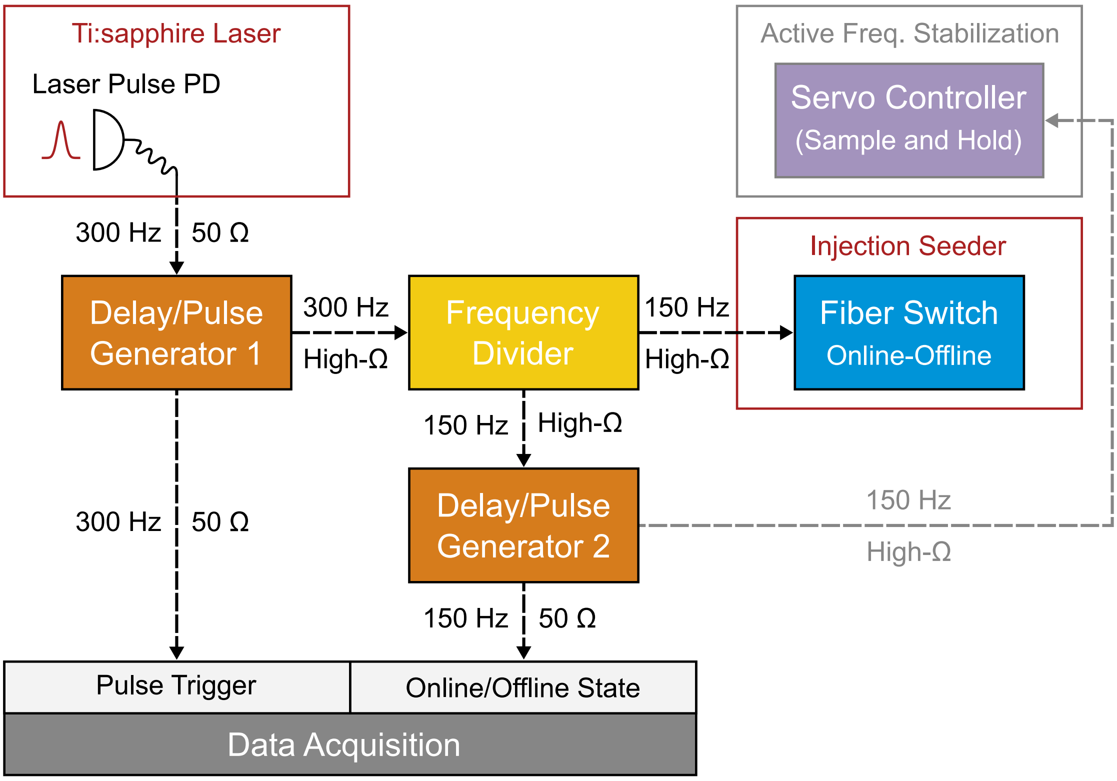

Figure 5.29: Block diagram of the devices generating the trigger signals for the Hohenheim-DIAL. All signals are derived from the laser pulse which is detected with a fast photodiode (PD). The dashed lines indicate electrical connections, labeled with the frequency of the corresponding periodical signal and the coupling impedance. The signal for the servo controller of the active frequency stabilization is optional.

the photodiode would exhibit multiple crossings at the set threshold, e.g., due to complicated laser pulse forms. Hence, potential ambiguity of an incident laser pulse is avoided for the data acquisition, which receives an undelayed signal of 300 µs length from the pulse generator. The length is chosen to be notably longer than the laser pulse (in the order of ns), but still substantially shorter than the time period of the pulse repetition rate (ms). By this means, the DAQ is initiated with a clearly defined trigger.

A second signal from the delay generator addresses a frequency divider[80]. The frequency divider outputs a TTL signal that changes its high/low state at every rising edge of the triggering pulse. Therefore, periodical pulses at the laser repetition frequency yield an alternating signal with a period corresponding to the half fundamental frequency. Such a signal is convenient for controlling the online–offline frequency switch of the injection seeder. With the ability of shifting this signal in time by adjusting the triggering signal of the delay generator, the inertness of the online–offline switch (cf. Chapter 4.5) can be compensated if necessary. Coincidentally,

---

[80] custom-made by *DLR*, as part of the injection seeding system

for the fiber switch, delaying the trigger is not required. Due to its own behavior, the switching of the frequency is deferred, so that the Ti:sapphire laser pulse occurs at the end of the switching process (or shortly before the switch changes its state again), ensuring to reach the switching state completely and keeping the maximum available time for the active frequency stabilization of the Ti:sapphire resonator.

The DAQ system presumably asks for an online–offline state trigger signal which is delayed differently from the frequency switch. Likewise, if another signal is needed to sample and hold the online state of the Ti:sapphire laser's frequency stabilization, the delay and the length of the trigger pulse most likely have to be set independently. For this reason, a second device[81] for generating and delaying TTL pulses is implemented in the trigger sequence (specified jitter $< 1\,\mathrm{ps}$). It obtains the identical trigger signal as the online–offline switch. One output channel is connected to the DAQ, where the trigger pulse has the same length as the frequency divider (equaling the period of the laser repetition rate) and is delayed by the half pulse length in order to define the online/offline state temporal symmetrically around the laser pulse. The second output channel can optionally be used for the sample-and-hold input of the active frequency stabilization electronics. In doing so, some peculiarities[82] of the stabilization electronics' servo device have to be considered. Ultimately, the sample-and-hold signal has to start before the switching to the offline state begins, and end after having switched back to the online state.

In conclusion, the new trigger concept has the flexibility to provide several trigger signals. Two digital delay-and-pulse generators are used to address signals at the laser pulse repetition rate and at the half frequency thereof. Figure 5.30 gives an overview of all mentioned trigger signals. It also shows another optional signal that would sample and hold the active frequency stabilization only during the occurrence of the Ti:sapphire laser pulses. The photodiode responsible for the error signal of the active frequency stabilization captures the laser pulses of strong intensity as well. This might disturb the stabilization. However, a deteriorating effect due to the laser pulse was not observed so far, and thus, it was not necessary to use this hold-signal.

---

[81] *Agilent Technologies*, 33612A

[82] It was found that the analog electronic circuit of the device reacts with a retardation and prolongation of the sample-and-hold signal. As a result, the input trigger signal is not implemented one-to-one and has to be adapted beforehand.

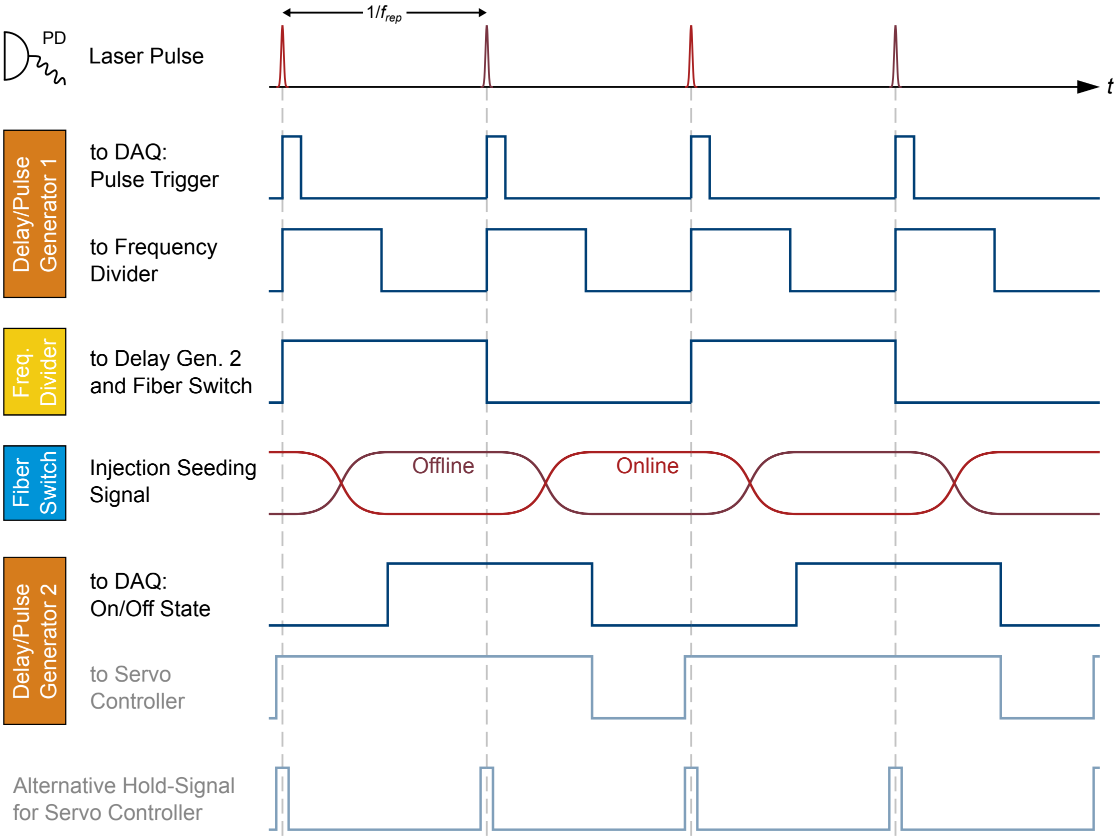

Figure 5.30: Temporal sequence of the signals generated by the individual trigger devices (see Figure 5.29). The red lines illustrate optical signals. The blue square-wave lines depict electrical signals. The two signals at the bottom (grayed out) are optional signals for the servo controller to sample and hold a specific status of the Ti:sapphire laser's active frequency stabilization. DAQ – data acquisition of the Hohenheim-DIAL receiver, PD – fast photodiode.

CHAPTER 6

Atmospheric Measurements

The characterization of a laser on the basis of individual parameters defines the compliance with the specified requirements and allows to assess beforehand the laser's suitability for the final application. Ultimately, the laser can only prove its proper functionality by testing within that application. In particular, if it is intended as lidar transmitter, the operation in the lidar system is essential, since the environmental conditions in such systems are usually harsher than in a laboratory.

From the outset, the Ti:sapphire laser developed within this thesis was implemented inside of the water-vapor DIAL of the *University of Hohenheim* and was used at the first opportunity for atmospheric measurements. Thus, the definitive behavior of the laser became immediately apparent. The feedback gained from the DIAL measurements helped with the optimization of the system. According to the progress of development, improved performance levels of the Ti:sapphire laser have been achieved for each of the completed field campaigns during this work. Besides having carried out extensive water-vapor measurements of the atmosphere, as well as dedicated measurements for the determination of the transmitter's spectral purity, a new measurement concept for spectral analysis of the atmosphere was also tested.

The organization of this chapter is as follows. First, an overview is given of important atmospheric measurement activities in which the transmitter of this work was engaged. This includes a short listing of its development status at that time. Subsequently, case studies of water-vapor measurements in the atmosphere with the Hohenheim-DIAL are discussed. The examples were chosen also with regard to a presentation of the laser performance. The first is a vertical pointing measurement at high power operation of the laser. Second, spatial scans of the water-vapor field are shown. The next section deals with special measurement techniques. The spectral purity of the Ti:sapphire laser was characterized with measurements on a hard target. To conclude, the measurement with a tuning online frequency as a spectral analysis method is demonstrated.

6.1 Water-Vapor DIAL Measurements

6.1.1 Field Campaigns and Measurement Activities

The first field campaign, in which the laser system of this work came into operation, took place in the context of the “Transregional Collaborative Research Centre 32” (TR32) in summer 2012 near Jülich, Germany [79]. At that time, the pump source of the Ti:sapphire laser was the *IBL* laser. The injection seeding system employed two DFB diode lasers and the electro-optic deflector (EOD) as online–offline frequency switch. For the active stabilization of the Ti:sapphire laser resonator, the devices of the previous transmitter were still used. A maximum output power of $P = 4\,\mathrm{W}$ was achieved. The atmospheric humidity measurements were executed with the laser operating at $P \approx 2\,\mathrm{W}$ in order not to risk any optical damage, especially of the sending fiber. During this campaign, six measurement days were accomplished (without taking test measurements into account).

In spring 2013 an extensive field campaign was completed within the research initiative “HD(CP)^2 – High Definition Clouds and Precipitation for advancing Climate Prediction”. The campaign was denominated as “HD(CP)^2 Observational Prototype Experiment” (HOPE) and conducted around Jülich. In brief, the project aims for a better understanding of processes that lead to cloud formation and precipitation. The findings will improve models for climate prediction. For this purpose, the combined measurements of several instruments during HOPE provided data of atmospheric variables at a precise scale for the model simulations, thus, enabling direct data–model intercomparisons. From the *University of Hohenheim*, the DIAL and the rotational Raman lidar (RRL) were operated to measure humidity and temperature. Meanwhile, the DIAL laser system was modified by the following. The fiber switch was installed in the injection seeding system, replacing the EOD as the online–offline frequency switch. First devices of the active stabilization (electro-optic modulator, servo controller) were also exchanged. Towards the end of the field campaign the current maximum output power of the Ti:sapphire laser ($P = 4\,\mathrm{W}$) had already become effective. The HOPE campaign was finished with an activity of the Hohenheim-DIAL comprised of 18 intensive observation periods (IOP) throughout the months of April and May. One IOP corresponds to a measurement day typically lasting approximately 3 to $12\,\mathrm{hours}$ according to weather or other conditions. In two cases, the laser operated for over $31\,\mathrm{hours}$ without interruption ($> 31\,\mathrm{h}$ on IOPs 13/14, and $> 35\,\mathrm{h}$ on IOPs 17/18). The humidity measurements of the Hohenheim-DIAL contributed to many research results. These and more information can be found in the references, e.g., [47, 48, 172–177].

In September and October of the same year, additional comprehensive measurement phases were carried out at Stuttgart-Hohenheim. These measurements were conducted for system testing and intercomparisons of the *IPM*’s differential absorption lidar and rotational Raman lidar to radiosondes launched directly on site. The DIAL transmitter was operating essentially with the same configuration as before. This measurement activity comprised 11 days in total. An example of a humidity measurement including error analysis is discussed in [47].

Another field campaign in which the Hohenheim-DIAL and the RRL participated was the “Surface Atmospheric-Boundary-Layer Exchange” (SABLE) campaign in summer 2014. It was organized by the research unit FOR 1695, “Agricultural Landscapes under Global Climate Change – Processes and Feedbacks on a Regional Scale”. The focus of the SABLE campaign was the interaction in the soil-vegetation-atmosphere continuum. The observation site was located in Kraichgau, near Pforzheim, in the southwest of Germany. The ongoing development of the DIAL brought about more changes for the laser transmitter. The Ti:sapphire laser's active stabilization now was completely exchanged, incorporating the integrated PDH unit and the transimpedance amplified photodiode. Moreover, the revised concept and devices for triggering the DIAL measurement provided additional benefits. Owing to the stronger frequency noise behavior of the DFB diode laser, it was decided to engage the sample-and-hold option of the servo controller to keep the Ti:sapphire laser resonator stabilized to the ECDL only (see also Chapters 5.6.2 and 5.8). By then, the maximum output power of the laser had been increased to $P = 7\,\mathrm{W}$, but for the campaign only a portion of it was put into use since the main emphasis was on scanning measurements. The SABLE campaign covered the month August, with eight IOPs and three special observation periods (SOP) in addition. During the latter, measurements with conical and other volume patterns of the DIAL scanner, as well as the frequency tuning measurements (see Section 6.2.2) were performed. Further details about the campaign and its results are to be found in the literature [48, 178, 179].

Thereafter, the laser system went through major development steps. The *PLA* laser was set up as new pump source. A second next-generation ECDL was acquired as offline-frequency injection seeder. Accordingly, the wavelength meter was prepared for a two-output analog signal regulation. Finally, the operation of the Ti:sapphire laser with an average output power of $P = 10\,\mathrm{W}$ was achieved. The performance was demonstrated with atmospheric humidity measurements in summer 2016. This activity comprised five sporadic measurement periods. An example of the results is presented in the next section and in [180].

In summer 2017, the Hohenheim-DIAL and the RRL participated, alongside other instruments, in a major field campaign outside Germany [181]. The Land–Atmosphere Feedback Experiment (LAFE) took place at the *Atmospheric Radiation Measurement (ARM) Climate Research Facility* Southern Great Plains (SGP) site in Oklahoma, USA. Many remote-sensing instruments were assembled there to investigate meteorological exchange processes between the inhomogeneous land surface and the atmosphere above it. The measurement phase in August was preceded by an extended transport and setup phase of the systems in spring of the same year. The DIAL trailer and the RRL truck were brought from Germany (Bremerhaven) to the USA (Galveston, Texas) with a vehicle carrier vessel. The overseas transport lasted five weeks, the transport in total over seven weeks, during which the laser transmitter and the other system components inside the Hohenheim-DIAL could not be air-conditioned. However, the devices were carefully prepared to resist as well as possible the uncommon high temperature and humidity variations, as well as the increased vibrations and accelerations occurring in transit. The system arrived well at the SGP site, and the DIAL operation was carried out with great success. The condition of the laser transmitter remained unchanged, still offering an output power of up to $P = 10\,\mathrm{W}$. The DIAL measurements were performed in scanning configuration to capture the spatial humidity field. The laser operation was set slightly below the 10 W level, where a power fraction of 2 W was sent into the atmosphere. The campaign brought about 13 IOPs and 4 SOPs, which included also the occurrence of a solar eclipse. Recently, first results of this research event have been published [182, 183]. The Table 6.1 summarizes the completed field campaigns and measurement activities, together with the corresponding development status of the laser system.

Intensive Measurements		**Pump**	**Injection Seeder**		**Ti:sapphire Laser**				**Observation**
Year	**Location, Name**	**Laser**	**Diode Laser**	**Switch**	**Freq. Stab.**	P_{max}	P	P_{atm}	**Mode(s)**
2012	Jülich, TR32	*IBL*	DFBs	EOD	previous	4 W	2 W	$<$ 2 W	vertical, scanning
2013	Jülich, HOPE	*IBL*	DFBs	Fiber Switch	interim	4 W	$\leq$ 4 W	$\leq$ 4 W	vertical, scanning
2013	Hohenheim	*IBL*	DFBs	Fiber Switch	interim	4 W	4 W	$<$ 4 W	vertical
2014	Pforzheim, SABLE	*IBL*	ECDL, DFB	Fiber Switch	enhanced	7 W	4 W	$<$ 2 W	scanning, vertical
2016	Hohenheim	*PLA*	ECDLs	Fiber Switch	enhanced	10 W	10 W	9 W	vertical
2017	*ARM* SGP, LAFE	*PLA*	ECDLs	Fiber Switch	enhanced	10 W	9 W	$\leq$ 2 W	scanning, vertical

Table 6.1: Completed field campaigns and measurement activities with corresponding development status of this DIAL transmitter. All locations are in Germany, except for LAFE (Oklahoma, USA). P_{max} – maximum achieved Ti:sapphire laser power so far, P – laser operation power during the measurement, P_{atm} – power sent into the atmosphere. The main observation mode of the Hohenheim-DIAL is mentioned first. See text and related chapters for more details on the individual components of the laser system.

6.1.2 Vertical Measurement at 10 W Laser Operation

First-time water-vapor DIAL measurements with the titanium–sapphire laser operating at its full output power were realized in summer 2016. The laser system was set to an operation power of $P = 10\,\mathrm{W}$. To provide the possibility of monitoring the power during the measurement, a small amount of $P_{mon} = (0.92 \pm 0.16)\,\mathrm{W}$ was directed onto the power meter, while the most part of the output power was sent into the atmosphere ($P_{atm} \approx 9\,\mathrm{W}$). The high power emission required the laser light to be sent out of the DIAL on a free-beam path including a beam expander and a bending mirror (see the setup of the DIAL system in Chapter 2.3.2). Hence, the humidity field was captured by a vertical line of sight, the atmosphere evolving over it in time.

The online frequency of the laser was set to $\nu_{on} = 366\,430\,000\,\mathrm{MHz}$ ($\lambda_{on} \approx 818.144\,\mathrm{nm}$ in vacuum). It was chosen such that the transmission of the atmosphere was $T_{wv}(R, \nu_{on}) \approx 1$ (see Equation 2.8), providing high sensitivity up to the maximum height R of primary interest (lower troposphere, $R \approx 3\,\mathrm{km}$). At the same time, this frequency value had the advantage of a minor Doppler-broadened Rayleigh backscattering, such that the correction term K of the DIAL equation (2.10) was neglected. The offline frequency was around $\nu_{off} = 366\,373\,360\,\mathrm{MHz}$ ($\lambda_{off} \approx 818.270\,\mathrm{nm}$ in vacuum). During the measurement, the frequency and linewidth of the emitted laser pulses were kept track of with the wavelength meter and logged over a certain period. The data acquisition recorded the backscatter lidar signal with a range resolution of $\Delta R = 15\,\mathrm{m}$ and pre-averaging the data with $\Delta t = 0.1\,\mathrm{s}$ on the temporal scale. For the subsequent humidity data analysis, the profiles were further averaged (see below). The higher temporal and spatial resolution of the raw data allowed to ascertain the optimum averaging settings.

The measurement presented here was made on 7 September 2016 in Stuttgart-Hohenheim (48°42′40.8″N, 9°12′15.1″E, 386 m above sea level). The meteorological conditions on this day were the following. A high-pressure system over central Europe blocked the westward and southward propagation of frontal systems, resulting in a mostly sunny and warm late summer day. Only small-scale boundary layer clouds developed during the day. The daily maximum 2 m-temperature in Hohenheim was 23.5 °C. The ground value of the absolute humidity was around $10\,\mathrm{g/m^3}$.

The observation of the water-vapor field with the Hohenheim-DIAL was performed between 13:38 UTC and 15:57 UTC. Figure 6.1 shows the time–height indicator of the vertical humidity profile for the entire period. The upper figure is scaled from the ground level up to an altitude of 7 km (hereinafter, all heights a.g.l., above ground level). The absolute humidity data was processed using a Savitzky–Golay filter (step size equal to the resolution of the raw data; window length 135 m), resulting in a range resolution $\Delta R \approx 67.5\,\mathrm{m}$ [48]. On the temporal domain, the data was averaged over $\Delta t = 10\,\mathrm{s}$, consecutively. The overlap between the emitted laser beam and the receiver telescope's field of view, yielded valid data for heights $\gtrsim 200\,\mathrm{m}$. The measurement was occasionally interrupted for a short time to verify the overlap alignment.

It can clearly be seen that water vapor dominates in the lower part of the atmosphere and that it decreases upwards with individual layers of high and low humidity. At an altitude around 2.8 km a layer can be recognized which gradually became drier towards the evening. Above a height of 5 km, signal noise prevails more and more. To obtain meaningful values of the absolute humidity there, larger averaging times would be necessary. Alternatively, the online frequency could be modified to a lower absorption of water vapor. Both of these actions entail compromises

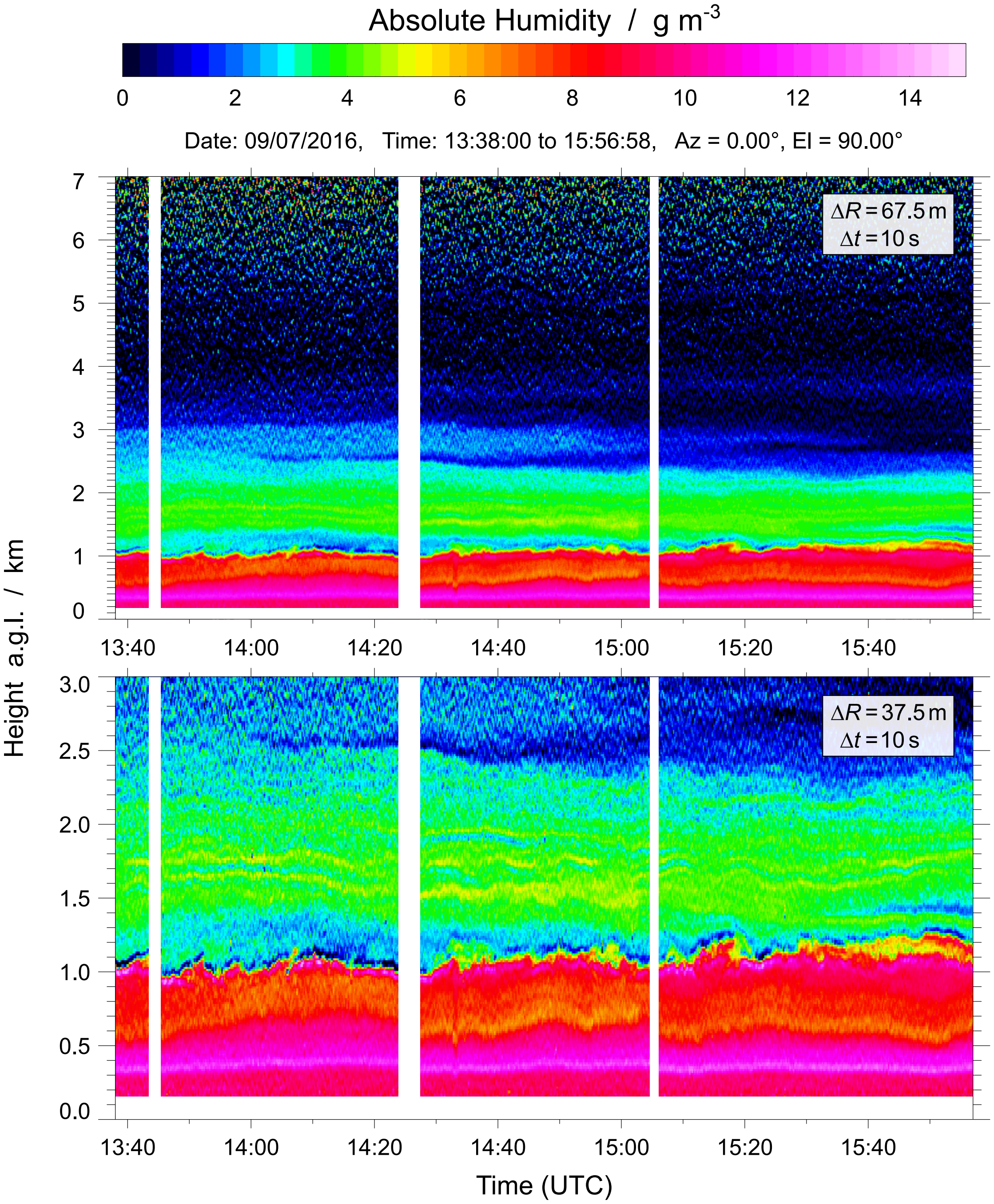

Figure 6.1: Example of a vertical-pointing water-vapor DIAL measurement. The laser transmitter was operating with an output power of $P = 10\,\mathrm{W}$. Thereof $\approx 9\,\mathrm{W}$ were sent into the atmosphere. A closer look with an increased range resolution ΔR reveals complex layer structures. The measurement was briefly interrupted to verify the overlap alignment.

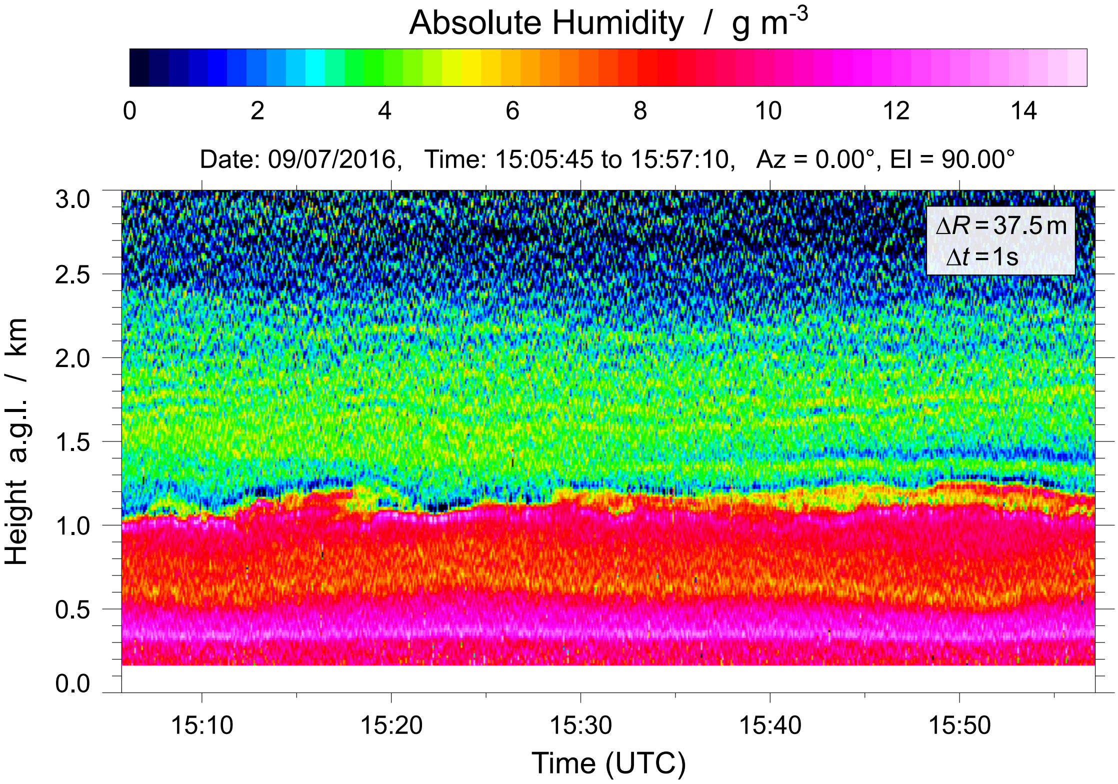

Figure 6.2: End period of the discussed measurement (cf. Figure 6.1), evaluated with an increased temporal resolution Δt. Fine details, such as the strong variability at the ABL top in the course of time, become visible. The observation of the humidity field with high spatial and temporal resolution is enabled by the high laser performance.

on the resolution or accuracy of the measured humidity field. The more suitable approach will depend, in the end, on the subject of meteorological investigation. This case illustrates why it is important to have a powerful transmitter. A long range, without compromises in resolution or accuracy of the measurement, is only achieved with a high laser power.

Of primary interest is the atmospheric boundary layer (ABL), the region from the ground level up to a height of $\approx 1.0\,\mathrm{km}$, in this case. Besides exhibiting a comparatively high absolute humidity, this region is characterized by turbulence. The ABL couples the planetary surface with the overlying atmosphere and plays a crucial role in the development of the weather [4]. Therefore, its exploration is of most importance for meteorology, and also a research focus of the *Institute of Physics and Meteorology*. The ABL is magnified in the lower image of Figure 6.1, which depicts the measurement for the vertical range up to $3\,\mathrm{km}$. This plot was realized with a range resolution of $\Delta R \approx 37.5\,\mathrm{m}$. Time scale and temporal resolution are the same as above. Figure 6.2 is an enlarged display of the time span from 15:06 UTC to 15:57 UTC, where now also the temporal resolution was increased to $\Delta t = 1\,\mathrm{s}$. The figures with the high resolution allow identifying fine details, notably at the top of the ABL, revealing a complex layer structure and

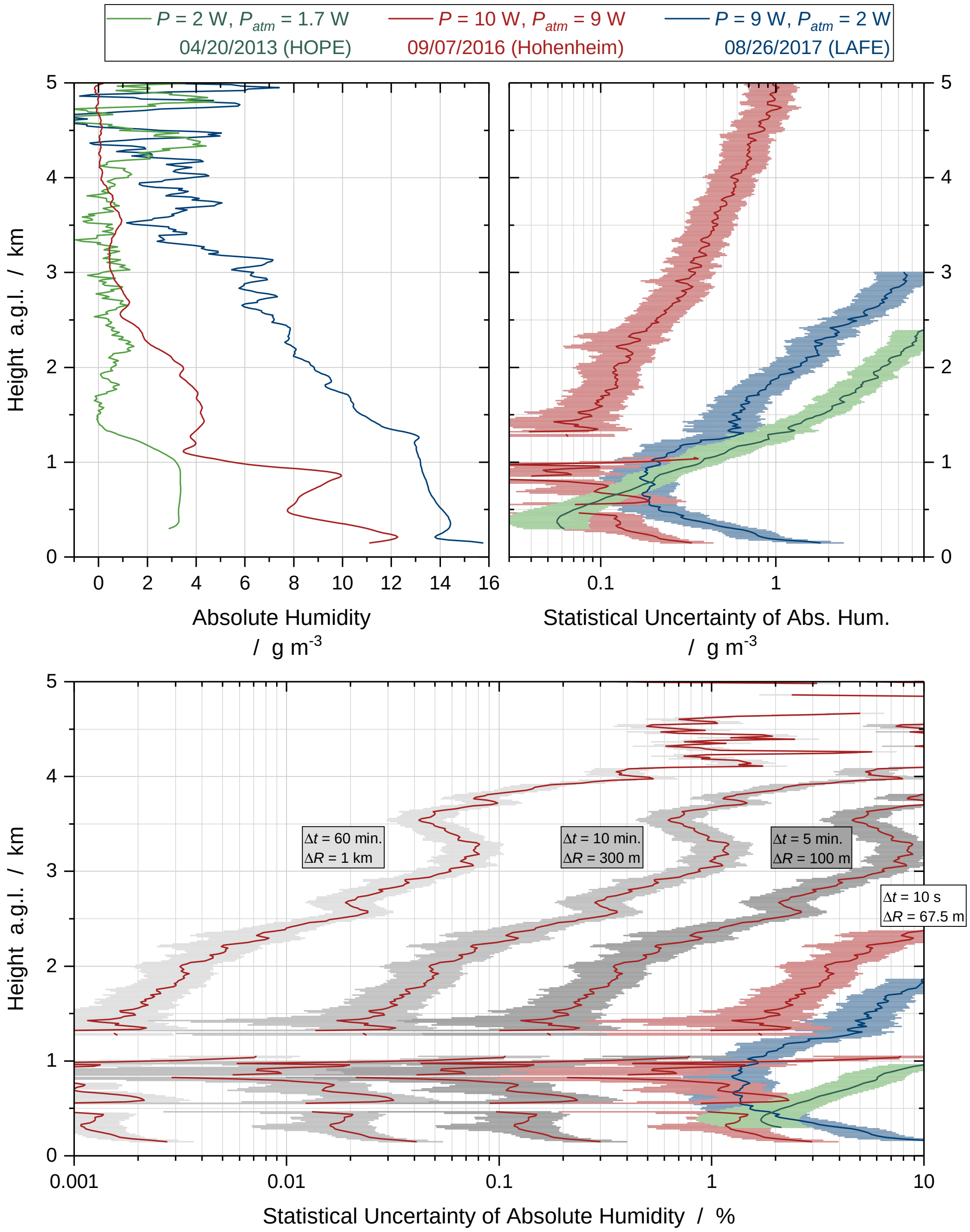

Figure 6.3: Instrumental noise analysis for the discussed case and two similar measurements. **Top left:** Mean profile of the entire time series used for the evaluation (30–60 min). **Top right:** Absolute value of the statistical uncertainty; adapted from [13]. **Bottom:** Resulting statistical uncertainty in percent. For the 2016 measurement, additionally, scaled versions of different resolutions are shown (with gray colored areas for the error bars).

the rapid fluctuation of moisture. This was largely possible thanks to the achieved performance of the transmitter.

Regarding the accuracy and the precision of the DIAL system, a distinction is made between systematic and noise errors. Various factors contribute to these. For an exact specification of the systematic error, end-to-end simulations are most suitable [6, 51, 52]. However, the systematic errors attributable to the laser transmitter's frequency stability and linewidth can be estimated by comparing the achieved performance (see Chapter 5.7.3) with the results from the references, e.g., [11, p. 3857] and [6, Figure 22]. With a frequency stability of $\delta\nu \approx 2\,\mathrm{MHz}$, a laser linewidth of $\Delta\nu \approx 60\,\mathrm{MHz}$, and an absorption linewidth of $\Delta\nu_{wv} \approx 6\,\mathrm{GHz}$, the relative error due to the frequency instability is $\ll 1\,\%$, the ratio $\Delta\nu/\Delta\nu_{wv} = 0.01$, and hence, the relative error due to the laser bandwidth $< 1\,\%$. The latter is achieved even for large optical depths, i.e., high altitudes. The combination of all error sources, which partially compensate, yield an overall systematic error of $< 1\,\%$ within the entire troposphere.

To make a statement about the noise error of the system, for the measurement here at $10\,\mathrm{W}$ laser operation, an analysis according to LENSCHOW *et al.* was carried out [184]. In this method, the contributions to the variance of the water-vapor measurement, by the instrumental noise and the change of atmosphere itself, are determined. A time series of the measurement is used to calculate the autocovariance function, at every range (height). Then, an extrapolation of the function to lag zero allows to estimate the contributions of the correlated and the uncorrelated variance. As a statistical (random) process, the instrumental noise is represented by the uncorrelated contribution. The fluctuation of the atmosphere, however, is correlated. By separating the correlated contribution from the total variance at lag zero, the statistical uncertainty of the measurement is obtained. The time series used for this evaluation was extracted from 15:06 UTC to 15:56 UTC, having a duration of $50\,\mathrm{minutes}$. Figure 6.3 presents the results up to a height of $5\,\mathrm{km}$, for the here discussed measurement, as well as, for two similar measurements executed at other dates, for comparison. The mean profile (top left) was averaged over the entire time series, showing the general magnitude and course of the absolute humidity. The statistical uncertainty (top right) was evaluated with the water-vapor data of resolution $\Delta t \approx 10\,\mathrm{s}$ and $\Delta R \approx 67.5\,\mathrm{m}$. It is given in $\mathrm{g/m^3}$, like the absolute humidity. The error bars (colored area) are the corresponding root mean square value from the evaluation. Gaps in the curve occurred, where the noise analysis method could not distinguish precisely enough the correlated from the uncorrelated variance. By dividing the statistical uncertainty by the mean profile, the relative value of the statistical uncertainty was obtained (bottom; in percent). This graph shows three additional curves. These are scaled representations of the measurement in 2016, for different resolutions. For the statistical uncertainty, the relation

$$\frac{\Delta\rho}{\rho} \propto \frac{1}{\sqrt{P_{atm}\,\Delta t\,\Delta R^3}} \tag{6.1}$$

holds [6, 12, 21]. With this, the scaling factor was determined for the resolutions specified by the most demanding requirement of the *World Meteorological Organization* (*WMO*, Nowcasting/Very Short Range Forecasting) and its three classifications 'Threshold' (uncertainty $10\,\%$, $\Delta t = 60\,\mathrm{min}$, $\Delta R = 1\,\mathrm{km}$), 'Breakthrough' (uncertainty $5\,\%$, $\Delta t = 10\,\mathrm{min}$, $\Delta R = 300\,\mathrm{m}$), and 'Goal' (uncertainty $2\,\%$, $\Delta t = 5\,\mathrm{min}$, $\Delta R = 100\,\mathrm{m}$) [185].

The figure demonstrates that a very low statistical uncertainty of absolute humidity was achieved. The 'Threshold' case is fulfilled over the whole depicted height range. The 'Breakthrough' case is fulfilled up to a height of $\approx 4\,\mathrm{km}$. The 'Goal' case is fulfilled up to a height of $\approx 2.5\,\mathrm{km}$. Even at the (original) high resolution, $\Delta t = 10\,\mathrm{s}$, $\Delta R = 67.5\,\mathrm{m}$, the statistical uncertainty is $\lesssim 2\,\%$ within the ABL, and $< 5\,\%$ up to a height of $2\,\mathrm{km}$. Therefore, it can be stated that especially in the main region of interest, the ABL, a system performance with high precision in the water-vapor measurement was accomplished.

The two further measurements exhibit a comparable behavior, but generally higher values for the statistical uncertainty. The higher instrumental noise can be attributed to the lower emission power, according to Equation (6.1). The corresponding operation power of the laser P, and the fraction sent into the atmosphere P_{atm} are indicated. For the measurement during HOPE, additionally, a different system configuration should be considered. Among other things, the online frequency was set to a stronger water-vapor absorption, so that the statistical error increased faster with height. More error analyses of the Hohenheim-DIAL are discussed in the literature, e.g., [13, 47, 48, 172, 173].

Finally, the monitoring instruments proofed a stable operation of the laser. The total emitted power remained constant except for a minor decrease by approximately $\Delta P = 0.4\,\mathrm{W}$ until the end of the measurement. This was correlated with the typical power decline of the pump laser. The specific evaluation of the wavelength meter data logging was previously discussed in Chapter 5.7.3.

6.1.3 Scanning Measurements

In this section, measurement examples of the Hohenheim-DIAL in scanning mode are presented. The first two measurements were taken during the SABLE campaign on 21 August 2014 (IOP 8). After a passage of a frontal system three days before, high pressure established from south-west. During day, there were fair weather conditions with weak south-westerly winds, interrupted only by episodes of cumulus clouds. In northern Germany also scattered showers occurred. Information on the instrument's location, the surrounding area, and more scanning measurements is to be found in reference [48].

The scanner unit of the DIAL was programmed to run repeatedly a range–height indicator (RHI) pattern. Throughout an RHI scan, the azimuth angle is fixed, while the elevation angle is varied. Here, the elevation angles from approximately $\varepsilon = 1°$ to $121°$ were covered. The angular range was limited by nearby standing trees. The scanning speed was $0.2\,°/\mathrm{s}$. Hence, one RHI scan was completed in $10\,\mathrm{minutes}$. The azimuth home position of the scanner was oriented $\approx 19°$ clockwise from north.

The laser was operated at typical online and offline frequencies for ground-based water-vapor DIAL ($\nu_{on} = 366\,429\,726\,\mathrm{MHz}$, $\nu_{off} = 366\,373\,404\,\mathrm{MHz}$). The laser delivered $P = 4\,\mathrm{W}$ of output power. Thereof, only $P_{atm} \approx 1.3\,\mathrm{W}$ were used for the transmission into the atmosphere, to prevent any risk of damaging the sending telescope's fiber, or the laser itself due to a back-reflected power fraction by stimulated Brillouin scattering (see also Chapter 2.3.2).

For the data processing, the consecutive lidar profiles of every $\Delta t = 10\,\mathrm{s}$ were averaged, yielding an angular resolution of $\Delta\varepsilon = 2°$. Figure 6.4 shows the RHI scan started at 08:43 UTC. The azimuth angle of the scanner was 33.34° clockwise from the home position. The range res-

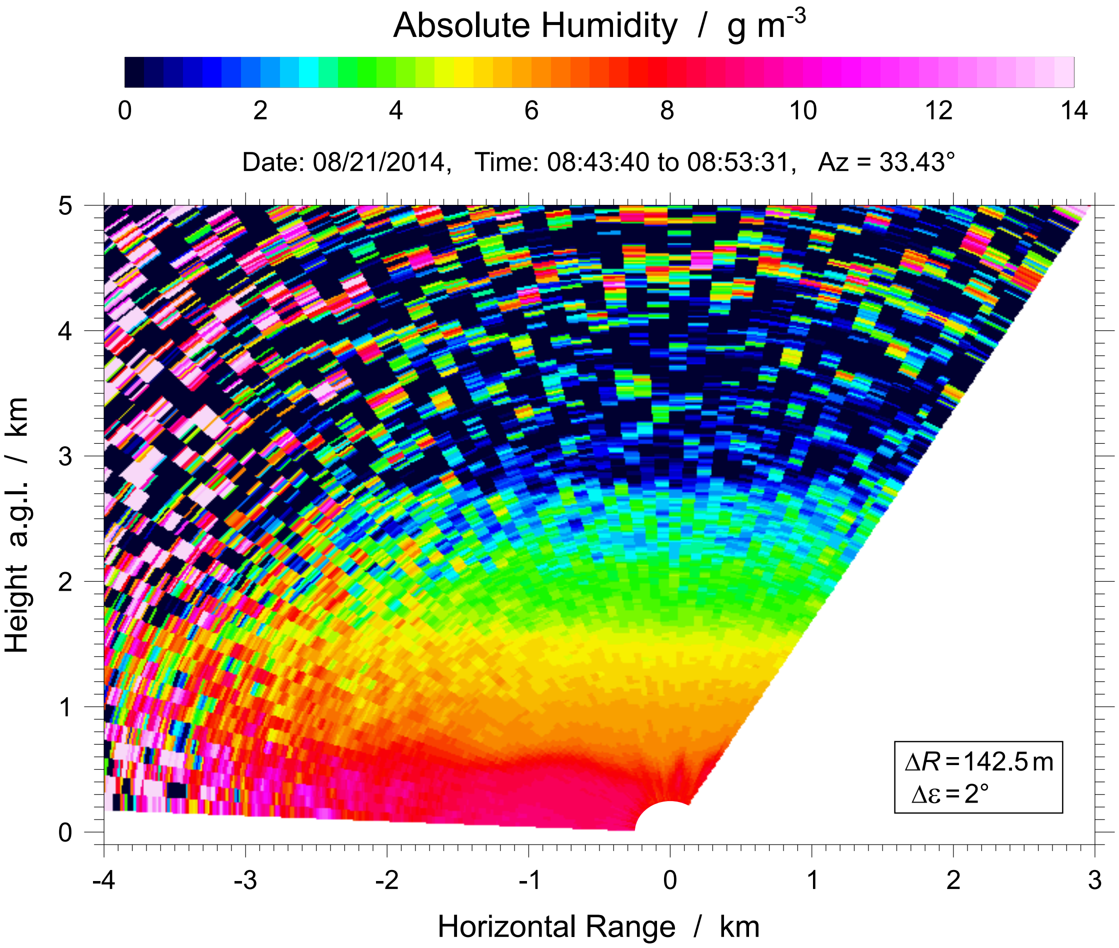

Figure 6.4: Scanning water-vapor DIAL measurement with the Hohenheim-DIAL. The scan pattern is a range–height indicator (varying elevation, fixed azimuth angle). The systems location is at the origin of the axes. The measurement was made during the SABLE field-campaign.

olution of the calculated humidity field is $\Delta R \approx 142.5\,\mathrm{m}$. A scan at a later time of the day (started at 15:27 UTC) is depicted in Figure 6.5. The azimuth orientation of the scanner was changed to $286.53°$. Here, the absolute humidity was calculated with a higher range resolution, resulting in $\Delta R \approx 67.5\,\mathrm{m}$, but a reduced maximum distance of detection. Both figures demonstrate that this distance is not circular around the origin of the laser pulse emission. The signal-to-noise ratio decreases in the horizontal direction at shorter ranges than in the vertical direction. This is explained by the absorption of the online laser pulses along the propagation path. Within the ABL the absorption is stronger, because of the higher moisture there. For this reason, in particular low-elevation scanning measurements demand a powerful laser transmitter. A higher resolution, of course, allows for recognition of more details of the measurement. In Figure 6.5, clouds at a height of approximately $1.5\,\mathrm{km}$ which were moving towards the DIAL system are also observed. Normally, no signal is received for ranges beyond the clouds, since

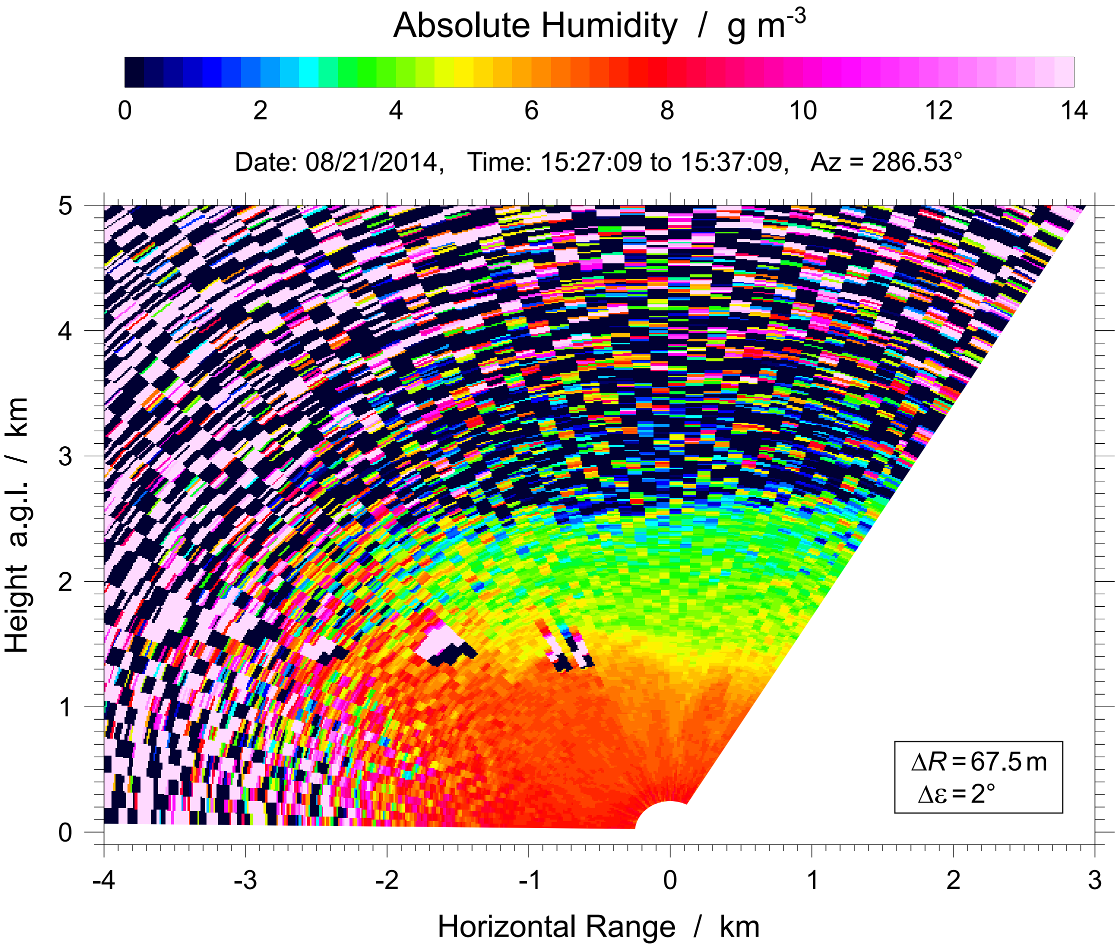

Figure 6.5: RHI water-vapor DIAL scan at a later time of the day, and different azimuth angle orientation of the scanner. The humidity data evaluation was carried out with an increased range resolution ΔR, resulting in a finer detection but shorter maximum range. Clouds approaching the system during the measurement are recognized at an altitude of about $1.5\,\mathrm{km}$.

their high optical depth (relative humidity around $100\,\%$) leads to an entire absorption of the laser radiation. However, if the clouds are not too dense, the signal can pass through, as in this case.

An example scan with a low elevation angle is shown in Figure 6.6. The humidity measurement was made on 5 August 2017 (IOP 3) during the LAFE campaign. More details about the field-campaign (the site, the instrumentation, and the observational strategy) are reported in [182]. The discussed measurement period of low-elevation scans was started at 17:40 UTC (12:40 local time) and lasted $50\,\mathrm{minutes}$. A mostly clear sky had developed during the day with strong south-westerly winds (wind speeds of $\approx 50\,\mathrm{km/h}$), and a well-mixed boundary layer. At that time, the $2\,\mathrm{m}$-temperature was around $33\,°\mathrm{C}$, and the dewpoint around $19\,°\mathrm{C}$. The top of the ABL was at $\approx 1.3\,\mathrm{km}$ height.

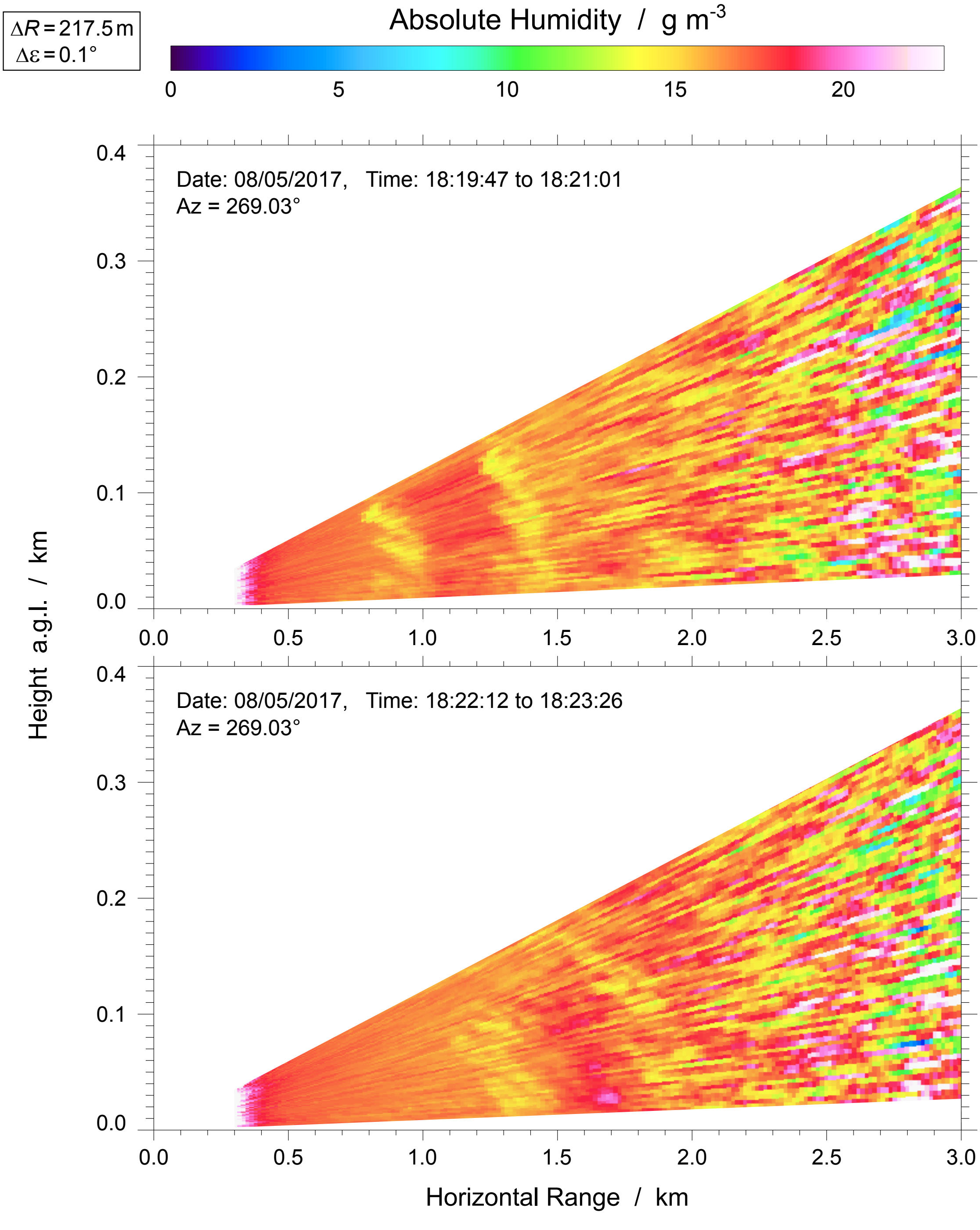

Figure 6.6: Surface layer scan of the humidity field with the Hohenheim-DIAL during the LAFE field-campaign. With the low-elevation RHI at high resolution, structures of lower moisture (presumably dust plumes) were captured. Their temporal evolution is illustrated here with two scans. The color scale was adapted to provide optimum contrast of these structures.

The line-of-sight of the Hohenheim-DIAL's scanner covered the elevation angles from $\varepsilon \approx 0°$ to $7°$. One scan of this sector was captured within approximately $70\,\mathrm{seconds}$. The depicted measurement was evaluated with a range resolution of $\Delta R \approx 217.5\,\mathrm{m}$, and a temporal resolution of $\Delta t = 1\,\mathrm{s}$. Hence, the angular resolution is $\Delta\varepsilon = 0.1°$. To obtain a transmission in the atmosphere of $T_{wv}(R, \nu_{on}) \approx 1$ at a range of $R \approx 4\,\mathrm{km}$, the online frequency of the laser was set to $\nu_{on} = 366\,422\,210\,\mathrm{MHz}$ ($\nu_{off} = 366\,373\,190\,\mathrm{MHz}$), which was lower than used previously and due to a generally higher absolute humidity ($\gtrsim 16\,\mathrm{g/m^3}$). The Ti:sapphire laser was operated at an output power of $P = 9.4\,\mathrm{W}$. Thereof, $P_{atm} \approx 1.6\,\mathrm{W}$ were sent into the atmosphere, being limited by the sending fiber, but also eye-safety.

Low-elevation scans permit investigation of the atmospheric surface layer, for instance over heterogeneous terrain to identify differences in the interaction of land and atmosphere. Furthermore, small structures and turbulence phenomena can be detected at high resolution. In the top panel of Figure 6.6, some type of plumes with lower moisture are recognized at a horizontal range of $R \approx 0.9\,\mathrm{km}$ and $R \approx 1.4\,\mathrm{km}$. Further scans revealed that these were moving away from the location of the DIAL system (at the origin) and spreading out over time. After two further scans ($\approx 2\,\mathrm{min}$) the plumes were located at a horizontal range of $R \approx 1.3\,\mathrm{km}$ and $R \approx 1.9\,\mathrm{km}$, as can be seen in the bottom panel of the figure.

6.2 Special DIAL Measurements

6.2.1 Determination of Spectral Purity

The spectral purity of a laser quantifies the fraction of the emitted radiation that lies within the desired frequency band. Despite injection seeding, there is a residual amount of the laser output at other frequencies. Spectral purity is a particular challenge for powerful, pulsed lasers, above all when applied for the narrowband water-vapor DIAL technique. High values, starting from $99.5\,\%$ are required, as stated in Chapter 2.2.1. Otherwise, the accuracy in the measurement of the absolute humidity is significantly degraded [11,21].

Usually, the spectral purity is measured indirectly by determination of the impure fraction of the total laser output,

$$SP := \frac{P_{pur}}{P_{tot}} = 1 - \frac{P_{imp}}{P_{tot}}\,, \tag{6.2}$$

with $P_{tot} = P_{pur} + P_{imp}$ [114]. Potential methods make use of a multipass absorption cell, the evaluation of an interferometer pattern, or the propagation through the atmosphere with a strong back-reflection by a definite target. The latter represents best practice and has the advantage of characterizing the entire DIAL system. It is utilized that DIAL emits laser pulses at online and offline frequency. Provided that at the online frequency the atmosphere completely absorbs the pure fraction of the laser output (i.e., the optical depth is high enough), then, the residual detected backscatter signal can be attributed to the impure fraction, $P_{imp} = P_{on}$. At the offline frequency, the absorption is very low and equal for all laser modes (pure or impure). Hence, this backscatter signal corresponds to the value of the total share, $P_{tot} = P_{off}$ [21].

What must be ensured, is that the spectrally pure laser radiation is entirely absorbed in the atmosphere. Moreover, the signal intensities and the measurement time must allow for a result of sufficient precision. All this depends on: the choice of the laser frequency, the present atmospheric condition, how strongly the target backscatters the signal, and the detector's sensitivity. Generally, for the measurement, the online frequency is tuned to the peak of a strong water-vapor absorption line. In the atmosphere, the propagation path should be long enough (distance to target $\gtrsim 5\,\mathrm{km}$), and a high optical depth should be given (≈ 7) [26, 65]. As a backscattering target, a hard target (e.g., a hill or mountain) is favored due to its intense scattering capability and fixed position. A compact cloud can also be expedient, albeit such measurements should be accepted with some reservation due to the variability that clouds potentially exhibit. The detector of a DIAL is already very sensitive; however, its noise has to be considered.

For the evaluation, it must also be considered whether the measured signal profiles have been pre-averaged. This refers to the temporal averaging carried out by most lidar systems already during the acquisition of the raw data. Potential reasons are insufficient recording speed of the hardware or the avoidance of high amounts of data. In some cases, this compilation of profiles is also done subsequently to facilitate the handling of the data. Whilst the final mean values of the online and the offline signal should remain unaffected by pre-averaging profiles, the corresponding standard deviations decrease for larger pre-averaging times. The resulting value and error of the spectral purity behaves accordingly. The highest error is obtained for the raw data, i.e., without pre-averaging, characterizing the laser on a shot-to-shot basis, or at very short pre-averaging times. The here presented spectral purity measurements were evaluated with the raw data, and additionally with pre-averaged profiles (temporal resolutions $\Delta t = 1\,\mathrm{s}$ and $10\,\mathrm{s}$). The latter may be more appropriate for the characterization of the DIAL operation, whereby a comparison to other systems is possible as well.

The spectral purity measurements were performed mainly on a hard target during the SABLE campaign. For the vertical pointing DIAL measurements with the $10\,\mathrm{W}$ laser operation, high (passing) clouds were used as target by way of trial. The measurements were carried out in DIAL operation mode, i.e., switching alternately between on- and offline frequency at the pulse repetition rate of the laser. As the sole difference, the laser's online frequency was set to the peak of the water-vapor absorption line, $\nu_{on} = 366\,436\,000\,\mathrm{MHz}$ ($\lambda_{on} \approx 818.130\,\mathrm{nm}$ in vacuum). The data profiles were recorded on a single-shot basis ($f_{rep} = 250\,\mathrm{Hz}$) during the SABLE campaign. Since 2016, in order to reduce the data amount, the raw data was saved pre-averaging every $\Delta t = 0.1\,\mathrm{s}$ ($f_{rep} = 300\,\mathrm{Hz}$, 15 online and offline laser pulses each). The evaluation consisted of, optionally further averaging of the profiles, a background subtraction, as well as the selection of the signal values at a certain range bin and the calculation of the spectral purity. As background signal for the SABLE measurements, the mean value of the (noise) signal in the range region from $R = 22.5\,\mathrm{km}$ to $30\,\mathrm{km}$ was taken. From 2016 on, also the record length of the profiles was reduced, and hence, the range region from $R = 19.6\,\mathrm{km}$ to $20\,\mathrm{km}$ was used for the background subtraction. The approach for the range bin selection was different depending on the target type.

The hard target of the SABLE campaign was a low hill located at a distance of $R \approx 7.3\,\mathrm{km}$ from the DIAL. When pointing on the hard target, the scanner was oriented horizontally. Therefore, the propagation path was within the atmospheric boundary layer close to the ground level, providing a high number density of water vapor. In combination with the local meteorological conditions and the choice of the absorption line peak, values clearly above an optical depth of 10 were determined. Consequently, complete absorption of the spectrally pure fraction at the

Measurement period, UTC	**Distance**	***SP***	**Δ*SP* (raw data, 1 s, 10 s)**
08/05/2014, 14:40–14:50	$7.350\,\mathrm{km}$	$100.001\,\%$	$0.514\,\%, 0.046\,\%, 0.016\,\%$
08/19/2014, 16:22–16:36	$7.305\,\mathrm{km}$	$99.987\,\%$	$0.543\,\%, 0.317\,\%, 0.100\,\%$
08/25/2014, 10:33–10:46	$7.290\,\mathrm{km}$	$99.998\,\%$	$0.294\,\%, 0.028\,\%, 0.010\,\%$

Table 6.2: Measurements on a hard target during the SABLE campaign for the determination of the laser transmitter's spectral purity (*SP*). The error value ΔSP depends on the pre-averaging of the profiles (Δt in parenthesis).

online frequency was guaranteed. Spectral purity measurements of three different days are discussed. The results are summarized in Table 6.2. The duration of each measurement was at least $10\,\mathrm{minutes}$. The precise location of the hard target was defined by the range bin of maximum intensity in the offline signal. Minor variations of the location between the measurements are explained by slightly different pointing directions of the scanner. Every individual measurement maintained its target position. This allowed to perform the averaging of all profiles beforehand, and then execute the further evaluation.

The characterization of spectral purity is illustrated in Figures 6.7 and 6.8. The backscatter signals of the offline and the online laser pulses are shown for the case of the 25 August 2014 (Figure 6.7). In this images, the background was subtracted, and the profiles averaged temporally with $\Delta t = 10\,\mathrm{s}$. The range resolution corresponds to the recording setting of the DAQ, $\Delta R = 15\,\mathrm{m}$. It can be seen that in the signal of the offline frequency, at the distance of the hard target, the intensity is strong and nearly constant during the entire measurement period. In the online frequency signal, in contrast, even for low intensities only noise is perceived at this range location.

The range profiles of the totally averaged data and the calculated spectral purity thereof are plotted in Figure 6.8 around the target's location for all three measurement cases. For the offline signals, the backscattering of the hard target is clearly recognized, where the location and the intensity varies. Apparently, the hard target exhibits also a certain width. It is assumed that this is due to the slope of the low hill. The long-term average of the online signal reveals that a very small amount of intensity was registered at the position of the hard target. This is attributed to the residual impure fraction of the laser radiation. The spectral purity was determined as described above from these offline and online signal intensities at identical range values. The listed results are the values at which the offline signal was strongest. Horizontal dashed lines mark this range location in the graphs for each measurement case. Over the width of the hard target, the spectral purity values are to some extent constant. Off the location of the hard target the spectral purity fluctuates around the value of $100\,\%$, since the online and the offline signal consist there only of remaining noise. The measurement case of 5 August 2014 delivers even on the hard target a value above $100\,\%$. An explanation for this could be a too low intensity of the backscatter signal. Hence, the impure fraction at the online frequency vanished in the noise of the detector, as the range profiles demonstrate. In the event that a residual noise value becomes negative, the spectral purity exceeds the theoretically ideal value. On these grounds either a more sensitive detector or a longer measurement period would have been necessary. Having said that, the measurement error still allows the true spectral purity value to be below $100\,\%$.

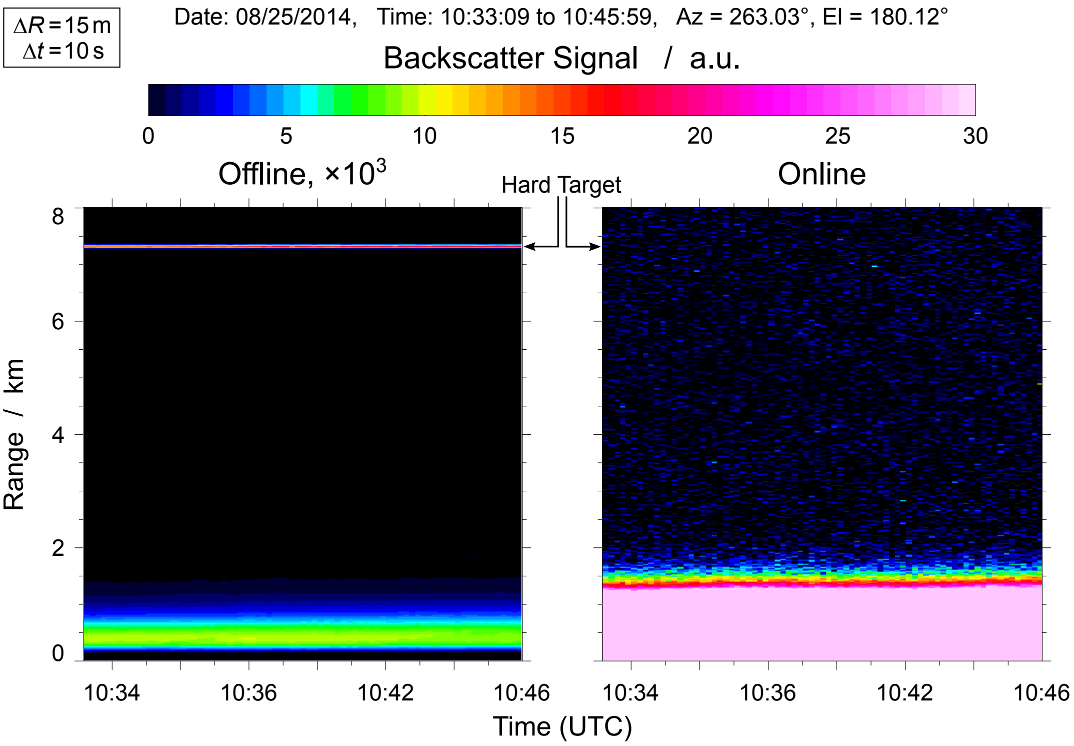

Figure 6.7: Offline and online backscatter signals of a DIAL measurement on a hard target.

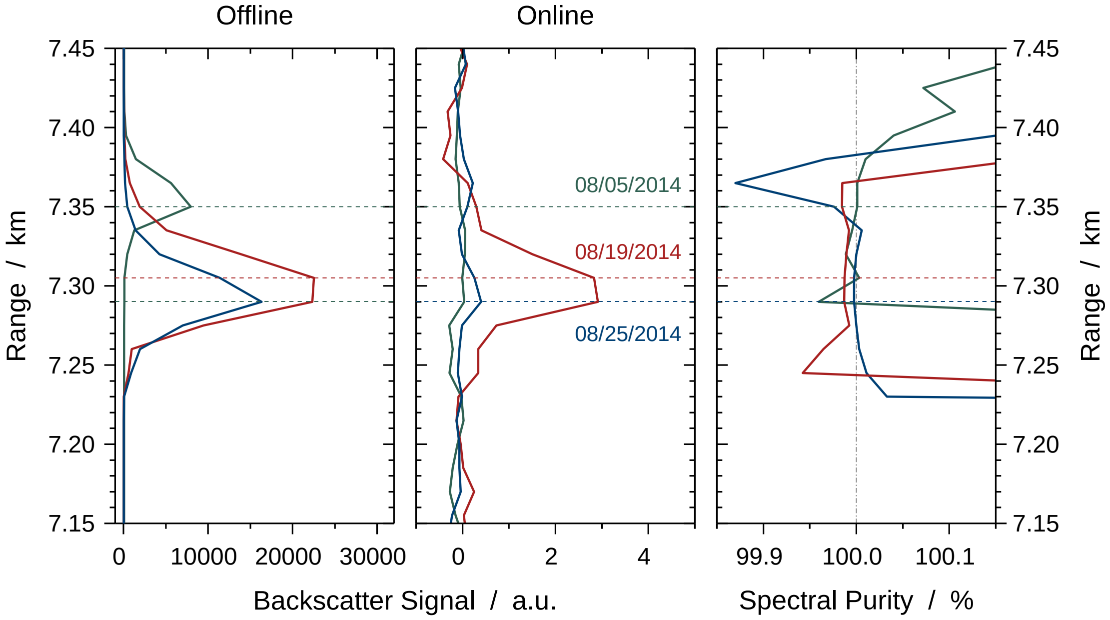

Figure 6.8: Range profiles of the fully time-averaged offline and online signals as well as resulting spectral purity for all three measurement cases.

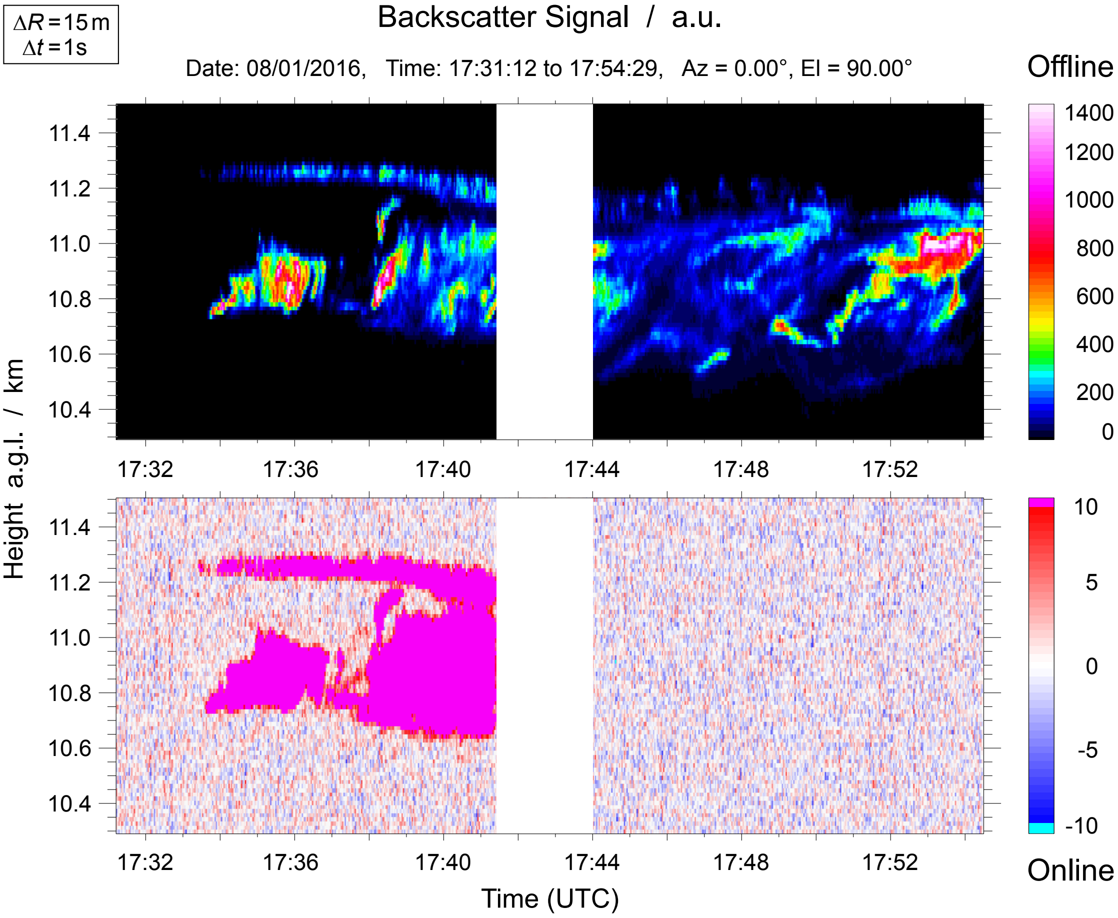

Figure 6.9: Background-corrected offline and online backscatter signals of a DIAL-measurement on a high cloud at 10 W laser operation. First, the laser frequencies were configured for humidity observation. For the characterization of the spectral purity, the online frequency was then changed to the peak of the water-vapor absorption line. Due to the high absorption, only noise is detected in the online signal, indicating the high spectral purity of the laser radiation.

The spectral purity's error values were calculated via propagation of uncertainty. As uncertainty the standard deviations from the averaging procedure of the online and offline signals were used. As explained above, these values depend on the pre-averaging of the profiles.

During the measurement activities in summer 2016, with the laser operating at the power level of $P = 10\,\mathrm{W}$, a spectral purity measurement was made by way of trial. On 1 August 2016 at approximately 17:30 UTC, high clouds at a height of $\approx 11\,\mathrm{km}$ passed the vertical line of sight of the Hohenheim-DIAL, which was acquiring humidity profiles. In order to start the characterization, the online frequency was changed from the previous setting at the slope of the absorption line to its peak (see value above). Figure 6.9 shows the recorded backscatter signals of the offline and the online frequency laser pulses. On the one hand, the presence of

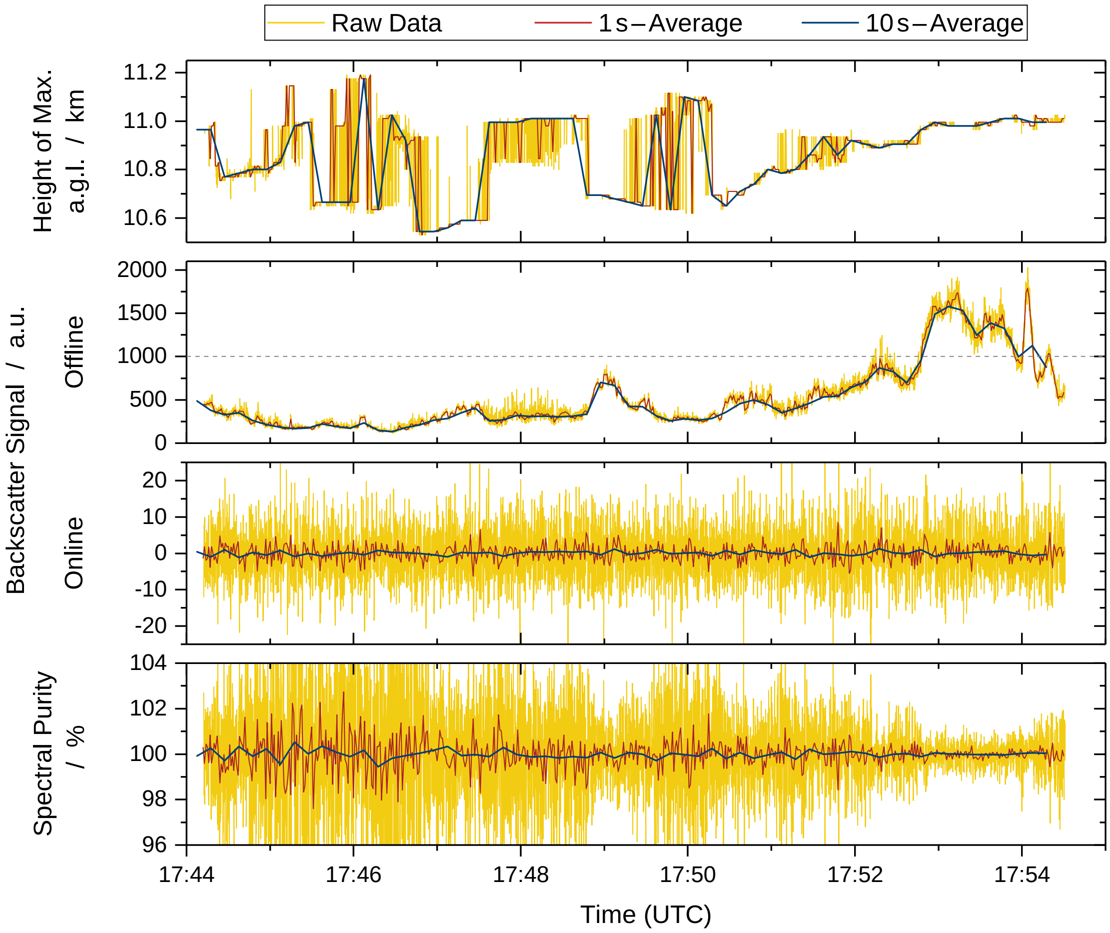

Figure 6.10: Evaluation of the cloud measurement. The time series of the location of maximum offline intensity, the offline and the online signal intensities, as well as the resulting spectral purity for each profile are shown. The total spectral purity was then determined considering profiles with an offline intensity > 1000, for which the variation is clearly lower.

the cloud was clearly visible in the offline signal. The data acquisition was interrupted for the reconfiguration of the online diode laser. On the other hand, the cloud was detected also in the online signal prior to the modification of the frequency. After the online frequency was set to the peak of the absorption line, besides the detector noise, no signal was perceived anymore. This indicates that the spectrally impure fraction of the laser was low.

However, obtaining significant results for spectral purity was challenging with this measurement. The cloud did not provide ideal conditions, with generally weak backscatter intensities in the offline signal or a too short measurement period. Under these circumstances, only an evaluation with limited precision was possible. For the approach, the range bin (height) of maximum offline intensity was identified for each recorded profile. Successively, the online and offline signal values at this range bin were read out and the spectral purity was calculated individually.

The four parameters are plotted as a time series in Figure 6.10 for the data sets of different temporal resolution. Most of the time, the intensity values of the offline backscatter signal are low (≈ 500). The online signal, generally, is dominated by the noise of the detector. Accordingly, the values of the spectral purity, calculated for every profile, fluctuate. However, towards the end of the measurement, the cloud became denser, yielding higher offline signal intensities. The range bin of the maximum offline intensity was more localized, as well. As a consequence of the higher offline intensities, the variation of the spectral purity is lower. For offline intensity values > 1000, this is particularly noticeable. The final spectral purity value was, thus, determined from the mean of all selected profiles, for which the offline signal exceeded this value. The resulting value was $SP = (99.97 \pm 0.49)\,\%$ for the raw data ($\Delta t = 0.1\,\mathrm{s}$), $SP = (99.97 \pm 0.16)\,\%$ for the pre-averaged data with $\Delta t = 1\,\mathrm{s}$, and $SP = (100.003 \pm 0.040)\,\%$ for the pre-averaged data with $\Delta t = 10\,\mathrm{s}$.

In summary, the spectral purity measurements specify a high spectral purity of the laser, fulfilling the requirements of Section 2.2.1. The characterization with the hard target delivers more reliable results, due to the fixed location and high intensity backscattering. The measurement on a high cloud showed that the offline backscatter signal was mostly very low, limiting the precision of the measurement. The spectral performance of the laser operating at $P = 10\,\mathrm{W}$ is quite similar to the situation during the hard target measurements. The characterization with the wavelength meter (see Section 5.7.3) confirms this. Finally, the humidity measurements of the Hohenheim-DIAL demonstrated a high accuracy of the system.

6.2.2 Online Frequency Tuning

The classic DIAL methodology requires the emission at two frequencies which can be adjusted within a certain spectral range according to the meteorological conditions or the subject of investigation. However, once the prevailing circumstances are clear, the frequencies are set to suitable values and kept for the measurement phase. It is switched between the two frequencies during the measurement, but a continuous tuning of the frequency is not performed. As shown below, in a slightly modified form, the DIAL technique offers the possibility to examine the atmosphere spectroscopically by continuously tuning one of the two frequencies. Since the frequency control technique implemented in this work provides versatile tuning capabilities of the laser, and tuning frequency measurements are highly useful for atmospheric spectroscopy, first tuning experiments with this transmitter were made at the end of the SABLE campaign [178]. An example of the importance of atmospheric spectroscopy and the experimental execution of a lidar measurement with a tuning laser was provided in [186].

Further motivation is given by the following. A diode laser that is tuning adequately could have the potential of replacing two (or more) diode lasers as injection seeders operating at fixed frequencies. Moreover, the frequency of the laser could be adjusted with the scanning pattern of the DIAL system, resulting in seamless measurements between two configurations, e.g., vertical and low-elevation directions. Generally, the extension of the continuously-tunable emission spectrum of the Ti:sapphire laser could be studied by switching from one tuning injection seeder to another. For the sake of completeness, it is noted that the output of the Ti:sapphire laser is always—due to its pulsed operation—a sampled reproduction of the continuously tuned frequency of the injection seeder. The sampling occurs at the repetition rate of the laser pulses.

To begin with, an analytical expression is derived for the frequency-dependent absorption of the atmosphere as function of the detected backscatter signal. Consider first a transmitter emitting at a single (tunable) frequency only, i.e., without successive switching to other frequencies. Starting with the basic lidar equation (2.3) in the representation

$$\hat{P}(R,\nu) = C(R)\,\beta(R,\nu)\,\exp\left[-2\int_0^R \alpha(r,\nu)\,\mathrm{d}r\right] + \hat{P}_{bg}(\nu)\,, \tag{6.3}$$

it is solved for the extinction coefficient $\alpha(r,\nu)$. The system factors of the lidar were summarized in a constant $C(R)$, yet depending on the range R where the scattering occurs, and the transmission term was explicitly written down. The extinction coefficient is approached as usual by taking the logarithm and then the derivative with respect to R,

$$\ln\left[\hat{P}(R,\nu) - \hat{P}_{bg}(\nu)\right] = \ln[C(R)\,\beta(R,\nu)] - 2\int_0^R \alpha(r,\nu)\,\mathrm{d}r \tag{6.4}$$

$$2\int_0^R \alpha(r,\nu)\,\mathrm{d}r = \ln\left[\frac{C(R)\,\beta(R,\nu)}{\hat{P}(R,\nu) - \hat{P}_{bg}(\nu)}\right] \tag{6.5}$$

$$\alpha(R,\nu) = \frac{1}{2}\frac{\mathrm{d}}{\mathrm{d}R}\ln\left[\frac{C(R)\,\beta(R,\nu)}{\hat{P}(R,\nu) - \hat{P}_{bg}(\nu)}\right]. \tag{6.6}$$

Before proceeding to the cross section σ which is included in the extinction coefficient α (cf. Equation 2.9 on page 8), two potentially unknown quantities are recognized already. From the system constant, $C(R) = O(R)/R^2$ remains (system factors independent of R drop out), and the backscatter coefficient $\beta(R,\nu)$ must also be defined. Simplifying assumptions might be possible, for instance, the same β for moderate variations of ν. If these parameters can be determined additionally, the evaluation of the signal can be continued.

Now consider an operation of the transmitter switching between a fixed frequency (e.g., offline) and a tunable frequency (e.g., online). With the DIAL methodology, the differential extinction coefficient is readily obtained. Rearranging the narrowband water-vapor DIAL equation (2.10) enables to calculate the absorption cross section at the tuning frequency,

$$\sigma_{wv}(R,\nu_{on}) = \sigma_{wv}(R,\nu_{off}) + \frac{1}{2\,N_{wv}(R)}\left\{\frac{\mathrm{d}}{\mathrm{d}R}\ln\left[\frac{\hat{P}(R,\nu_{off}) - \hat{P}_{bg}(\nu_{off})}{\hat{P}(R,\nu_{on}) - \hat{P}_{bg}(\nu_{on})}\right] + K\right\}. \tag{6.7}$$

For this, the cross section at the fixed (offline) frequency must be known, as well as the number density of water vapor. The values can be ascertained with other instruments, databases, or estimated from the standard atmosphere. The correction term K (specified by Equation 2.11) also may be taken into account.

For the atmospheric measurements, the configuration of the transmitter and the other DIAL components mostly agreed with the configuration during regular operation. Only the frequency control setting of the injection seeding system was altered. Instead of stabilizing the external-cavity diode laser with the analog output of the wavelength meter to a constant frequency, a frequency tuning function was registered in the control software (see also Chapters 4.3.2 and 4.4.2).

Several measurements with different frequency patterns and DIAL scanner orientations were executed. In what follows, one specific case is elaborated. Other cases are briefly outlined at the end of this section.

The measurement was performed on 20 August 2014 (SOP 1 of the SABLE campaign) between 11:54 UTC and 12:12 UTC. Injection seeding with alternate switching between the two diode lasers was engaged. The DFB diode laser was set to a fixed offline frequency, $\nu_{\mathit{off}} = 366\,373\,460\,\mathrm{MHz}$. As seeder with the tuning (online) frequency, the ECDL was used. The software of the wavelength meter was programmed to drive the ECDL's frequency according to

$$\nu_{on}(t) = \nu_0 + \nu_{amp}\,\mathrm{triangle}\left(\frac{t}{T}\right). \tag{6.8}$$

Thus, the time dependent behavior of the online frequency was a triangle wave function, with a cycle duration of $T = 100\,\mathrm{s}$. The center frequency was set to $\nu_0 = 366\,429\,786\,\mathrm{MHz}$, and the function had an amplitude of $\nu_{amp} = \pm\,9629\,\mathrm{MHz}$. With these settings, it was possible to cover one side of the water-vapor absorption line, from its near wing up to the peak and even slightly beyond it[1,2] The range was chosen to exploit the mode-hop-free tuning range of the ECDL, yet preserving a small safety distance to its maximum limits.

The data processing of the detected backscatter signals consisted in averaging of the profiles (temporal resolution $\Delta t = 1\,\mathrm{s}$) and calculating the absorption cross section at the online frequency with Equation (6.7). The derivative was computed, again, with a Savitzky–Golay filter, which smoothed the data in the spatial dimension and led to a range resolution of $\Delta R \approx 67.5\,\mathrm{m}$. In this measurement, the pointing direction of the scanner was nearly horizontal. It was assumed that the atmospheric conditions were the same along the measured line of sight. That is why, for all ranges R, the ground-level value of the water-vapor number density, and of the absorption cross section of the offline frequency, was taken. The number density was obtained from a radiosonde[3] launched on-site, $N_{wv}(R) \approx N_{wv,rs}(0) = 2.05 \times 10^{23}\,\mathrm{m}^{-3}$ (temperature $T = 15.43\,°\mathrm{C}$, pressure $p = 977.73\,\mathrm{hPa}$, and relative humidity $RH = 48.02\,\%$). For the absorption cross section of the offline frequency, it was referred to the HITRAN 2012 database [46] (with same input parameters from the radiosonde), yielding $\sigma_{wv}(R, \nu_{\mathit{off}}) \approx \sigma_{wv,db}(0, \nu_{\mathit{off}}) = 4.86 \times 10^{-29}\,\mathrm{m}^{-2}$. A Doppler-broadening correction was not applied (i.e., $K = 0$).

A time–range plot of the generated result is presented in Figure 6.11 for an interval of 300 s, corresponding to three cycle durations of the frequency function. The plot shows the periodic variation of the online absorption cross section $\sigma_{wv}(R, \nu_{on})$ with time. Thus, the tuning over the atmospheric water-vapor absorption line is visible. The time–range indicator demonstrates that the magnitude of $\sigma_{wv}(R, \nu_{on})$ is approximately constant with the range R. As expected for the horizontal pointing direction, the absorption cross section of water vapor is independent of the measurement distance. Only the signal-to-noise ratio is reduced with increasing range, since the laser pulses at the online frequency become absorbed more and more. This illustrates impressively the relation of the chosen online frequency and the maximum attainable range, or signal-to-noise ratio, respectively (for a given temporal resolution). Consequently, the importance of providing sufficient laser power for the DIAL methodology is emphasized.

---

[1] The starting point was at $\nu = 366\,420\,157\,\mathrm{MHz}$ ($\tilde{\nu} \approx 12\,222.461\,\mathrm{cm}^{-1}$, or $\lambda \approx 818.166\,\mathrm{nm}$ in vacuum).

[2] The ending point was at $\nu = 366\,439\,416\,\mathrm{MHz}$ ($\tilde{\nu} \approx 12\,223.103\,\mathrm{cm}^{-1}$, or $\lambda \approx 818.123\,\mathrm{nm}$ in vacuum).

[3] *Vaisala*, RS92-SGP

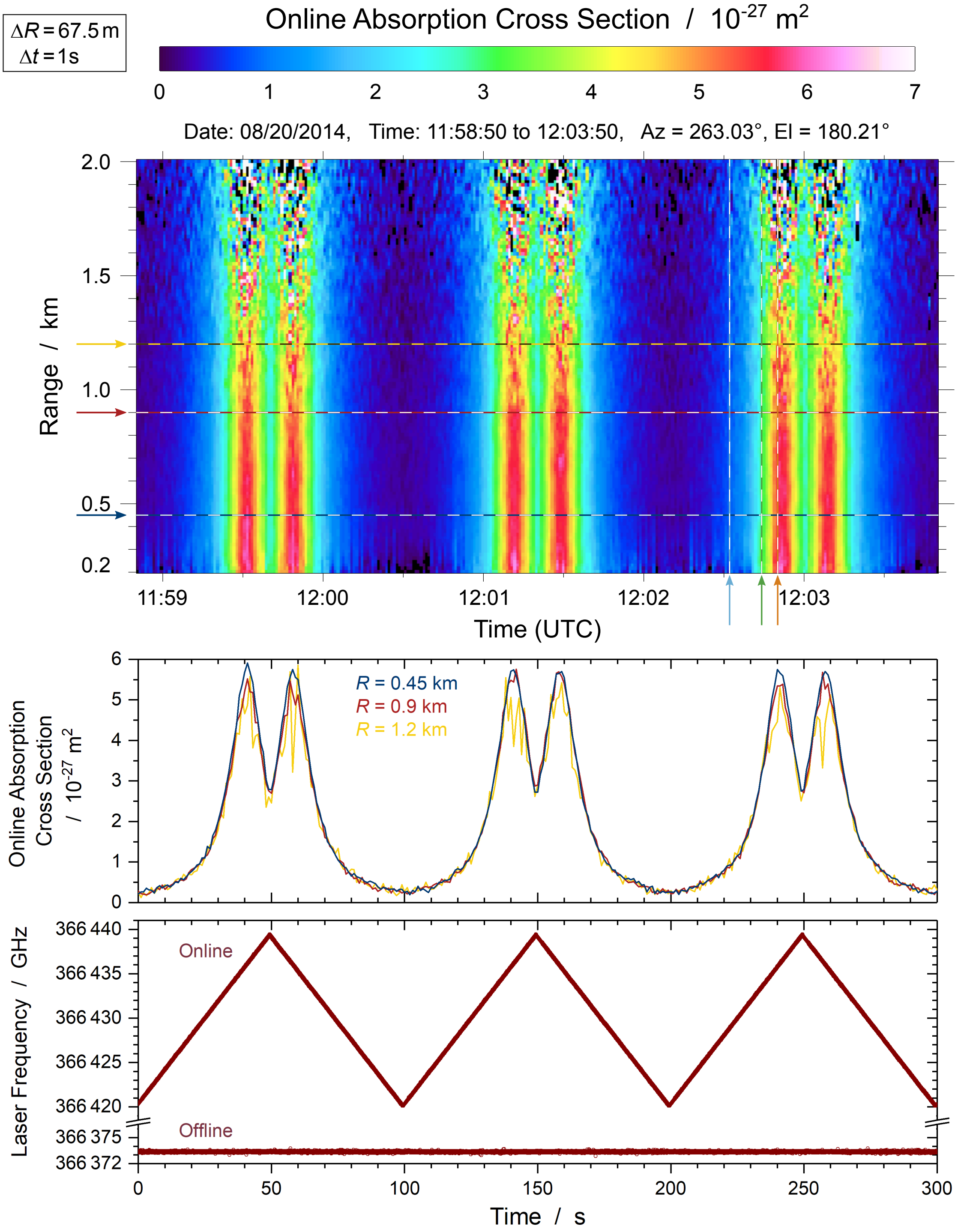

Figure 6.11: Time–range indicator (**top**) of the determined cross section $\sigma_{wv}(R, \nu_{on})$ for a period $3\,T = 300\,\mathrm{s}$. Arrows indicate the data extraction of the time series (**middle**) and the profiles (Figure 6.12). The laser pulses' frequency was measured with a wavelength meter (**bottom**).

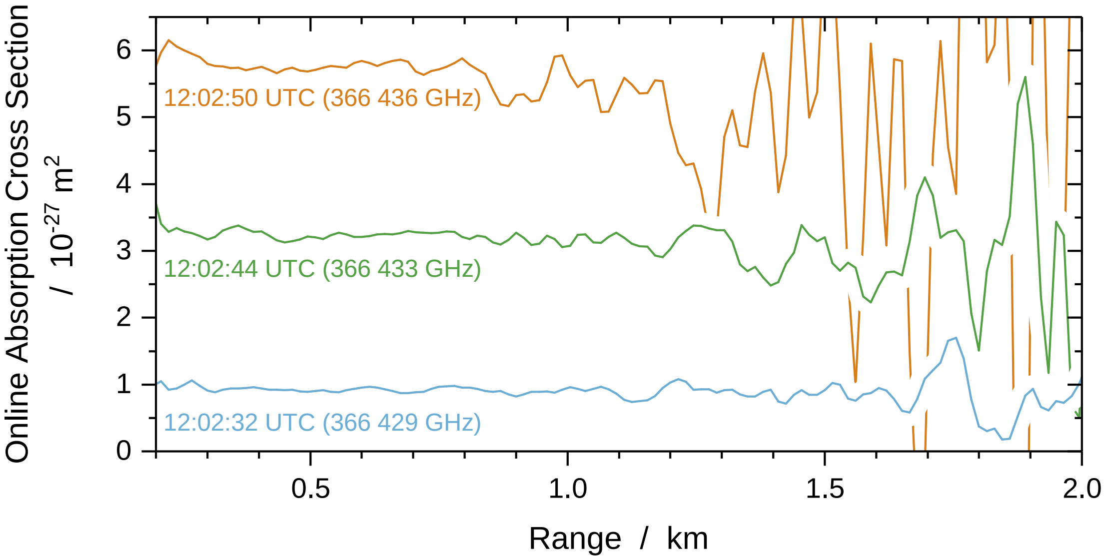

Figure 6.12: Range profiles at different positions on the absorption line (see also Figure 6.11).

The data was analyzed in more detail by extracting time series (single data rows) and profiles (data columns). The time series at range $R = 0.45\,\mathrm{km}$, $R = 0.9\,\mathrm{km}$, and $R = 1.2\,\mathrm{km}$ are depicted in the middle panel of Figure 6.11. The absorption lines are clearly visible and have been captured as intended. The peak is well pronounced, having been adequately passed over with the selected tuning range. Also the wing of the absorption line could still be detected. The results of the time series at different ranges are discussed further below and compared to the spectrum derived from the HITRAN database. The laser frequency of the Ti:sapphire laser and the ECDL (online injection seeder) were logged with their respective wavelength meters. The bottom panel of Figure 6.11 shows, for the corresponding time period, how the alternating Ti:sapphire laser pulses followed the triangle function at the online frequency, while remaining constant at the offline frequency. Three profiles at different times (i.e., different online frequencies, and accordingly, different positions on the absorption line) are traced in Figure 6.12. The profiles underline the aforementioned fact that the absorption cross section has about the same value for increasing range until noise prevails. A larger measurement range is reached, the lower the absorption is.

The combination of the online absorption cross section time series with the laser frequency measurement allows to draw the spectrum of the water-vapor absorption line over the span of the tuning range. All data points of the entire measurement period (extracted at the three mentioned ranges) were plotted as a function of the online laser frequency (see Figure 6.13. The laser frequency data of the injection seeder's wavelength meter was used, since it was continuous at the online frequency, and allowed for a more precise interpolation (temporal assignment of the measuring data). However, a comparison of the two wavelength meters showed that their absolute values were well within the accuracy specifications. A function was fitted to the data of each extracted time series. The shape function Λ in the Equation (2.14) for the cross section σ of the

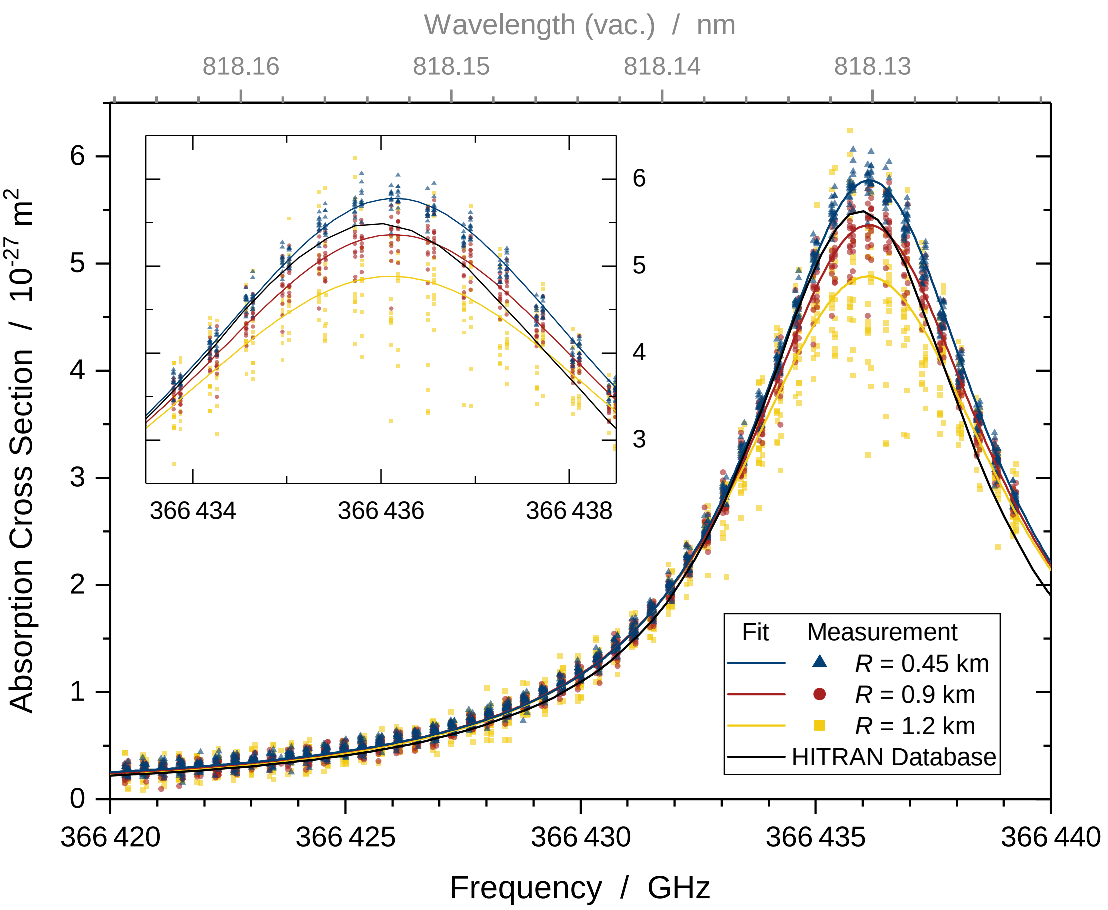

Figure 6.13: Data points of the online absorption cross section measurement extracted from the time series at different range R as function of the tuning frequency. A Voigt profile was fitted to each series. The spectrum obtained from the HITRAN database is also shown.

absorption line was approximated for convenience by a Voigt profile [11, 187–190]. Therefore, the fit was executed with this function. The fit function and its resulting parameters are detailed in Appendix B.2.

Figure 6.13 depicts the measuring data together with the fitted functions. For comparison, the corresponding spectrum computed with the HITRAN database has also been added. The progression of the absorption lines determined via the measurement conform well with the spectral line from the database, but with some minor deviations. For one thing, there is a slight stretching or shift on the frequency scale. This could be related to an inaccuracy leftover carried over from the synchronization of the wavelength meter and the DIAL measurement, or just to the frequency accuracy of the wavelength meter. An error in the database with regard to pressure broadening and shift is conceivable, as well.

Most notably, the absolute values of $\sigma_{wv}(R, \nu_{on})$, and the amplitudes of the fitted Voigt profiles, differ. On their own, the measurement values are lower at larger ranges R. It is unclear whether this is associated with the decreasing signal-to-noise ratio, or due to a variation of the atmospheric conditions. Due to the inverse proportionality of the (differential) absorption cross section to the number density of water vapor (see Equation 6.7), a variation of N_{wv} directly affects the absolute value of $\sigma_{wv}(R, \nu_{on})$. Consequently, if—contrary to the previously made assumption—the water-vapor number density changed along the measured line-of-sight, this would explain the different line strengths at the three ranges, $R = 0.45\,\mathrm{km}$, $R = 0.9\,\mathrm{km}$, and $R = 1.2\,\mathrm{km}$. Here, as for the humidity measurements with DIAL, Equation (2.12) holds for the relative error.

In comparison with the HITRAN spectrum, the following remarks are made. The calculation of the relative deviation of the fitted functions to the HITRAN curve is influenced by the above-mentioned stretching/shift on the frequency scale as well as the variation of the peak amplitude, and hence, only partially appropriate. Ignoring this, for the fitted function closest to the HITRAN spectrum ($R = 0.9\,\mathrm{km}$), the deviation was $< 5\,\%$ around the peak ($\nu = 366\,431.6\,\mathrm{GHz}$ to $366\,437.5\,\mathrm{GHz}$) and $\lesssim 10\,\%$ beyond that ($\nu < 366\,431.6\,\mathrm{GHz}$, and $\nu = 366\,437.5\,\mathrm{GHz}$ to $366\,438.5\,\mathrm{GHz}$). The section at the right was disregarded, because of the apparent frequency stretching/shift. Furthermore, on this side of the spectrum another absorption line exists (peak at $\nu \approx 366\,461\,\mathrm{GHz}$, amplitude $\approx 2.5 \times 10^{-27}\,\mathrm{m}^2$) which was not taken into account for the fit but could have an effect on the values. Finally, the use of the water vapor number density from the radiosonde involves its instrumental errors. The value of $N_{wv,rs}$ was determined from the radiosonde's measured variables T, and RH (see Appendix A.5). The latter are specified to have a total uncertainty in sounding of $\Delta T = \pm 0.5\,\mathrm{K}$, and $\Delta RH = \pm 5\,\%$. For the above-mentioned value of $N_{wv,rs}(0)$, this results in $\Delta N_{wv,rs}(0) = \pm 0.23 \times 10^{23}\,\mathrm{m}^{-3}$, and thus $\Delta N_{wv,rs}(0)/N_{wv,rs}(0) \approx \pm 11\,\%$. Within these considerations the fitted function from the measurement and the spectrum of the database are well in agreement.

The experimental determination of the absorption line with the tuning frequency method is also interesting for the study of the correction term K in the DIAL equation. The effect of K depends on the specific location of the online frequency relative to the peak of the absorption line, as detailed by SPÄTH [44, 50]. It is proportional to the second derivative of the absorption cross section with respect to the frequency. Figure 6.14 depicts $\mathrm{d}^2\sigma_{wv}/\mathrm{d}\nu^2$, calculated for the fitted curves of the measurement, and for the HITRAN spectrum. For the latter, a Savitzky–Golay smoothing filter (polynomial order 8, points of window 20) was included in the derivation procedure, because the low number of data points available from the database at this scale, would otherwise lead to oscillations in the result. The graph shows that the correction term changes its sign along the slope of the absorption line and vanishes at the inflection point of the slope. The observations made above, concerning the differences of the curves, apply also here. In this case, however, the precision of the absolute frequency is of more significance, since it decides at which value the zero crossings are.

In conclusion, the presented lidar operation with tuning laser frequency renders interesting possibilities for spectroscopic analyses of the atmosphere. It benefits from the remote and range-resolved sensing ability. The example of a DIAL measurement with tuning online frequency demonstrated the acquisition of a continuous section of the absorption spectrum. This technique has a particular advantage that the receiver consists of a typical DIAL detector, i.e., no sophisticated filters are needed. It offers the opportunity for comprehensive investigations related to the strength and shape of the absorption line with high resolution. Here, the first test

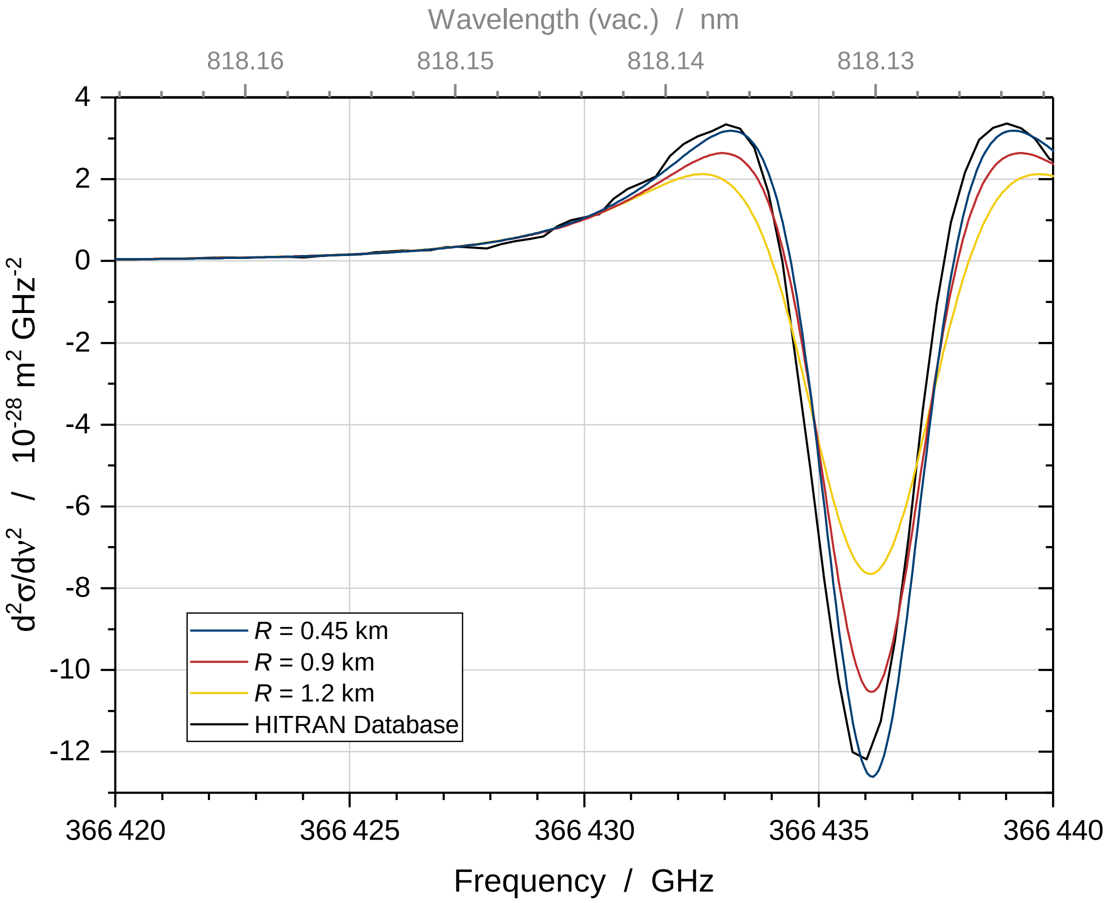

Figure 6.14: Second derivative of the absorption cross section with respect to the frequency for the fit functions and the HITRAN curve of Figure 6.13.

of concept and evaluation was introduced, the focus having been on the experimental feasibility. A further refined analysis and the application of a more precise spectral line shape function could increase the accuracy of the result. Potentially, atmospheric variables might be extracted from the measurement, as well, e.g., temperature [11, 190–192]. In combination with a second derivative analysis, the tuning measurement provides an experimental identification of frequency values where no or only minor corrections K of the DIAL equation in Schotland-approximation are necessary. The treated case indicated as well that within the mode-hop-free tuning range high and low absorption cross section values of water vapor are reached. Therefore, a DIAL operation with one sole diode laser as injection seeder is conceivable, rapidly tuning between a frequency at the slope (online) and a frequency at the wing (offline) of the same absorption line.

Other types of tuning measurements have already been accomplished. For instance, a DIAL observation similar to the one described, but with a vertical observation direction, is available. Measurements with the operation of a single diode laser were carried out as well. Then, Equation (6.6) could be applied for the evaluation. Furthermore, different tuning patterns were tested.

An operation that subsequently switched to five fixed frequencies on the slope of the absorption line was successfully realized with the driving function

$$\nu_{on}(t) = \nu_1 - \nu_{inc}\, \mathrm{trunc}\left[\frac{n}{2}\left\{\mathrm{triangle}\left(\frac{t}{T}\right) + 1\right\}\right], \tag{6.9}$$

a combination of a triangle wave and a truncation function. The first of the frequencies was set to $\nu_1 = 366\,436\,000\,\mathrm{MHz}$, i.e., on the absorption peak. The others were set to lower frequencies, equally spaced by $\nu_{inc} \approx 4000\,\mathrm{MHz}$. The publication presenting the complete results of these measurements is in preparation.

CHAPTER 7

Summary and Outlook

7.1 Summary

In this thesis, I reported on a new transmitter for a water-vapor differential absorption lidar. The transmitter is a pulsed Ti:sapphire laser system which is pumped with the second harmonic of a Nd:YAG master-oscillator power-amplifier, injection seeded alternately with two diode lasers, and actively frequency stabilized. The basic concept of the transmitter is based on the previous works [25, 26, 30, 31]. I developed the new laser system from the ground up, implementing significant changes and improvements in all of its essential components. I characterized the system and demonstrated an unprecedented performance. The transmitter is applied in the DIAL of the *University of Hohenheim*. The DIAL is mobile, ground-based, and able to capture the water-vapor field in the lower troposphere through scanning measurements. The performance of the transmitter enables humidity measurements with high spatial and temporal resolution as well as high accuracy.

As **pump source**, two Nd:YAG MOPAs of different manufacturers were consecutively used. The pump lasers were both custom-built according to the demands of the transmitter. They are fully diode-pumped, Q-switched, and frequency-doubled. I determined the relevant properties of these pump lasers. They were considerably enhanced compared to the pump source of the previous transmitter. This is particularly the case for the latest Nd:YAG MOPA, which achieved:

- A maximum average output power of $P_{532} = 63.2\,\mathrm{W}$ at $532\,\mathrm{nm}$, corresponding to a maximum pulse energy of $E_{532} = 211\,\mathrm{mJ}$ at $300\,\mathrm{Hz}$ pulse repetition rate. It can supply the Ti:sapphire laser with more than enough power for pumping.
- A beam profile close to a top-hat. As a consequence, the pumping efficiency is very high (see Ti:sapphire laser below).
- A more compact setup of the laser head, as well as a substantially reduced space and weight requirement of the control electronics. In addition, the electrical power consumption was decreased from approximately $10\,\mathrm{kW}$ to $4.2\,\mathrm{kW}$.

I also investigated other attributes like the long-term stability of the output power and the frequency, as these are of general interest for lidar transmitters.

The **injection seeding system**, originally presented in [112], had previously undergone experimental modifications [113], and was again substantially changed within this work. I replaced the previous diode lasers with commercially available, state-of-the-art ECDLs and drivers. I realized the frequency control with an analog output channel of the wavelength meter, rendering a faster and more precise regulation. Now, a 2x1-MEMS fiber switch alternately guides the laser light of the two fiber-coupled ECDLs to the Ti:sapphire laser setup, and hence acts as the online–offline switch. I analyzed the whole injection seeding path and optimized it to cause the least power losses possible while offering the flexibility to exchange parts when necessary. As a result:

- The frequency stability of the diode lasers is eminently improved. A long-term measurement of the diode laser stabilized to the online frequency yielded a standard deviation $\delta\nu < 1\,\mathrm{MHz}$. This is below the resolution limit of the wavelength meter, exploiting the highest accuracy of the device.
- More power for seeding the Ti:sapphire laser is now available. The power of the seed lasers measured directly in front of the Ti:sapphire laser resonator was between $P = 17\,\mathrm{mW}$ to $20\,\mathrm{mW}$.
- The fiber switch leads to perfectly coinciding beam profiles of the two ECDLs and exhibits a remarkably low crosstalk between their signals, $< (-61 \pm 4)\,\mathrm{dB}$. The switching speed is quick enough for the active stabilization of the laser resonator.
- The advanced frequency control features versatile tuning possibilities. In combination with the online–offline switch, even more options are available for varying the frequency of the Ti:sapphire laser pulses.

The **Ti:sapphire laser** is the main laser of the system. I realized the design and the setup of the laser in such manner that it meets the high energetic and spectral requirements of scanning water-vapor DIAL measurements in the lower troposphere. The development also takes efficiency and robustness into account, being of particular relevance for the application in a mobile lidar system. With the formalism of ray transfer matrices and Gaussian beams, I calculated the eigenmode of the laser resonator as a function of the thermal lens which arises in the titanium–sapphire crystal. I determined the point of dynamically stable operation for a resonator configuration without and with an additional compensating lens. As geometrical layout of the resonator, I chose a four-mirror, unidirectional-ring resonator in bow-tie arrangement. The core component is a cooling mount in which the laser crystal is housed. Within this work, different crystal cooling mounts were designed and manufactured at the institutes workshop. They were used and compared with respect to the thermal lens' focal length. The cavity is actively stabilized to the frequency of the injection seeder with the PDH technique. I implemented advanced optical and electronic components as well as an increased phase modulation frequency. I characterized the Ti:sapphire laser in detail, showing the attainment of a new performance level:

- Using a M^2 device, I carried out several measurement series of the thermal lens' focal length as function of the pump power. This enabled verifying and refining the theoretical calculations of the resonator design. For both cooling mount constructions (one with a circular-cut and another with a square-cut crystal shape) similar behavior was found.

- The Ti:sapphire laser delivers stable operation at high average output powers of up to $P = 10\,\mathrm{W}$ at $\lambda = 818\,\mathrm{nm}$. This corresponds to a pulse energy of $E = 33.\overline{3}\,\mathrm{mJ}$ at $300\,\mathrm{Hz}$ pulse repetition rate. The pulse duration is $\Delta t \approx 30\,\mathrm{ns}$. The highest average output power reached was $P_{max} = 11.8\,\mathrm{W}$ ($E_{max} = 39.\overline{3}\,\mathrm{mJ}$), representing the damage threshold of the laser at a modified configuration of the intracavity compensating lens.

- The input–output power curves yielded slope efficiencies from $\eta_{slope} = (66 \pm 8)\,\%$ to $(75 \pm 9)\,\%$ and optical conversion efficiencies from $\eta_{total} = 29\,\%$ to $35\,\%$ for the $10\,\mathrm{W}$ operation state.

- Single-frequency operation was achieved with a high frequency stability. The evaluation of long-term measurements with a wavelength meter, at $10\,\mathrm{W}$ average output power and frequency-locked operation, gave a standard deviation of $\delta\nu < 1\,\mathrm{MHz}$ at constant frequency operation, and $\delta\nu < 2\,\mathrm{MHz}$ at alternating online–offline frequency switching. Both values are below the resolution limit of the measuring device. The frequency behavior closely follows the frequency of the injection seeder. The linewidth also remains permanently below the resolution limit of the wavelength meter, $\Delta\nu < 63\,\mathrm{MHz}$.

- The laser operates in the Gaussian mode, TEM_{00}. The beam exhibits an astigmatism due to the different focal lengths of the thermal lens in the tangential and the sagittal plane. This is largely compensated with the cylindrical lens, operating the laser close to the dynamically stable operation. At $P = 10\,\mathrm{W}$, the beam quality factors were $M_x^2 = 1.06 \pm 0.06$ and $M_y^2 = 1.02 \pm 0.06$.

- The Ti:sapphire laser is flexible with regard to its emission wavelength. Alternate switching between two different frequencies is implemented by virtue of the DIAL principle. Additionally, continuous tuning of the frequency is possible and various tuning patterns can be programmed.

- During DIAL measurements, the laser endured numerous hours of operation without damage, including two cases of uninterrupted operation for over $31\,\mathrm{hours}$.

The achievement of this performance, especially at the power level of $P = 10\,\mathrm{W}$, was a long-term goal in the application of ground-based scanning water-vapor DIAL as well as space-borne systems. Table 7.1 lists the essential parameters in comparison to the requirements discussed in Chapter 2.2.1.

The Ti:sapphire laser system acts as **transmitter of the water-vapor DIAL** of the *University of Hohenheim*. The laser system was installed in the DIAL at early stage. Thus, it already came into operation for DIAL measurements while being developed. Operating this transmitter in the Hohenheim-DIAL, I participated in many field campaigns (national and international). The humidity measurements that we gained provided important insight into the highly variable lower troposphere, especially the atmospheric boundary layer (ABL) and its interaction with

Parameter	**Symbol**	**Requirement**	**This System**	**(Page)**
Wavelength (vac.)	λ	720–730 nm 815–825 nm 925–945 nm 1400–1500 nm	818 nm	
Average output power	P	10 W	10 W	(124 *ff.*)
Repetition rate	f_{rep}	100–1000 Hz	300 Hz	(124)
Pulse energy	E	100–10 mJ	$33.\overline{3}$ mJ	(124 *ff.*)
Pulse duration (FWHM)	Δt	$\lesssim 200\,\mathrm{ns}$	$\approx 30\,\mathrm{ns}$	(128 *f.*)
Bandwidth (FWHM)	$\Delta\nu$	$< 390\,\mathrm{MHz}$	$< 63\,\mathrm{MHz}^{r}$	(133)
Frequency stability (1σ)	$\delta\nu$	$< 210\,\mathrm{MHz}$	$< 2\,\mathrm{MHz}^{r,i}$	(138)
Spectral purity	SP	$> 99.5\,\%$	$\geq 99.97\,\%^{r}$	(162 *ff.*)
Tunability, coarse		$\approx$ 1–3 nm	$-4\,/\,+12\,\mathrm{nm}^{i}$	(62)
Tunability, fine (mode-hop free)		$\gtrsim 20\,\mathrm{GHz}$	$\approx 20\,\mathrm{GHz}^{i}$	(62)
Energy stability (pulse to pulse)	ΔE	$\gtrsim 96\,\%$	$\geq 99.3\,\%$	(128)
Conversion efficiency (opt.–opt.)	η_{total}	$\gtrsim 20\,\%$	29–35 %	(126)
Linear polarization ratio		$\gtrsim 99\,\%$	$> 99.97\,\%$	(130)
Beam quality	M^2	$\lesssim 2$	≤ 1.06	(142)
Beam divergence	θ	$\lesssim 1\,\mathrm{mrad}$	0.45 mrad	(143)
Pointing stability	$\Delta\theta$	$\lesssim 10\,\mu\mathrm{rad}$	$\leq 3\,\mu\mathrm{rad}$	(142)
Annotations:	i: imposed by injection seeder r: resolution limit of characterizing instrument or method			

Table 7.1: Requirements for a laser transmitter of a (ground-based) water-vapor DIAL and achieved performance of the Ti:sapphire laser system developed within this work. The system fulfills all requirements, even the higher frequency specifications of a space-borne platform (cf. Table 2.1). Page numbers refer to text passages where the results are discussed.

land surface (see Chapter 6 for references). The measurements also contributed to further studies, incorporating model simulations. In this thesis, the following atmospheric measurements were presented and analyzed.

- For the first time, water-vapor DIAL measurements with 10 W laser operation were carried out. The laser light was directed into the atmosphere on a free-beam path, conducting the observations in vertical pointing mode. The performance of the laser transmitter allowed for high temporal and spatial resolution (e.g., $\Delta t = 1\,\mathrm{s}$ and $\Delta R \approx 37.5\,\mathrm{m}$, respectively) of the humidity field, revealing fine details at the top of the atmospheric boundary layer. The systematic error was estimated to be $< 1\,\%$. A noise error analysis of the atmospheric measurement showed that the statistical uncertainty was $\lesssim 2\,\%$ in the ABL and $< 5\,\%$ up to a height of 2 km for a resolution of $\Delta t = 10\,\mathrm{s}$, $\Delta R = 67.5\,\mathrm{m}$.

- Two humidity measurement examples in scanning mode with the Hohenheim-DIAL and the new transmitter were shown, since this type of measurement is one of the main interests of the *Institute of Physics and Meteorology*. The surface layer scan revealed complex structures of lower moisture shifting away during the measurement.

- The spectral purity of the laser was assessed by pointing on a hard target and on a distant cloud, quantifying the proportion of the desired radiation at the seed laser frequency against the (total) power spectrum. The obtained values of spectral purity were $> 99.98\,\%$ for the more reliable hard target measurements and $\geq 99.97\,\%$ for the cloud measurement. Therefore, the requirements for a ground-based and even a space-borne water-vapor DIAL are fulfilled.

- Furthermore, I worked on a special measurement type, for which the frequency of the laser was tuned during operation. In analogy to the approach of the DIAL equation, an expression for the frequency dependence of the absorption in the atmosphere was derived. I discussed in detail a measurement where the online frequency was continuously tuned with a triangular function while the offline frequency remained constant. The evaluation of the resulting absorption cross section and its second derivative allowed a spectroscopic analysis of the atmosphere, exhibiting very good agreement with the spectrum of the database HITRAN (≈ 5–$10\,\%$ deviation in the absorption cross-section's absolute value).

7.2 Outlook

The presented work has resulted in significant progress of the water-vapor DIAL of the *University of Hohenheim*. In the following, a few remaining tasks and some ideas for future development are discussed. The issues are structured according to the main components of the system.

For the pump laser, a control software facilitating the routine operation of the laser is essential. The start-up and shutdown procedures are time-consuming and need permanent attention of the operator. If these procedures could be automated, this would be a considerable relief. Likewise, the logging of power values, beam profiles, etc. has to be improved. Increasing the performance stability and the robustness of the device would also be desirable. This refers, in particular, to the gradually falling output power. A more compact development of the pump laser could be contemplated at a later stage. Since for the 10 W operation of the Ti:sapphire laser less than the full output power of the current pump laser is sufficient, a MOPA setup with a single pump chamber in the amplifying stage is conceivable. However, the top-hat beam profile must be maintained so as not to reduce the pumping efficiency. Other laser types (e.g., green laser diodes) as pump source might be an option as soon as they become available.

In the case of the injection seeding system, the next step should introduce a *LabVIEW* program automatically switching between the monitoring signals of the two ECDLs and the HeNe laser for the wavelength meter. This would allow to actively stabilize the offline-frequency ECDL as well, and to undertake the calibration with the HeNe laser at regular intervals. The second analog regulation output for the wavelength meter was already retrofitted. Later on, this program could be extended by a routine that systematically adapts the set values for the frequencies by feedback from the real-time DIAL measurements. This requires a more extensive programming effort due to an implementation of the code in, both, the software for the injection seeder and for the data acquisition, as well as the communication between both. Besides, for long time periods, the single-frequency operation of the diode lasers, especially the mode-hop-free tuning, requires human involvement (setting and verifying of a suitable pair of values for the current and the temperature). Regarding the further development of the hardware, more laser power for seeding would only be relevant if an even higher power level of the Ti:sapphire laser is to be reached. The limitation by the damage threshold of the fiber switch could be overcome by a new model. Such a model could also enhance its lifetime (i.e., an increased number of switching cycles) and reduce the insertion losses. At the moment, however, it seems that the technical progress stagnates. Overall, the injection seeding beam path has almost completely been optimized in terms of power losses. Nevertheless, there might be room for improvement in the mating sleeves for the fiber connections.

The Ti:sapphire laser has attained a high performance level combined with stable operation demanding only a few interventions. The servo controller of the active frequency stabilization needs to be resetted manually from time to time, when the correction signal for the piezo actuator reaches the regulation bound. The large dislocation of the piezo from its central position is accompanied by a horizontal movement of the laser beam mode, and thus, leads to a small decrease of the output power. A solution could be to control the servo device with a computer and a software that automatically resets the correction signal before the regulation bounds are reached or if the deviation becomes too large. On the other hand, it was found that the correction signal predominantly drifted in one direction, being related to a progressively rising temperature in the trailer (laboratory) after the devices are turned on. Therefore, —to address the cause of the problem—either the entire Ti:sapphire laser would have to be installed in an actively temperature-stabilized casing, or the temperature stability of the trailer's air-conditioning would have to be improved.

There are a few more general suggestions for the further development of the Ti:sapphire laser. A software which regularly logs all instruments monitoring the performance of the laser and which disables the laser in case of malfunction would simplify (long-term) operation. It would be interesting to investigate the exchange or even the omission of intra-cavity elements in the Ti:sapphire laser. The birefringent filter is most likely indispensable, but it should be replaced with a new one, specifically designed for the operation wavelength around $818\,\mathrm{nm}$. As was shown, the existing birefringent filter is not entirely ideal for this wavelength region. At higher laser powers or lower seed powers, this would put the good spectral properties of the laser at risk. The Faraday rotator and the half-wave plate ensure the unidirectional laser emission. If sufficient and permanently present injection seeding is guaranteed, it could be tested whether these elements can be eliminated from the resonator. The advantage of these measures would consist in lower losses in the cavity and hence a more efficient laser operation, as well as less risk of damage in the resonator. Instead of the concave cylindrical lens, a suitable optical material with negative thermo-optic coefficient $\mathrm{d}n/\mathrm{d}T$ could be used to compensate the thermal lens [193]. This would lead to a completely different dynamic behavior, potentially offering stable laser operation at a larger pump power range, equal eigenmode sizes for tangential and sagittal plane, and perhaps even higher output powers.

Although a high average output power has been achieved, it is worth considering how this could still be increased. With an output coupler mirror of moderately reduced reflectivity (e.g., $R = 55\,\%$ or $50\,\%$) more laser power from inside of the cavity could be extracted. Simultaneously, the power load on the intracavity elements would be relieved, allowing an increase of the power level. Of course, this approach is at the expense of the pumping efficiency. From the results of the input–output power measurements, it can be assumed that the limitation by optical damage of the laser is associated to the pulse energy rather than to the average power. Consequently, the Ti:sapphire laser resonator could withstand the operation at a higher average power if the same pulse energy, but a higher pulse repetition rate would be given. Then, all other devices of the DIAL would have to support the higher pulse repetition rate, which could also pose a challenge. Besides, since the pump laser already provides more power than needed, the power sent into the atmosphere could be increased in a quite simple way, by implementing a second Ti:sapphire laser resonator in the system. Here, the issues consist in timing the laser pulses adequately and in the additional operator effort. Other laser resonator configurations (e.g., with two laser crystals or a magnifying telescope to increase the mode volume) or an additional power-amplifying stage are conceivable, as well. Such concepts potentially require a completely new design and setup of the laser and would be projects for a more distant future.

Concerning the special atmospheric measurements presented in Chapter 6, it would already be of interest to extend them. To determine the spectral purity to more decimal places, more and longer measurements on a distant, well-defined, and constant hard target are necessary. The frequency tuning measurements should be repeated and studied closer, in comparison to the available measurements and spectroscopic databases. The application of other tuning patterns should also be elaborated.

In conclusion, I recommend to concentrate on the tasks enabling a long-term operation of a laser system less dependent on human intervention, for which the above-mentioned software developments are the major factor. The experimental activities on the transmitter should ideally be carried out on a second test system. The hardware development of the Hohenheim-DIAL that is most urgent at the moment, however, is the beam path directing the laser light to the scanner and finally into the atmosphere. The current setup asks for a fiber which is capable to guide the entire output power of the transmitter without getting damaged or occurring inconvenient side-effects as stimulated Brillouin scattering. Alternatively, a sophisticated arrangement of a free-beam path for the scanner could be possible.

Appendices

APPENDIX **A**

Theoretical Notes

A.1 General Eigenmode Solution

In the following, the derivation of Equations (5.9) to (5.12) in Chapter 5.2.1 is described in more detail [58, 136]. When a Gaussian beam propagates through optical structures, defined by an $ABCD$ matrix (Equation 5.3), the complex beam parameter q (Equation 5.4) transforms according to

$$q_2 = \frac{A\, q_1 + B}{C\, q_1 + D}\,, \tag{A.1}$$

where q_1 and q_2 represent the situation before and after the transformation, respectively. In a resonator, after one round trip, self-consistency of the beam requires $q_2 \overset{!}{=} q_1 =: q$. Solving the $ABCD$ law (A.1) for q yields

$$\frac{1}{q_\pm} = -\frac{(A-D)}{2B} \pm i\, \frac{1}{2B}\sqrt{-(A-D)^2 - 4BC}\,. \tag{A.2}$$

By comparing the real and the imaginary part of Equation (5.4) with this equation it is possible to assign

$$R(z) = -\frac{2B}{(A-D)}\,, \tag{A.3}$$

and

$$w(z)^2 = -\frac{\lambda}{\pi}\, \frac{1}{\pm\frac{1}{2B}\sqrt{-(A-D)^2 - 4BC}}\,. \tag{A.4}$$

The term under the square root must be nonnegative to get real solutions, or

$$(A-D)^2 + 4BC \overset{!}{<} 0\,. \tag{A.5}$$

For the beam parameters z and w_0, it is advantageous to find an expression similar to Equations (5.5) and (5.6). First, the combination of the latter two gives

$$\frac{\lambda\,R}{\pi\,w^2} = \frac{\pi\,{w_0}^2}{\lambda\,z} \tag{A.6}$$

$$= \frac{z_R}{z}\;. \tag{A.7}$$

Then, rearranging Equation (5.5) for z, Equation (5.6) for w_0, and using (A.7) leads to

$$z = R\,\frac{1}{1+\left(\frac{\lambda\,R}{\pi\,w^2}\right)^2} \tag{A.8}$$

$${w_0}^2 = w^2\,\frac{1}{1+\left(\frac{\pi\,w^2}{\lambda\,R}\right)^2}\;. \tag{A.9}$$

Now, inserting Equations (A.3) and (A.4) into Equations (A.8) and (A.9) results in

$${w_0}^2 = \mp\frac{\lambda}{\pi}\,\frac{\sqrt{(A-D)^2+4BC}}{-2C}\;, \tag{A.10}$$

and

$$z = \frac{A-D}{2C}\;. \tag{A.11}$$

The determinant of a ray transfer matrix is generally unity, $AD-BC=1$. The condition allows to rewrite the square root term (A.5),

$$-\left(A-D\right)^2-4BC = \cdots = 4-\left(A+D\right)\;. \tag{A.12}$$

With this, also Equations (A.4) and (A.10) are rewritten, and finally, Equations (5.9) to (5.12) are obtained.

A.2 Ray Transfer Matrices

The ray transfer matrix of a (thin) lens of focal length f is

$$\mathbf{M}_f = \begin{pmatrix} 1 & 0 \\ -\frac{1}{f} & 1 \end{pmatrix}. \tag{A.13}$$

The matrix for a propagation in free space of length L (optical, i.e., effective length) is

$$\mathbf{M}_L = \begin{pmatrix} 1 & L \\ 0 & 1 \end{pmatrix}. \tag{A.14}$$

The total matrix for a transfer through, first, a lens, and then, free space (see Figure 5.3 on page 87) is calculated by

$$\mathbf{M}_{\mathit{tot1}} = \mathbf{M}_L\, \mathbf{M}_f = \begin{pmatrix} 1-\frac{L}{f} & L \\ -\frac{1}{f} & 1 \end{pmatrix}. \tag{A.15}$$

This matrix corresponds to, e.g., a ring resonator with planar mirrors and one lens.

The total matrix for a transfer through a lens of focal length f_1, free space of length L_1, a second lens of focal length f_2, and free space of length L_2 (see Figure 5.5 on page 90) is calculated by

$$\mathbf{M}_{\mathit{tot2}} = \mathbf{M}_{L_2}\, \mathbf{M}_{f_2}\, \mathbf{M}_{L_1}\, \mathbf{M}_{f_1} \tag{A.16}$$

$$= \begin{pmatrix} 1-\frac{L_1+L_2}{f_1}-\frac{L_2}{f_2}+\frac{L_1\,L_2}{f_1\,f_2} & L_1+L_2-\frac{L_1\,L_2}{f_2} \\ -\frac{1}{f_1}-\frac{1}{f_2}+\frac{L_1}{f_1\,f_2} & 1-\frac{L_1}{f_2} \end{pmatrix}. \tag{A.17}$$

This matrix corresponds to, e.g., a ring resonator with planar mirrors and two lenses. The total length of the resonator is $L = L_1 + L_2$.

A.3 Eigenmode Solution for a Resonator with Two Lenses

The situation may be as described in the subsection *Ring Resonator with Two Lenses* of Chapter 5.2.1 (page 90). Using the items $ABCD$ of the matrix $\mathbf{M}_{tot2}$, and inserting them into Equations (5.9) to (5.12) yields

$$R = \frac{-\frac{L_1 - L_2}{f_2} + \frac{L_2 + L_1\left(1 - \frac{L_2}{f_2}\right)}{f_1}}{2\left(L_2 + L_1\left(1 - \frac{L_2}{f_2}\right)\right)}\,, \tag{A.18}$$

$$w^2 = \frac{\lambda}{\pi}\,\frac{2\left(L_2 + L_1\left(1 - \frac{L_2}{f_2}\right)\right)}{\sqrt{4 - \left(2 - \frac{L_1 + L_2}{f_2} - \frac{L_2 + L_1\left(1 - \frac{L_2}{f_2}\right)}{f_1}\right)^2}}\,, \tag{A.19}$$

$$z = \frac{-\frac{L_1 - L_2}{f_2} + \frac{L_2 + L_1\left(1 - \frac{L_2}{f_2}\right)}{f_1}}{2\left(\frac{1}{f_2} + \frac{1 - \frac{L_1}{f_2}}{f_1}\right)}\,, \tag{A.20}$$

$${w_0}^2 = \frac{\lambda}{\pi}\,\frac{\sqrt{4 - \left(2 - \frac{L_1 + L_2}{f_2} - \frac{L_2 + L_1\left(1 - \frac{L_2}{f_2}\right)}{f_1}\right)^2}}{2\left(\frac{1}{f_2} + \frac{1 - \frac{L_1}{f_2}}{f_1}\right)}\,. \tag{A.21}$$

A.4 Transmission through the Four-Mirror Ring-Cavity

When light is injected (in one direction) into a four-mirror ring-cavity, there are four beam paths leaving the cavity. Let mirror number 1 be the mirror through which the light is injected (e.g., the output coupler of the laser resonator). At this mirror, the incident electromagnetic wave is partially reflected and superimposed with the transmitted fractions (see Chapter 5.6.2; page 111 *f*). For the remaining mirrors (2, 3, and 4), the exiting beams are superpositions of the transmitted fractions merely. The complex amplitude of the transmitted electromagnetic wave $E_{t,n}$ at each mirror ($n = 2, 3, 4$) can be expressed by the incident wave E_i.

$$E_{t,n} = t_{\mathit{ring},n}(\omega)\, E_i \;, \tag{A.22}$$

where the complex transmission coefficient of the cavity, t_{ring}, differs,

$$t_{\mathit{ring},2}(\omega) = t_1\, t_2\, e^{-i\omega L_{12}/c}\, Q \;, \tag{A.23}$$

$$t_{\mathit{ring},3}(\omega) = -t_1\, t_3\, r_2\, e^{-i\omega (L_{12}+L_{23})/c}\, Q \;, \tag{A.24}$$

$$t_{\mathit{ring},4}(\omega) = t_1\, t_4\, r_2\, r_3\, e^{-i\omega (L_{12}+L_{23}+L_{34})/c}\, Q \;. \tag{A.25}$$

with the abbreviation

$$Q = \frac{1}{1 - r_1\, r_2\, r_3\, r_4\, e^{-i\omega L/c}} \tag{A.26}$$

$$= \frac{1 - r_1\, r_2\, r_3\, r_4\, e^{+i\omega L/c}}{1 + r_1^2\, r_2^2\, r_3^2\, r_4^2 - 2\, r_1\, r_2\, r_3\, r_4\, \cos\left(\omega L/c\right)} \;. \tag{A.27}$$

The mirror's amplitude reflection coefficients and amplitude transmission coefficients are given by r_1, r_2, r_3, r_4, and t_1, t_2, t_3, t_4, respectively. The lengths L_{12}, L_{23}, L_{34}, and L_{41} are the distances between the corresponding mirrors of the ring cavity. Hence, $L = L_{12} + L_{23} + L_{34} + L_{41}$ is the total length. The result is a function of the laser frequency $\omega = 2\pi\nu$. The transmitted intensities are $I_t \propto E_t E_t^*$.

A.5 Calculation of Water-Vapor Quantities

The number density of water vapor (total number of water molecules per volume) N_{wv}, is calculated from the absolute humidity (mass of water vapor per volume) ρ_{wv} by

$$N_{wv} = \frac{1}{m_{H_2O}} \rho_{wv} \,, \tag{A.28}$$

where m_{H_2O} is the molecular mass of water.

The absolute humidity is determined by the ideal gas law in the form

$$\rho_{wv} = \frac{e_{wv}}{R_{wv} T} \tag{A.29}$$

$$= \frac{m_{H_2O}\, e_{wv}}{k_B\, T} \,, \tag{A.30}$$

where e_{wv} is the vapor pressure of water, R_{wv} the specific gas constant of water vapor ($R_{wv} = R/M_{wv} = k_B\, N_A/M_{wv} = k_B/m_{H_2O}$), T the temperature, and k_B the Boltzmann constant.

The relative humidity RH (in $\%$) is the ratio of the vapor pressure e_{wv}, and the saturation vapor pressure E_{wv},

$$RH = \frac{e_{wv}}{E_{wv}}\, 100 \,. \tag{A.31}$$

The saturation vapor pressure E_{wv} depends on the temperature. It can be calculated with approximation formulas, e.g., the Magnus equation,

$$E_{wv} = E_0 \exp\left(\frac{C_1\, \vartheta}{C_2 + \vartheta} \right) , \tag{A.32}$$

with the temperature ϑ in °C, and $E_0 = 6.112\,\mathrm{hPa}$, $C_1 = 17.12$, $C_2 = 243.12\,°\mathrm{C}$ [194].

The combination of Equations (A.28) to (A.32) yields

$$N_{wv} = \frac{1}{k_B\, T} \frac{RH}{100} E_0 \exp\left(\frac{C_1\, \vartheta}{C_2 + \vartheta} \right) . \tag{A.33}$$

Use $\vartheta = (T - 273.15\,\mathrm{K})\, \frac{°\mathrm{C}}{\mathrm{K}}$.

If temperature and relative humidity are obtained from a measurement with respective errors, ΔRH and ΔT, then the error of the water-vapor number density is

$$\Delta N_{wv} = N_{wv} \left[\left(\frac{\Delta RH}{RH} \right)^2 + \left(\Delta T \left\{ \frac{C_1\, C_2\, \frac{\mathrm{K}}{°\mathrm{C}}}{(T - C_3)^2} - \frac{1}{T} \right\} \right)^2 \right]^{1/2} , \tag{A.34}$$

where $C_3 = (273.15\,\mathrm{K} - C_2\, \frac{\mathrm{K}}{°\mathrm{C}}) = 30.03\,\mathrm{K}$.

APPENDIX **B**

Supplementary Results

B.1 M^2 Analysis

Table B.1 lists the results for the M^2 measurement discussed at the end of Chapter 5.7.4.

P	P_{532}	M_x^2	M_y^2	$w_{0,x}$	$w_{0,y}$	θ_x	θ_y	z_x	z_y
W	W	–	–	mm	mm	mrad	mrad	mm	mm
4.8	21.7	1.19	1.03	0.56	0.69	0.56	0.39	1853 ± 408	400 ± 234
6.3	23.9	1.06	1.03	0.57	0.66	0.49	0.40	1758 ± 397	303 ± 222
7.4	25.8	1.09	1.02	0.60	0.65	0.47	0.41	1566 ± 374	283 ± 220
9.0	27.7	1.07	1.02	0.63	0.62	0.44	0.43	1224 ± 333	234 ± 214
10.3	29.8	1.06	1.02	0.61	0.59	0.45	0.45	974 ± 303	233 ± 214
10.2	29.6	1.05	1.02	0.60	0.59	0.45	0.45	883 ± 292	233 ± 214
7.9	25.7	1.07	1.02	0.60	0.63	0.47	0.42	1398 ± 354	267 ± 218
4.8	21.6	1.08	1.02	0.53	0.67	0.54	0.40	1824 ± 405	385 ± 232
2.3	17.8	1.10	1.04	0.48	0.68	0.61	0.39	1899 ± 414	477 ± 243

Table B.1: Results from the M^2 analysis of the Ti:sapphire laser as function of its output power P or pump power P_{532}. Two measurement series were carried out: increasing, and decreasing power. The parameters are explained in Chapter 5.7.4. The accuracy for the not explicitly stated cases is 5 %.

B.2 Online Frequency Tuning

The fits in Chapter 6.2.2 (plotted in Figure 6.13) were carried out with a software[1]. The function used is a Voigt profile,

$$\begin{aligned} y &= y_0 + (f_G * f_L)(x) \\ &= y_0 + \int_{-\infty}^{\infty} f_G(u)\, f_L(x-u)\, \mathrm{d}u\,, \end{aligned} \tag{B.1}$$

which is a convolution of a Gaussian function $f_G(x)$, and a Lorentzian function $f_L(x)$,

$$f_G(x) = \sqrt{\frac{4\ln 2}{\pi}}\,\frac{1}{w_G}\, e^{-4\ln 2\,\frac{x^2}{w_G{}^2}}\,, \tag{B.2}$$

$$f_L(x) = \frac{2A}{\pi}\,\frac{w_L}{4(x-x_c)^2 + w_L{}^2}\,. \tag{B.3}$$

In the equations, y_0 is the offset, w_G and w_L are the full width at half maximum of the Gaussian and the Lorentzian function, respectively, x_c is the center location, as well as A the area. Hence,

$$y = y_0 + A\,\frac{2\ln 2}{\pi^{3/2}}\,\frac{w_L}{w_G{}^2}\int_{-\infty}^{\infty}\frac{e^{-v^2}}{\left(\sqrt{\ln 2}\,\frac{w_L}{w_G}\right)^2 + \left(\sqrt{4\ln 2}\,\frac{x-x_c}{w_G} - v\right)^2}\,\mathrm{d}v\,. \tag{B.4}$$

It is assigned $x := \nu_{on}$, and $y := \sigma_{wv}(R, \nu_{on})$. The Gaussian width w_G is related to Doppler broadening, and the Lorentzian width w_L is related to collision broadening. The full width at half maximum of the Voigt profile w_V can be derived via $w_V \approx 0.5346\, w_L + \sqrt{0.2166\, w_L{}^2 + w_G{}^2}$.

For the fit, the parameters were initialized each time with the values: $y_0 = 6 \times 10^{-29}\,\mathrm{m}^2$, $x_c = 366\,436\,\mathrm{GHz}$, $A = 5.4 \times 10^{-26}\,\mathrm{m}^2\,\mathrm{GHz}$, $w_G = 1\,\mathrm{GHz}$, and $w_L = 6\,\mathrm{GHz}$. Table B.2 lists the fit results of the parameters, for the three time series at different range R.

Fit Parameter	**Range of Data Extraction** $R = 0.45\,\mathrm{km}$	 $R = 0.9\,\mathrm{km}$	 $R = 1.2\,\mathrm{km}$
y_0 (m^2)	$(6.45 \pm 0.93) \times 10^{-29}$	$(4.44 \pm 0.95) \times 10^{-29}$	$(3.13 \pm 3.16) \times 10^{-29}$
x_c (GHz)	$366\,436.14 \pm 2.41$	$366\,436.13 \pm 3.05$	$366\,436.10 \pm 6.83$
A (m^2 GHz)	$(5.37 \pm 0.69) \times 10^{-26}$	$(5.30 \pm 0.85) \times 10^{-26}$	$(5.13 \pm 1.86) \times 10^{-26}$
w_G (GHz)	0.41 ± 0.39	$(0.00 \pm 1.06) \times 10^{-4}$	1.65 ± 0.49
w_L (GHz)	5.97 ± 0.06	6.35 ± 0.04	6.45 ± 0.27

Table B.2: Fit results of the parameters of the function (B.4).

---

[1] *OriginLab*, OriginPro 2017G SR2

APPENDIX **C**

Technical Drawings

The following pictures show the CAD model of the Ti:sapphire laser and drawings of the clamp shells of the circular-cut and the square-cut crystal cooling mount versions. The model and drawings were created with the software *Autodesk Inventor*. For many commercial parts, the CAD model could be downloaded from the manufacturer's website. The remaining parts and the in-house developments (especially the cooling mounts) were own modeling work. It should be noted that the depicted CAD model is not a complete representation of the real setup. For instance, the laser case was modeled, but omitted in the pictures for the sake of clarity. Only the main laser beams were illustrated. Optical fibers, cables, and water tubes were not implemented. The empty areas close to the injection seeding path were previously required for the alternative online–offline switch (electro-optic deflector) arrangement. For the drawings, only the essential dimensions were included.

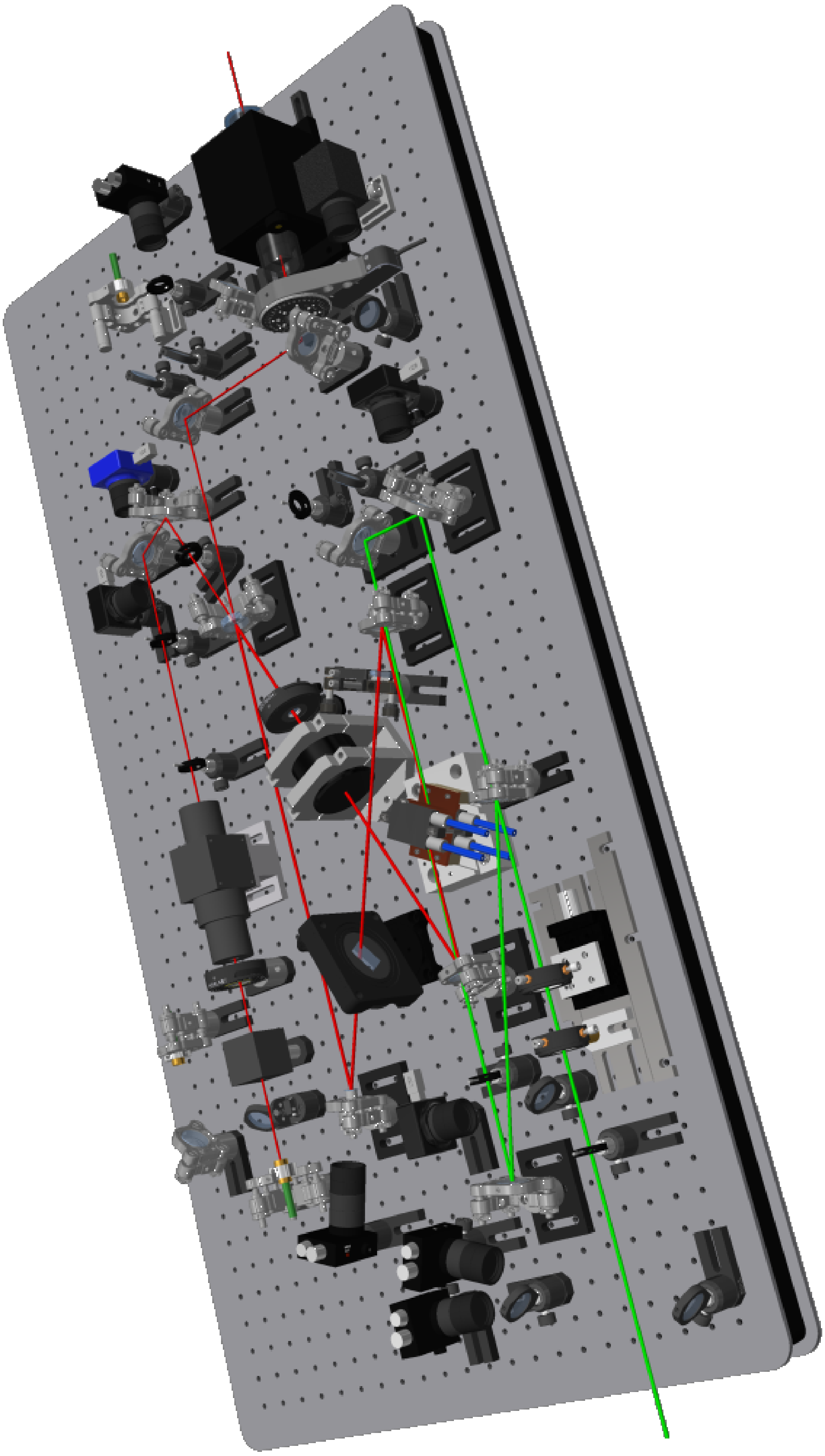

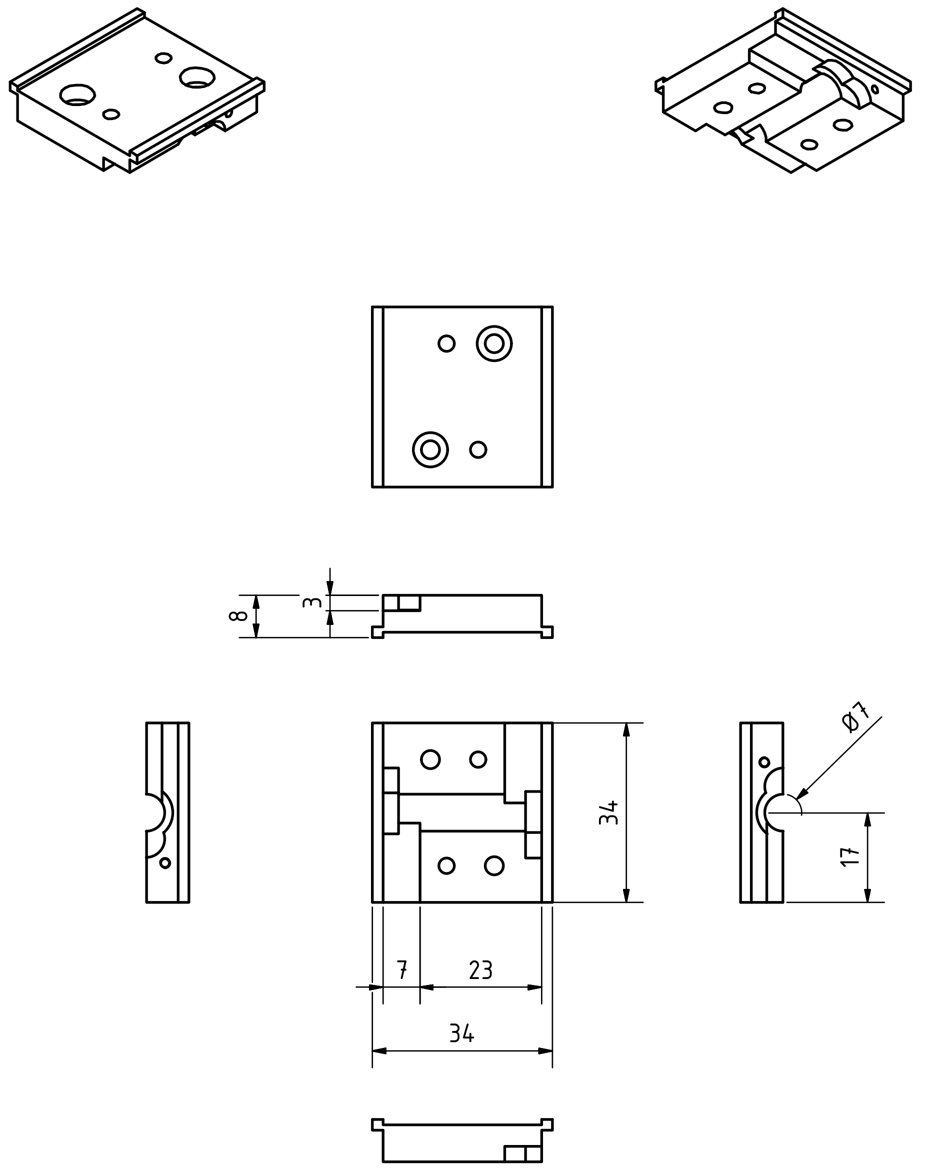

For Information Only Not For Manufacturing Purposes		Sizes in mm	University of Hohenheim	Institute of Physics and Meteorology
			Circular-cut Crystal Cooling Mount	
	Date	Name	Clamp Shell - Top	
Author		S. Metzendorf		
Norm				
	© 2018			

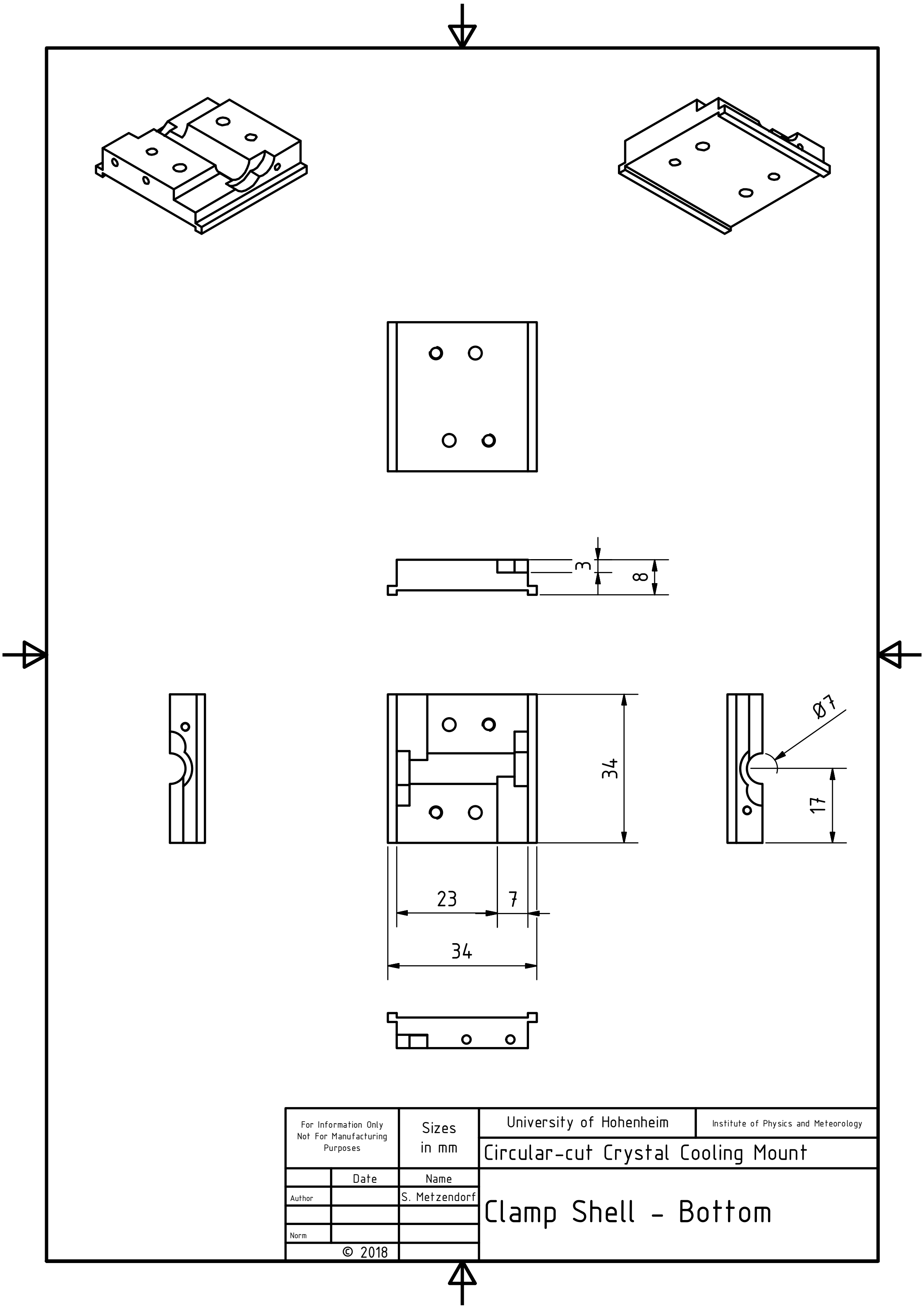
3
8
34
Ø7
17
23
7
34
For Information Only
Not For Manufacturing
Purposes
Sizes
in mm
University of Hohenheim
Institute of Physics and Meteorology
Circular-cut Crystal Cooling Mount
Date
Name
Author
S. Metzendorf
Clamp Shell - Bottom
Norm
© 2018

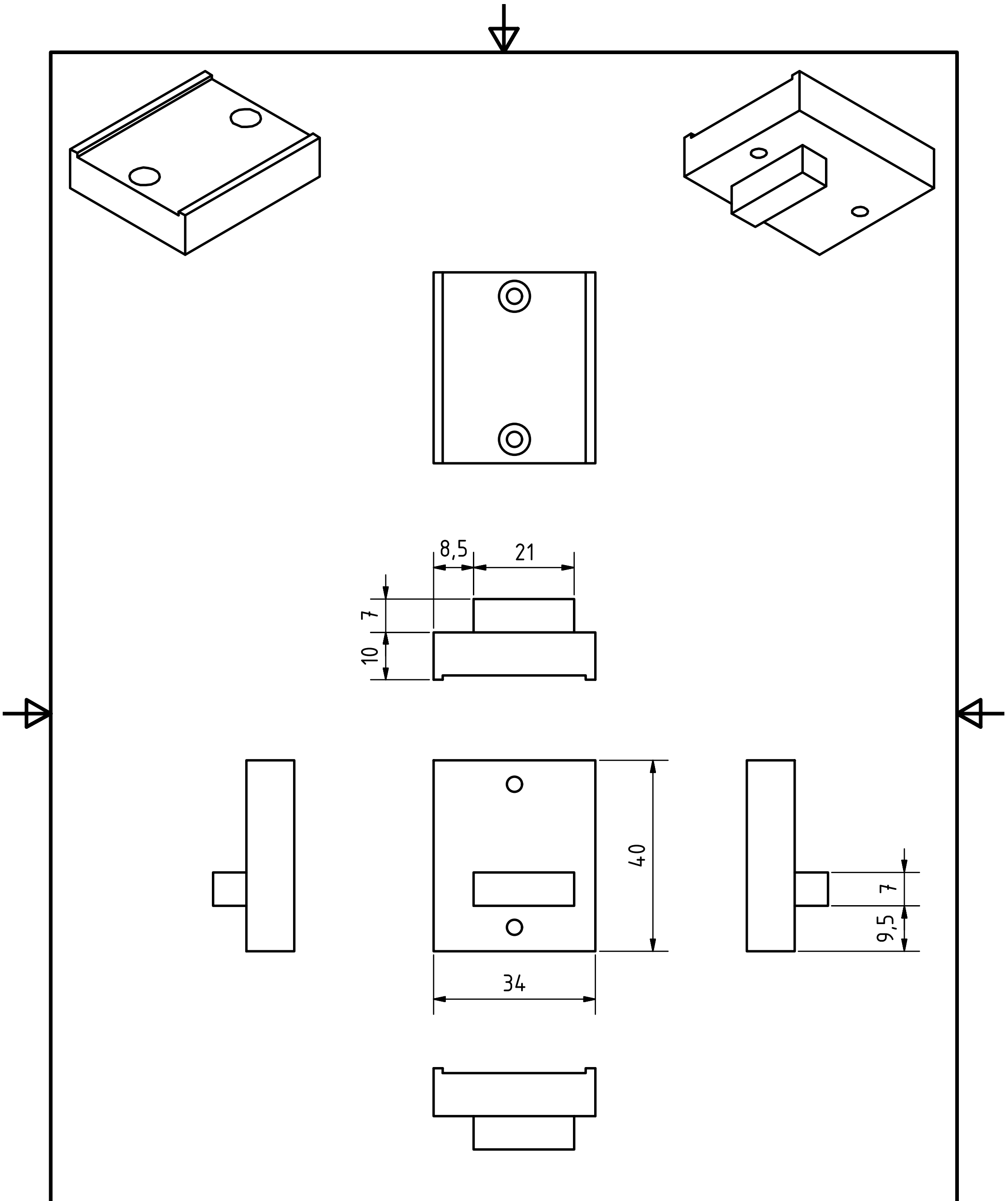

For Information Only Not For Manufacturing Purposes	Sizes in mm	University of Hohenheim	Institute of Physics and Meteorology
		Square-cut Crystal Cooling Mount	
	Date	Name	Clamp Shell - Top
Author		S. Metzendorf	
Norm			
© 2018			

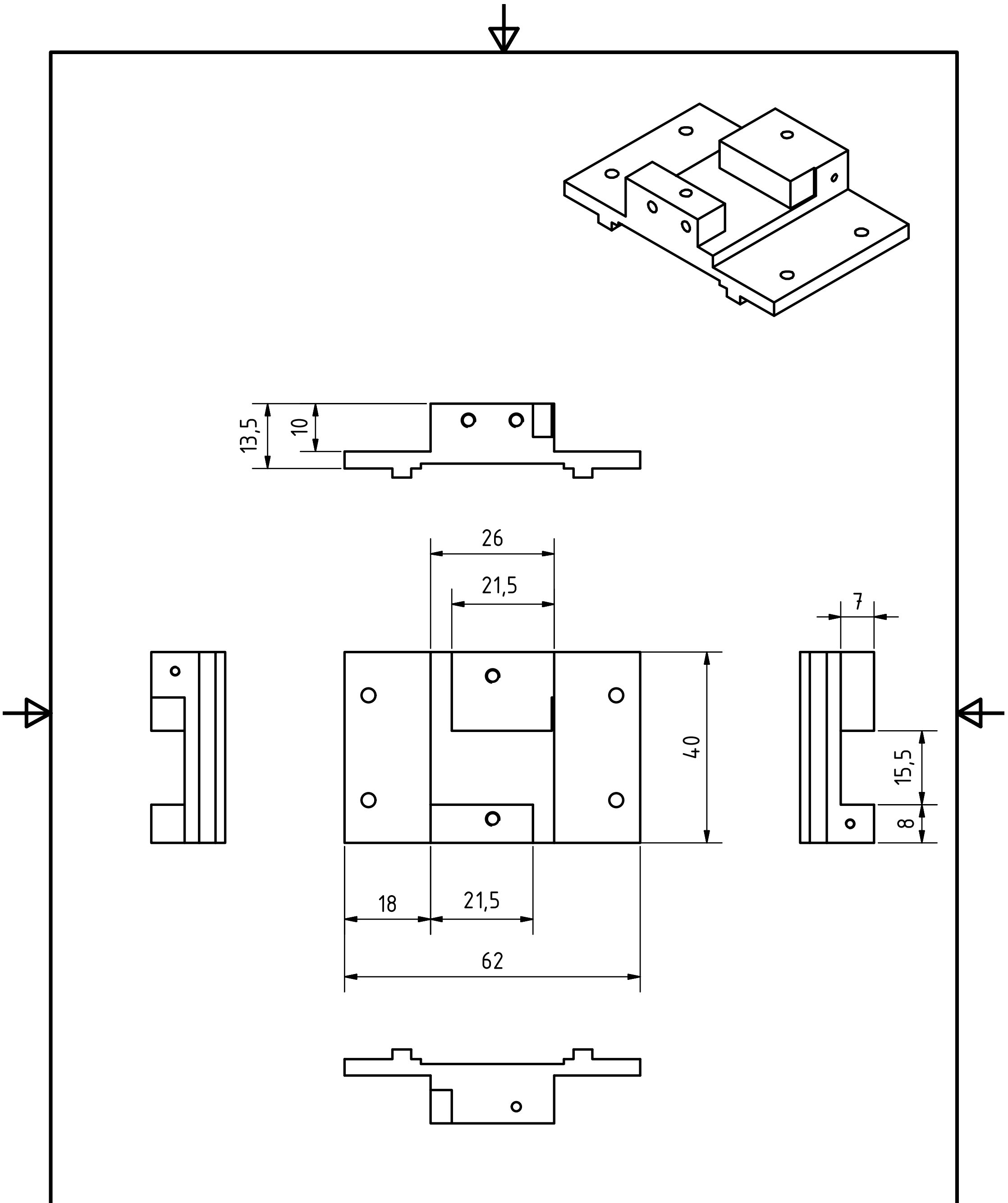

For Information Only Not For Manufacturing Purposes		Sizes in mm	University of Hohenheim	Institute of Physics and Meteorology
			Square-cut Crystal Cooling Mount	
	Date	Name	Clamp Shell - Bottom	
Author		S. Metzendorf		
Norm				
	© 2018			

APPENDIX D

Photos

Figure D.1: The water-vapor DIAL of the *University of Hohenheim*. The energy compartment in the front is decoupled from the rest of the trailer. The main compartment comprehends the laboratory and the scanner room in the rear part.

Figure D.2: Inside of the laboratory compartment, looking to the rear.

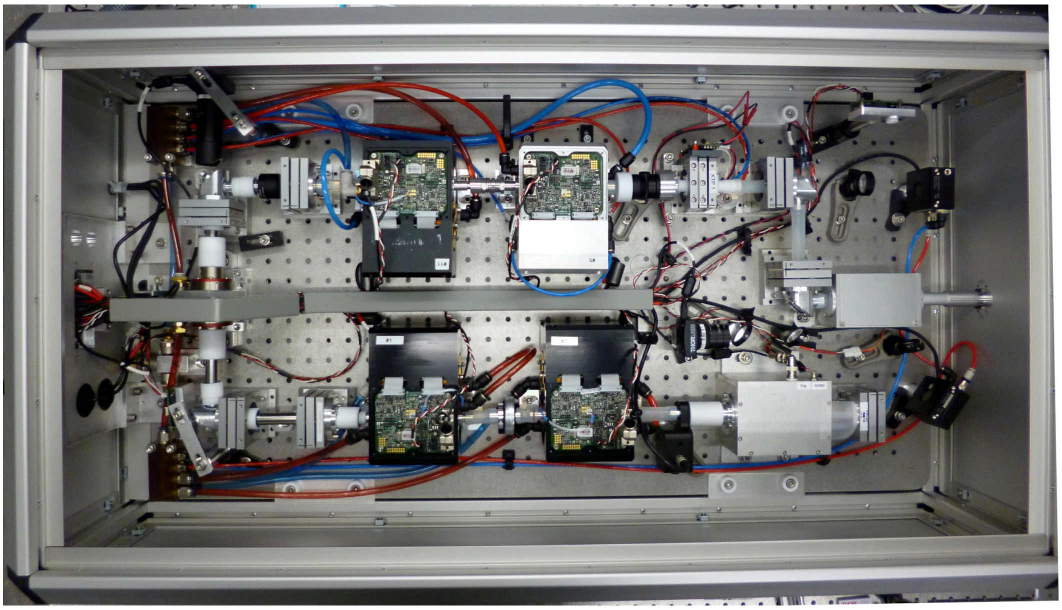

Figure D.3: View inside the *PLA* pump laser.

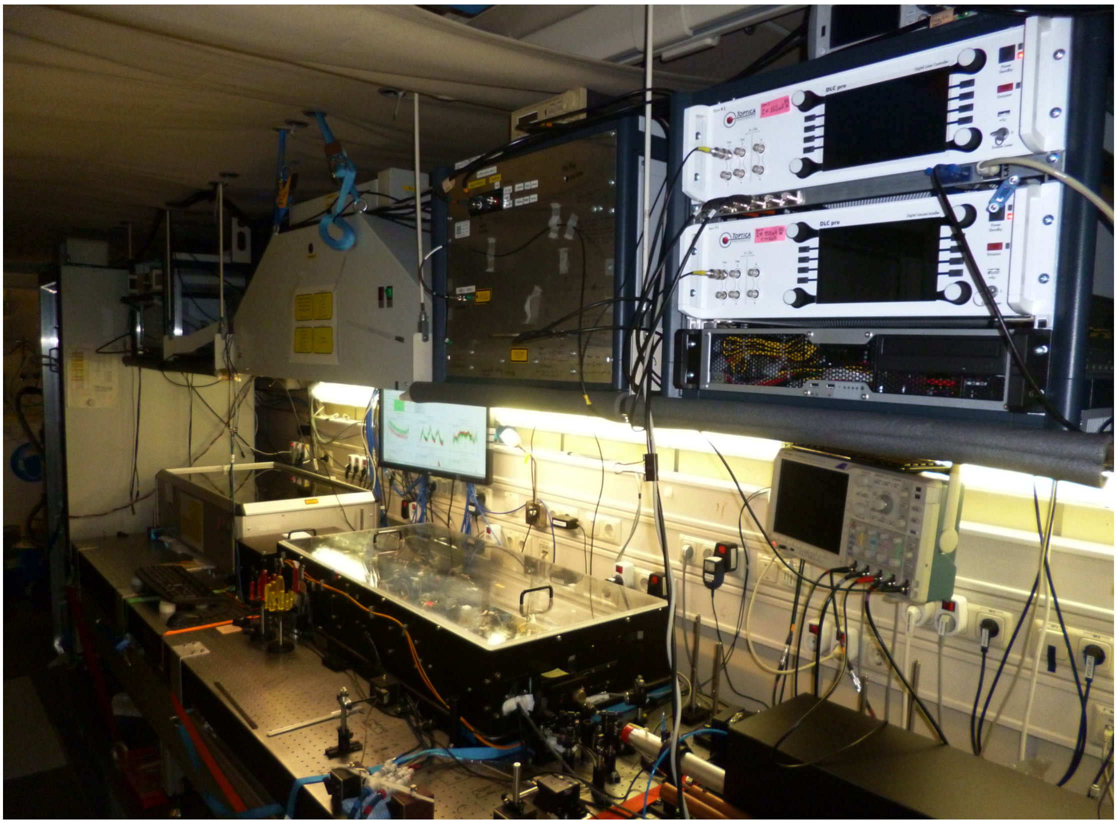

Figure D.4: Looking towards the front, on the entire laser system. The two racks at the top contain the injection seeding system.

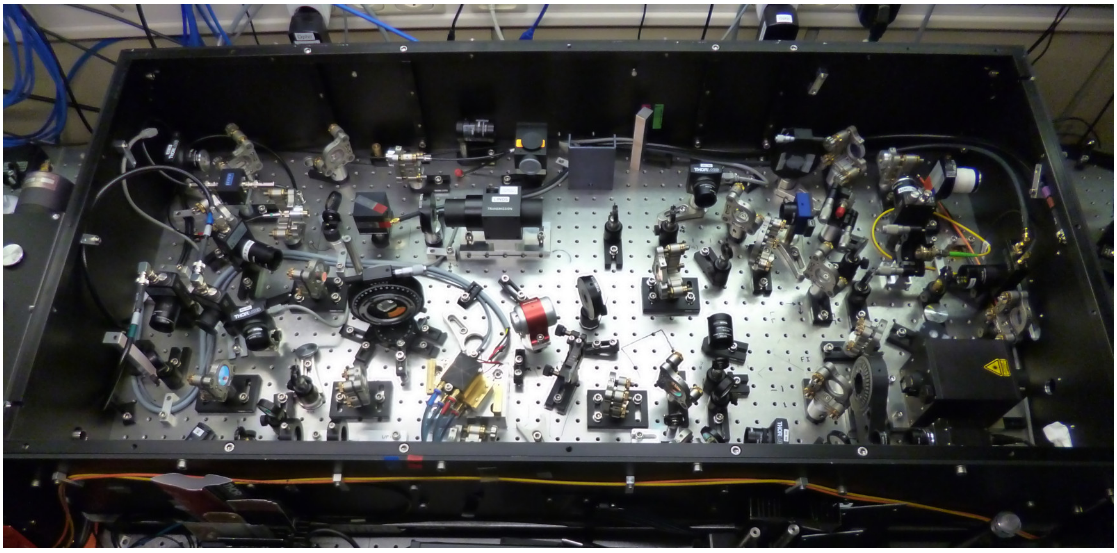

Figure D.5: View inside the Ti:sapphire laser.

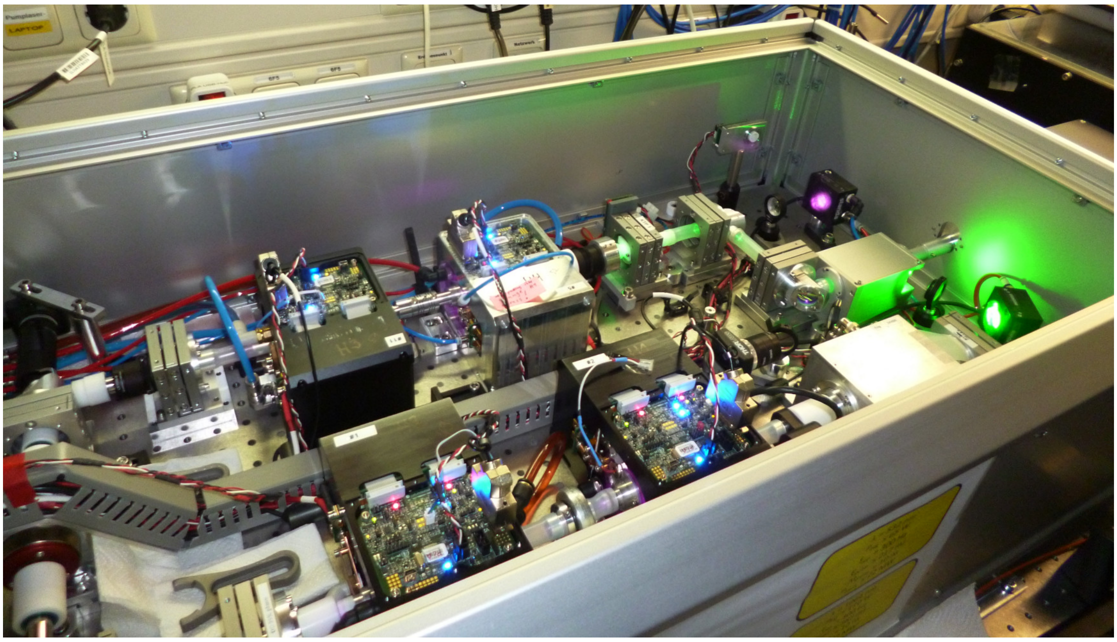

Figure D.6: The pump laser in operation. The camera used to take this picture, misleadingly represents the infrared laser radiation (visible on the power meter) as a violet color.

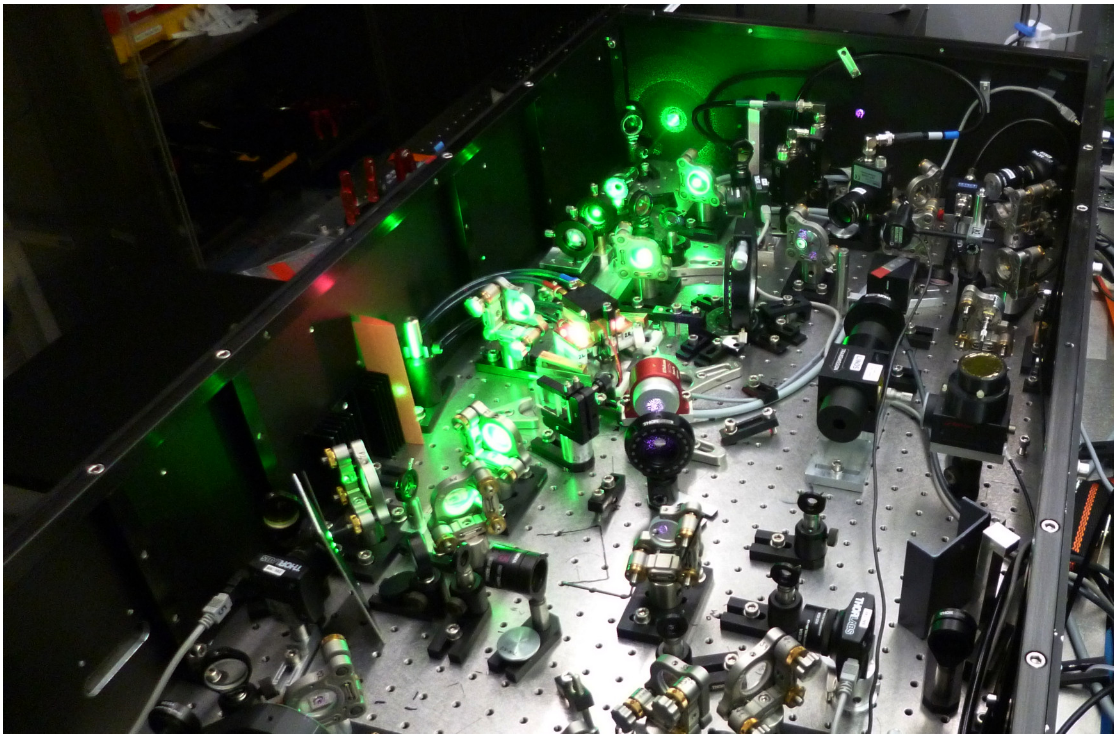

Figure D.7: The Ti:sapphire laser in operation. The pump laser beam is partially perceived.

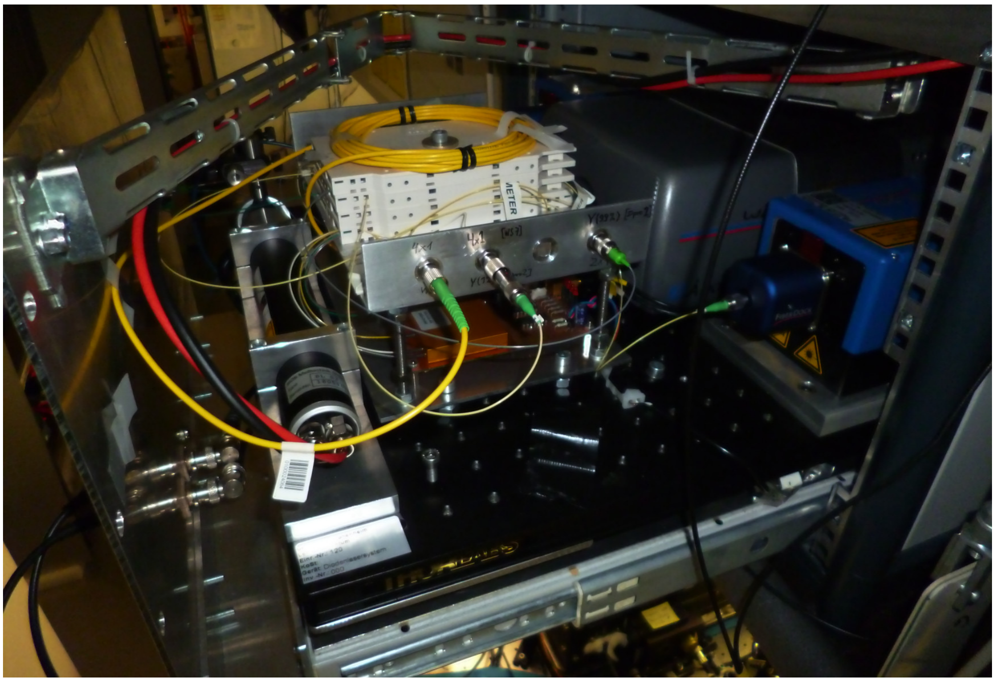

Figure D.8: Interior of the rack with the optical instruments of the injection seeding system.

Figure D.9: Scanner unit of the Hohenheim-DIAL, essentially consisting of a small sending telescope, a big receiving telescope, as well as safety devices (radar, camera, and sun detectors).

Bibliography

[1] J. T. Kiehl and K. E. Trenberth, *Earth's Annual Global Mean Energy Budget*, **Bull. Am. Meteorol. Soc.**, 78 (1997), pp. 197–208, `http://dx.doi.org/10.1175/1520-0477(1997)078<0197:EAGMEB>2.0.CO;2`.

[2] D. L. Hartmann, A. M. G. Klein Tank, M. Rusticucci, L. V. Alexander, S. Brönnimann, Y. Charabi, F. J. Dentener, E. J. Dlugokencky, D. R. Easterling, A. Kaplan, B. J. Soden, P. W. Thorne, M. Wild, and P. M. Zhai, *Chapter 2. Observations: Atmosphere and Surface*, in: Climate Change 2013: The Physical Science Basis. Contribution of Working Group I to the Fifth Assessment Report of the Intergovernmental Panel on Climate Change, T. F. Stocker, D. Qin, G.-K. Plattner, M. Tignor, S. K. Allen, J. Boschung, A. Nauels, Y. Xia, V. Bex, and P. M. Midgley (Eds.), Cambridge University Press, Cambridge, United Kingdom, 2013, `http://ipcc.ch/report/ar5/wg1`.

[3] Core Writing Team, R. K. Pachauri, and L. A. Meyer (Eds.), *Climate Change 2014: Synthesis Report. Contribution of Working Groups I, II and III to the Fifth Assessment Report of the Intergovernmental Panel on Climate Change*, IPCC, Geneva, Switzerland, 2014, `http://ipcc.ch/report/ar5/syr`.

[4] R. B. Stull, *An Introduction to Boundary Layer Meteorology*, Kluwer Academic Publishers, Dordrecht, The Netherlands, 1988, `http://dx.doi.org/10.1007/978-94-009-3027-8`.

[5] V. Wulfmeyer, H.-S. Bauer, M. Grzeschik, A. Behrendt, F. Vandenberghe, E. V. Browell, S. Ismail, and R. A. Ferrare, *Four-Dimensional Variational Assimilation of Water Vapor Differential Absorption Lidar Data: The First Case Study within IHOP_2002*, **Mon. Weather Rev.**, 134 (2006), pp. 209–230, `http://dx.doi.org/10.1175/MWR3070.1`.

[6] V. Wulfmeyer, R. M. Hardesty, D. D. Turner, A. Behrendt, M. P. Cadeddu, P. Di Girolamo, P. Schlüssel, J. Van Baelen, and F. Zus, *A review of the remote sensing of lower tropospheric thermodynamic profiles and its indispensable role for the*

understanding and the simulation of water and energy cycles, **Rev. Geophys.**, 53 (2015), pp. 819–895, `http://dx.doi.org/10.1002/2014RG000476`.

[7] U. SCHUMANN (Ed.), *Atmospheric Physics*, Research Topics in Aerospace, Springer-Verlag, Berlin, 2012, `http://dx.doi.org/10.1007/978-3-642-30183-4`.

[8] A. BEHRENDT, *Chapter 10. Temperature Measurements with Lidar*, in: Lidar: Range-Resolved Optical Remote Sensing of the Atmosphere, C. Weitkamp (Ed.), vol. 102 of Springer Series in Optical Sciences, Springer-Verlag, New York, 2005, pp. 273–305, `http://dx.doi.org/10.1007/b106786`.

[9] R. M. SCHOTLAND, *Some Observations of the Vertical Profile of Water Vapor by Means of a Laser Optical Radar*, in: Proc. 4th Symposium on Remote Sensing of the Environment, pp. 273–283, Ann Arbor, Michigan, 12–24 April 1966.

[10] R. M. SCHOTLAND, *Errors in the Lidar Measurement of Atmospheric Gases by Differential Absorption*, **J. Appl. Meteorol.**, 13 (1974), pp. 71–77, `http://dx.doi.org/10.1175/1520-0450(1974)013<0071:EITLMO>2.0.CO;2`.

[11] J. BÖSENBERG, *Ground-based differential absorption lidar for water-vapor and temperature profiling: methodology*, **Appl. Opt.**, 37 (1998), pp. 3845–3860, `http://dx.doi.org/10.1364/AO.37.003845`.

[12] V. WULFMEYER AND J. BÖSENBERG, *Ground-based differential absorption lidar for water-vapor profiling: assessment of accuracy, resolution, and meteorological applications*, **Appl. Opt.**, 37 (1998), pp. 3825–3844, `http://dx.doi.org/10.1364/AO.37.003825`.

[13] A. BEHRENDT, V. WULFMEYER, D. D. TURNER, A. BREWER, D. LANGE, F. SPÄTH, S. K. MUPPA, S. METZENDORF, A. CHOUKULKAR, T. A. BONIN, T. J. WAGNER, AND R. K. NEWSOM, *Capabilities and Limitations of Lidar Regarding Turbulence Measurements in the Boundary Layer*, in: 23rd AMS Symposium on Boundary Layers and Turbulence, no. 12.3, Oklahoma City, USA, 11–15 June 2018, `https://www.ametsoc.org/index.cfm/ams/meetings-events/ams-meetings/23rd-symposium-on-boundary-layers-and-turbulence-21st-conference-on-air-sea-interaction/`.

[14] R. BHAWAR, P. DI GIROLAMO, D. SUMMA, C. FLAMANT, D. ALTHAUSEN, A. BEHRENDT, C. KIEMLE, P. BOSSER, M. CACCIANI, C. CHAMPOLLION, T. DI IORIO, R. ENGELMANN, C. HEROLD, D. MÜLLER, S. PAL, M. WIRTH, AND V. WULFMEYER, *The water vapour intercomparison effort in the framework of the Convective and Orographically-induced Precipitation Study: airborne-to-ground-based and airborne-to-airborne lidar systems*, **Q. J. R. Meteorol. Soc.**, 137 (2011), pp. 325–348, `http://dx.doi.org/10.1002/qj.697`.

[15] A. BEHRENDT, V. WULFMEYER, H.-S. BAUER, T. SCHABERL, P. DI GIROLAMO, D. SUMMA, C. KIEMLE, G. EHRET, D. N. WHITEMAN, B. B. DEMOZ, E. V. BROWELL, S. ISMAIL, R. FERRARE, S. KOOI, AND J. WANG, *Intercomparison of Water Vapor*

Data Measured with Lidar during IHOP_2002. Part I: Airborne to Ground-Based Lidar Systems and Comparisons with Chilled-Mirror Hygrometer Radiosondes, **J. Atmos. Oceanic Technol.**, 24 (2007), pp. 3–21, `http://dx.doi.org/10.1175/JTECH1924.1`.

[16] A. BEHRENDT, V. WULFMEYER, T. SCHABERL, H.-S. BAUER, C. KIEMLE, G. EHRET, C. FLAMANT, S. KOOI, S. ISMAIL, R. FERRARE, E. V. BROWELL, AND D. N. WHITEMAN, *Intercomparison of Water Vapor Data Measured with Lidar during IHOP_2002. Part II: Airborne-to-Airborne Systems*, **J. Atmos. Oceanic Technol.**, 24 (2007), pp. 22–39, `http://dx.doi.org/10.1175/JTECH1925.1`.

[17] V. WULFMEYER, *Ground-based differential absorption lidar for water-vapor and temperature profiling: Development and specifications of a high-performance laser transmitter*, **Appl. Opt.**, 37 (1998), pp. 3804–3824, `http://dx.doi.org/10.1364/AO.37.003804`.

[18] V. WULFMEYER AND C. WALTHER, *Future performance of ground-based and airborne water-vapor differential absorption lidar. I. Overview and theory*, **Appl. Opt.**, 40 (2001), pp. 5304–5320, `http://dx.doi.org/10.1364/AO.40.005304`.

[19] V. WULFMEYER AND C. WALTHER, *Future performance of ground-based and airborne water-vapor differential absorption lidar. II. Simulations of the precision of a near-infrared, high-power system*, **Appl. Opt.**, 40 (2001), pp. 5321–5336, `http://dx.doi.org/10.1364/AO.40.005321`.

[20] EUROPEAN SPACE AGENCY, *WALES – WAter vapour Lidar Experiment in Space*, Reports for Assessment, ESA SP-1257(2), ESTEC, Noordwijk, The Netherlands, 2001, `http://esamultimedia.esa.int/docs/sp_1257_2_walessc.pdf`.

[21] S. ISMAIL AND E. V. BROWELL, *Airborne and spaceborne lidar measurements of water vapor profiles: a sensitivity analysis*, **Appl. Opt.**, 28 (1989), pp. 3603–3615, `http://dx.doi.org/10.1364/AO.28.003603`.

[22] D. BRUNEAU, P. QUAGLIA, C. FLAMANT, M. MEISSONNIER, AND J. PELON, *Airborne lidar LEANDRE II for water-vapor profiling in the troposphere. I. System description*, **Appl. Opt.**, 40 (2001), pp. 3450–3461, `http://dx.doi.org/10.1364/AO.40.003450`.

[23] K. ERTEL, H. LINNÉ, AND J. BÖSENBERG, *Injection-seeded pulsed Ti:sapphire laser with novel stabilization scheme and capability of dual-wavelength operation*, **Appl. Opt.**, 44 (2005), pp. 5120–5126, `http://dx.doi.org/10.1364/AO.44.005120`.

[24] H. VOGELMANN AND T. TRICKL, *Wide-range sounding of free-tropospheric water vapor with a differential-absorption lidar (DIAL) at a high-altitude station*, **Appl. Opt.**, 47 (2008), pp. 2116–2132, `http://dx.doi.org/10.1364/AO.47.002116`.

[25] M. SCHILLER, *A high-power laser transmitter for ground-based and airborne water-vapor measurements in the troposphere*, Doctoral thesis, Universität Hohenheim, Stuttgart, Germany, 2009, `http://opus.uni-hohenheim.de/volltexte/2010/454/`.

[26] G. WAGNER, A. BEHRENDT, V. WULFMEYER, F. SPÄTH, AND M. SCHILLER, *High-power Ti:sapphire laser at 820 nm for scanning ground-based water-vapor differential absorption lidar*, **Appl. Opt.**, 52 (2013), pp. 2454–2469, `http://dx.doi.org/10.1364/AO.52.002454`.

[27] S. ISMAIL, R. A. FERRARE, E. V. BROWELL, G. CHEN, B. ANDERSON, S. A. KOOI, A. NOTARI, C. F. BUTLER, S. BURTON, M. FENN, J. P. DUNION, G. HEYMSFIELD, T. N. KRISHNAMURTI, AND M. K. BISWAS, *LASE Measurements of Water Vapor, Aerosol, and Cloud Distributions in Saharan Air Layers and Tropical Disturbances*, **J. Atmos. Sci.**, 67 (2010), pp. 1026–1047, `http://dx.doi.org/10.1175/2009JAS3136.1`.

[28] M. WIRTH, A. FIX, P. MAHNKE, H. SCHWARZER, F. SCHRANDT, AND G. EHRET, *The airborne multi-wavelength water vapor differential absorption lidar WALES: system design and performance*, **Appl. Phys. B**, 96 (2009), pp. 201–213, `http://dx.doi.org/10.1007/s00340-009-3365-7`.

[29] J. LÖHRING, A. MEISSNER, D. HOFFMANN, A. FIX, G. EHRET, AND M. ALPERS, *Diode-pumped single-frequency-Nd:YGG-MOPA for water–vapor DIAL measurements: design, setup and performance*, **Appl. Phys. B**, 102 (2011), pp. 917–935, `http://dx.doi.org/10.1007/s00340-010-4314-1`.

[30] G. WAGNER, *Theoretical analysis and design of high-performance frequency converters for LIDAR systems*, Doctoral thesis, Universität Hohenheim, Stuttgart, Germany, 2009, `http://opus.uni-hohenheim.de/volltexte/2010/411/`.

[31] G. WAGNER, V. WULFMEYER, AND A. BEHRENDT, *Detailed performance modeling of a pulsed high-power single-frequency Ti:sapphire laser*, **Appl. Opt.**, 50 (2011), pp. 5921–5937, `http://dx.doi.org/10.1364/AO.50.005921`.

[32] S. JORDA, *“Ich versuche, mit intuitiven Bildern zu arbeiten” – Interview mit dem Pionier der Laserspektroskopie Theodor W. Hänsch*, **Physik Journal**, 9 (2010), pp. 49–51, `http://www.pro-physik.de/details/physikjournalArticle/prophy61977article/article.html`.

[33] G. A. RINES, H. H. ZENZIE, R. A. SCHWARZ, Y. ISYANOVA, AND P. F. MOULTON, *Nonlinear conversion of Ti:sapphire laser wavelengths*, **IEEE J. Sel. Top. Quantum Electron.**, 1 (1995), pp. 50–57, `http://dx.doi.org/10.1109/2944.468372`.

[34] D. DEPENHEUER, J. KOHL-LANDGRAF, H. GLÄSSER, AND T. WALTHER, *A pulsed laser system with large spectral coverage extended by non-linear frequency conversion*, **Appl. Phys. B**, 97 (2009), pp. 583–589, `http://dx.doi.org/10.1007/s00340-009-3601-1`.

[35] C. WEITKAMP (Ed.), *Lidar: Range-Resolved Optical Remote Sensing of the Atmosphere*, vol. 102 of Springer Series in Optical Sciences, Springer-Verlag, New York, 2005, `http://dx.doi.org/10.1007/b106786`.

[36] U. WANDINGER, *Chapter 1. Introduction to Lidar*, in: Lidar: Range-Resolved Optical Remote Sensing of the Atmosphere, C. Weitkamp (Ed.), vol. 102 of Springer Series in Optical Sciences, Springer-Verlag, New York, 2005, pp. 1–18, `http://dx.doi.org/10.1007/b106786`.

[37] V. WULFMEYER AND T. JANJIĆ, *Twenty-Four-Hour Observations of the Marine Boundary Layer Using Shipborne NOAA High-Resolution Doppler Lidar*, **J. Appl. Meteorol.**, 44 (2005), pp. 1723–1744, `http://dx.doi.org/10.1175/JAM2296.1`.

[38] R. ENGELMANN, T. KANITZ, H. BAARS, B. HEESE, D. ALTHAUSEN, A. SKUPIN, U. WANDINGER, M. KOMPPULA, I. S. STACHLEWSKA, V. AMIRIDIS, E. MARINOU, I. MATTIS, H. LINNÉ, AND A. ANSMANN, *The automated multiwavelength Raman polarization and water-vapor lidar Polly^{XT}: the neXT generation*, **Atmos. Meas. Tech.**, 9 (2016), pp. 1767–1784, `http://dx.doi.org/10.5194/amt-9-1767-2016`.

[39] D. BRUNEAU, P. QUAGLIA, C. FLAMANT, M. MEISSONNIER, AND J. PELON, *Airborne lidar LEANDRE II for water-vapor profiling in the troposphere. II. First results*, **Appl. Opt.**, 40 (2001), pp. 3462–3475, `http://dx.doi.org/10.1364/AO.40.003462`.

[40] E. V. BROWELL, S. ISMAIL, AND W. B. GRANT, *Differential absorption lidar (DIAL) measurements from air and space*, **Appl. Phys. B**, 67 (1998), pp. 399–410, `http://dx.doi.org/10.1007/s003400050523`.

[41] D. M. WINKER, R. H. COUCH, AND M. P. MCCORMICK, *An overview of LITE: NASA's Lidar In-space Technology Experiment*, in: Proc. IEEE, vol. 84, pp. 164–180, February 1996, `http://dx.doi.org/10.1109/5.482227`.

[42] R. M. MEASURES, *Laser Remote Sensing*, John Wiley & Sons, New York, 1984. ISBN 0-471-08193-0.

[43] J. BÖSENBERG, *Chapter 8. Differential-Absorption Lidar for Water Vapor and Temperature Profiling*, in: Lidar: Range-Resolved Optical Remote Sensing of the Atmosphere, C. Weitkamp (Ed.), vol. 102 of Springer Series in Optical Sciences, Springer-Verlag, New York, 2005, pp. 213–239, `http://dx.doi.org/10.1007/b106786`.

[44] F. SPÄTH, *3-D Observations of Absolute Humidity from the Land Surface to the Lower Troposphere with Scanning Differential Absorption Lidar*, Doctoral thesis, Universität Hohenheim, Stuttgart, Germany, 2016, `http://opus.uni-hohenheim.de/volltexte/2016/1290/`.

[45] A. ANSMANN, *Errors in ground-based water-vapor DIAL measurements due to Doppler-broadened Rayleigh backscattering*, **Appl. Opt.**, 24 (1985), pp. 3476–3480, `http://dx.doi.org/10.1364/AO.24.003476`.

[46] L. S. ROTHMAN, I. E. GORDON, Y. BABIKOV, A. BARBE, D. CHRIS BENNER, P. F. BERNATH, M. BIRK, L. BIZZOCCHI, V. BOUDON, L. R. BROWN, A. CAMPARGUE, K. CHANCE, E. A. COHEN, L. H. COUDERT, V. M. DEVI, B. J. DROUIN, A. FAYT, J.-M. FLAUD, R. R. GAMACHE, J. J. HARRISON, J.-M. HARTMANN, C. HILL, J. T. HODGES, D. JACQUEMART, A. JOLLY, J. LAMOUROUX, R. J. LE ROY, G. LI, D. A. LONG, O. M. LYULIN, C. J. MACKIE, S. T. MASSIE, S. MIKHAILENKO, H. S. P. MÄLLER, O. V. NAUMENKO, A. V. NIKITIN, J. ORPHAL, V. PEREVALOV, A. PERRIN, E. R. POLOVTSEVA, C. RICHARD, M. A. H. SMITH, E. STARIKOVA, K. SUNG, S. TASHKUN, J. TENNYSON, G. C. TOON, V. G. TYUTEREV, AND G. WAGNER, *The HITRAN2012 molecular spectroscopic database*, **J. Quant. Spectrosc. Ra.**, 130 (2013), pp. 4–50, `http://dx.doi.org/10.1016/j.jqsrt.2013.07.002`.

[47] F. SPÄTH, A. BEHRENDT, S. K. MUPPA, S. METZENDORF, A. RIEDE, AND V. WULFMEYER, *High-resolution atmospheric water vapor measurements with a scanning differential absorption lidar*, **Atmos. Chem. Phys. Discuss.**, 14 (2014), pp. 29057–29099, `http://dx.doi.org/10.5194/acpd-14-29057-2014`.

[48] F. SPÄTH, A. BEHRENDT, S. K. MUPPA, S. METZENDORF, A. RIEDE, AND V. WULFMEYER, *3-D water vapor field in the atmospheric boundary layer observed with scanning differential absorption lidar*, **Atmos. Meas. Tech.**, 9 (2016), pp. 1701–1720, `http://dx.doi.org/10.5194/amt-9-1701-2016`.

[49] A. ANSMANN AND J. BÖSENBERG, *Correction scheme for spectral broadening by Rayleigh scattering in differential absorption lidar measurements of water vapor in the troposphere*, **Appl. Opt.**, 26 (1987), pp. 3026–3032, `http://dx.doi.org/10.1364/AO.26.003026`.

[50] F. SPÄTH, A. BEHRENDT, AND V. WULFMEYER, *Sensitivity of the Rayleigh-Doppler Effect with Respect to Wavelength and Backscatter Coefficient*, in: 27th International Laser Radar Conference (ILRC 2015), no. PS-C3.14, New York City, USA, 5–10 July 2015.

[51] P. DI GIROLAMO, D. SUMMA, H. BAUER, V. WULFMEYER, A. BEHRENDT, G. EHRET, B. MAYER, M. WIRTH, AND C. KIEMLE, *Simulation of the performance of WALES based on an end-to-end model*, in: 22nd International Laser Radar Conference (ILRC 2004), no. S10O-7, Matera, Italy, 12–16 July 2004, `http://www.spacebooks-online.com/product_info.php?products_id=17276`.

[52] P. DI GIROLAMO, A. BEHRENDT, C. KIEMLE, V. WULFMEYER, H. BAUER, D. SUMMA, A. DÖRNBRACK, AND G. EHRET, *Simulation of satellite water vapour lidar measurements: Performance assessment under real atmospheric conditions*, **Remote Sens. Environ.**, 112 (2008), pp. 1552–1568, `http://dx.doi.org/10.1016/j.rse.2007.08.008`.

[53] EUROPEAN SPACE AGENCY, *WALES – Water Vapour Lidar Experiment in Space, Technical and Programmatic Annex*, Reports for Mission Selection, Annex to ESA SP-

1279(3), ESTEC, Noordwijk, The Netherlands, 2004, `http://esamultimedia.esa.int/docs/EEUCM/WALES_TPA.pdf`.

[54] S. Ismail and E. V. Browell, *Recent Lidar Technology Developments and Their Influence on Measurements of Tropospheric Water Vapor*, **J. Atmos. Oceanic Technol.**, 11 (1994), pp. 76–84, `http://dx.doi.org/10.1175/1520-0426(1994)011<0076:RLTDAT>2.0.CO;2`.

[55] A. Petrova-Mayor, V. Wulfmeyer, and P. Weibring, *Development of an eye-safe solid-state tunable laser transmitter in the 1.4–1.5 μm wavelength region based on Cr4+:YAG crystal for lidar applications*, **Appl. Opt.**, 47 (2008), pp. 1522–1534, `http://dx.doi.org/10.1364/AO.47.001522`.

[56] C. Kränkel, *Rare-Earth-Doped Sesquioxides for Diode-Pumped High-Power Lasers in the 1-, 2-, and 3-μm Spectral Range*, **IEEE J. Sel. Top. Quantum Electron.**, 21 (2015), pp. 250–262, `http://dx.doi.org/10.1109/JSTQE.2014.2346618`.

[57] Y. Zhao, T. K. Lea, and R. M. Schotland, *Correction function for the lidar equation and some techniques for incoherent CO_2 lidar data reduction*, **Appl. Opt.**, 27 (1988), pp. 2730–2740, `http://dx.doi.org/10.1364/AO.27.002730`.

[58] A. E. Siegman, *Lasers*, University Science Books, Mill Valley, CA, USA, 1986, `http://www.uscibooks.com/siegman.htm`. ISBN 978-0-935702-11-8.

[59] J. L. Machol, T. Ayers, K. T. Schwenz, K. W. Koenig, R. M. Hardesty, C. J. Senff, M. A. Krainak, J. B. Abshire, H. E. Bravo, and S. P. Sandberg, *Preliminary measurements with an automated compact differential absorption lidar for the profiling of water vapor*, **Appl. Opt.**, 43 (2004), pp. 3110–3121, `http://dx.doi.org/10.1364/AO.43.003110`.

[60] A. R. Nehrir, K. S. Repasky, and J. L. Carlsten, *Micropulse water vapor differential absorption lidar: transmitter design and performance*, **Opt. Express**, 20 (2012), pp. 25137–25151, `http://dx.doi.org/10.1364/OE.20.025137`.

[61] S. M. Spuler, K. S. Repasky, B. Morley, D. Moen, M. Hayman, and A. R. Nehrir, *Field-deployable diode-laser-based differential absorption lidar (DIAL) for profiling water vapor*, **Atmos. Meas. Tech.**, 8 (2015), pp. 1073–1087, `http://dx.doi.org/10.5194/amt-8-1073-2015`.

[62] A. Dinovitser, L. J. Gunn, and D. Abbott, *Towards quantitative atmospheric water vapor profiling with differential absorption lidar*, **Opt. Express**, 23 (2015), pp. 22907–22921, `http://dx.doi.org/10.1364/OE.23.022907`.

[63] T. N. Vu, *Development and analysis of all diode laser ns-MOPA systems for high peak power applications*, Doctoral thesis, Technische Universität Berlin, Germany, 2017, `http://dx.doi.org/10.14279/depositonce-5713`.

[64] R. J. DE YOUNG AND N. P. BARNES, *Profiling atmospheric water vapor using a fiber laser lidar system*, **Appl. Opt.**, 49 (2010), pp. 562–567, `http://dx.doi.org/10.1364/AO.49.000562`.

[65] A. FIX, G. EHRET, J. LÖHRING, D. HOFFMANN, AND M. ALPERS, *Water vapor differential absorption lidar measurements using a diode-pumped all-solid-state laser at 935 nm*, **Appl. Phys. B**, 102 (2011), pp. 905–915, `http://dx.doi.org/10.1007/s00340-010-4310-5`.

[66] G. POBERAJ, A. FIX, A. ASSION, M. WIRTH, C. KIEMLE, AND G. EHRET, *Airborne all-solid-state DIAL for water vapour measurements in the tropopause region: system description and assessment of accuracy*, **Appl. Phys. B**, 75 (2002), pp. 165–172, `http://dx.doi.org/10.1007/s00340-002-0965-x`.

[67] H. VOGELMANN, R. SUSSMANN, T. TRICKL, AND T. BORSDORFF, *Intercomparison of atmospheric water vapor soundings from the differential absorption lidar (DIAL) and the solar FTIR system on Mt. Zugspitze*, **Atmos. Meas. Tech.**, 4 (2011), pp. 835–841, `http://dx.doi.org/10.5194/amt-4-835-2011`.

[68] H. VOGELMANN, *Entwicklung und Aufbau eines Hochleistungs-Wasserdampf-LIDAR-Systems auf der Zugspitze*, Doctoral thesis, Institut für Meteorologie und Klimaforschung, Institut für atmosphärische Umweltforschung (IMK-IFU), Garmisch-Partenkirchen, Germany, 2005.

[69] D. BRUNEAU, H. CAZENEUVE, C. LOTH, AND J. PELON, *Double-pulse dual-wavelength alexandrite laser for atmospheric water vapor measurement*, **Appl. Opt.**, 30 (1991), pp. 3930–3937, `http://dx.doi.org/10.1364/AO.30.003930`.

[70] K. ERTEL, *Application and Development of Water Vapor DIAL Systems*, Doctoral thesis, Universität Hamburg, Germany, 2004.

[71] M. OSTERMEYER, *Investigation and development of a pulsed laser system in rod geometry thought for pumping a lidar system for atmospheric research.* GEPRIS – Geförderte Projekte der DFG, Deutsche Forschungsgemeinschaft, 2004–2011, `http://gepris.dfg.de/gepris/projekt/5414830`.

[72] V. WULFMEYER, *High-power, injection-seeded Ti:sapphire laser designed for frequency conversion of a 200-W diode-laser pumped laser system.* GEPRIS – Geförderte Projekte der DFG, Deutsche Forschungsgemeinschaft, 2004–2011, `http://gepris.dfg.de/gepris/projekt/5414832`.

[73] D. ALTHAUSEN, *Entwicklung einer mobilen Plattform mit Scanner zur Bestimmung von Profilen der absoluten Feuchte in der Atmosphäre.* GEPRIS – Geförderte Projekte der DFG, Deutsche Forschungsgemeinschaft, 2004–2011, `http://gepris.dfg.de/gepris/projekt/5414866`.

[74] A. Behrendt, A. Blyth, M. Dorninger, N. Kalthoff, C. Flamant, P. Di Girolamo, and E. Richard, *Convective Precipitation in complex terrain: Results of the COPS campaign*, **Meteorol. Z.**, 22 (2013), pp. 367–372, `http://dx.doi.org/10.1127/0941-2948/2013/0541`.

[75] V. Wulfmeyer, A. Behrendt, C. Kottmeier, U. Corsmeier, C. Barthlott, G. C. Craig, M. Hagen, D. Althausen, F. Aoshima, M. Arpagaus, H.-S. Bauer, L. Bennett, A. Blyth, C. Brandau, C. Champollion, S. Crewell, G. Dick, P. Di Girolamo, M. Dorninger, Y. Dufournet, R. Eigenmann, R. Engelmann, C. Flamant, T. Foken, T. Gorgas, M. Grzeschik, J. Handwerker, C. Hauck, H. Höller, W. Junkermann, N. Kalthoff, C. Kiemle, S. Klink, M. König, L. Krauss, C. N. Long, F. Madonna, S. Mobbs, B. Neininger, S. Pal, G. Peters, G. Pigeon, E. Richard, M. W. Rotach, H. Russchenberg, T. Schwitalla, V. Smith, R. Steinacker, J. Trentmann, D. D. Turner, J. Van Baelen, S. Vogt, H. Volkert, T. Weckwerth, H. Wernli, A. Wieser, and M. Wirth, *The Convective and Orographically-induced Precipitation Study (COPS): the scientific strategy, the field phase, and research highlights*, **Q. J. R. Meteorol. Soc.**, 137 (2011), pp. 3–30, `http://dx.doi.org/10.1002/qj.752`.

[76] V. Wulfmeyer, A. Behrendt, H.-S. Bauer, C. Kottmeier, U. Corsmeier, A. Blyth, G. Craig, U. Schumann, M. Hagen, S. Crewell, P. Di Girolamo, C. Flamant, M. Miller, A. Montani, S. Mobbs, E. Richard, M. W. Rotach, M. Arpagaus, H. Russchenberg, P. Schlüssel, M. König, V. Gärtner, R. Steinacker, M. Dorninger, D. D. Turner, T. Weckwerth, A. Hense, and C. Simmer, *RESEARCH CAMPAIGN: The Convective and Orographically Induced Precipitation Study*, **Bull. Am. Meteorol. Soc.**, 89 (2008), pp. 1477–1486, `http://dx.doi.org/10.1175/2008BAMS2367.1`.

[77] A. Behrendt, S. Pal, F. Aoshima, M. Bender, A. Blyth, U. Corsmeier, J. Cuesta, G. Dick, M. Dorninger, C. Flamant, P. Di Girolamo, T. Gorgas, Y. Huang, N. Kalthoff, S. Khodayar, H. Mannstein, K. Träumner, A. Wieser, and V. Wulfmeyer, *Observation of convection initiation processes with a suite of state-of-the-art research instruments during COPS IOP 8b*, **Q. J. R. Meteorol. Soc.**, 137 (2011), pp. 81–100, `http://dx.doi.org/10.1002/qj.758`.

[78] A. Behrendt, V. Wulfmeyer, A. Riede, G. Wagner, S. Pal, H. Bauer, M. Radlach, and F. Späth, *Three-dimensional observations of atmospheric humidity with a scanning differential absorption Lidar*, in: Remote Sensing of Clouds and the Atmosphere XIV, vol. 7475 of Proc. SPIE, pp. 74750L–1–10, Berlin, Germany, 31 August–1 September 2009, `http://dx.doi.org/10.1117/12.835143`.

[79] TR32, *Transregional Collaborative Research Centre 32*. Patterns in Soil-Vegetation-Atmosphere Systems: Monitoring, Modelling & Data Assimilation, `http://www.tr32.de/`. Accessed 28 March 2018.

[80] J. MILOVAC, K. WARRACH-SAGI, A. BEHRENDT, F. SPÄTH, J. INGWERSEN, AND V. WULFMEYER, *Investigation of PBL schemes combining the WRF model simulations with scanning water vapor differential absorption lidar measurements*, **J. Geophys. Res. Atmos.**, 121 (2016), pp. 624–649, `http://dx.doi.org/10.1002/2015JD023927`.

[81] E. P. IPPEN AND R. H. STOLEN, *Stimulated Brillouin scattering in optical fibers*, **Appl. Phys. Lett.**, 21 (1972), pp. 539–541, `http://dx.doi.org/10.1063/1.1654249`.

[82] A. RIEDE, A. BEHRENDT, V. WULFMEYER, D. ALTHAUSEN, U. WANDINGER, V. KLEIN, A. MEISTER, AND M. SCHILLER, *Transmitter-Receiver Unit of the UHOH Water Vapor DIAL with a Scanning 800-mm Telescope Mirror*, in: 26th International Laser Radar Conference (ILRC 2012), no. S1P-12, Porto Heli, Greece, 25–29 June 2012.

[83] K. GÜREL, V. J. WITTWER, M. HOFFMANN, C. J. SARACENO, S. HAKOBYAN, B. RESAN, A. ROHRBACHER, K. WEINGARTEN, S. SCHILT, AND T. SÜDMEYER, *Green-diode-pumped femtosecond Ti:Sapphire laser with up to 450 mW average power*, **Opt. Express**, 23 (2015), pp. 30043–30048, `http://dx.doi.org/10.1364/OE.23.030043`.

[84] P. W. ROTH, D. BURNS, AND A. J. KEMP, *Power scaling of a directly diode-laser-pumped Ti:sapphire laser*, **Opt. Express**, 20 (2012), pp. 20629–20634, `http://dx.doi.org/10.1364/OE.20.020629`.

[85] W. KOECHNER, *Solid-State Laser Engineering*, vol. 1 of Springer Series in Optical Sciences, Springer-Verlag, New York, 6th, rev. and updated ed., 2006, `http://dx.doi.org/10.1007/0-387-29338-8`.

[86] D. B. COYLE, D. V. GUERRA, AND R. B. KAY, *An interactive numerical model of diode-pumped, Q-switched/cavity-dumped lasers*, **J. Phys. D: Appl. Phys.**, 28 (1995), p. 452, `http://stacks.iop.org/0022-3727/28/i=3/a=002`.

[87] M. OSTERMEYER, P. KAPPE, R. MENZEL, AND V. WULFMEYER, *Diode-pumped Nd:YAG master oscillator power amplifier with high pulse energy, excellent beam quality, and frequency-stabilized master oscillator as a basis for a next-generation lidar system*, **Appl. Opt.**, 44 (2005), pp. 582–590, `http://dx.doi.org/10.1364/AO.44.000582`.

[88] D. L. SIPES, *Highly efficient neodymium:yttrium aluminum garnet laser end pumped by a semiconductor laser array*, **Appl. Phys. Lett.**, 47 (1985), pp. 74–76, `http://dx.doi.org/10.1063/1.96256`.

[89] A. K. COUSINS, *Temperature and thermal stress scaling in finite-length end-pumped laser rods*, **IEEE Journal of Quantum Electronics**, 28 (1992), pp. 1057–1069, `http://dx.doi.org/10.1109/3.135228`.

[90] D. G. HALL, R. J. SMITH, AND R. R. RICE, *Pump-size effects in Nd:YAG lasers*, **Appl. Opt.**, 19 (1980), pp. 3041–3043, `http://dx.doi.org/10.1364/AO.19.003041`.

[91] S. B. SUTTON AND G. F. ALBRECHT, *Optical distortion in end-pumped solid-state rodlasers*, **Appl. Opt.**, 32 (1993), pp. 5256–5269, `http://dx.doi.org/10.1364/AO.32.005256`.

[92] A. E. SIEGMAN, *How to (Maybe) Measure Laser Beam Quality*, in: DPSS (Diode Pumped Solid State) Lasers: Applications and Issues, no. MQ1 in OSA Trends in Optics and Photonics, 1998, `http://dx.doi.org/10.1364/DLAI.1998.MQ1`.

[93] A. PARENT, M. MORIN, AND P. LAVIGNE, *Propagation of super-Gaussian field distributions*, **Opt. Quantum Electron.**, 24 (1992), pp. S1071–S1079, `http://dx.doi.org/10.1007/BF01588606`.

[94] P. LAPORTA AND M. BRUSSARD, *Misalignment sensitivity of laser-diode pumped solid-state lasers*, **Opt. Commun.**, 85 (1991), pp. 47–53, `http://dx.doi.org/10.1016/0030-4018(91)90050-N`.

[95] A. BEHRENDT. Private communication, July 2018.

[96] E. HAMMANN, *High-resolution measurements of temperature and humidity fields in the atmospheric boundary layer with scanning rotational Raman lidar*, Doctoral thesis, Universität Hohenheim, Stuttgart, Germany, 2016, `http://opus.uni-hohenheim.de/volltexte/2016/1257`.

[97] A. STRÄSSER, T. WALTINGER, AND M. OSTERMEYER, *Injection seeded frequency stabilized Nd:YAG ring oscillator following a Pound-Drever-Hall scheme*, **Appl. Opt.**, 46 (2007), pp. 8358–8363, `http://dx.doi.org/10.1364/AO.46.008358`.

[98] M. OSTERMEYER, T. WALTINGER, AND M. GREGOR, *Frequency stabilization of a Q-switched Nd:YAG laser oscillator with stability better 300 kHz following an rf-sideband scheme*, **Opt. Commun.**, 282 (2009), pp. 3302–3307, `http://dx.doi.org/10.1016/j.optcom.2009.04.063`.

[99] R. MENZEL, *Photonics*, Springer-Verlag, Berlin, 2 ed., 2007, `http://dx.doi.org/10.1007/978-3-540-45158-7`.

[100] N. I. ZHELUDEV, S. M. SALTIEL, AND P. YANKOV, *Second harmonic generators as a new class of light polarizers and analyzers*, **Sov. J. Quantum Electron.**, 17 (1987), p. 948, `http://dx.doi.org/10.1070/QE1987v017n07ABEH009544`.

[101] H. SUN, *Thin lens equation for a real laser beam with weak lens aperture truncation*, **Opt. Eng.**, 37 (1998), pp. 2906–2913, `http://dx.doi.org/10.1117/1.601877`.

[102] S. A. SELF, *Focusing of spherical Gaussian beams*, **Appl. Opt.**, 22 (1983), pp. 658–661, `http://dx.doi.org/10.1364/AO.22.000658`.

[103] Y. K. PARK, G. GIULIANI, AND R. L. BYER, *Stable single-axial-mode operation of an unstable-resonator Nd:YAG oscillator by injection locking*, **Opt. Lett.**, 5 (1980), pp. 96–98, `http://dx.doi.org/10.1364/OL.5.000096`.

[104] R. L. SCHMITT AND L. A. RAHN, *Diode-laser-pumped Nd:YAG laser injection seeding system*, **Appl. Opt.**, 25 (1986), pp. 629–633, `http://dx.doi.org/10.1364/AO.25.000629`.

[105] P. BROCKMAN, C. H. BAIR, J. C. BARNES, R. V. HESS, AND E. V. BROWELL, *Pulsed injection control of a titanium-doped sapphire laser*, **Opt. Lett.**, 11 (1986), pp. 712–714, `http://dx.doi.org/10.1364/OL.11.000712`.

[106] E. S. FRY, Q. HU, AND X. LI, *Single frequency operation of an injection-seeded Nd:YAG laser in high noise and vibration environments*, **Appl. Opt.**, 30 (1991), pp. 1015–1017, `http://dx.doi.org/10.1364/AO.30.001015`.

[107] J. C. BARNES, N. P. BARNES, L. G. WANG, AND W. EDWARDS, *Injection seeding. II. Ti:Al_2O_3 experiments*, **IEEE J. Quant. Electron.**, 29 (1993), pp. 2684–2692, `http://dx.doi.org/10.1109/3.250391`.

[108] V. WULFMEYER, S. SCHMITZ, J. BÖSENBERG, S. LEHMANN, AND C. SENFF, *Injection-seeded alexandrite ring laser: performance and application in a water-vapor differential absorption lidar*, **Opt. Lett.**, 20 (1995), pp. 638–640, `http://dx.doi.org/10.1364/OL.20.000638`.

[109] V. WULFMEYER AND J. BÖSENBERG, *Single-mode operation of an injection-seeded alexandrite ring laser for application in water-vapor and temperature differential absorption lidar*, **Opt. Lett.**, 21 (1996), pp. 1150–1152, `http://dx.doi.org/10.1364/OL.21.001150`.

[110] J. E. BJORKHOLM AND H. G. DANIELMEYER, *Frequency control of a pulsed optical parametric oscillator by radiation injection*, **Appl. Phys. Lett.**, 15 (1969), pp. 171–173, `http://dx.doi.org/10.1063/1.1652954`.

[111] G. EHRET, A. FIX, V. WEISS, G. POBERAJ, AND T. BAUMERT, *Diode-laser-seeded optical parametric oscillator for airborne water vapor DIAL application in the upper troposphere and lower stratosphere*, **Appl. Phys. B**, 67 (1998), pp. 427–431, `http://dx.doi.org/10.1007/s003400050526`.

[112] H. R. KHALESIFARD, A. FIX, G. EHRET, M. SCHILLER, AND V. WULFMEYER, *Fast-switching system for injection seeding of a high-power Ti:sapphire laser*, **Rev. Sci. Instrum.**, 80 (2009), `http://dx.doi.org/10.1063/1.3184011`.

[113] F. SPÄTH, S. METZENDORF, A. BEHRENDT, H.-D. WIZEMANN, G. WAGNER, AND V. WULFMEYER, *Online/offline injection seeding system with high frequency-stability and low crosstalk for water vapor DIAL*, **Opt. Commun.**, 309 (2013), pp. 37–43, `http://dx.doi.org/10.1016/j.optcom.2013.07.003`.

[114] N. P. BARNES AND J. C. BARNES, *Injection Seeding I: Theory*, **IEEE J. Quant. Electron.**, 29 (1993), pp. 2670–2683, `http://dx.doi.org/10.1109/3.250390`.

[115] SIOS MESSTECHNIK GMBH, *Stabilized HeNe Laser, SL 03-Series. (Data sheet; Werkprüfzeugnis)*, Am Vogelherd 46, 98693 Ilmenau, Germany, 2014, `http://www.sios-de.com/wp-content/uploads/2016/02/SL-03_e_2014.pdf`. Accessed 13 April 2016.

[116] HIGHFINESSE GMBH, *WS7 Super-Precision Wavelength Meter. (Technical Specifications; Calibration Certificate)*, Auf der Morgenstelle 14 D, 72076 Tübingen, Germany, 2016, `http://www.highfinesse.com/misc/miscfiles/07_WS7_web.pdf`. Accessed 12 February 2017.

[117] TOPTICA PHOTONICS AG, *DL pro, Grating Stabilized Diode Laser Head; DLC pro, Digital Laser Controller. (Production and Quality Control Data Sheets; Manuals)*, Lochhamer Schlag 19, 82166 Gräfelfing/München, Germany, 2014, `http://www.toptica.com/products/tunable-diode-lasers/ecdl-dfb-lasers/dl-pro`. Accessed 9 January 2018.

[118] SCHÄFTER+KIRCHHOFF GMBH, *Fiber Collimators 60FC-... (Catalog Extract)*, Kieler Str. 212, 22525 Hamburg, Germany, 2016, `http://www.sukhamburg.com/download/fk60fc_e.pdf`. Accessed 12 May 2016.

[119] P. MOULTON, *Ti-doped sapphire: tunable solid-state laser*, **Opt. News**, 8 (1982), p. 9, `http://dx.doi.org/10.1364/ON.8.6.000009`.

[120] P. F. MOULTON, *Spectroscopic and laser characteristics of Ti:*Al_2O_3, **J. Opt. Soc. Am. B**, 3 (1986), pp. 125–133, `http://dx.doi.org/10.1364/JOSAB.3.000125`.

[121] K. F. WALL AND A. SANCHEZ, *Titanium Sapphire Lasers*, **Lincoln Laboratory Journal**, 3 (1990), pp. 447–462, `https://www.ll.mit.edu/publications/journal/journalarchives03-3.html`.

[122] S. C. KUMAR, G. K. SAMANTA, K. DEVI, S. SANGUINETTI, AND M. EBRAHIM-ZADEH, *Single-frequency, high-power, continuous-wave fiber-laser-pumped Ti:sapphire laser*, **Appl. Opt.**, 51 (2012), pp. 15–20, `http://dx.doi.org/10.1364/AO.51.000015`.

[123] R. L. AGGARWAL, A. SANCHEZ, M. M. STUPPI, R. E. FAHEY, A. J. STRAUSS, W. R. RAPOPORT, AND C. P. KHATTAK, *Residual infrared absorption in as-grown and annealed crystals of Ti:*Al_2O_3, **IEEE J. Quant. Electron.**, 24 (1988), pp. 1003–1008, `http://dx.doi.org/10.1109/3.221`.

[124] P. LACOVARA, L. ESTEROWITZ, AND M. KOKTA, *Growth, spectroscopy, and lasing of titanium-doped sapphire*, **IEEE J. Quant. Electron.**, 21 (1985), pp. 1614–1618, `http://dx.doi.org/10.1109/JQE.1985.1072563`.

[125] A. SANCHEZ, A. J. STRAUSS, R. L. AGGARWAL, AND R. E. FAHEY, *Crystal growth, spectroscopy, and laser characteristics of Ti:*Al_2O_3, **IEEE J. Quant. Electron.**, 24 (1988), pp. 995–1002, `http://dx.doi.org/10.1109/3.220`.

[126] W. R. RAPOPORT AND C. P. KHATTAK, *Titanium sapphire laser characteristics*, **Appl. Opt.**, 27 (1988), pp. 2677–2684, `http://dx.doi.org/10.1364/AO.27.002677`.

[127] GT CRYSTAL SYSTEMS, LLC, *Ti:Sapphire; HEM Sapphire. (Data sheets)*, 35 Congress Street, Salem, MA 01970, USA, 2012, `https://gtat.com/products/ti-sapphire`. Accessed 19 January 2018.

[128] F. CANOVA, J.-P. CHAMBARET, G. MOUROU, M. SENTIS, O. UTEZA, P. DELAPORTE, T. ITINA, J.-Y. NATOLI, M. COMMANDRE, AND C. AMRA, *Complete characterization of damage threshold in titanium doped sapphire crystals with nanosecond, picosecond, and femtosecond laser pulses*, in: Laser-Induced Damage in Optical Materials: 2005, vol. 5991 of Proc. SPIE, pp. 599123–1–7, Boulder, CO, USA, 7 February 2006, `http://dx.doi.org/10.1117/12.638769`.

[129] B. JUNGBLUTH, *Gewinngeschaltete Ti:Saphir-Laser mit ultrabreitem Abstimmbereich*, Doctoral thesis, Rheinisch-Westfälische Technische Hochschule Aachen, Germany, 2011, `http://publications.rwth-aachen.de/record/52286`.

[130] R. PASCHOTTA, *Encyclopedia of Laser Physics and Technology*. Articles on, e.g., 'Ultrafast Lasers' and 'Ultrashort Pulses', `https://www.rp-photonics.com/encyclopedia.html`. Accessed 17 January 2018.

[131] V. MAGNI, *Resonators for solid-state lasers with large-volume fundamental mode and high alignment stability*, **Appl. Opt.**, 25 (1986), pp. 107–117, `http://dx.doi.org/10.1364/AO.25.000107`.

[132] J. P. LÖRTSCHER, J. STEFFEN, AND G. HERZIGER, *Dynamic stable resonators: a design procedure*, **Opt. Quant. Electron.**, 7 (1975), pp. 505–514, `http://dx.doi.org/10.1007/BF00619328`.

[133] J. STEFFEN, J. P. LÖRTSCHER, AND G. HERZIGER, *Fundamental mode radiation with solid-state lasers*, **IEEE J. Quant. Electron.**, 2 (1972), pp. 239–245, `http://dx.doi.org/10.1109/JQE.1972.1076948`.

[134] R. CHESLER AND D. MAYDAN, *Convex-Concave Resonators for TEM_{00} Operation of Solid-State Ion Lasers*, **J. Appl. Phys.**, 43 (1972), pp. 2254–2257, `http://dx.doi.org/10.1063/1.1661486`.

[135] W. KOECHNER, *Thermal Lensing in a Nd:YAG Laser Rod*, **Appl. Opt.**, 9 (1970), pp. 2548–2553, `http://dx.doi.org/10.1364/AO.9.002548`.

[136] H. KOGELNIK AND T. LI, *Laser Beams and Resonators*, **Appl. Opt.**, 5 (1966), pp. 1550–1567, `http://dx.doi.org/10.1364/AO.5.001550`.

[137] V. MAGNI, *Multielement stable resonators containing a variable lens*, **J. Opt. Soc. Am. A**, 4 (1987), pp. 1962–1969, `http://dx.doi.org/10.1364/JOSAA.4.001962`.

[138] S. De Silvestri, P. Laporta, and V. Magni, *Rod thermal lensing effects in solid-state laser ring resonators*, **Opt. Commun.**, 65 (1988), pp. 373–376, `http://dx.doi.org/10.1016/0030-4018(88)90106-X`.

[139] V. Wulfmeyer, *DIAL-Messungen von vertikalen Wasserdampfverteilungen. Ein Lasersystem für Wasserdampf- und Temperaturmessungen in der Troposphäre*, Doctoral thesis, Examensarbeit Nr. 34, Max-Planck-Institut für Meteorologie, Universität Hamburg, Germany, 1995.

[140] N. Hodgson and H. Weber, *Laser Resonators and Beam Propagation*, vol. 108 of Springer Series in Optical Sciences, Springer-Verlag, Berlin, 2nd ed., 2005, `http://dx.doi.org/10.1007/b106789`.

[141] P. H. Klein, *Thermal Conductivity, Thermal Diffusivity, and Specific Heat of Solids from a Single Experiment, with Application to $Y_{1.98}Nd_{0.02}O_3$*, **J. Appl. Phys.**, 38 (1967), pp. 1598–1603, `http://dx.doi.org/http://dx.doi.org/10.1063/1.1709729`.

[142] E. Hecht, *Optik*, Oldenbourg, München, 3rd ed., 2001.

[143] Q. Yin, H. Lu, and K. Peng, *Investigation of the thermal lens effect of the TGG crystal in high-power frequency-doubled laser with single frequency operation*, **Opt. Express**, 23 (2015), pp. 4981–4990, `http://dx.doi.org/10.1364/OE.23.004981`.

[144] A. A. Jalali, J. Rybarsyk, and E. Rogers, *Thermal lensing analysis of TGG and its effect on beam quality*, **Opt. Express**, 21 (2013), pp. 13741–13747, `http://dx.doi.org/10.1364/OE.21.013741`.

[145] J. D. Mansell, J. Hennawi, E. K. Gustafson, M. M. Fejer, R. L. Byer, D. Clubley, S. Yoshida, and D. H. Reitze, *Evaluating the effect of transmissive optic thermal lensing on laser beam quality with a Shack–Hartmann wavefront sensor*, **Appl. Opt.**, 40 (2001), pp. 366–374, `http://dx.doi.org/10.1364/AO.40.000366`.

[146] A. Kasapi, G. Y. Yin, and M. Jain, *Pulsed Ti:sapphire laser seeded off the gain peak*, **Appl. Opt.**, 35 (1996), pp. 1999–2004, `http://dx.doi.org/10.1364/AO.35.001999`.

[147] G. P. A. Malcolm and A. I. Ferguson, *Ti:sapphire laser pumped by a frequency doubled diode pumped Nd:YLF laser*, **Opt. Commun.**, 82 (1991), pp. 299–304, `http://dx.doi.org/10.1016/0030-4018(91)90463-N`.

[148] H. Walther and J. L. Hall, *Tunable dye laser with narrow spectral output*, **Appl. Phys. Lett.**, 17 (1970), pp. 239–242, `http://dx.doi.org/10.1063/1.1653382`.

[149] R. C. Jones, *A New Calculus for the Treatment of Optical Systems I. Description and Discussion of the Calculus*, **J. Opt. Soc. Am.**, 31 (1941), pp. 488–493, `http://dx.doi.org/10.1364/JOSA.31.000488`.

[150] A. L. BLOOM, *Modes of a laser resonator containing tilted birefringent plates*, **J. Opt. Soc. Am.**, 64 (1974), pp. 447–452, `http://dx.doi.org/10.1364/JOSA.64.000447`.

[151] D. R. PREUSS AND J. L. GOLE, *Three-stage birefringent filter tuning smoothly over the visible region: theoretical treatment and experimental design*, **Appl. Opt.**, 19 (1980), pp. 702–710, `http://dx.doi.org/10.1364/AO.19.000702`.

[152] X. ZHU, *Explicit Jones transformation matrix for a tilted birefringent plate with its optic axis parallel to the plate surface*, **Appl. Opt.**, 33 (1994), pp. 3502–3506, `http://dx.doi.org/10.1364/AO.33.003502`.

[153] R. W. P. DREVER, J. L. HALL, F. V. KOWALSKI, J. HOUGH, G. M. FORD, A. J. MUNLEY, AND H. WARD, *Laser phase and frequency stabilization using an optical resonator*, **Appl. Phys. B**, 31 (1983), pp. 97–105, `http://dx.doi.org/10.1007/BF00702605`.

[154] R. V. POUND, *Electronic Frequency Stabilization of Microwave Oscillators*, **Rev. Sci. Inst.**, 17 (1946), pp. 490–505, `http://dx.doi.org/10.1063/1.1770414`.

[155] V. WULFMEYER, M. RANDALL, A. BREWER, AND R. M. HARDESTY, *2-μm Doppler lidar transmitter with high frequency stability and low chirp*, **Opt. Lett.**, 25 (2000), pp. 1228–1230, `http://dx.doi.org/10.1364/OL.25.001228`.

[156] V. WULFMEYER AND M. RANDALL, *Frequency stable pulsed laser.* US Patent No. 6 633 596 B1, 14 October 2003.

[157] A. STRÄSSER, *Neue Prinzipien zur Realisierung von gepulsten, frequenzstabilisierten Lasern mit hoher mittlerer Leistung und exzellenter Strahlqualität*, Doctoral thesis, Universität Potsdam, Germany, 2007, `http://opus.kobv.de/ubp/volltexte/2008/1749/`.

[158] L. A. RAHN, *Feedback stabilization of an injection-seeded Nd:YAG laser*, **Appl. Opt.**, 24 (1985), pp. 940–942, `http://dx.doi.org/10.1364/AO.24.000940`.

[159] S. W. HENDERSON, E. H. YUEN, AND E. S. FRY, *Fast resonance-detection technique for single-frequency operation of injection-seeded Nd:YAG lasers*, **Opt. Lett.**, 11 (1986), pp. 715–717, `http://dx.doi.org/10.1364/OL.11.000715`.

[160] T. WALTHER, M. P. LARSEN, AND E. S. FRY, *Generation of Fourier-transform-limited 35-ns pulses with a ramp-hold-fire seeding technique in a Ti:sapphire laser*, **Appl. Opt.**, 40 (2001), pp. 3046–3050, `http://dx.doi.org/10.1364/AO.40.003046`.

[161] T. W. HÄNSCH AND B. COUILLAUD, *Laser frequency stabilization by polarization spectroscopy of a reflecting reference cavity*, **Opt. Commun.**, 35 (1980), pp. 441–444, `http://dx.doi.org/10.1016/0030-4018(80)90069-3`.

[162] F. RIEHLE, *Frequency Standards*, Wiley-VCH Verlag GmbH & Co. KGaA, Weinheim, 2005, `http://dx.doi.org/10.1002/3527605991`.

[163] E. D. BLACK, *An introduction to Pound–Drever–Hall laser frequency stabilization*, **Am. J. Phys.**, 69 (2001), pp. 79–87, `http://dx.doi.org/10.1119/1.1286663`.

[164] QUBIG GMBH, *EO-T80M5-NIR; ADU (Data sheets; Manuals)*, Balanstr. 57, D-81541 München, Germany, 2013, `http://www.qubig.com`. Accessed 9 February 2018.

[165] E. A. WHITTAKER, M. GEHRTZ, AND G. C. BJORKLUND, *Residual amplitude modulation in laser electro-optic phase modulation*, **J. Opt. Soc. Am. B**, 2 (1985), pp. 1320–1326, `http://dx.doi.org/10.1364/JOSAB.2.001320`.

[166] M. E. INNOCENZI, H. T. YURA, C. L. FINCHER, AND R. A. FIELDS, *Thermal modeling of continuous-wave end-pumped solid-state lasers*, **Appl. Phys. Lett.**, 56 (1990), pp. 1831–1833, `http://dx.doi.org/10.1063/1.103083`.

[167] A. C. DEFRANZO AND B. G. PAZOL, *Index of refraction measurement on sapphire at low temperatures and visible wavelengths*, **Appl. Opt.**, 32 (1993), pp. 2224–2234, `http://dx.doi.org/10.1364/AO.32.002224`.

[168] I. H. MALITSON, *Refraction and Dispersion of Synthetic Sapphire*, **J. Opt. Soc. Am.**, 52 (1962), pp. 1377–1379, `http://dx.doi.org/10.1364/JOSA.52.001377`.

[169] HIGHFINESSE GMBH, *WS Ultimate Wavelength Meter. (Technical Specifications; Calibration Certificate)*, Auf der Morgenstelle 14 D, 72076 Tübingen, Germany, 2016, `http://www.highfinesse.com/misc/miscfiles/08_WSU_1_web.pdf`. Accessed 12 February 2017.

[170] J. A. MCKAY, *Assessment of a multibeam Fizeau wedge interferometer for Doppler wind lidar*, **Appl. Opt.**, 41 (2002), pp. 1760–1767, `http://dx.doi.org/10.1364/AO.41.001760`.

[171] T. T. KAJAVA, H. M. LAURANTO, AND R. R. E. SALOMAA, *Fizeau interferometer in spectral measurements*, **J. Opt. Soc. Am. B**, 10 (1993), pp. 1980–1989, `http://dx.doi.org/10.1364/JOSAB.10.001980`.

[172] S. K. MUPPA, A. BEHRENDT, F. SPÄTH, V. WULFMEYER, S. METZENDORF, AND A. RIEDE, *Turbulent Humidity Fluctuations in the Convective Boundary Layer: Case Studies Using Water Vapour Differential Absorption Lidar Measurements*, **Boundary-Layer Meteorol.**, 158 (2016), pp. 43–66, `http://dx.doi.org/10.1007/s10546-015-0078-9`.

[173] V. WULFMEYER, S. K. MUPPA, A. BEHRENDT, E. HAMMANN, F. SPÄTH, Z. SORBJAN, D. D. TURNER, AND R. M. HARDESTY, *Determination of Convective Boundary Layer Entrainment Fluxes, Dissipation Rates, and the Molecular Destruction of Variances: Theoretical Description and a Strategy for Its Confirmation with a Novel Lidar System Synergy*, **J. Atmos. Sci.**, 73 (2016), pp. 667–692, `http://dx.doi.org/10.1175/JAS-D-14-0392.1`.

[174] E. HAMMANN, A. BEHRENDT, F. LE MOUNIER, AND V. WULFMEYER, *Temperature profiling of the atmospheric boundary layer with rotational Raman lidar during the HD(CP)^2 Observational Prototype Experiment*, **Atmos. Chem. Phys.**, 15 (2015), pp. 2867–2881, `http://dx.doi.org/10.5194/acp-15-2867-2015`.

[175] A. BEHRENDT, V. WULFMEYER, E. HAMMANN, S. K. MUPPA, AND S. PAL, *Profiles of second- to fourth-order moments of turbulent temperature fluctuations in the convective boundary layer: first measurements with rotational Raman lidar*, **Atmos. Chem. Phys.**, 15 (2015), pp. 5485–5500, `http://dx.doi.org/10.5194/acp-15-5485-2015`.

[176] A. MACKE, P. SEIFERT, H. BAARS, C. BARTHLOTT, C. BEEKMANS, A. BEHRENDT, B. BOHN, M. BRUECK, J. BÜHL, S. CREWELL, T. DAMIAN, H. DENEKE, S. DÜSING, A. FOTH, P. DI GIROLAMO, E. HAMMANN, R. HEINZE, A. HIRSIKKO, J. KALISCH, N. KALTHOFF, S. KINNE, M. KOHLER, U. LÖHNERT, B. L. MADHAVAN, V. MAURER, S. K. MUPPA, J. SCHWEEN, I. SERIKOV, H. SIEBERT, C. SIMMER, F. SPÄTH, S. STEINKE, K. TRÄUMNER, S. TRÖMEL, B. WEHNER, A. WIESER, V. WULFMEYER, AND X. XIE, *The HD(CP)^2 Observational Prototype Experiment (HOPE) – an overview*, **Atmos. Chem. Phys.**, 17 (2017), pp. 4887–4914, `http://dx.doi.org/10.5194/acp-17-4887-2017`.

[177] HD(CP)^2, *High definition clouds and precipitation for advancing climate prediction*, `http://www.hdcp2.eu`. Accessed 28 March 2018.

[178] S. METZENDORF, V. WULFMEYER, A. BEHRENDT, F. SPÄTH, AND A. RIEDE, *Frequency-Agile Ti:Sapphire Laser System with High Power and High Pulse Energy for Spectroscopic Applications*, in: The European Conference on Lasers and Electro-Optics (CLEO Europe 2015), no. CA-12.5, Munich, Germany, 21–25 June 2015, `http://www.osapublishing.org/abstract.cfm?URI=CLEO_Europe-2015-CA_12_5`.

[179] SABLE, *Surface Atmospheric-Boundary-Layer Exchange*, `https://www.uni-hohenheim.de/ipm_lidar/SABLE2014/SABLE.htm`. Accessed 13 July 2018.

[180] S. METZENDORF, F. SPÄTH, A. BEHRENDT, A. RIEDE, S. MUPPA, AND V. WULFMEYER, *High-Resolution Water Vapor DIAL Measurements with a 10-W Ti:sapphire Laser*, in: 28th International Laser Radar Conference (ILRC 2017), no. 326, Bucharest, Romania, 25–30 June 2017, `http://ilrc28.inoe.ro/`.

[181] LAFE, *Land–Atmosphere Feedback Experiment*, `https://www.arm.gov/research/campaigns/sgp2017lafe`. Accessed 13 July 2018.

[182] V. WULFMEYER, D. D. TURNER, B. BAKER, R. BANTA, A. BEHRENDT, T. BONIN, W. A. BREWER, M. BUBAN, A. CHOUKULKAR, E. DUMAS, R. M. HARDESTY, T. HEUS, J. INGWERSEN, D. LANGE, T. R. LEE, S. METZENDORF, S. K. MUPPA, T. MEYERS, R. NEWSOM, M. OSMAN, S. RAASCH, J. SANTANELLO, C. SENFF, F. SPÄTH, T. WAGNER, AND T. WECKWERTH, *A New Research Approach for Observing*

and Characterizing Land–Atmosphere Feedback, **Bull. Am. Meteorol. Soc.**, 99 (2018), pp. 1639–1667, `http://dx.doi.org/10.1175/BAMS-D-17-0009.1`.

[183] D. D. TURNER, V. WULFMEYER, A. BEHRENDT, T. A. BONIN, A. CHOUKULKAR, R. K. NEWSOM, W. A. BREWER, AND D. R. COOK, *Response of the Land-Atmosphere System Over North-Central Oklahoma During the 2017 Eclipse*, **Geophys. Res. Lett.**, 45 (2018), pp. 1668–1675, `http://dx.doi.org/10.1002/2017GL076908`.

[184] D. H. LENSCHOW, V. WULFMEYER, AND C. SENFF, *Measuring Second- through Fourth-Order Moments in Noisy Data*, **J. Atmos. Oceanic Technol.**, 17 (2000), pp. 1330–1347, `http://dx.doi.org/10.1175/1520-0426(2000)017<1330:MSTFOM>2.0.CO;2`.

[185] WMO, *World Meteorological Organization – Observing Systems Capability Analysis and Review Tool (OSCAR).* Requirement # 704, `https://www.wmo-sat.info/oscar/requirements/view/704`. Accessed 26 July 2018.

[186] B. WITSCHAS, C. LEMMERZ, AND O. REITEBUCH, *Horizontal lidar measurements for the proof of spontaneous Rayleigh–Brillouin scattering in the atmosphere*, **Appl. Opt.**, 51 (2012), pp. 6207–6219, `http://dx.doi.org/10.1364/AO.51.006207`.

[187] B. E. GROSSMANN AND E. V. BROWELL, *Spectroscopy of water vapor in the 720-nm wavelength region: Line strengths, self-induced pressure broadenings and shifts, and temperature dependence of linewidths and shifts*, **J. Mol. Spectrosc.**, 136 (1989), pp. 264–294, `http://dx.doi.org/10.1016/0022-2852(89)90336-6`.

[188] B. E. GROSSMANN AND E. V. BROWELL, *Water-vapor line broadening and shifting by air, nitrogen, oxygen, and argon in the 720-nm wavelength region*, **J. Mol. Spectrosc.**, 138 (1989), pp. 562–595, `http://dx.doi.org/10.1016/0022-2852(89)90019-2`.

[189] E. V. BROWELL, S. ISMAIL, AND B. E. GROSSMANN, *Temperature sensitivity of differential absorption lidar measurements of water vapor in the 720-nm region*, **Appl. Opt.**, 30 (1991), pp. 1517–1524, `http://dx.doi.org/10.1364/AO.30.001517`.

[190] F. A. THEOPOLD AND J. BÖSENBERG, *Differential Absorption Lidar Measurements of Atmospheric Temperature Profiles: Theory and Experiment*, **Journal of Atmospheric and Oceanic Technology**, 10 (1993), pp. 165–179, `http://dx.doi.org/10.1175/1520-0426(1993)010<0165:DALMOA>2.0.CO;2`.

[191] M. ENDEMANN AND R. L. BYER, *Simultaneous remote measurements of atmospheric temperature and humidity using a continuously tunable IR lidar*, **Appl. Opt.**, 20 (1981), pp. 3211–3217, `http://dx.doi.org/10.1364/AO.20.003211`.

[192] B. WITSCHAS, C. LEMMERZ, AND O. REITEBUCH, *Daytime measurements of atmospheric temperature profiles (2–15 km) by lidar utilizing Rayleigh–Brillouin scattering*, **Opt. Lett.**, 39 (2014), pp. 1972–1975, `http://dx.doi.org/10.1364/OL.39.001972`.

[193] A. GATEJ, *Modeling and compensation of thermally induced optical effects in highly loaded optical systems*, Doctoral thesis, Rheinisch-Westfälische Technische Hochschule Aachen, Germany, 2014, `http://publications.rwth-aachen.de/record/444604`.

[194] F. SPÄTH. Private communication, July 2018.

List of Publications

Peer-Reviewed Publications:

- V. Wulfmeyer, D. D. Turner, B. Baker, R. Banta, A. Behrendt, T. Bonin, W. A. Brewer, M. Buban, A. Choukulkar, E. Dumas, R. M. Hardesty, T. Heus, J. Ingwersen, D. Lange, T. R. Lee, S. Metzendorf, S. K. Muppa, T. Meyers, R. Newsom, M. Osman, S. Raasch, J. Santanello, C. Senff, F. Späth, T. Wagner, and T. Weckwerth, *A New Research Approach for Observing and Characterizing Land–Atmosphere Feedback*, **Bull. Am. Meteorol. Soc.**, 99 (2018), pp. 1639–1667, `https://doi.org/10.1175/BAMS-D-17-0009.1`.

- F. Späth, A. Behrendt, S. K. Muppa, S. Metzendorf, A. Riede, and V. Wulfmeyer, *3-D water vapor field in the atmospheric boundary layer observed with scanning differential absorption lidar*, **Atmos. Meas. Tech.**, 9 (2016), pp. 1701–1720, `http://dx.doi.org/10.5194/amt-9-1701-2016`.

- S. K. Muppa, A. Behrendt, F. Späth, V. Wulfmeyer, S. Metzendorf, and A. Riede, *Turbulent Humidity Fluctuations in the Convective Boundary Layer: Case Studies Using Water Vapour Differential Absorption Lidar Measurements*, **Boundary-Layer Meteorol.**, 158 (2016), pp. 43–66, `http://dx.doi.org/10.1007/s10546-015-0078-9`.

- F. Späth, A. Behrendt, S. K. Muppa, S. Metzendorf, A. Riede, and V. Wulfmeyer, *High-resolution atmospheric water vapor measurements with a scanning differential absorption lidar*, **Atmos. Chem. Phys. Discuss.**, 14 (2014), pp. 29057–29099, `http://dx.doi.org/10.5194/acpd-14-29057-2014`.

- F. Späth, S. Metzendorf, A. Behrendt, H.-D. Wizemann, G. Wagner, and V. Wulfmeyer, *Online/offline injection seeding system with high frequency-stability and low crosstalk for water vapor DIAL*, **Opt. Commun.**, 309 (2013), pp. 37–43, `http://dx.doi.org/10.1016/j.optcom.2013.07.003`.

Selected Contributions to Conferences:

- S. Metzendorf, F. Späth, A. Behrendt, A. Riede, S. Muppa, and V. Wulfmeyer, *High-Resolution Water Vapor DIAL Measurements with a 10-W Ti:sapphire Laser*, in: 28th International Laser Radar Conference (ILRC 2017), no. 326, Bucharest, Romania, 25–30 June 2017, `http://ilrc28.inoe.ro`.
- S. Metzendorf, V. Wulfmeyer, A. Behrendt, F. Späth, and A. Riede, *Frequency-Agile Ti:Sapphire Laser System with High Power and High Pulse Energy for Spectroscopic Applications*, in: The European Conference on Lasers and Electro-Optics (CLEO Europe 2015), no. CA-12.5, Munich, Germany, 21–25 June 2015, `http://www.osapublishing.org/abstract.cfm?URI=CLEO_Europe-2015-CA_12_5`.
- S. Metzendorf, A. Behrendt, F. Späth, and V. Wulfmeyer, *High-Power Laser Transmitter of the UHOH Water Vapor DIAL*, in: 26th International Laser Radar Conference (ILRC 2012), no. S1P-11, Porto Heli, Greece, 25–29 June 2012.
- S. Metzendorf, D. Depenheuer, T. Führer, and T. Walther, *Vertikal emittierende Laserdioden als Seed-Quelle eines gepulsten Titan:Saphir-Lasers*, in: Verhandl. DPG, no. Q 21.71, Hannover, Germany, 8–12 March 2010, `http://www.dpg-verhandlungen.de/year/2010/conference/hannover/part/q/session/21/contribution/71`.

Acknowledgments

I would like to express my gratitude to all who contributed to the success of this work.

First, I would like to thank Prof. Dr. Volker Wulfmeyer for the opportunity to carry out this doctoral thesis at the *Institute of Physics and Meteorology* and for being my supervisor. With his valuable knowledge, enabling of funding, and the confidence he placed in me, he supported me greatly.

I am also very thankful to Prof. Dr. Paolo Di Girolamo for the kind readiness of being the co-reviewer of my dissertation, despite some challenges which arose during the postal delivery of my thesis. My sincere thanks go to the third anonymous reviewer, as well as Prof. Dr. Thilo Streck and Prof. Dr. Uwe Beifuß for being members of the defense committee.

I thank Dr. Andreas Behrendt, head of the remote sensing group, for his advice, especially during the preparation of my presentations. I have appreciated working closely together with our team members Dr. Andrea Riede, Dr. Florian Späth, Dr. Eva Hammann, Dr. Shravan Muppa, and Dr. Diego Lange. Even during intense times (often related to field campaigns), we always managed to get things up and running. Thank you for accompanying me on my doctoral journey!

I am especially grateful to master mechanic Alexander Geißler for the design and manufacturing of numerous parts of the laser system. Most notably, I will remember our intensive and productive work on the crystal cooling mounts. Thanks to him I was able to considerably expand my knowledge in the area of mechanics.

I would like to acknowledge Dr. Götz Zinner from *Bernhard Halle Nachfl. GmbH* for providing the simulated transmission curves of the birefringent filter, Dr. Enrico Vogt from *Qubig GmbH* for providing the original *Mathematica* program for the calculation of the PDH error signal, and Dipl.-Ing. Stefan Recker from the *Institute for Engineering Design and Industrial Design (IKTD)* at *University of Stuttgart* for the precise measurement of the circular-cut crystal cooling mount's clamp shells.

Furthermore, I would like to thank the following people: Dr. Gerd Wagner, former member of the group, for answering my questions about the previous laser system and useful hints for the new development, Dr. Hans-Stefan Bauer for providing information about the weather situation for the discussed atmospheric measurements cases, Priv.-Doz. Dr. Hans-Dieter Wizemann and Monika Walther for lending me laboratory equipment, the institute's administrative assistants, Elisabeth Ott and Andrea Haley, for the help with big and small things, as well as Stephan, Thomas, Oliver, Josipa, and all other members of *IPM* for fruitful discussions about professional and personal topics.

I am particularly indebted to all proofreaders, especially Rudolf and Maria-Inti.

I would like to express my heartful gratitude to my family for their permanent encouragement and faithful support.

List of Abbreviations

ABL	Atmospheric Boundary Layer
AOI	Angle of Incidence
APD	Avalanche Photodiode
ARM	*Atmospheric Radiation Measurement Climate Research Facility*
BBO	Beta-Barium Borate
CAD	Computer-Aided Design
COPS	Convective and Orographically-induced Precipitation Study
DAQ	Data Acquisition System
DC	Direct Current
DFB	Distributed Feedback
DFG	*Deutsche Forschungsgemeinschaft* (German Research Foundation)
DLR	*Deutsches Zentrum für Luft- und Raumfahrt* (German Aerospace Center)
DIAL	Differential Absorption Lidar
ECDL	External-Cavity Diode Laser
EOD	Electro-Optic Deflector
EOM	Electro-Optic Modulator
FC/APC	Ferrule Connector Angled Physical Contact
FC/PC	Ferrule Connector Physical Contact
FEA	Finite Element Analysis
FOM	Figure of Merit
FSR	Free Spectral Range
FWHM	Full Width at Half Maximum
GSM	Global System for Mobile communications
HeNe	Helium–Neon
HD(CP)^2	High Definition Clouds and Precipitation for advancing Climate Prediction

HITRAN	High Resolution Transmission database
HOPE	HD(CP)^2 Observational Prototype Experiment
IBL	*IBL Innovative Berlin Laser*
IOP	Intensive Observation Period
IPCC	*Intergovernmental Panel on Climate Change*
IPM	*Institute of Physics and Meteorology*
IR	Infrared
KTP	Potassium Titanyl Phosphate
LAFE	Land–Atmosphere Feedback Experiment
MEMS	Micro-Electro-Mechanical System
MgO:LN	Magnesium Oxide-doped Lithium Niobate
MOPA	Master-Oscillator Power-Amplifier
NCAR	*National Center for Atmospheric Research*
Nd:YAG	Neodymium-doped Yttrium Aluminum Garnet
OPO	Optical Parametric Oscillator
OSA	Optical Spectrum Analyzer
PBSC	Polarizing Beam Splitter Cube
PCI	Peripheral Component Interconnect
PDH	Pound–Drever–Hall
PID	Proportional–Integral–Derivative
PLA	*Proton Laser Applications*
PPI	Plan Position Indicator
RF	Radio Frequency
RHI	Range–Height Indicator
RMS	Root Mean Square
RRL	Rotational Raman Lidar
RS-232	Recommended Standard 232 (for serial communication)
TEM	Transverse Electromagnetic Mode
TGG	Terbium Gallium Garnet
Ti:sapphire	Ti:Al$_2$O$_3$, Titanium-doped sapphire, or titanium–sapphire
Tm:LuYAG	Thulium-doped Lutetium Yttrium Aluminum Garnet
TR32	Transregional Collaborative Research Centre 32
TTL	Transistor–Transistor Logic
SABLE	Surface Atmospheric-Boundary-Layer Exchange
SBS	Stimulated Brillouin Scattering
SGP	Southern Great Plains
SHG	Second Harmonic Generation
SOP	Special Observation Period
UPS	Uninterruptible Power Supply
UTC	Coordinated Universal Time
USB	Universal Serial Bus
WMO	*World Meteorological Organization*